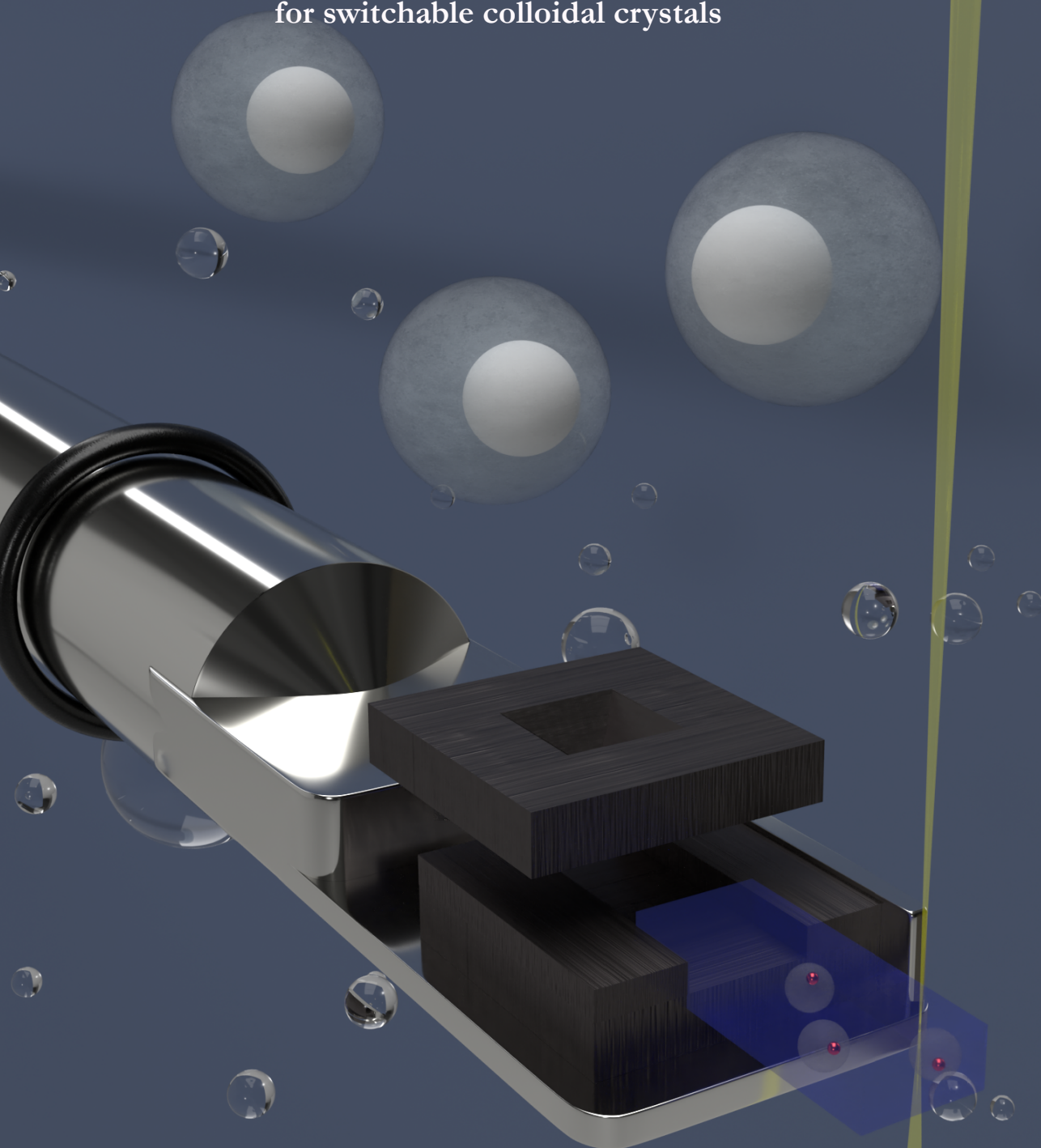


Rattle-type particles

Tuning colloidal interactions and electrokinetics
for switchable colloidal crystals



Tom A.J. Welling

Rattle-type particles

**Tuning colloidal interactions and electrokinetics for
switchable colloidal crystals**

Cover: Illustration of a dedicated liquid-cell electron microscopy holder surrounded by rattle-type particles designed by Albert Grau-Carbonell.

PhD thesis, Utrecht University, The Netherlands, June 2022

ISBN 978-94-6423-780-1

A digital version of this thesis is available at <http://www.colloid.nl>

Rattle-type particles

Tuning colloidal interactions and electrokinetics for switchable colloidal crystals

Rammelaardeeltjes

Het afstemmen van kolloïdale interacties en elektrokinetiek voor
schakelbare kolloïdale kristallen

(met een samenvatting in het Nederlands)

Proefschrift

ter verkrijging van de graad van doctor aan de Universiteit Utrecht
op gezag van de rector magnificus, prof. dr. H.R.B.M. Kummeling,
ingevolge het besluit van het college voor promoties in het openbaar te verdedigen
op 1 juni 2022 des middags te 12.15 uur

door

Thomas Arnoldus Josephus Welling

geboren op 22 februari 1993

te Oosterhout

Promotor: Prof. dr. A. van Blaaderen

Co-promotoren: Dr. ir. M.A. van Huis

Dr. J. de Graaf

The research in this thesis was financially supported by the European Research Council (ERC) via the ERC Consolidator Grant NANO-INSITU (grant No. 683076).

Contents

Chapter 1.	Introduction	1
Chapter 2.	Observation of unrestricted 3D Brownian motion of nanoparticles using liquid-phase scanning transmission electron microscopy	13
Chapter 3.	Hydrodynamic interactions between the core and shell in rattle-type particles	37
Chapter 4.	Tunability of interactions between the core and shell in rattle-type particles studied with liquid-cell electron microscopy	57
Chapter 5.	Frequency-controlled electrophoretic mobility of a particle within a porous, hollow shell	93
Chapter 6.	Switchable colloidal crystals using assemblies of rattle-type particles with index-matched shells and alternating current electric fields	135
	Bibliography	155
	Summary	171
	Samenvatting	175
	Acknowledgements	179
	List of Publications	183
	Oral and Poster Presentations	185
	About the author	187

1

Introduction

In this thesis we investigate rattle-type, also referred to in literature as yolk-shell, colloidal particles, which consist of a core particle smaller than a micron in diameter within a hollow shell. In particular, we study the electrostatic, van der Waals and hydrodynamic interactions between the core and the shell as well as how the core particle can be manipulated with an electric field. Lastly, we use what we learned to show a proof-of-principle of how self-assembled rattle-type particles can function as a switchable photonic colloidal crystal.

1.1. COLLOIDAL PARTICLES

Colloids are generally defined as particles with a size between 1 and 1000 nm, in at least one direction, dispersed in a solvent. Colloids are small compared to macroscopic objects but large compared to atoms and molecules. They are an integral part of our daily lives, as colloids are used in toothpaste, food, paints, displays (such as electronic-ink, e-ink displays) and other products. A characteristic property of colloidal particles is that they undergo diffusive Brownian motion. Even though he was not the first to observe it, Brownian motion is named after Robert Brown, who in 1827 used a microscope to observe the motion of pollen grains, as it is often described in textbooks. In 1991 a researcher (D.H. Deutsch)¹ was doubting whether Brown actually investigated 'real' diffusive Brownian motion in his research. His arguments were that Brown's system was too noisy and that he did not use cover slips which at the time were not yet invented. He furthermore argued that the microscope that Brown used was not powerful enough, the pollen particles were much too large, too light or too heavy, which meant Brown had been looking at vibrations or drying-induced motion etc. However, G. Cadée countered in a letter to Nature, that Deutsch had not read Brown's original work that well as Brown clearly stated that he did not look at the motion of pollen particles themselves:² "*if he had read Brown's papers more thoroughly, he would have noted that Brown did not describe the movements of pollen grains, which indeed are too large for Brownian motion, but described movements of particles inside pollen grains (see also the title of his paper).*" He was referring to the paper by Brown³ entitled "*A brief account of microscopical observations made in the*

month of June, July and August, 1827, on the particles contained in the pollen of plants and the general existence of active molecules." In short, Brown used the pollen particles and the motion of the micron-sized particles therein like a yolk-shell or rattle-type system, which is a system that will be discussed at length in this thesis. This also makes it much less likely that even without the use of cover glasses his observations were influenced by external vibrations and/or drying forces. Brown also mentioned himself that in some grasses, the membrane of the pollen was so transparent that the motion of the particles could be seen inside the pollen grains, where currents or evaporation could be excluded as a cause of the movements observed. Deutsch did not agree.⁴ B.J. Ford, however, had already convinced most scientists that Brown had observed 'real' Brownian motion as he had redone Brown's experiments as closely as he could and made video recordings of what he observed.⁵

Back in the day the leading theoretical improvement was made by Albert Einstein who used the colloid-atom analogy to explain the so-called Brownian motion in 1905.⁶ Shortly after, Jean Baptiste Perrin successfully tested Einstein's theory experimentally in 1908 by measuring both the translational and rotational diffusion of particles using light microscopy.⁷ Brownian motion occurs due to the difference in size between a colloidal particle and the atoms or molecules of the solvent. A colloid is hit by solvent molecules constantly, but the number of collisions is not entirely equal during a very short period of time. Due to the size of the colloidal particle, the net momentum transfer is significant enough to move the particle. The short displacements and uncorrelated fluctuations in the collisions with the fluid molecules lead to a random walk of the colloidal particles through the fluid.

Brownian motion is driven by thermal energy and allows colloidal particles to explore their environment. If the thermal energy dominates the gravitational energy, colloidal suspensions may reach thermodynamic equilibrium states. The height distribution of the particles is then determined by interactions with other particles. Colloidal particles show thermodynamic properties similar to those of atomic systems, which make them a superb model system to study condensed matter physics phenomena such as homogeneous^{8,9} and heterogeneous¹⁰ crystal nucleation.¹¹ Colloidal crystals are good examples of the analogy between colloids and atomic systems as they can be used to study crystallization and melting.^{12,13} Colloidal particles are easier to directly observe by optical or electron microscopy than atoms due to their longer length-scale and their much slower diffusion. Furthermore, there are extensive possibilities to make a diversity of colloidal particles with different sizes,¹⁴ shapes¹⁵ and surface charges.^{16,17} Moreover, the interactions between colloids can be more easily tuned than those of atoms or molecules by the ability to change the temperature,¹⁸ solvent properties (such as ionic strength)^{19,20} as well as to apply external fields such as electric^{17,21-24} or magnetic fields^{25,26} in order to form different colloidal structures.

1.2. RATTLE-TYPE PARTICLES

Rattle-type particles or yolk-shell particles are hollow particles incorporating a core particle.²⁷⁻³² When the void of the hollow particle is filled with a fluid, the core can be made to be mobile and able to explore the volume within the shell through Brownian motion,^{33,34} as indicated in Figure 1.1 The small core particles are often metal or metal oxide nanoparticles

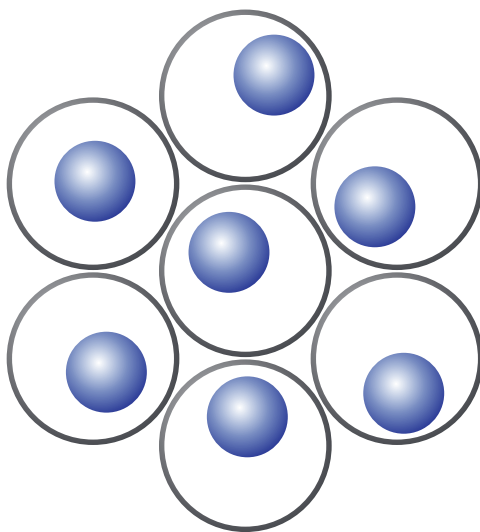


Figure 1.1: Rattle-type particles consisting of a mobile core particle within a shell, where the shells are assembled on a hexagonal lattice.

with specific catalytic,^{31,35} optical^{34,36} or magnetic³³ properties. Small ions and molecules can travel through the porous shell, which allows them to interact with the core particle inside. Rattle-type particles are promising for application in catalysis,^{31,37–42} biomedicine,^{43,44} drug delivery,^{45,46} sensing,^{47–51} adsorbents,^{52,53} lithium-ion batteries,⁵⁴ optical devices,^{34,36} and many other fields.

The work in our group in collaboration with the group of Prof. Nagao (Tohoku University, Sendai, Japan) is focused on the interactions within rattle-type particles. The aim is to understand the interactions with and without external fields applied, so that these particles can be used, for instance, to make switchable colloidal crystal devices. Colloidal crystals composed of complex building blocks are promising materials for optical,⁵⁵ electrical⁵⁶ and biomedical applications.⁵⁷ Soft materials consisting of building blocks with movable parts is an effective way to tune their optical or electrical properties with external stimuli. This would diversify the applications of colloidal crystals as chemical⁵⁸ or biological sensors,⁵⁹ displays^{60,61} and printings.^{62,63} Thermosensitive polymers^{64,65} or the application of external electric and magnetic fields^{66,67} are ways of controlling the arrangement of building blocks in the formation of colloidal crystals.

Previously reported switchable colloidal systems required reconfiguration or changes in the distances between the building blocks via external magnetic^{68–70} or electric fields.^{19,23,71} Colloidal crystals with rattle particles as building blocks are promising materials for switchable colloidal crystals without such a requirement.^{33,34} It was previously shown that the shells could be assembled on a 2D lattice and that the position of the core particles within the structure could subsequently be controlled by an external magnetic field³³ or AC electric

field.³⁴ The assembled structures of these yolk-shell particles had a lattice constant similar to the wavelength of visible light. If the outer shells of these particles are refractive index-matched with the solvent inside and outside these shells, while the cores are not index-matched, these structures would have uniquely switchable optical properties. Without an external field the random positions of the core particles within the shell due to colloidal diffusion would lead to significantly broadening of the Bragg peaks. However, an external electric or magnetic field could position dielectric or magnetic cores at well-defined positions within the shells and sharpen the Bragg peaks.

1.3. COLLOIDAL INTERACTIONS

Colloidal particles in a medium interact through various ways. The most common interactions include steric, van der Waals, and electrostatic interactions.^{72–75} Steric interactions describe the repulsion when particles, or the polymer chains on their surfaces, begin to overlap and are thus short-ranged. Van der Waals interactions originate from fluctuating dipole moments and depend on the difference in refractive index between the particle and the dispersing medium. When two particles are identical and have a different refractive index than the medium, the van der Waals interaction between them is always attractive. If the refractive index of the medium is the same as that of the particles at all frequencies, the van der Waals interaction vanishes. Finally, particles usually carry a net charge. When a charged colloidal particle is immersed in an electrolyte solution, mobile electrolyte ions form an ionic cloud around the particle due to electrostatic interactions between the ions, and the particle surface charges. Close to the particle surface the counter-ion concentration is higher than the co-ion concentration. Due to the thermal motion of the ions, the distribution of the counter-ions around the particle has a diffuse structure and decays as a function of distance from the particle surface. The diffuse ionic cloud around the particle is called the electric double layer. The presence of the electric double layer around a charged particle changes how colloidal particles interact with each other. In vacuum, where there is no electric double layer, the interaction between charged particles would drop off linearly with the inverse of the distance between the particles. In solution, the ions in the electric double layer screen the interaction between the charged particles.

Derjaguin and Landau, and Verwey and Overbeek were two pairs of scientists who independently derived a theory to explain the interactions between two charged spherical particles. The aptly named Derjaguin-Landau-Verwey-Overbeek (DLVO) theory assumes that the electrostatic forces and the van der Waals forces are independent and can be summed up at each interacting distance for two particles.^{72–75} The potential of mean force

$$U = U_{\text{VdW}} + U_{\text{ES}} \quad (1.1)$$

is used to calculate the full interaction potential via DLVO theory. Many additional assumptions such as a constant electric potential on the surface of the particles are also made.^{72–75} The van der Waals potential between two spheres is calculated as

$$U_{\text{VdW}} = -\frac{A}{3} \left(\frac{a_1 a_2}{r^2 - (a_1 + a_2)^2} + \frac{a_1 a_2}{r^2 - (a_1 - a_2)^2} + \frac{1}{2} \log \left(\frac{r^2 - (a_1 + a_2)^2}{r^2 - (a_1 - a_2)^2} \right) \right) \quad (1.2)$$

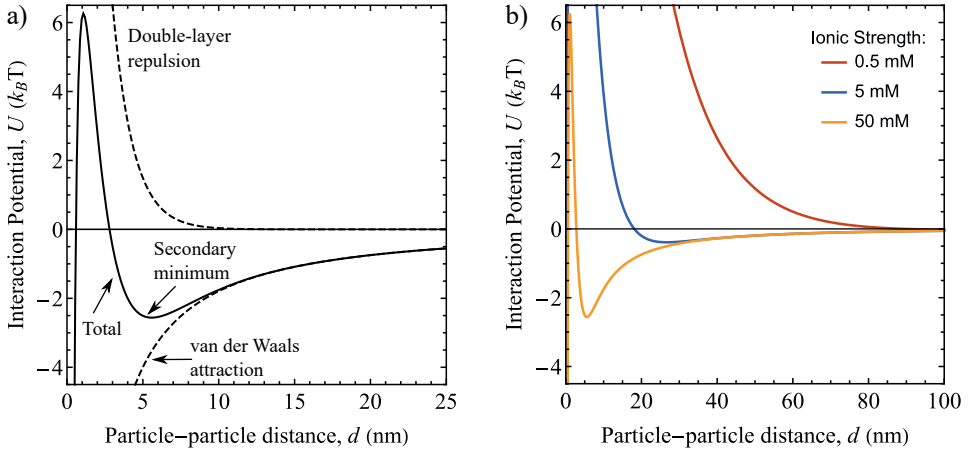


Figure 1.2: Interaction potentials between two charged colloidal spheres calculated using Equations 1.2 and 1.3. a) Interaction potential for two charged spheres showing both the double-layer repulsion and van der Waals attraction contributions. The spheres have a radius of 250 nm and a surface potential of 15 mV. The Hamaker constant was $4.6 \cdot 10^{-21}$ J and the ionic strength was 50 mM. b) Influence of the ionic strength on the interaction potential. Besides the ionic strength, the same parameters were used as in (a).

and the electrostatic interaction between two charged spherical particles is calculated via

$$U_{\text{ES}} = \lambda_b \frac{Q_1 Q_2}{(1 + \kappa a_1)(1 + \kappa a_2)} \frac{e^{-\kappa(r - a_1 - a_2)}}{r}. \quad (1.3)$$

Here A is the Hamaker constant, a is the radius of the charged particles, r the center-to-center distance, λ_b is the Bjerrum length, Q is the number of charges, e is the elementary charge, ϵ_0 is the permittivity of the vacuum, ϵ_m is the dielectric constant of the medium, κ is the inverse Debye screening length which is the distance from the particle surface at which the inhomogeneous distributions in the ion concentrations drop to $1/e$ of the values at the particle surface and is usually interpreted as the distance over which charged particles interact significantly as compared to their thermal energy. The Debye screening length κ^{-1} depends on the ion concentration that screens the charge on the particle. The inverse Debye screening length can be calculated as follows:

$$\kappa = \sqrt{\frac{2N_A c e^2}{\epsilon_0 \epsilon_m k_B T}} \quad (1.4)$$

where N_A is Avogadro's number, and c is the ion concentration in the bulk. According to the Debye screening length formula one can tune the repulsive range between two charged particles by changing the salt concentration of the electrolyte solution. Typical Debye screening lengths in water range from several hundred nanometer for deionized water to a few nanometer at high salt concentrations.

Interaction potentials between two charged spheres are shown in Figure 1.2. It shows how the van der Waals attraction and electrostatic repulsion combine to form the complete interaction potential in DLVO theory. A secondary minimum in the interaction potential is possible when the double-layer repulsion is relatively short-ranged as compared to the van der Waals attraction. The range of the repulsion is tunable via the ionic strength (as well as the surface charge) as shown in Figure 1.2b.

The analogy between colloidal and atomic systems breaks down when comparing dynamics rather than thermodynamic equilibrium properties. The direct inter-particle interactions previously mentioned represent atoms and molecules well. However, the movement of a colloidal particle through its dispersion displaces the fluid in between particles which consequently induces a force on another particle, which does not happen for atoms as they move in vacuum. These indirect interactions are called hydrodynamic interactions. Due to their origin being the same as that of the Brownian motion of particles, studying dynamics of colloidal particles is rather complicated.

In this thesis we investigate the interactions, such as van der Waals and electrostatic interactions, of the previously mentioned rattle-type particles. As the sphere-in-shell geometry is not as simple as two charged spherical particles, the interactions cannot be described analytically by DLVO. However, the same principles of double layers and van der Waals interactions still apply and can be studied via experiments and finite-element calculations. Furthermore, the rattle geometry is perfect for studying hydrodynamic interactions of a single particle interacting via the medium with its environment. It is of great interest to study these complex interactions on a single particle level in an enclosed environment. Lastly, we also manipulate the interactions within the rattle geometry by using external electric fields. The influence of external electric fields on charged colloidal particles in liquid is discussed in the next section.

1.4. ELECTRIC FIELDS AND CHARGED COLLOIDS

External fields are useful tools for manipulating colloids to exhibit physical behavior or to form structures that would be unattainable in equilibrium. They can influence colloids in a variety of ways. First, electric fields can induce the motion of a charged particle directly via electrophoresis. This is applied in electrophoretic displays currently on the market for so-called e-readers.^{76–78} The motion of charged particles is used to manipulate the optical appearance of display pixels filled with particles. For example, oppositely charged and differently colored pigment particles can be manipulated by an electric field to modify the grey values of a pixel.^{76,77} Besides directly moving charged particles using electrophoresis, charged particles can also be manipulated by inducing polarization using electric fields. Polarization by electric fields can be due to a large dielectric constant difference between a particle and the solvent. This is only possible when particles are of the order of a micron and the effect disappears quickly when going to smaller particle sizes as the effect scales with the volume of the particle. For smaller particles, polarization effects can still affect the interactions between particles, but in a different way. In this case the frequency of the electric field is chosen to be around or below the frequency that is associated with the ions moving a distance that is comparable to

the double layer thickness. In this situation the double layer, which can extend far beyond the particle size, is polarized and causes a change in the interactions between particles. An example is the electric field induced chaining of 30 nm gold particles in water.⁷⁹

In the section on rattle-type particles above we mentioned that a switchable colloidal crystal can be made with such particles if the position of the core particle can be controlled via external stimuli. An external electric field could potentially be used to make such a switchable colloidal crystal using either electrophoresis or polarization effects. If the shells are assembled on a lattice, the core particle could be used to force the core particle to one side using electrophoresis. On the other hand, the core particle could be forced to remain in the middle of the shell by polarizing both the double layer around the particle and the double layer originating from the inside of the shell. Additionally, the ions can also move through the porous shells under the influence of the electric field and/or indirectly by flow induced by the electric fields. These possibilities will be explored in this thesis.

1.5. MICROSCOPY

Colloidal particles have the benefit that they can be imaged directly with microscopy techniques, due to their convenient size. Both liquid-cell electron microscopy^{80,81} and confocal laser scanning microscopy^{82,83} were used in this thesis. Liquid-cell electron microscopy uses high-energy electrons to image particles and yields the highest spatial resolution. However, imaging with electrons through liquids is a relatively new technique and causes a multitude of problems that we will discuss later in this section. Confocal microscopy on the other hand is a much more established technique. In confocal microscopy, out-of-focus light is blocked out by a small pinhole in the focal plane. As a result only a thin slice of the sample contributes to the image formation. In this way, several slices at different heights in the sample can be used to create a 3D image of the sample. This is a huge advantage over conventional light microscopy or electron microscopy where the image represents a 2D projection of a 3D sample. By incorporating a fluorescent dye into the particles and exciting it with a laser, the background signal can be greatly reduced. Optical sectioning and fluorescent labeling allows for the recording of high signal-to-noise images or 3D ‘image stacks’ that allow for reliable tracking of the movement of the particle in 3D.⁸²⁻⁸⁴

1.5.1. Electron microscopy

Electron microscopy has several advantages compared to light microscopy. Due to the short wavelength of high-energy electrons the resolution of electron microscopy is significantly better than that of light microscopy. Imaging with an electron microscope on a thin sample in vacuum can yield Ångström spatial resolution.^{85,86} Electrons also interact with matter in a different way than light and as such can generate signals differing from mass-thickness contrast and fluorescence. However, the strong interaction of electrons with the sample also leads to considerable disadvantages.⁸⁷ It requires the microscope column to be kept at high-vacuum conditions as the beam would otherwise not even reach the sample. The sample should also be very thin for electrons to pass through at all and form an image. Lastly, some samples are easily damaged by the electron beam. Despite these limitations, the great

spatial resolution and various kinds of signals make electron microscopy a powerful tool for the characterization of nanomaterials. The electron microscope gives access to imaging of materials at atomic resolution, electron diffraction to determine crystal structures, probing of energy states, spatial spectroscopy and elemental mapping.^{85,86,88,89}

There are three main types of electron microscopy, namely scanning (SEM), transmission (TEM) and scanning transmission (STEM) electron microscopy. In SEM, a relatively low-energy electron beam (0.5 – 30 keV) is scanned over the sample to build up an image pixel by pixel. Due to the low acceleration voltage, the electrons cannot penetrate deep into the sample. By collecting the signal coming from the surface of the sample, the SEM yields topological information. TEM in contrast uses high-energy electrons (100 – 300 keV) in a parallel beam travelling through the sample to create a projected image on a camera underneath the sample. STEM uses a focused high-energy electron beam to raster-scan across the sample. Images can then be built up per pixel. A bright-field image can be constructed by recording the intensity of the transmitted beam. However, by collecting the electrons that have scattered from the sample under certain angles using an annular dark field detector, a dark-field image can be constructed. The high-energy electrons of TEM and STEM have the additional benefit of increased resolution compared to SEM.

1.5.2. Liquid-cell electron microscopy

For a long time, samples had to be thin and dry due to the high-vacuum conditions in the transmission electron microscope (TEM). Drying colloidal particles results in several disadvantages. Aggregation and collapse due to the drying process are common drawbacks of making TEM samples out of colloidal suspensions. Furthermore, liquid-based processes such as diffusion of particles in a liquid, the interactions between particles in liquid and their self-assembly, liquid-phase chemical reactions (*e.g.* ion-exchange for nanoparticles), many applications that rely on a liquid to perform such as battery operation, and the structure of biological materials cannot be studied directly in a dry state. While environmental EM has been an option for decades, a more practical solution has finally been achieved in recent years due to the use of modern microfabrication techniques to produce chips with strong but electron-transparent windows. Liquid-phase electron microscopy (LPEM) or liquid-cell electron microscopy (LCEM)^{80,81} has developed rapidly as a method recently and is increasingly being used to image liquid-based processes. A typical liquid-cell configuration is shown in Figure 1.3 and consists of two silicon chips containing a small electron-transparent silicon nitride (SiN) membrane known as the “window” in the center of the cell. The liquid between the two chips is contained and shielded from the high-vacuum of the microscope column. A spacer on one of the chips determines the initial thickness of the liquid layer between the chips. The thickness of commercial spacers are between 50 nm and 5 μm , which allows us to choose an adequate spacer chip depending on the dimensions of the sample under investigation. However, due to the high-vacuum of the microscope column, the electron-transparent SiN membranes bulge outward which leads to an increased liquid thickness in the area that is available for imaging. This usually results in a liquid thickness of at least a micron,

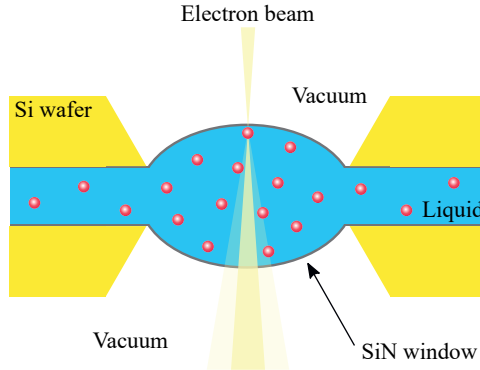


Figure 1.3: Typical configuration of a liquid-cell within the vacuum of an electron microscope with a STEM probe focused on the top part of the liquid-cell.

which severely limits the spatial resolution due to multiple scattering events of electrons in the SiN windows and the relatively thick liquid layer.

In this thesis we used STEM to image samples in liquids. When the STEM probe is focused on the top window the resolution is noise-limited. Inelastic scattering and multiple scattering events can be neglected when the particle is on the top window.^{90,91} STEM imaging on the bottom window is limited by the broadening of the STEM probe due to electron-liquid scattering events before the probe reaches the particle on the bottom.^{90,91} Furthermore, the thickness of the liquid layer, the nature of the particles, and the electron dose used for imaging, all influence the theoretical resolution achievable in LC-STEM.⁹¹ In general, the thicker the liquid layer is, the worse the resolution becomes. However, this effect is less pronounced for particles on the top window, compared to those on the bottom window.⁹⁰ The nature of the particles has a more dramatic effect. For a liquid layer of $1\text{ }\mu\text{m}$, where particles are situated halfway between the top and bottom window, a gold particle can be imaged with approximately 10 times higher resolution than a carbon particle when imaged with a common electron dose of $10 - 100\text{ e}^- \text{ nm}^{-2}$. Lastly, the spatial resolution theoretically scales with the electron dose rate d as $\text{res} \approx d^{-1/4}$,⁹¹ which means that even a reduction of the electron dose rate by 3 orders of magnitude only decreases the spatial resolution by a factor of 5. This indicates that extremely low dose rates are useful for many liquid-phase experiments where electrons can easily damage the sample.

The electron beam irradiation damage in dry samples has been extensively studied⁸⁷ and can be classified into electronic damage and knock-on damage. Electronic damage includes electrostatic charging and electronic excitations including ionizations, while knock-on damage includes displacement of atoms, structural damage such as amorphization, and a loss of material.⁸⁷ The presence of liquid in liquid-phase electron microscopy adds additional processes occurring in the liquid layer itself, which changes the chemistry of the suspending medium dramatically. For example, molecular, ionic and radical species as well as hydrated electrons are generated, while the pH changes due to the generation of H_3O^+ and OH^-

species. As a result the ionic strength also changes and electric fields may be established. These “indirect” effects of the electron beam irradiation along with the “direct” effects such as charging and bond-breaking in the particles should be carefully considered when performing and analyzing liquid-phase electron microscopy experiments. Additionally, it is almost never assumed in physics and/or physical chemical descriptions of any process that there is a net excess charge present in solutions, which is almost always occurring in liquid-cell experiments due to the nature of the electron beam. In order to study the mobility and interactions of particles, as done in this thesis, the effects of the electron beam effects must be explored first. As such there will be a heavy emphasis on such effects throughout the chapters containing liquid-cell electron microscopy experiments.

1.6. SCOPE OF THIS THESIS

This thesis is focused on imaging rattle-type particles using various microscopy techniques in order to study particle mobility, particle-shell interactions and ways to manipulate the core particle using external fields. Understanding how these rattle-type particles behave is not only interesting fundamentally but also allows us to tailor the particles to our needs in applications such as switchable photonic crystals. On the other hand, rattle-type particles are the ideal particles to probe the local environment within the liquid-cell inside an electron microscope. For example, we can gain insight into the influence of the electron beam on the local environment and how it changes physical interactions between particles. In this thesis we employed both laser scanning confocal microscopy and the recently emerged liquid-cell electron microscopy techniques to investigate rattle-type particles, thereby bringing the study of particle interactions to the nanoscale. We briefly outline below how each chapter contributes to these general topics in this thesis.

In **Chapter 2** we studied the first requirement for reliable experiments on the dynamics and interactions of particles in liquid-cell electron microscopy: unrestricted Brownian motion of free particles. This was done by employing viscous liquids and lower electron doses than was the norm in literature. In this way, unhindered Brownian motion of gold nanoparticles smaller than 100 nm was observed at high spatial resolution, which makes liquid-cell electron microscopy an important candidate for nanoscale self-assembly experiments in real space and in real time. In **Chapter 3** we used 3D confocal microscopy experiments to study the diffusion of a confined particle within a rigid spherical shell. We synthesized a rattle particle with a fluorescent core, which could be imaged while diffusing within the shell. We found that the diffusion coefficient of the core particle depended on the position of the core within the shell and the direction in which the core particle moved. The diffusion coefficient of the core moving in the direction towards the shell wall decreased as the core particle approached the shell wall closer, while the diffusion coefficient in the direction along the shell wall remained constant, independent of position within the shell. These experimental results were in excellent agreement with finite-element calculations. In **Chapter 4** rattle-type particles in water were imaged using liquid-cell electron microscopy at nanometer spatial resolution. The interactions between the core particle and the inner shell wall were tuned using the electron dose rate, pH, and most importantly the salt concentration. We found

interesting phenomena such as a nearly flat electric potential within the shell in deionized water, which led to reduced repulsive interactions between the core particle and the inner shell wall. Furthermore, the interactions within a nanorattle were investigated using liquid-cell electron microscopy, showing that this technique can be used to investigate interactions of nanoparticles, which has been a great experimental challenge recently. In **Chapter 5** we manipulated the mobility of a core particle within a rattle geometry with AC electric fields in water. At frequencies below 2 kHz the particle moved parallel to the electric field, similar to electrophoresis of a free particle. At intermediate frequencies, from 3 to 40 kHz, the particle was confined in the direction parallel to the electric field, while it could still move orthogonally due to thermal fluctuations. This was confirmed by finite-element calculations to likely be caused by changes in the ionic concentrations within the shell. At high frequencies, above 40 kHz, the influence of the electric field was minimal and the particle was able to move as if no electric field was being applied. In **Chapter 6** we combined the knowledge gained in the previous two chapters to create a switchable colloidal crystal with rattle-type particles as building blocks. We showed that when the shells of rattle particles were assembled on a lattice, applying AC electric fields of low frequencies the particles collectively moved parallel to the electric field creating a lattice of the core particles. When no electric field was applied, though, the particles moved around in the hollow shells via thermal fluctuations. The electric field was shown to quickly create order or disorder of the core particles. Furthermore, the optical reflections of a 3D assembly of rattle particles could be altered by applying a low-frequency electric field. The ratio of the intensity of the Bragg peaks when the electric field was off or on was explained by Debye-Waller factors, which allowed us to make predictions on how to improve the system.

Observation of unrestricted 3D Brownian motion of nanoparticles using liquid-phase scanning transmission electron microscopy

ABSTRACT

In theory, liquid-cell (scanning) transmission electron microscopy (LC(S)TEM) is the ideal method to measure 3D diffusion of nanoparticles (NPs) on a single particle level, beyond the capabilities of optical methods. However, particle diffusion experiments have been especially hard to explain in LC(S)TEM as the observed motion thus far has been slower than theoretical predictions by 3-8 orders of magnitude due to electron beam effects. Here we show direct experimental evidence of unrestricted diffusion for two systems; charge-neutral 77 nm gold nanoparticles in glycerol and negatively charged 350 nm titania particles in glycerol carbonate (GC) using LCSTEM. The high viscosities of the used media and a low electron dose rate allowed us to observe Brownian motion that is not significantly altered by the electron beam. The resulting diffusion coefficient agrees excellently with a theoretical value assuming free diffusion. We confirmed that the particles are also moving in the direction parallel to the electron beam by simulating STEM images using Monte Carlo simulations. Simulations and experiments showed blurring of the particles when they were deeper inside the cell, which was attributed to a broadening of the electron probe due to electron-solvent scattering. These results make clear that direct observation of 3D diffusion of NPs is possible, which is of critical importance for the study of interparticle interactions or in-situ colloidal self-assembly using LC(S)TEM.

2.1. INTRODUCTION

Direct visualization of dynamic processes of sub-micron particles in liquids via microscopy techniques has helped researchers acquire many insights in interesting topics such as interparticle interactions and colloidal self-assembly.⁹²⁻⁹⁴ Liquid-cell (scanning) transmission electron microscopy^{80,81} (LC(S)TEM) has recently emerged as a powerful tool to observe dynamic processes of nanoparticles (NPs) in liquid with nanometer spatial resolution.⁹⁵⁻¹¹⁸ However, the electron beam significantly influenced the observed phenomena in many cases. So far, strongly slowed down diffusion of NPs was observed in LC(S)TEM studies.⁹⁵⁻¹¹⁸ Possible explanations for this phenomenon, apart from trivial difficulties such as the imaging system not being fast enough to image free Brownian motion, include hydrodynamic slowing down near the window's surface,^{99,105} a highly viscous ordered liquid layer near the windows,^{99,104} and strong (sometimes beam-induced) interactions with the liquid-cell windows.^{95,99,104,105,107} Observing 3D Brownian motion in the electron microscope that is not significantly altered by the electron beam and/or the presence of the windows would open the way for many experiments, including studies on colloidal self-assembly of NP dispersions.¹¹⁹ The objective of this work is to find conditions and identify key experimental parameters for which 3D Brownian motion is observable in LC(S)TEM.

In this study we combine a low dose scanning transmission electron microscopy (STEM) technique with viscous liquid media having a high dielectric constant to observe bulk diffusion of gold NPs and titania particles in LC(S)TEM. The significantly faster diffusion of particles in comparison to many previous liquid-cell electron microscopy studies that we report on in this work underlines the importance of choosing a suitable electron microscopy imaging technique, electron dose rate and solvent in order to study dynamic processes in LC(S)TEM without artefacts.

2.2. METHODS

2.2.1. Liquid-cell electron microscopy

In order to image the NPs in the electron microscope, we used a liquid flow TEM holder with corresponding microchips (Hummingbird Scientific, USA). The microchips have 50 nm thick amorphous silicon nitride (SiN_x) windows with a size of 50 by 200 μm . The spacer on one of the chips was 500 nm, but insertion in the microscope makes the windows bulge outwards, resulting in a thicker liquid layer. The two Si chips were glow-discharged for 2 minutes prior to the experiment in order to make their surfaces more hydrophilic. The microchip with spacer was then placed in a dedicated holder. A 1 μL droplet of the dispersion was dropcasted onto the microchip. The second microchip was put onto the spacer chip with the hydrophilic side facing the opposite chip. The excess liquid was removed with filter paper. The liquid flow capability of the holder was not used. The used dispersions were titania particles dispersed in glycerol carbonate (GC) (4-(Hydroxymethyl)-1,3-dioxolan-2-one, Sigma-Aldrich 455067) and gold NPs dispersed in glycerol (Sigma-Aldrich CAS 56-81-5).

The liquid STEM experiments were carried out using a transmission electron microscope (Tecnai-F20, Thermo-Fischer Scientific), equipped with a field emission gun, and operating

at 200 kV. The semi-convergence angle of the electron probe was 10 mrad. The annular dark-field (ADF) detector was used with a camera length of 120 mm. Image series were acquired with TEM imaging & analysis software (TIA). For the experiments with titania particles, the beam current measured via the fluorescent screen in vacuum was approximately 30 pA, while it was measured to be roughly 13 pA when the liquid cell holder was inserted. A frame time of 0.2 s was used for most image series. The number of pixels was 256×256 or 512×512 , which resulted in a pixel size of 17.5–49.5 nm depending on the magnification and amount of pixels. For the experiments with gold NPs, the beam current in vacuum ranged from 4 to 217 pA, depending on the spotsize. A frame time of 0.5 or 1 s was used. The number of pixels was 512×512 pixels, which resulted in a pixel size of 12 nm. The electron dose rate was calculated by using the screen current in vacuum and the total frame size. It is worthwhile to mention that in STEM, the value for the electron dose rate is not the only relevant entity. It is likely that the pixel dwell time and total frame time are also important parameters.¹²⁰ The liquid thickness was calculated via^{90, 104}

$$\frac{I_{\text{screen}}}{I_0} = \exp \left(- \left(\frac{t_{\text{SiN}_x}}{l_{\text{SiN}_x}} + \frac{t_{\text{liquid}}}{l_{\text{liquid}}} \right) \right), \quad (2.1)$$

where $\frac{I_{\text{screen}}}{I_0}$ is the ratio between the screen currents measured with and without the sample inserted, t_{SiN} and t_{liquid} the thickness of the SiN and the liquid, respectively, and l_{SiN} and l_{liquid} the mean free path lengths of electrons through the SiN and the liquid, respectively. We used $l_{\text{SiN}} = 0.79 \mu\text{m}$ for the SiN windows and $l_{\text{liquid}} = 2.6 \mu\text{m}$ for glycerol, to calculate the liquid thickness of our sample.¹⁰⁴

2.2.2. Particle tracking

The positions of the titania particles in each frame were tracked using the ImageJ plugin MTrackJ.¹²¹ The position for a particle was determined manually for each frame. The tracking error for the particles of 350 nm diameter, determined by tracking a particle that was stuck on the window, was 13 ± 4 nm. The positions of the gold NPs were determined using Trackpy, based on the feature-finding and linking algorithms of Crocker & Grier.¹²² No drift was observed and no drift correction was applied for all videos.

2.2.3. Monte Carlo simulations using CASINO

To simulate ADF-STEM images we used the CASINO software.^{123–125} The used physics model for the total and partial cross sections in the simulation software was that of an empirical analytical fit to the Mott cross sections by Browning *et al.*¹²⁶ The specific parameters of the sample and the electron probe were taken to be as close to the experimental parameters as possible.

For the 350 nm titania particle in GC, a layer of $2.3 \mu\text{m}$ of glycerol carbonate was put between two 50 nm thick Si_3N_4 windows. A 350 nm titania particle was positioned at various heights within the glycerol carbonate layer. The electron probe was set to have a semi-convergence angle of 10 mrad and a diameter of 1 nm. The beam distribution was Gaussian. The electron probe had an energy of 200 keV and had its focal point on the top window minus one particle radius. The pixel size was 17.5 nm and the number of simulated electrons per

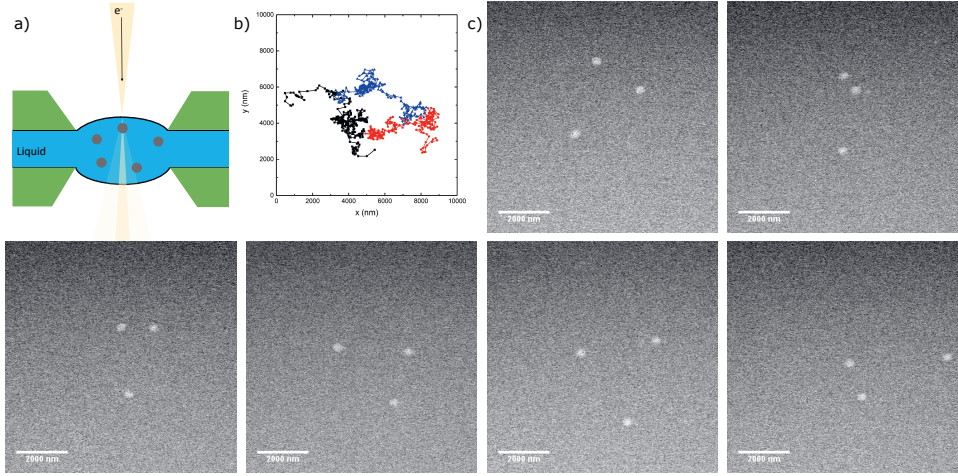


Figure 2.1: Motion of 350 nm titania particles within the liquid-cell. a) Schematic of the liquid-cell configuration in the microscope. A focused STEM beam probes the sample, which consists of titania particles dispersed in glycerol carbonate in between SiN_x windows. b) Full trajectories of the particles shown in the panels in c and in Supporting Movie 1 during 100 s. c) Stills of an ADF-STEM recording showing particle movement in time. The frame time was 0.5 s and frames were acquired continuously (no delay between frames). The frame dimensions are 512 by 512 pixels with a pixel size of 17.5 nm. The electron dose rate was $2 \text{ e}^- \text{ nm}^{-2} \text{ s}^{-1}$. The scale bar is 2000 nm.

pixel N was 375, as calculated from the beam current I and the pixel dwell time τ via

$$N = \frac{I \cdot \tau}{e} \quad (2.2)$$

where e is the electron charge. The ADF detector with a quantum efficiency of 100% was set to have a minimum and maximum semi-angle of 33 and 450 mrad, respectively.

For the 77 nm gold NP in glycerol, a layer of $2 \mu\text{m}$ of glycerol was between two 50 nm thick Si₃N₄ windows. A 77 nm gold NP was positioned at various heights within the glycerol layer. The electron probe was set to have a semi-convergence angle of 10 mrad and a diameter of 1 nm. The beam distribution was Gaussian. The electron probe had an energy of 200 keV and had its focal point on the top window minus one particle radius. The pixel size was 12.2 nm and the number of simulated electrons per pixel N was 663. The ADF detector with a quantum efficiency of 100% was set to have a minimum and maximum semi-angle of 33 and 450 mrad, respectively.

2.3. RESULTS & DISCUSSION

For this work, we studied two different systems. One with bigger particles in a less viscous solvent and one with smaller particles in a more viscous solvent. The bigger particles serve as a first check whether free diffusion is at all possible within the electron microscope. The smaller

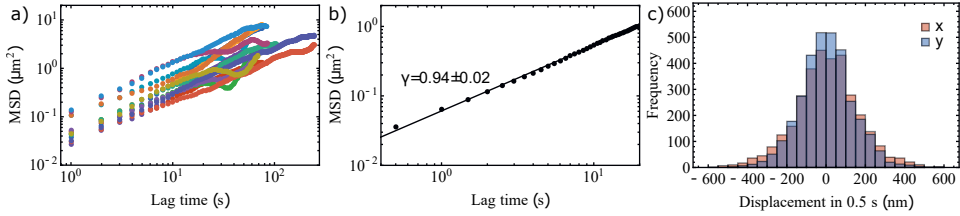


Figure 2.2: The MSD of 350 nm titania particles in the liquid cell. a) Single particle trajectories for 14 particles that were tracked for at least 100 s. The frame time was 0.2 or 0.5 s and the frames were acquired continuously. The frames for various videos were with dimensions of 256 by 256 or 512 by 512 pixels. The pixel size for various videos was between 17.5 and 49.5 nm. b) MSD averaged over all the single particle trajectories from a). The slope of the averaged MSD is 0.94 ± 0.02 , indicating slightly subdiffusive behavior. c) Displacement histograms of the steps taken by the particles between frames in the x and y direction.

particles allow us to explore the feasibility for 3D diffusion experiments for NPs smaller than 100 nm as these are small enough to change their position away from focus conditions.

First, glycerol carbonate (GC) was used as a solvent wherein spherical 350 nm sized TiO_2 particles were dispersed. These particles were synthesized via the method by Mine *et al.*¹²⁷ and have a polydispersity of 10%. GC is a solvent with a high viscosity ($\eta = 0.147 \text{ Pa}\cdot\text{s}$) and high dielectric constant ($\epsilon_r = 111.5$).¹²⁸ The high dielectric constant is believed to decrease the induced electric fields due to STEM irradiation.¹²⁹ Moreover, because of the strong resemblance of properties of GC to water, it is proposed as a low vapor pressure green alternative in cases where for instance a low vapor pressure/high boiling point is important.^{130,131} In combination with a low electron dose rate ($0.6\text{-}2.4 \text{ e}^- \text{ nm}^{-2} \text{ s}^{-1}$ in this study), the influence of the electron beam can be minimized. This dose rate is at least one order of magnitude lower than previous LC(S)TEM NP diffusion studies. It has been shown theoretically⁹¹ that the spatial resolution scales with the electron dose d as $\text{res} \propto d^{-1/4}$. This indicates that even a reduction of the electron dose rate by 3 orders of magnitude only decreases the spatial resolution by a factor of 5, which indicates that extremely low dose rates are useful for many experiments. Moreover, in case the particle density is not too high, the actual accuracy of the spatial coordinates of the particles can be significantly higher than the resolution.¹²¹

The dispersion was enclosed between two silicon microchips with 50-nm-thick electron-transparent amorphous silicon nitride (SiN) windows (Figure 1a). The chips are loaded on a dedicated TEM holder and inserted in the electron microscope. Multiple annular dark-field (ADF) STEM videos of the observed particle diffusion can be found in Appendix C. Figure 1 shows several frames of raw ADF-STEM footage showing individual particle diffusion, along with their complete trajectory (Appendix A). The trajectories of 14 particles (observations longer than 100 s) were obtained and the mean squared displacement (MSD) is shown in Figure 2a.

The ensemble averaged MSD was determined by making use of lag times:^{132–134}

$$\langle (\vec{r}(\Delta + n\tau) - \vec{r}(n\tau))^2 \rangle = \frac{1}{N_p} \sum_{i=1}^{N_p} \frac{1}{N\tau - \Delta} \sum_{n=1}^{N-\Delta/\tau} (\vec{r}_i(\Delta + n\tau) - \vec{r}_i(n\tau))^2 \quad (2.3)$$

Here $\vec{r}_i(n)$ is the position of particle i in frame n , N the total amount of frames, τ the duration of 1 frame and N_p the total amount of particles. The lag time Δ replaces the function of time in the more straightforward MSD analysis. The value for D was then determined by a weighted least-square fit to the obtained ensemble averaged MSD (Figure 2b) with a function $f = D/4 \cdot \Delta$. The fit to the ensemble averaged MSD yielded a diffusion coefficient $D = (12.8 \pm 0.2) \cdot 10^{-3} \mu\text{m}^2\text{s}^{-1}$.

Next, we calculated the diffusion coefficient of 350 nm titania particles in pure GC at 25 °C via the Stokes-Einstein relation, thus assuming free 3D diffusion:

$$D = \frac{k_B T}{6\pi\eta a}, \quad (2.4)$$

where k_B is the Boltzmann constant, T the absolute temperature, η the dynamic viscosity and a is the radius of the particles. The calculated diffusion coefficient of $D = 11.5 \cdot 10^{-3} \mu\text{m}^2\text{s}^{-1}$ agrees relatively well with the experimentally obtained diffusion coefficient. The deviation from the experimental value obtained from the ensemble averaged MSD can be explained due to a slight deviation in temperature or liquid composition leading to a significant change in viscosity.

It is likely that the entrapment of the liquid between windows has an influence on the motion of the particles. We analyzed the slope of the MSD in a logarithmic plot (Figure 2b). The obtained MSD was fitted to a function $f = C\Delta^\gamma$, with C a fitting constant. If the value of γ is 1, the motion is truly Brownian, if it is less than 1 it indicates subdiffusive behavior, while it shows superdiffusive behavior for $\gamma > 1$.

The slope of the MSD is 0.94 ± 0.02 indicating slightly subdiffusive behavior. The small deviation could be explained by the influence of the windows. We calculated the liquid thickness with the method reported by Verch *et al.*¹⁰⁴ and found that the liquid thickness is $2.3 \pm 0.7 \mu\text{m}$. It is likely that, within the time frame of our observations, particles notice the presence of the static hindrance of the windows, leading to seemingly subdiffusive behavior. The much more pronounced subdiffusive behavior often found in LC(S)TEM experiments was not found in this study.¹³⁵ Additional evidence for Brownian diffusion is shown in Figure 2, where the displacements of particles per frame is normally distributed.

As the liquid layer is less than 10 times the particle diameter in thickness, some hydrodynamic slowing down of the particles is expected. For a particle size of 350 nm in liquid between two parallel plates $2.3 \mu\text{m}$ apart, particles are expected to slow down by approximately 15% when moving parallel to the two plates.¹³⁶ However, due to insufficient knowledge on the exact temperature and liquid composition, it could not be accurately tested. It could however, lead to differences in MSDs of individual particles. We stress that hydrodynamic slowing down should always be considered in future dynamic liquid cell experiments, especially for much lower liquid thicknesses.

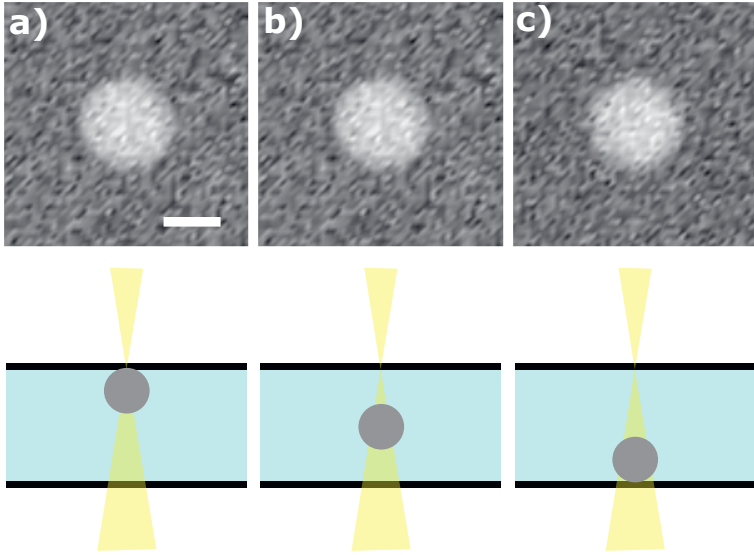


Figure 2.3: Simulated ADF-STEM images of a 350 nm titania particle using the software CASINO. The particle was positioned at different heights in the liquid-cell; a) on the top window, b) in the middle of the cell and c) on the bottom window. The liquid thickness used was $2.3\,\mu\text{m}$. The input parameters for the Monte Carlo simulations were the same as used in the experiment for video S1. The pixel size was 17.5 nm, the pixel dwell time was $1.9\,\mu\text{s}$ and the electron dose rate was $2\,\text{e}^-\text{nm}^{-2}\text{s}^{-1}$. The focal point was on the top window and the semi-convergence angle α of the electron probe was 10 mrad. The scalebar is 200 nm.

To investigate whether the particle also move in the direction parallel to the STEM probe, we simulated ADF-STEM images using the experimental conditions for a 350 nm titania particle at various heights in the liquid cell, using the CASINO software.^{123–125} Figure 2.3 shows the simulated ADF-STEM images for a titania particle at the top, middle and bottom of the liquid cell. No obvious difference is observed, because at 350 nm size the particle is too large to move out of focus or be significantly influenced by beam broadening effects. This agrees with experiments where we do not see any change in focus conditions for the freely diffusing particles between frames. Since no hopping motion is observed and the experimental diffusion coefficient is close to that expected for free diffusion, it is likely that the particle is also diffusing in the third dimension. Below we will demonstrate that this is the case for smaller NPs.

Many LC(S)TEM studies also show a significant influence of the electron beam on the acquired data. Effects like radiolysis,¹³⁷ bubble formation,¹³⁷ momentum transfer¹⁰⁸ and increased temperature¹⁰⁸ have all been analyzed (details in Appendix B). However, the charged titania particles we believe the reduction of charging and electric field effects is the main reason that free diffusion is observed. Woehl *et al.* have previously explained the repulsion of titania

particles from the window by discussing electric fields.¹⁰⁶ However, their electron dose rate was 2-3 orders of magnitude higher than the dose rates used in this study. In the modeling of beam-induced electric fields by Jiang, positive charges concentrate within the probed region of a focused STEM probe, leading to electric fields that are cylindrically symmetric around the probed region with their strength decaying away from the probe,¹³⁸ via¹³⁹

$$|E| = \frac{\rho}{2\pi\epsilon_0\epsilon_r R}. \quad (2.5)$$

Here ρ is the induced charge density, which depends on the used electron dose rate and the width of the STEM probe, ϵ_r the relative dielectric constant of the medium and R the distance from the STEM probe. The electric field arises due to emission of secondary and Auger electrons, which are not immediately neutralized, leaving behind a positively charged region.¹³⁸ In liquid, like in our experiment, the electric field will be screened by ions present in the solution. Since the titania particles are negatively charged and the entire field of view is quickly scanned by the probe, an effect of the electric field would be seen by the titania particles not being able to leave the field of view. However, during our observations 51 titania particles leave and 44 titania particles enter the field of view (Appendix A), indicating a negligible effect of the induced electric fields or effects like thermophoresis with the used electron dose rates and solvent. We hypothesize that the low electron dose rate results in a lower induced charge density ρ , which in addition is screened by charged species and their conductivity in the strongly polar solvent. Using GC as a liquid could therefore be important because of its high ϵ_r . A high dielectric constant liquid screens the charges that are induced by the beam on the windows. The addition of salt would help the screening of charges even more.

LC-(S)TEM is primarily useful to observe NPs in a liquid environment in real time beyond the capability of optical methods. Ideally, we would have imaged NPs in glycerol carbonate as in that medium less bubble formation occurs than in glycerol. However, as the diffusion coefficient of a particle scales with the inverse of their radius, NPs would move too fast in glycerol carbonate. We thus decided to use glycerol as a liquid medium for charge-neutral 77 nm gold NPs with polyethylene glycol (PEG) ligands, synthesized via a slightly modified procedure based on the protocol of Hanske *et al.*¹⁴⁰ (Appendix A). Glycerol has a viscosity of $\eta = 0.9$ Pa·s at 25 °C, which is an order of magnitude higher than that of glycerol carbonate, and has a dielectric constant of 42.5. We dispersed the gold NPs coated with PEG in a mixture of 98 vol% of glycerol and 2 vol% of water. Figure 2.4 shows various frames of Supporting Movie 4 in which gold particles are diffusing within the liquid-cell. In any given frame, distinct particles are clearly blurred to various extents, indicating they are at different heights within the liquid cell.

In order to determine whether the motion is anomalous due to electron beam effects,¹³⁵ we first analyze the tracks obtained from Supporting Movie 4 (Figure 2.5a). Figure 2.5b shows the histogram of displacements between two consecutive frames over all frames of Supporting Movie 4. We observe that on average the displacements in x are slightly higher than the displacements in y , which may be related to the scanning direction. The MSDs for the individual particles are shown in Figure 2.5c, whereas an ensemble averaged MSD is shown

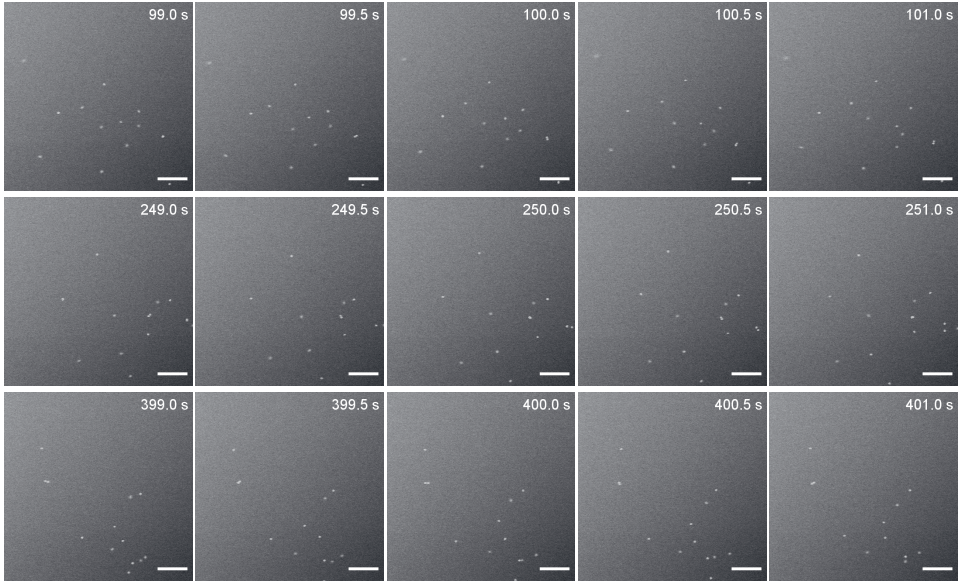


Figure 2.4: Motion of 77 nm gold NPs within the liquid-cell. The frame time was 0.5 s and frames were acquired continuously (no time between frames). The frame was 512 by 512 pixels with a pixel size of 12.2 nm. The electron dose rate was $9 \text{ e}^- \text{ nm}^{-2} \text{ s}^{-1}$. Individual frames taken from video S4. The scalebar is $1 \mu\text{m}$.

in Figure 2.5d. The slope of the ensemble averaged MSD in a log-log plot is 0.98 ± 0.01 indicating Brownian diffusion. The diffusion coefficient obtained from the ensemble averaged MSD is $D = (8.8 \pm 0.1) \cdot 10^{-3} \mu\text{m}^2 \text{ s}^{-1}$. This is in reasonable agreement with the diffusion coefficient calculated via Equation 2.4 for 77 nm Au NPs with PEG ligands (hydrodynamic radius $a = 42 \text{ nm}$) in 98/2 vol% glycerol/water at 25°C (viscosity $\eta = 0.65 \text{ Pa}\cdot\text{s}$), which is $D = 8.0 \cdot 10^{-3} \mu\text{m}^2 \text{ s}^{-1}$. A slight change in either temperature or water content could explain the discrepancy between the experimental and theoretical result, which is not unreasonable since both are hard to control precisely.

Next, we focus our attention to the motion of the particles in the z direction. Figure 2.6 shows the same particle at different times in Supporting Movie 4. In a time span of 100 seconds it moves from being in focus near the top of the liquid-cell to blurry near the bottom of the cell and then moves back to the top.

To show that a different z position within the liquid-cell can indeed lead to a blurring of the particle as shown in Figure 2.6 (and Figure A7), we used the Monte Carlo software CASINO^{123–125} to simulate ADF-STEM images of the gold NPs as well. Figure 2.7 shows the simulated ADF-STEM images of a 77 nm gold NP at various heights z within the liquid cell. The simulations confirm that the image of the gold NP becomes blurry as it moves closer to

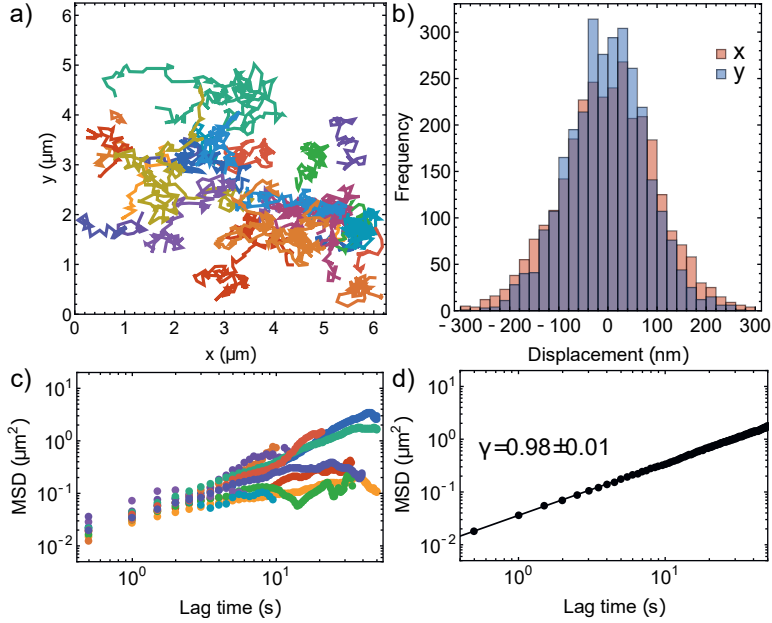


Figure 2.5: Analysis of diffusion of 77 nm gold NPs in the liquid-cell. a) First 30 tracks obtained from video S4. b) Histogram of displacements between consecutive frames in the x and y direction. c) MSDs of 10 individual tracks obtained from video S4. d) Ensemble averaged MSD from all individual MSDs in video S4. The slope of the ensemble averaged MSD is 0.98 ± 0.01 .

the bottom of the cell. This could be due to the particle moving out of focus and broadening of the STEM probe as it travels through more liquid before encountering the gold NP.

This raises the question whether it is possible to get a z coordinate for the particle simply by looking at the broadening of the imaged particle. Ideally, we would perform three-dimensional ADF imaging by through-focal series analogous to van Benthem and coworkers,¹⁴¹ however, the NPs move too fast to use this procedure effectively. However, the blurring of the particles at various z heights within the cell may give us an indication of their positions. Blurring of the particles when moving in 3 dimensions happens via 2 ways.

First, if the particle is out of focus, it experiences a broader part of the probe instead of the most focussed part. The depth of focus δ_z depends on the semi-convergence angle α of the electron probe and can therefore be tuned depending on the range in z needed in the experiment. To estimate how big this effect would be for the 77 nm gold NPs we use¹⁴²

$$\delta_z = \frac{d}{\alpha}, \quad (2.6)$$

which yields $\delta_z = 7.7 \mu\text{m}$ for our experimental conditions ($d = 77 \text{ nm}$ and $\alpha = 10 \text{ mrad}$). Since the particle can move at most $2 \mu\text{m}$ in the vertical direction we assume that this is not the main effect leading to the blurring of the particles.

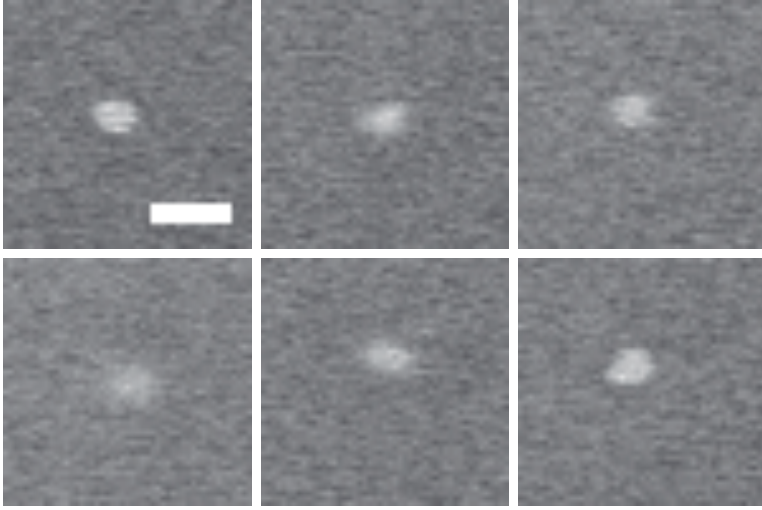


Figure 2.6: A single gold NP in the experimental video S4 at $t = 106, 132, 166, 188, 193$ and 206 s. Due to its mobility in z , it becomes more or less blurry depending on the position in the cell. The scalebar indicates 200 nm.

Second, the liquid, in this case glycerol, broadens the probe due to electron-solvent scattering, making the probe broader in the bottom of the cell. This effect can be calculated using⁹⁰

$$d_{\text{blur}} = 1.2 \cdot 10^3 T^{3/2} \frac{Z}{E} \sqrt{\frac{\rho}{W}}, \quad (2.7)$$

where d_{blur} is the broadening of the electron probe, T is the thickness of the sample, Z is the average atomic number, W the average atomic weight, ρ the mass density and E the energy of the electrons in eV. The beam broadening d_{blur} is plotted as a function of glycerol thickness in Figure 2.8a. For a thickness of $2 \mu\text{m}$, we obtain $d_{\text{blur}} = 26$ nm, which is sufficient to explain the blurring of our particles at different heights in the liquid-cell.

To combine both effects, beam broadening and defocus conditions, we used CASINO to simulate the ADF-STEM images of a 77 nm gold NP at many different z heights in the liquid cell. We then fitted the NP in the simulated image in the same way as for the experimental videos, using Trackpy. The full width at half maximum (FWHM) of the fitted simulated particle at different z heights in the liquid cell is shown in Figure 2.8b. The values of the FWHM for the experimental particles found in Supporting Movie 4 are shown in Figure 2.8c. The experimentally found FWHMs go beyond those found in the simulations, which may be due to the liquid thickness being slightly larger than calculated. However, just as we would expect from the simulations, the histogram has a longer tail towards higher values of the FWHM, indicating that the FWHM increases more rapidly towards the lower parts of the liquid cell. We therefore believe that the simulations give a reasonable representation of the blurring of particles at different heights in the liquid-cell and that the blurring of the probe,

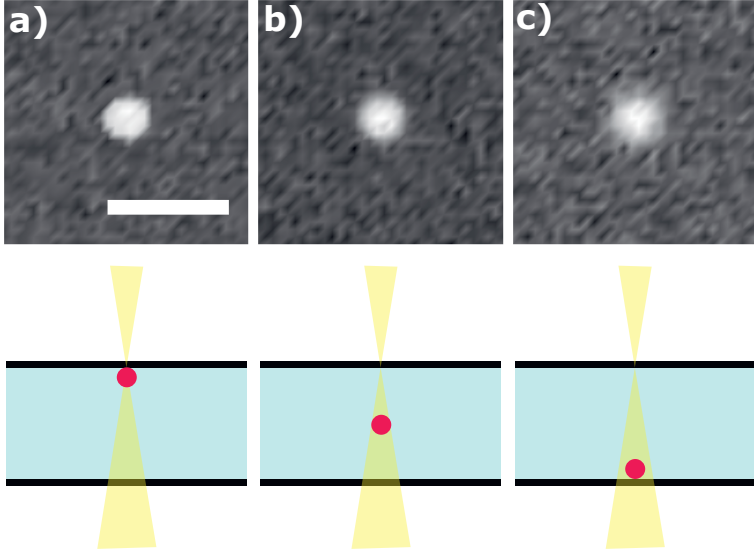


Figure 2.7: Simulated ADF-STEM images of a 77 nm gold NP using the software CASINO. The particles were put in different heights in the liquid-cell, namely a) on the top window, b) in the middle of the cell and c) on the bottom window. The liquid thickness used was 2 micron. The input parameters for the Monte Carlo simulations were the same as used in the experiment for video S4. The pixel size was 12.2 nm, the pixel dwell time was $1.9 \mu\text{s}$ and the electron dose rate was $9 \text{ e}^- \text{ nm}^{-2} \text{ s}^{-1}$. The focal point was on the top window and the semi-convergence angle α of the electron probe was 10 mrad. The scalebar is 200 nm.

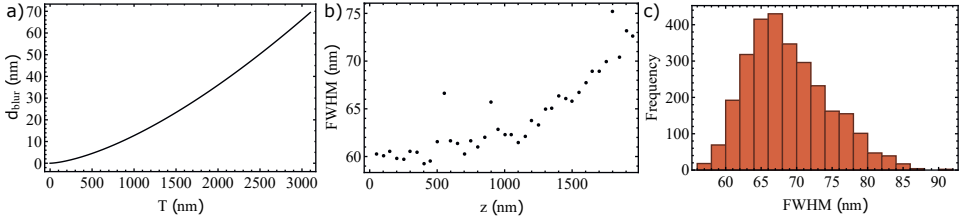


Figure 2.8: a) Beam broadening d_{blur} as calculated via Equation 2.7 as function of glycerol thickness. b) The FWHM of the 77 nm gold particle in simulated ADF-STEM images (see Figure 2.7) at various z heights inside the liquid-cell. The FWHM starts to increase when the beam is blurred sufficiently by the amount of liquid it has to travel through before it hits the particle. c) Histogram of experimental FWHM of all the single particles found in all frames in Supporting Movie 4.

d_{blur} , is sufficient to explain the blurring. Due to inherent noise at such low electron dose rates, however, we find that it is merely possible to provide a rough estimate of the particle position in z , rather than a precise coordinate. Also, the simulations show that in the top

Dose rate ($\text{e}^- \text{nm}^{-2} \text{s}^{-1}$)	D ($10^3 \mu\text{m}^2 \text{s}^{-1}$)	γ
0.6	8.0 ± 0.3	0.99 ± 0.04
1.6	8.1 ± 0.1	0.92 ± 0.01
3	11.0 ± 0.1	1.01 ± 0.01
9	8.8 ± 0.1	0.98 ± 0.01
17	7.8 ± 0.1	1.02 ± 0.01

Table 2.1: Diffusion coefficient D and slope γ obtained from MSD analysis from videos of diffusing gold NPs at various dose rates.

1000 nm of the liquid cell, the FWHM of particles should be roughly the same, as the blurring of the beam remains under 15% of the particle diameter in that region. Evidently, when the beam broadening exceeds 15% of the particle diameter, changes in the FWHM of the particle are noticeable. We do think using the broadening of the beam to infer z coordinates may be possible for smaller particles for similar liquid thicknesses.

As we did with the titania particles, we will consider the influence of the electron beam on the mobility of the gold NPs. We varied the electron dose rate via the strength of the condenser lens (Supporting Movies 3 to 5). Table 2.1 shows no large difference in MSD analysis for different dose rates. However, we noticed that at an electron dose rate of $17 \text{ e}^- \text{nm}^{-2} \text{s}^{-1}$ particles started to be repelled from the field of view (Supporting Movie 5). As the particles are almost charge-neutral, phenomena related to charge are unlikely to explain this. However, the electric fields originating from beam-sample interactions must always be considered.¹³⁸ We calculated the temperature rise within the sample due to the electron probe (Appendix B) and found it to be less than 1 K. However, we remark that a temperature gradient of less than 1 K could be sufficient to explain why the particles start to leave the field of view via thermophoresis. Thermophoresis is the phenomenon where particles are driven towards the colder or warmer region of the liquid depending on the details of the particle-solvent interface.¹⁴³ A temperature difference of 1 K between the irradiated area and non-irradiated area could lead to a significant decrease in particle concentration in the irradiated region.^{144–146} This thermophobic effect could lead the particles from the heated part of the irradiated region towards the colder region outside the field of view. However, the physical mechanisms are complex and not yet fully understood.¹⁴³

At even higher electron dose rates, we observed that particles became stuck on the window. As the particles are charge-neutral, beam-induced charging effects may not be an important factor. It is more likely that at higher electron dose rates the PEG ligands on the surface of the NP may be affected. However, a definitive explanation can not be given at this time.

2.4. CONCLUSION

We conclude that 3D Brownian motion of NPs can be observed in LCSTEM under the right conditions, whereas previously only strongly hindered motion due to particle-window

interactions was observed. Viscous solvents, GC and glycerol, helped slow down the particles, allowing them to be imaged within the time resolution of the available microscope system. These polar and viscous solvents, and especially a very low electron dose rate, helped mitigate electron beam effects normally leading to anomalous diffusion of particles in LC(S)TEM experiments. The obtained diffusion coefficients for both the negatively charged titania and the charge-neutral gold particles are close to those expected for free 3D single particle diffusion. No anomalous behavior was found for low electron dose rates as effects that could influence the motion such as electric fields and thermophoresis were suppressed. We thus conclude that observing Brownian motion of particles is indeed possible in a liquid cell and we have identified the electron dose rate and possibly the dielectric constant of the medium as important design parameters for the experiments.

For future work on 3D motion of particles in LC(S)TEM, we think both the dielectric constant and the viscosity of the solvent should be carefully considered, along with a suppression of the electron dose rate and the imaging mode. STEM has a higher resolution in experiments with liquid thicknesses larger than approximately 100 nm,⁹¹ provides a way of gauging the z positions of NPs as shown in this work, and likely causes less severe charging effects than TEM.¹³⁸ We therefore propose STEM as the preferred imaging mode.

We expect that, with the rapid improvements to EM detectors and sparse sampling approaches,¹⁴⁷ 3D Brownian motion experiments of much smaller particles will be possible in the near future. This makes it possible to conduct studies on NP interactions for NPs moving freely in solution, but also to study the (directed) self-assembly of NPs in real space and in real time using LC(S)TEM.¹⁴⁸

AUTHOR CONTRIBUTIONS

Kanako Watanabe (Tohoku University) synthesized the titania particles under supervision of Daisuke Nagao (Tohoku University). Maarten Bransen (Utrecht University) synthesized the gold particles. Sina Sadighikia and Albert Grau-Carbonell (Utrecht University) helped setup the initial liquid-cell experiments.

ACKNOWLEDGEMENTS

We thank Fabian Hagemans for the measurement of the viscosity of glycerol carbonate. We also thank Sina Sadighikia and Albert Grau-Carbonell for the critical reading of the chapter. The authors also acknowledge the EM square center at Utrecht University for access to the microscopes. Especially, Chris Schneijdenberg and Hans Meeldijk are thanked for their assistance.

APPENDIX A: SUPPORTING FIGURES

Condition	T (°C)	η (Pa·s)	D ($10^{-3}\mu\text{m}^2/\text{s}$)
LCSTEM	-	-	12.8 ± 0.2
Theory 100 v% GC	20	0.147	8.3
Theory 100 v% GC	25	0.109	11.5
Theory 99 v% GC	20	0.112	10.9
Theory 99 v% GC	25	0.084	14.8
Theory 96 v% GC	20	0.070	17.5
Theory 96 v% GC	25	0.054	23.1

Table A1: Comparison between the obtained experimental and calculated diffusion coefficients for 350 nm titania particles.

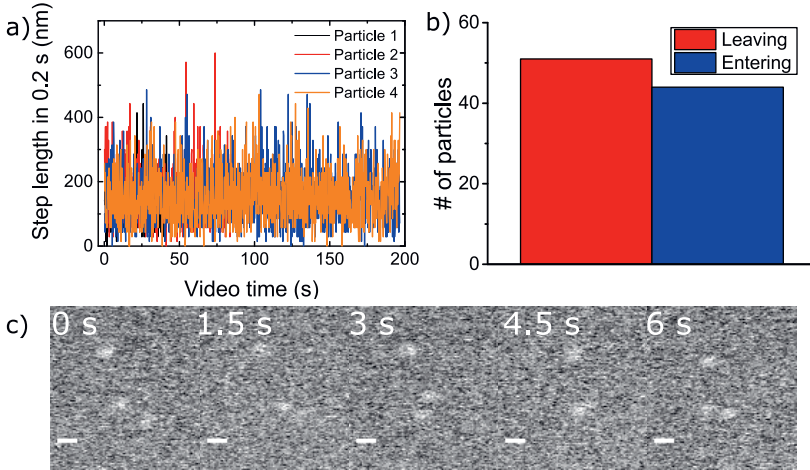


Figure A1: Strong indications that the titania particles are not moving over the window, but instead exhibit 3D Brownian motion unaltered by the beam. a) Step lengths per frame (0.2 s per frame) showing a negligible amount of frames for which particles do not move, indicating the observed motion is not a stepping motion over the windows. b) Histogram of the amount of particles leaving or entering the field of view in all recorded videos. The difference between leaving and entering of particles is statistically irrelevant, indicating the beam is not attracting or repelling particles significantly. c) ADF-STEM footage in which particles are observed to move underneath each other during several frames. This indicates the movement of particles does indeed take place in 3D and not close to a wall as might have been induced by the beam and/or interactions with the wall. The scalebar is 500 nm.

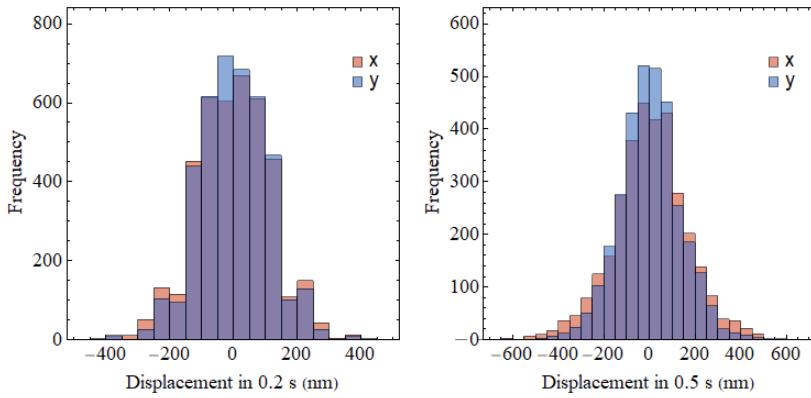


Figure A2: Histograms of displacement between frames for 350 nm titania particles in glycerol carbonate. They represent a normal distribution, indicating Brownian motion.

Condition	T (°C)	η (Pa·s)	D ($10^{-3} \mu\text{m}^2/\text{s}$)
LCSTEM	-	-	8.8 ± 0.1
Theory 100 v% glycerol	20	1.41	3.6
Theory 100 v% glycerol	25	0.91	5.7
Theory 98 v% glycerol	20	1.00	5.1
Theory 98 v% glycerol	25	0.65	8.0
Theory 96 v% glycerol	20	0.73	7.0
Theory 96 v% glycerol	25	0.48	10.8

Table A2: Comparison between the obtained experimental and calculated diffusion coefficients for 77 nm gold particles.

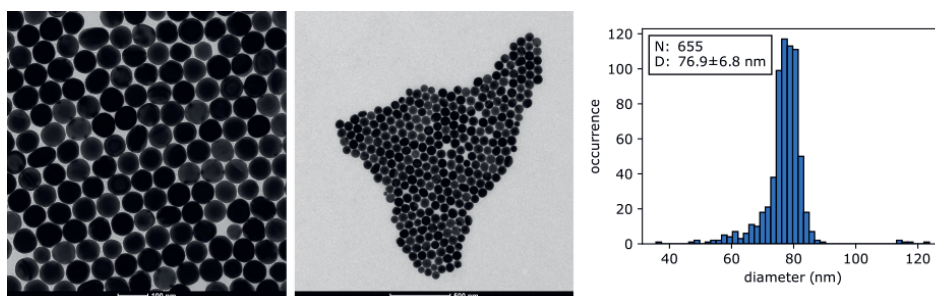


Figure A3: Representative TEM images of the gold NPs used in the diffusion experiments. The diameter of the NPs is 77 ± 7 nm, a polydispersity of less than 10%. Cetyltrimethylammonium chloride (CTAC) capped spherical gold nanoparticles with an average diameter of 77 nm were synthesized using a seeded growth and oxidative etching procedure reported elsewhere.¹⁴⁰ To functionalize the surface with thiol-terminated poly(ethylene glycol) molecules (PEG-SH), CTAC-stabilised particles were collected from 400 mL of the as synthesized nanoparticle solution by means of centrifugation (1000 g for 30 min). The particles were re-dispersed in 40 mL of an aqueous solution containing 0.5 g L^{-1} α -methoxy- ω -mercapto PEG (M_w 5000 g mol^{-1} , *Rapp Polymere GmbH*) and left to react overnight. To ensure full removal of the CTAC ligands, the functionalization procedure was repeated by collecting the particles using centrifugation and re-dispersing the particles in 40 mL of a fresh 0.5 g L^{-1} PEG-SH solution. The zeta potential in water was measured to be less than 5 mV.

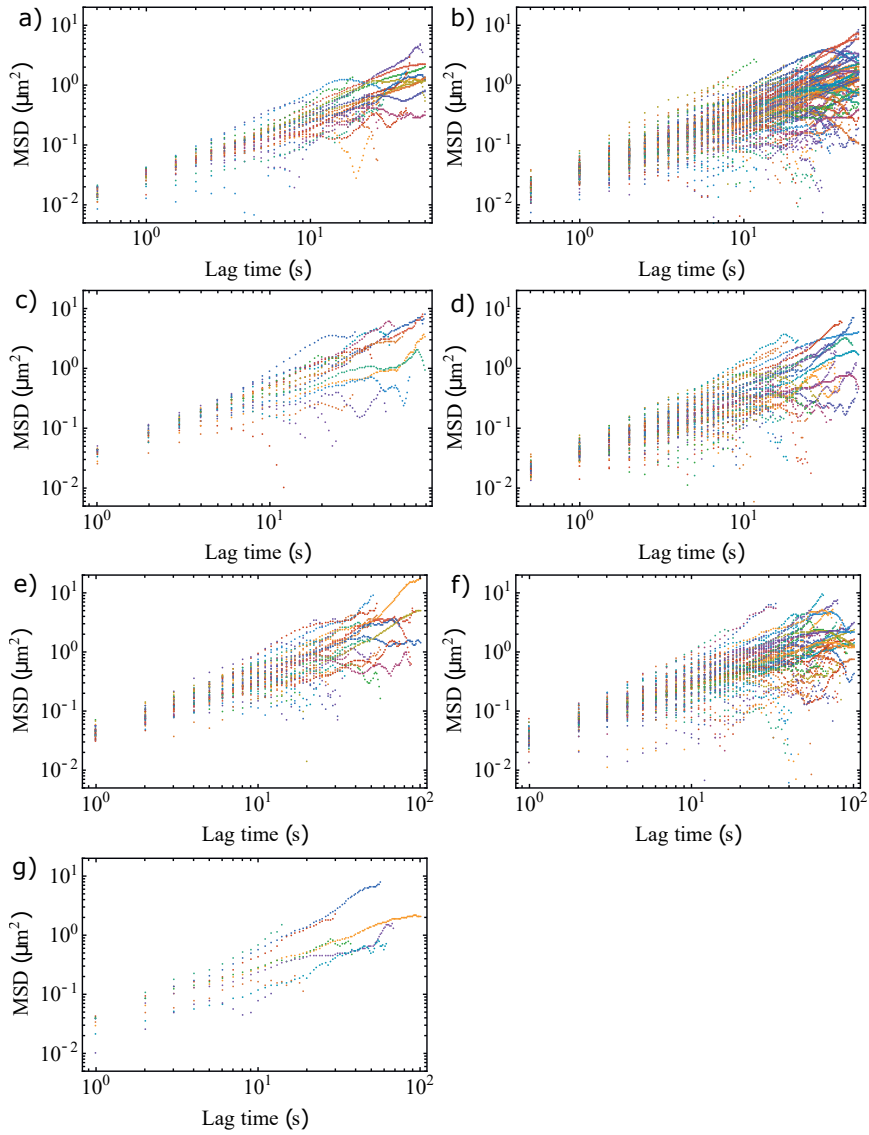


Figure A4: Individual MSDs for various electron dose rates: a) $17 \text{ e}^- \text{ nm}^{-2} \text{ s}^{-1}$, b-c) $9 \text{ e}^- \text{ nm}^{-2} \text{ s}^{-1}$, d-e) $3 \text{ e}^- \text{ nm}^{-2} \text{ s}^{-1}$, f) $1.6 \text{ e}^- \text{ nm}^{-2} \text{ s}^{-1}$ and g) $0.6 \text{ e}^- \text{ nm}^{-2} \text{ s}^{-1}$.

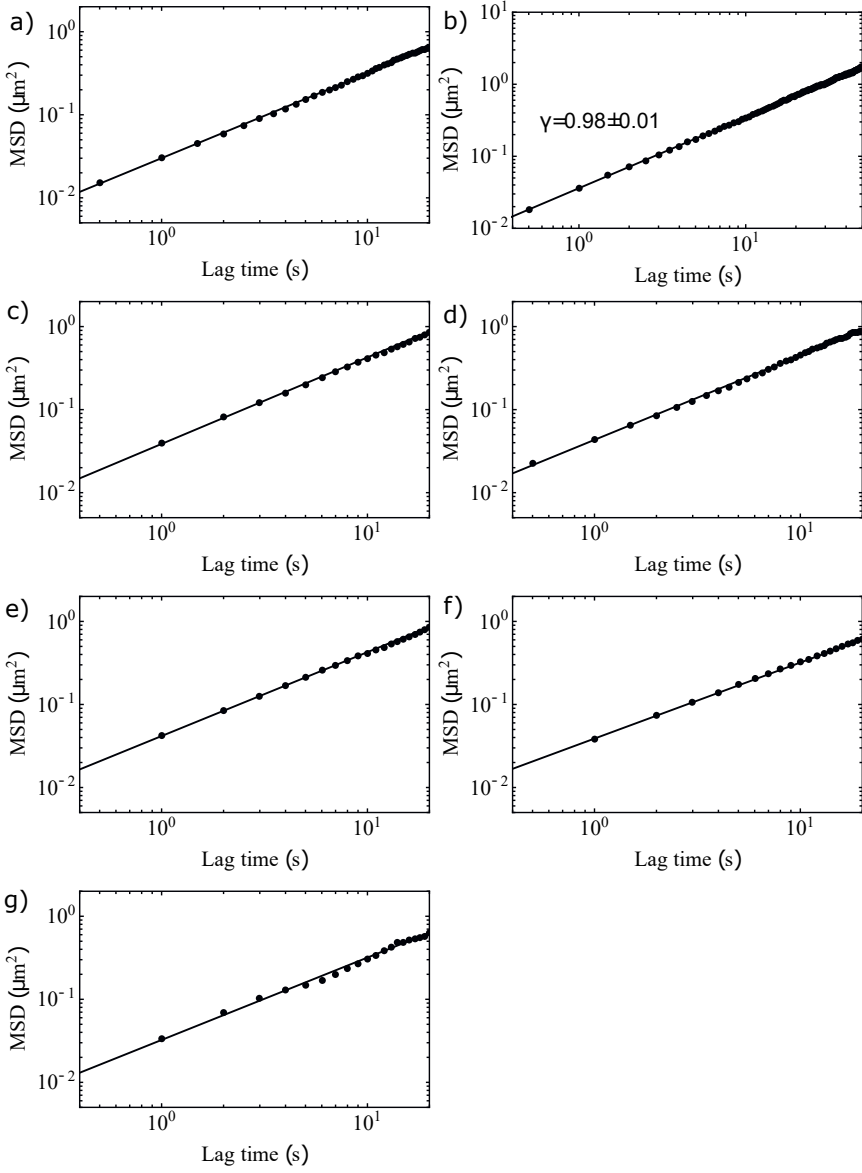


Figure A5: Ensemble MSDs for various electron dose rates: a) $17 \text{ e}^- \text{nm}^{-2} \text{s}^{-1}$, b-c) $9 \text{ e}^- \text{nm}^{-2} \text{s}^{-1}$, d-e) $3 \text{ e}^- \text{nm}^{-2} \text{s}^{-1}$, f) $1.6 \text{ e}^- \text{nm}^{-2} \text{s}^{-1}$ and g) $0.6 \text{ e}^- \text{nm}^{-2} \text{s}^{-1}$.

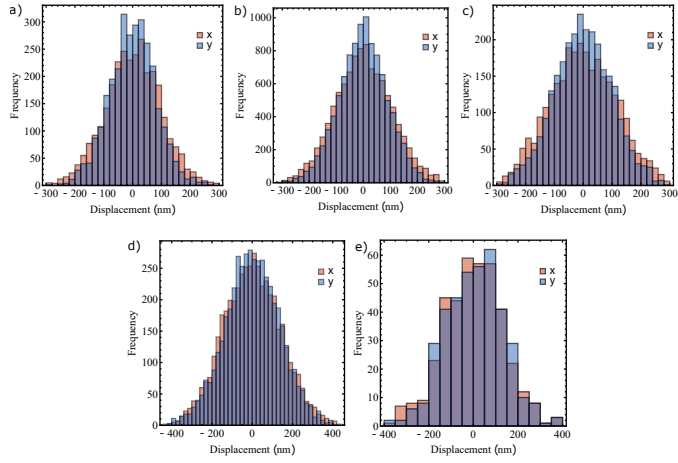


Figure A6: Displacement histograms for various electron dose rates: a) $17 \text{ e}^- \text{ nm}^{-2} \text{ s}^{-1}$, b) $9 \text{ e}^- \text{ nm}^{-2} \text{ s}^{-1}$, c) $3 \text{ e}^- \text{ nm}^{-2} \text{ s}^{-1}$, d) $1.6 \text{ e}^- \text{ nm}^{-2} \text{ s}^{-1}$ and e) $0.6 \text{ e}^- \text{ nm}^{-2} \text{ s}^{-1}$. Histograms a-c) show displacements in 0.5 s frame time. Histograms d-e) show displacements in 1 s frame time.

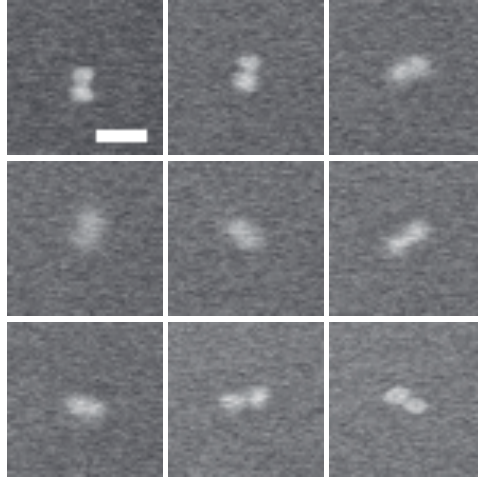


Figure A7: A dumbbell of gold NPs in the experimental Supporting Movie 4 at $t = 240, 270, 285, 294, 318, 327, 337, 360$ and 382 s . Due to its mobility in z , it becomes more or less blurry depending on the position in the cell. The scalebar indicates 200 nm.

APPENDIX B: ADDITIONAL ELECTRON DOSE RATE EFFECTS

Interactions of the incident electrons with the sample can lead to various beam-induced effects. In the main text we discuss the accumulation of charges in the sample and the induced electric fields. However, many studies have observed other electron beam effects. Effects like radiolysis,¹³⁷ bubble formation,^{137,149} momentum transfer¹⁰⁸ and temperature increase¹⁰⁸ have all been analyzed. For the dose rates used in this study, which are at least an order of magnitude lower than other studies, the effects are expected to be limited. Momentum transfer has been found to be negligible for electron dose rates orders of magnitude higher than ours.¹⁰⁸ These calculations were done for systems that are different to ours, but we believe they should not have a significant effect on our experiments.

Bubble formation was observed to occur if a higher beam current was used in experiments in both glycerol and glycerol carbonate (20-100 pA). The reason for the inconsistent current at which this happens is unknown.

Electron beam induced temperature rise in the liquid-cell

We calculate the expected temperature increase in the liquid-cell using the calculation from the Supplementary Information in a paper by Zheng *et al.*¹⁰⁸ We assume all the energy dissipation from the electron beam transfers to heat. For a liquid-cell in the high vacuum of the microscope, the induced temperature rise of the irradiated area is estimated using the heat conduction equation on a two-dimensional disk.¹⁰⁸

We assume a uniform thin film and steady-state. While our liquid-cell has a thickness of around 2 μm , the length and width of the liquid cell is much larger and thus we can assume a thin film. The steady state is however more of an issue. Since we use STEM, the electron probe is constantly changing position. For this calculation, we calculate the temperature increase due to a stationary STEM probe of 1 nm in diameter.

The two-dimensional heat conduction equation in cylindrical coordinates is

$$-k \cdot \left(\frac{d^2 T}{dr^2} + \frac{1}{r} \frac{dT}{dr} \right) = J \quad (2.8)$$

where k is the thermal conductivity, T the temperature distribution which depends on the radius r and J is the heat flux density.

We calculate the temperature at the edge of the STEM probe R_1

$$T_{R_1} = T_{RT} + \frac{Q}{2\pi k h} \ln \left(\frac{R_0}{R_1} \right), \quad (2.9)$$

where T_{RT} is the room temperature, h is the height of the liquid-cell and R_0 the width of the liquid cell, where the temperature equals room temperature. Furthermore, $Q = J_e \cdot \pi R_1^2 \cdot (dE/dX)$ is the total heat flux of the irradiated area, where J_e is the electron current density and dE/dX is the total energy loss per electron going through the liquid-cell. We assume $dE/dX = 120 \text{ eV}$. The temperature in the middle of the STEM probe T_C is then

$$T_C = T_{R_1} + \frac{1}{4k} J R_1^2. \quad (2.10)$$

The derivations can be found in the Supplementary Information of ref.¹⁰⁸

For a stationary STEM probe of 1 nm in diameter, an electron current of 139 pA (the highest used in the study of gold NPs), height of the liquid-cell $h = 2 \mu\text{m}$, the thermal conductivity $k = 0.28$ for glycerol, $R_0 = 1 \text{ mm}$ and $dE/dX = 120 \text{ eV}$, we find an increase in temperature of 0.2 K in the middle of the probe. Even though the temperature increase seems minimal, it is clear a temperature gradient is created.

APPENDIX C: SUPPORTING MOVIES



Supporting Movie 1: Titania particles (diameter 350 nm) diffusing in glycerol carbonate. The frame time is 0.5 s. The video is sped up 20 times. The pixel size is 17.5 nm and the frame is 512 by 512 pixels. The electron dose rate is $2 \text{ e}^- \text{ nm}^{-2} \text{ s}^{-1}$.



Supporting Movie 2: Titania particles (diameter 350 nm) diffusing in glycerol carbonate. The frame time is 0.5 s. The video is sped up 10 times. The pixel size is 24.5 nm and the frame is 256 by 256 pixels. The electron dose rate is $4 \text{ e}^- \text{ nm}^{-2} \text{ s}^{-1}$.



Supporting Movie 3: Au NPs (diameter 77 nm) diffusing in glycerol. The frame time is 0.5 s. The video is sped up 10 times. The pixel size is 12.2 nm and the frame is 5125 by 512 pixels. The electron dose rate is $3 \text{ e}^- \text{ nm}^{-2} \text{ s}^{-1}$.



Supporting Movie 4: Au NPs (diameter 77 nm) diffusing in glycerol. The frame time is 0.5 s. The video is sped up 10 times. The pixel size is 12.2 nm and the frame is 5125 by 512 pixels. The electron dose rate is $9 \text{ e}^- \text{ nm}^{-2} \text{ s}^{-1}$.



Supporting Movie 5: Au NPs (diameter 77 nm) diffusing in glycerol. The frame time is 0.5 s. The video is sped up 10 times. The pixel size is 12.2 nm and the frame is 5125 by 512 pixels. The electron dose rate is $17 \text{ e}^- \text{ nm}^{-2} \text{ s}^{-1}$.

Hydrodynamic interactions between the core and shell in rattle-type particles

ABSTRACT

Rattle-type particles consist of a mobile core within a hollow shell. In this chapter, rattle-type particles consisting of a fluorescent spherical silica core (490 nm in diameter) confined in a hollow, porous spherical silica shell (1.16 μm inner diameter, 40 nm shell thickness) were synthesized and subsequently investigated using 3D fluorescence confocal microscopy. The trajectories of the core particles were found using a 3D Gaussian fitting procedure and were used to determine diffusion coefficients as function of the 3D position within the shells. The standard deviation in the position of a stationary particle was found to be 8 nm in x and y directions and 40 nm in the z direction using our tracking method. Furthermore, the microscope calibration was investigated in order to allow for correcting errors in the determination of the z coordinate. Our results indicate that the core is less likely to be found close to the shell, showing a repulsive interaction between core and shell. This electrostatic repulsion was found to be longer ranged than expected based on the interactions between spheres. This is almost certainly due to the concave geometry of the shell. The diffusion coefficient of the confined core was found to be approximately 20% of that of a free colloid, when the core was in the middle of the rattle geometry. Additionally, diffusion became increasingly slow as the core approached the shell, particularly in the radial direction. The diffusion in the direction along the shell wall remained relatively constant within the whole rattle geometry. The position-dependent and direction-dependent diffusion coefficients found in the experiments were in good agreement with finite-element calculations solving Stokes' equations for fluid dynamics of an incompressible liquid.

3.1. INTRODUCTION

Colloidal particles that are dispersed in a fluid move around via diffusion. This is caused by the molecules of the medium colliding with the particle. As the forces exerted on the particle due to multiple collisions taking place is not balanced on all sides of the particle at any given time due to thermal fluctuations, the particle moves around. The particle then displaces the liquid medium it moves through, which results in hydrodynamic drag on the particle. The motion of particles due to thermal fluctuations, which we call Brownian motion, can be discussed in terms of a diffusion coefficient D

$$D = \frac{k_B T}{f}, \quad (3.1)$$

where k_B is the Boltzmann constant, T is the absolute temperature and f is the friction coefficient of the particle moving through a certain solvent. Assuming an incompressible fluid, the liquid flows around the particle with a no-slip boundary condition, which causes the hydrodynamic drag. The friction coefficient is the ratio between the force \vec{F} and the particle velocity \vec{v} . For the simplest case of a single, isolated, spherical particle with a stick boundary condition on the particle surface in a large reservoir of liquid the particle with a velocity \vec{v} in three dimensions produces a drag force given by the Stokes formula:¹⁵⁰

$$\vec{F} = -6\pi\eta a\vec{v}. \quad (3.2)$$

Here η is the solvent viscosity and a is the particle radius. Relating the drag force to the thermal fluctuations gives us the Stokes-Einstein equation, derived independently by Sutherland¹⁵¹ and Einstein:⁶

$$D = \frac{k_B T}{6\pi\eta a}. \quad (3.3)$$

The free diffusion of particles has been extensively studied and is well understood.^{152, 153} However, this is not the case for more complex cases. Diffusion in concentrated, confined 3D suspensions are upcoming areas of research due to the interest in dynamical behavior of biological and other soft matter systems. In general, the dynamics of colloidal particles in confinement is of great interest for nanoscience. For example, transport through zeolites, droplets migrating through microfluidic channels, or particles enclosed by other particles, are all affected by the condition that the liquid through which they move is not as easily displaced as in normal conditions, due to extra hydrodynamic drag. Even the diffusion of a single particle close to walls and/or in a confined geometry is a challenging problem.^{136, 154–163}

Over the past decades the study of diffusion has shifted towards diffusion in more complicated geometries. The classical problem of the motion of a single colloidal particle near a flat wall has been explored experimentally,^{155, 157, 158} theoretically^{164, 165} and by computer simulations.¹⁶⁶ Beyond that, diffusion of a particle between two parallel planar walls has also been studied.^{136, 154, 156, 159} The hydrodynamic drag on a particle is influenced by the presence of walls due to flow restrictions in combination with the stick boundary condition. The walls also break the symmetry around the particle and the diffusion coefficient thus has to be considered in terms of the symmetry of the system. In the case of a planar wall, the diffusion coefficient can be decomposed into components that are parallel and perpendicular

to the planar wall, which both depend on the separation distance between the particle and the wall. In all studies, both diffusion coefficients decrease as the particle approaches the wall more closely due to the hydrodynamic coupling of the particle and the wall. For the diffusion of a particle between two planar walls that were 4 particle diameters apart, the particle motion is already reduced significantly in the midplane between the two walls as compared to the free diffusion of an identical particle, due to the long-ranged nature of the hydrodynamic coupling between the particle and the walls.¹⁵⁶ Recently, other geometries, such as cylindrical and spherical cavities, where the particle is confined from all sides, have gained attention as well. Eral *et al.*¹⁶⁰ showed that the diffusion coefficient of colloidal particles in the center of a closed cylindrical cavity with both the height and the radius equal to 9 particle diameters, is 25% lower than the bulk diffusion coefficient in the same liquid. They also showed that the diffusion inside a closed cylindrical cavity is asymmetrical and that there is a transition region of about 3 particle diameters wide in which the radial D_r and azimuthal D_θ components of the anisotropic diffusion coefficient decrease to 10 and 40% of the bulk diffusion coefficient, respectively. This is in agreement with results from computer simulations on the hydrodynamics of a spherical particle entrapped in a closed cylinder.¹⁶⁷ The case of a spherical cavity has been investigated by Cervantes-Martínez *et al.* as they experimentally investigated the diffusion of fluorescent polystyrene spheres entrapped in spherical water droplets immersed in oil. They showed that the radial diffusion coefficient D_r (toward the liquid-liquid interface) dropped significantly as the particle approached the interface. However, the perpendicular diffusion coefficient D_p (along the curved surface) remained virtually unchanged except close to contact with the interface. At that point the particle had already significantly deformed the liquid-liquid interface. Due to the nature of this interface the fluid velocity at the interface is most likely not zero, resulting in different boundary conditions than in our system where the spherical confinement is due to a rigid silica shell. The particle systems used in this work will be explained in subsequent paragraphs.

A thorough theoretical study on diffusion inside a spherical cavity was carried out by modeling the behavior of a concentrated colloidal dispersion (but also just a single particle) in such 3D confinements.¹⁶² It provides useful insights on how the radial and perpendicular diffusion coefficients change due to hydrodynamic interactions in spherical cavities as a function of the geometry. Studying concentrated colloidal dispersions in spherical confinement is interesting as it could for instance gain insights into supraparticle formation.^{168–171} However, for now we focus on a single particle within spherical confinement. The study showed that the 3D spherical confinement breaks the symmetry of the drag on the diffusing particle, which results in an anisotropic hindrance of both the radial and perpendicular diffusion coefficients to a different extent. Furthermore, it shows that the particle diffused fastest in the middle of the shell. However, the diffusion coefficient is less than that of a free particle, even when the shell radius is 20 times larger than the particle radius, which shows the long-ranged nature of hydrodynamic interactions. The perpendicular diffusion coefficient stays constant until the particle is close to contact with the shell, while the parallel diffusion coefficient decreases more gradually. At particle-shell contact the diffusion is zero.

In this chapter we study the diffusion of a colloidal particle within a cavity. Interestingly, one of the most famous experiments for Brownian motion, by Robert Brown, was the observation of diffusing granules within pollen cells.³ So the observation from which Brownian motion got its name was the motion of a colloidal particle within a cavity. Nowadays colloidal particles within shells can be synthesized³⁴ and studied at a much higher resolution. We used 3D confocal microscopy to study the diffusion of a colloidal particle within a shell in viscous media. We observed the mobility of sub-micron silica particles within a porous silica shell in 3D and studied their position-dependent and direction-dependent diffusion.

3.2. METHODS

3.2.1. Synthesis of silica rattle particles

Chemicals. The following chemicals were used: absolute ethanol (**EtOH**, TechniSolv), fluorescein isothiocyanate isomer I, $\geq 90\%$ (**FITC**, Sigma-Aldrich), (3-aminopropyl)triethoxysilane, $\geq 98\%$ (**APTES**, Sigma-Aldrich), ammonium hydroxide solution (**ammonia**, $\sim 25\text{ w}\%$ NH_3 basis in water, Honeywell), tetraethoxy silicate, 98% (**TEOS**, Sigma-Aldrich), Milli-Q water (Millipore Direct-Q3 UV water purification system), N-[3-(trimethoxysilyl)-propyl]ethylenediamine, 97% (**EDAPTMS**, Sigma-Aldrich), hydrofluoric acid, $48\text{ w}\%$ (**HF**, Sigma-Aldrich), lithium chloride (**LiCl**, Sigma-Aldrich), glycerol, ≥ 99.5 (Sigma-Aldrich), Coumarin 153, 99% (Sigma-Aldrich), 4-(hydroxymethyl)-1,3-dioxolan-2-one (**glycerol carbonate**, Sigma-Aldrich), dimethyl sulfoxide (**DMSO**, $\leq 0.01\%$ water, Sigma-Aldrich), polyethyleneimine (**PEI**, $\leq 1\%$ water, Sigma-Aldrich), tetramethylammonium chloride, $\geq 98\%$ (Acros Organics), tetraethylammonium bromide, 98% (Sigma-Aldrich), tetrabutyl-ammonium bromide, $\geq 98\%$ (Sigma-Aldrich).

Synthesis. The synthesis was modified from the synthesis described in the thesis by W. Vlug.^{172,173} The rattle particles were synthesized in four main steps: growth of the fluorescent silica core, growth of a layer of organically modified silica (ormosil), growth of the outer silica shell and etching of the ormosil layer. This is schematically depicted in Figure 1.

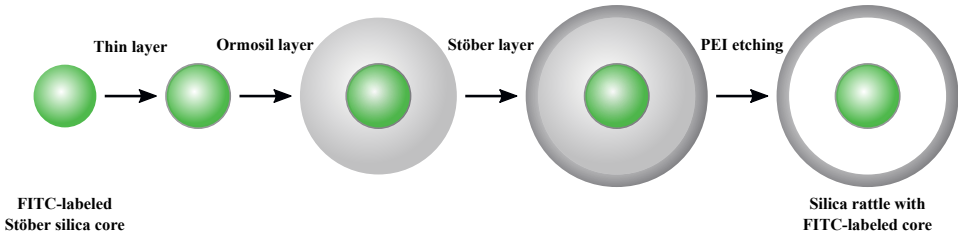


Figure 1: Schematic depiction of the steps in the synthesis of fluorescently-labeled silica rattle particles.

To grow the fluorescent cores, one of the silica precursors was first coupled to the fluorescent dye. 50.0 mg FITC and 5.00 mL of EtOH were combined and stirred for 15 minutes. 61.7 μL APTES was added and the mixture was stirred overnight in the dark. In a 1000 mL single neck round bottom flask, 330 mL EtOH and 33.86 mL of ammonia were combined. Under vigorous stirring, 14.36 mL TEOS was added all at once and immediately afterwards

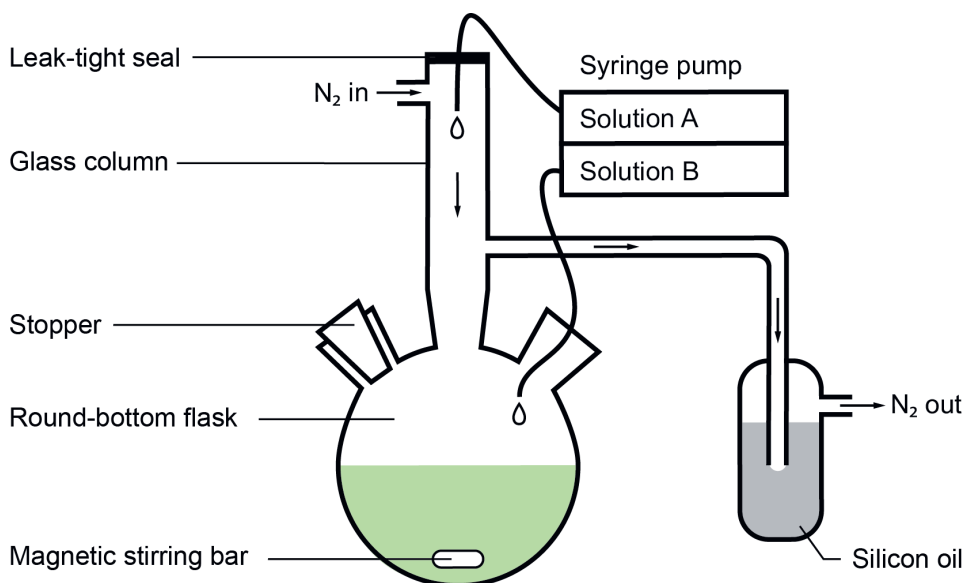


Figure 2: Schematic depiction of the setup used for the synthesis of the rattle particles.

the earlier prepared FITC-APTES was added all at once. After eight minutes, stirring was reduced and the flask was wrapped in aluminium foil to react in the dark overnight. Nearly 24 hours later the stirring was stopped. 150 mL of the reaction mixture was transferred to a clean round-bottom flask. In the setup shown in Figure 2, two solutions were added to the mixture using a syringe pump at 0.50 mL per hour under nitrogen flow and stirring. See Table 1 for the composition of these solutions. After 22 hours, stirring was stopped and the reaction mixture was washed three times with EtOH through centrifugation. After the last centrifugation step, the sediment was redispersed in 40.0 mL of EtOH (volume fraction particles $\phi = 0.007$).

7.50 mL of the particle dispersion was added to 61.9 mL EtOH, 8.50 mL Milli-Q water and 33.63 mL ammonia under gentle stirring. In the setup shown in Figure 2, two solutions (see Table 1) were added using a syringe pump at 0.30 mL/hr. After 15 hours, the reaction was stopped. The reaction mixture was washed with EtOH twice and redispersed in 5.00 mL EtOH ($\phi = 0.0136$). Of the particle dispersion prepared in the previous step, 16.9 mL was dispersed in a mixture of 89 mL EtOH, 12.0 mL Milli-Q water and 4.79 mL ammonia. Under gentle stirring 0.898 mL of TEOS was added. After 21 hours, stirring was stopped and the reaction mixture was washed three times with EtOH by centrifugation.

A surface-protecting etching process with polyethylenimine (PEI) was performed.¹⁷⁴ The total reaction volume of 10 mL contained 0.236 mg/mL particles and 0.01 mg/mL PEI in ethanol. The sample was sonicated for 1 min and subsequently stirred for 30 min (350 rpm) at 35 °C. The sample was then washed once in ethanol and once in water (5 min, 5000 g). In

Table 1: Composition of the solutions used for rattle synthesis.

	Solution A	Solution B
Core	1mL TEOS 6.86 mL EtOH	5.34 mL EtOH 0.712 mL ammonia 1.81 Milli-Q water
Ormosil layer	3.13 EtOH 1.18 mL TEOS 0.382 EDAMPTES	3.23 mL EtOH 1.01 mL Milli-Q water 0.410 mL ammonia
Shell	0.898 mL TEOS	-

10 mL water the sample was stirred for 22 hours (350 rpm) at 50 °C. Finally, the sample was centrifuged (5 min, 5000 g) and redispersed in water.

3.2.2. Confocal microscopy

All confocal microscopy measurements were performed on a Leica SP8 confocal microscope equipped with a white light laser (WLL) and a photomultiplier tube (PMT) as a detector.

Axial calibration confocal microscope. The calibration of the confocal microscope in the axial dimension and the influence of a refractive index mismatch on imaging were studied as described in ref.¹⁷⁵ A calibration cell was built by placing two #0 cover glasses (80-120 μm , Menzel-Gläser) on a microscope slide, leaving some space between them, and placing a #1.5 cover glass (160-190 μm , Marienfeld) on top of these. A small amount of UV glue (Norland Optical Adhesive) was used between each layer to secure all parts in place. The height of this cell was first determined using Fourier transform infrared (FTIR) spectroscopy as a reference. A Bruker Vertex 70 FTIR spectrometer was used with a selected diameter aperture of 0.25 mm to measure the transmission spectrum of the cell. A drop of immersion oil (Leica, Type F) was placed on the upper cover slip of the cell prior to measurement to avoid interference effects. The height of the cell was then also measured by finding the positions of the top and bottom glass of the cell, using a confocal microscope in reflection mode with a 20x/0.7 air objective. The excitation wavelength used was 495 nm and signal was detected from 485-505 nm using a PMT. Subsequently, the cell was filled with fluorescent solutions with different refractive indices and its height was measured again, now by imaging the medium in the cell in fluorescence mode, using a 93x/1.3 glycerol immersion objective, 495 nm excitation wavelength and detecting signal from 505-600 nm using a PMT. Water, a 90:10 v% glycerol:water solution, glycerol carbonate, all dyed with FITC, and Leica Type F immersion oil dyed with Coumarin 153 were used. A drop of 90:10 v% glycerol:water was placed on the objective for all these measurements, as this solution was also used for the measurements on rattle particles. The cell was flushed with the relevant liquid three times prior to measurements. A nitrogen flow was used to remove the liquids from the cell.

Three-dimensional imaging of moving cores. A 90:10 volume percent solution of glycerol and rattle particles in Milli-Q water was prepared with a final salt concentration of 5.00 mM LiCl ($\kappa^{-1} \approx 3.3 \text{ nm}$), in order to make the repulsive electrostatic interaction between the core

and the inner shell wall short-ranged. A 0.10 x 2.00 mm capillary (borosilicate glass, VitroCom Vitrotubes) was filled with this solution and fixed on a microscope slide (Menzel-Gläser) using UV glue. Sample slides were prepared at least several days before a measurement to allow the particles to sediment on the glass to avoid freely diffusing loose cores in the sample and ensure any observed moving particles were cores confined in a shell. The shell of some of the particles would be immobilized on the glass, while the core particle could still move around within the shell compartment.

Measurements were performed on a Leica SP8 confocal microscope equipped with a white light laser (WLL) and a Hybrid detector (HyD). A Leica motCORR 93x glycerol immersion objective with a numerical aperture of 1.3 was used. The motCORR objective could be used to minimize the effects of refractive index mismatch and chromatic aberrations. This was done by imaging a stationary particle in the xz -plane and varying the motCORR value until maximum intensity and minimal spatial extension in z was achieved.

Measurement parameters, like immersion liquid, laser power and scanning speed, were optimized by measuring both stationary and moving particles and evaluating the quality of the data sets, e.g. the degree of error in particle tracking results. The number of z -slices and size of a z -stack, and consequently the z pixel size, was chosen such that the convolution of the fluorescent particle and the point spread function (PSF) of the particle could be imaged within the whole 3D confinement of the shell, while keeping the time it takes to record one z -stack around 0.5-0.7 s. The optimal parameters, which were used for the final data acquisition, are given in Table 2.

Table 2: Optimized parameters used for data acquisition using a Leica SP8 confocal microscope.

Immersion liquid	90:10 v% glycerol:water
Excitation wavelength	495 nm
Detection wavelength	505-600 nm
Detector	PMT 2
Scan mode	<i>xyzt</i>
Scan direction	Bidirectional
Scanning speed	1800 Hz
Zoom	48.00
Pinhole	1 AU
Output power WLL	50.00%
Power laser line	5.00%
Pixel size x & y	41.336 nm
Pixel size z	150.00 nm
XY-pixels per frame	64
Z-slices per z-stack	~ 20
XY scan time	~ 0.0250 - 0.0350 s
Z-stack time	~ 0.500 - 0.700 s

Particle tracking. The x , y and z coordinates of core particles were determined from microscopy images by performing particle tracking in Python. We used a tracking method where a 3D Gaussian function was fitted to the data. This was done using Python 3.7 in Spyder 4. A 3D Gaussian function was defined in which the positions of the maxima in x , y and z were the unknowns. The images were transformed to arrays of brightness values and the Gaussian function was fitted to these arrays using a least-squares method. The Python script used for this method was written by M. Bransen and can be found in Appendix A.

The tracking error was estimated by analyzing data sets acquired from imaging stationary particles. Any “movement” observed in the results from tracking these particles was associated with tracking errors, while of course drift, irreproducible movement of the scanning mirrors could also be the cause of such errors. To analyze the error, the standard deviation of the lists of the x , y and z positions of the particle in each z -stack was calculated using Wolfram Mathematica (version 12.2).

The 3D Gaussian fitting was used to track the mobile particles as well and the feature sizes used were 21 pixels for x and y and 12 pixels for z , which corresponds to 868 nm in x and y and to 1800 nm in z . Pixel sizes can be found in Table 2.

Determination diffusion coefficient from experimental data. After the x , y and z coordinates of the particle were determined from all frames, the data was analyzed using Wolfram Mathematica (version 12.2). The displacement magnitude of the particle d_{xyz} within a certain time ($\Delta t = t_2 - t_1$), in our case the frame time (of the z -stack), was calculated as

$$d_{xyz}(\Delta t) = \sqrt{(x(t_2) - x(t_1))^2 + (y(t_2) - y(t_1))^2 + (z(t_2) - z(t_1))^2}. \quad (3.4)$$

As the scanning routine of the confocal microscope is known, Δt could be determined more accurately by using the x , y , z coordinates of the particle. For example, if the particle is found in the top left corner in the first frame and in the bottom right corner in the second frame, Δt should be more than the frame time. However, due to particle displacements being approximately 20 nm on average between frames in one direction, and the total z -stack is approximately 2645 by 2645 by 3000 nm, we expect this effect to be minimal. As such the frame time was used as Δt .

Due to the symmetry of the system, the diffusion coefficient has two components: a component in the radial direction and a component perpendicular to that direction (along the shell wall). As such we analyze the displacements along radial and perpendicular directions via the displacement vector \mathbf{d}

$$d_r(\Delta t) = \mathbf{d}(\Delta t) \cdot \hat{r}, \quad (3.5)$$

$$d_p(\Delta t) = \mathbf{d}(\Delta t) \cdot \hat{p}, \quad (3.6)$$

where \hat{r} and \hat{p} are the unit vectors in the radial and perpendicular direction, respectively. The diffusion coefficients in the radial and perpendicular direction are defined as:

$$D_r = [\mathbf{d}(\Delta t) \cdot \hat{r}][\mathbf{d}(\Delta t) \cdot \hat{r}]/(2\Delta t), \quad (3.7)$$

$$D_p = [\mathbf{d}(\Delta t) \cdot \hat{p}][\mathbf{d}(\Delta t) \cdot \hat{p}]/(4\Delta t). \quad (3.8)$$

As the radial and perpendicular diffusion coefficients are analyzed within a certain radial part of the shell Δr , the diffusion coefficient in such a segment was effectively calculated by using the variance of the displacements σ^2 in the radial and perpendicular directions, respectively:

$$D_r(\Delta r) = \sigma_{d_r}^2 / (2\Delta t), \quad (3.9)$$

$$D_p(\Delta r) = \sigma_{d_p}^2 / (4\Delta t). \quad (3.10)$$

The radial coordinate that was taken to determine in which radial segment Δr the displacement took place was taken as the middle point between the radial coordinates of the two frames over which the displacement occurred.

3.2.3. Finite-element calculations

The coordinates acquired using particle tracking were used to determine diffusion coefficients of the core. These were compared to theoretical diffusion coefficients calculated using COMSOL Modeling software (version 5.4), taking the hydrodynamics of the problem into account. A system with a spherical colloid of radius $R_{\text{core}} = 245 \text{ nm}$ within a shell of inner radius $R_{\text{shell}} = 584 \text{ nm}$ was set up to represent the rattle particles of the experiments. Both the particle and the shell surface were set to have a no-slip boundary condition. The spherical shell, including the core particle and the liquid, was placed within a cylindrical domain with open boundary conditions (zero normal stress) for the fluid. Stokes' equations were solved for fluid dynamics of an incompressible liquid. The fluid density was taken as $\rho = 1.26 \cdot 10^3 \text{ kg m}^{-3}$ and the dynamic viscosity used was $\eta = 0.45 \text{ kg m}^{-1} \text{ s}^{-1}$ in accordance with the experimental system.^{176,177} A constant velocity boundary condition was applied to the sphere to obtain the translational mobility. To ensure that the laminar flow condition is satisfied, a low velocity of the sphere was used: $v = 10^{-6} \text{ m s}^{-1}$. We solved for the force exerted by the fluid and shell wall on the particle by integrating the hydrodynamic stress tensor over the surface of the sphere. The position of the core particle inside the shell was varied to determine how the force changed with the radial position. Furthermore, the direction of the velocity condition on the core particle was changed to decouple the hydrodynamic force in the radial direction and the force perpendicular to that direction (along the shell wall). The force was then compared to the force on a particle that was free from confinement to determine the diffusion coefficient. When the velocity condition was directed in the radial direction, the rotational symmetry of the system was exploited to minimize the number of mesh elements required. A full 3D calculation was required when the velocity condition was directed along the shell as the rotational symmetry was broken. Constructing a sufficiently small mesh in this case was only feasible when local refinements of the elements on the surface of the core particle and the shell wall were used. Generally, an element size of 2 nm was employed on the surface of the core particle and the element size was allowed to grow radially outward. The mesh on the shell wall was also locally refined. Mesh refinement was performed for a few selected calculations and no significant difference for even smaller element sizes was found.

3.3. RESULTS & DISCUSSION

3.3.1. Microscope calibration and tracking errors

Before conducting the experiments on the diffusion of the core particle, we checked the axial calibration of the confocal microscope, because it is known to be difficult to correctly calibrate in this direction.¹⁷⁵ The calibration of the microscope was investigated as described in Section 3.2.2. The reference height of the calibration cell was determined using FTIR, by analyzing the Fabry-Pérot fringes observed in the cell's transmission spectrum, shown in Figure 3a. The spacing between the fringes was calculated using $2n \frac{\lambda_0 - \lambda_p}{\lambda_0 \lambda_p}$, where λ_0 is the position of a reference maximum and λ_p is the position of each of the subsequent maxima at a smaller wavelength, as indicated in Figure 3a. The refractive index n of the medium in the cavity is 1 in this case, as the cell was measured in air. The values found using this formula were plotted against the fringe order of each maximum and the height of the cell was given by the slope of a linear fit through these points. The reference height found in this way was $109.5 \pm 0.7 \mu\text{m}$.

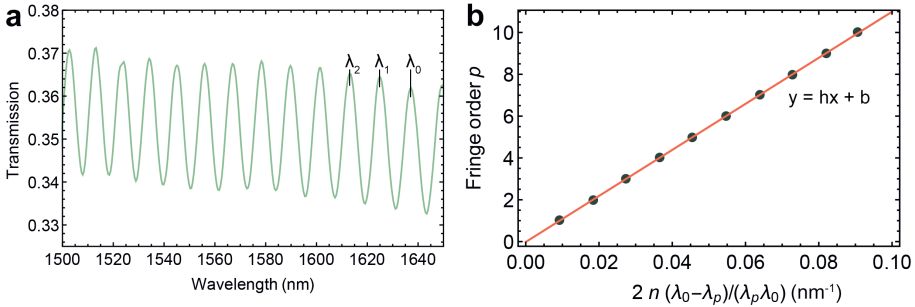


Figure 3: a) FTIR transmission spectrum of the calibration cell. b) Linear fit through a plot of the spacing between the maxima of the Fabry-Pérot fringes versus the fringe order of each maximum. The slope h is the height of the calibration cell.

The height of the calibration cell was determined from the confocal microscopy images, shown in Figure 4a and 4b, by plotting the mean pixel intensity for each z-position in the cell. As shown in Figure 4c, for the cell in air the difference between the positions of the intensity maxima was determined and taken to be the height of the cell. For the cell with 90:10 v% glycerol:water solution containing FITC (refractive index $n_D^{20} = 1.46$),¹⁷⁸ its height was determined by finding the difference between the positions where the intensity was half the maximum intensity, as shown in Figure 4d. The difference between the reference height ($109.5 \pm 0.7 \mu\text{m}$) and the height of the cell in air found using confocal microscopy ($115.4 \pm 0.2 \mu\text{m}$) indicates the microscope was not perfectly calibrated. The difference between the reference height and the cell height found with 90:10 v% glycerol:water ($115.1 \pm 0.2 \mu\text{m}$), the solvent used in the rattle particle experiments, was taken to be due to an incorrectly calibrated setup. The work of Besseling and coworkers showed that this axial miscalibration can easily distort the axial distances recorded in samples.¹⁷⁵ Consequently, data concerning

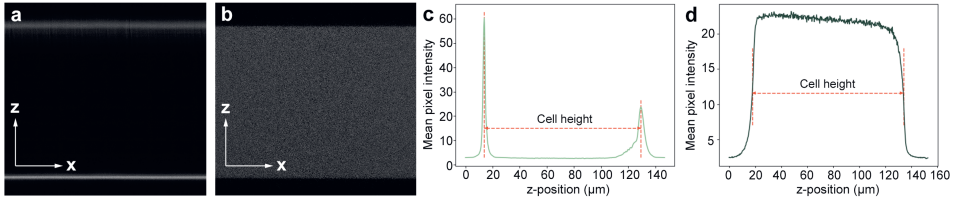


Figure 4: a) Image of the empty calibration cell in the xz -plane, recorded using a confocal microscope in reflection mode. b) Image of the calibration cell filled with a 90:10 v% glycerol:water solution ($n_D^{20} = 1.46$)¹⁷⁸ containing FITC, recorded using a confocal microscope in fluorescence mode. c) Plot of the mean pixel intensity versus the z -position as found in the confocal images of the empty cell. d) Plot of the mean pixel intensity versus the z -position as found in the confocal images of the cell containing a 90:10 v% glycerol:water solution.

the axial dimension acquired using this microscope and solvent were corrected with a factor of 109.5/115.1 to compensate for imperfect calibration and refractive index mismatch.

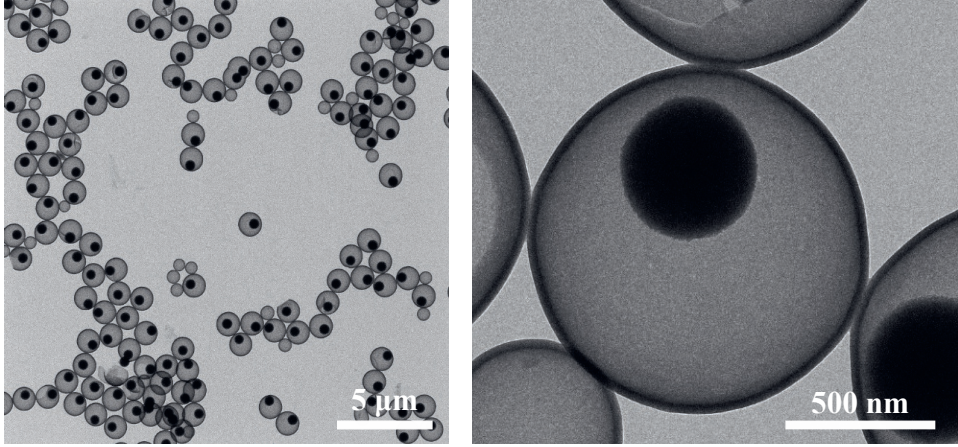


Figure 5: TEM images of the sample of rattle particles used for the confocal microscopy experiments. Average shell and core sizes are given in the main text.

Next, the tracking error of our experiments was investigated. We used the sample that was prepared as described in the Methods section. Characterization using TEM (Figure 5) showed that the particles had a mean core diameter of 490 ± 21 nm (polydispersity (pd) is 4.3%) and a mean inner shell diameter of 1158 ± 16 nm (pd is 1.3%). The shell thickness was approximately 40 nm.

For the determination of the tracking error we used the same parameters of the microscope and the same sample as in our experiment for the moving core particles. It was found that the

standard deviation of finding an immobile particle using the tracking procedure was found to be 8.1 ± 1.4 nm, 8.1 ± 1.1 nm and 39.9 ± 5.3 nm in the x , y and z directions, respectively.

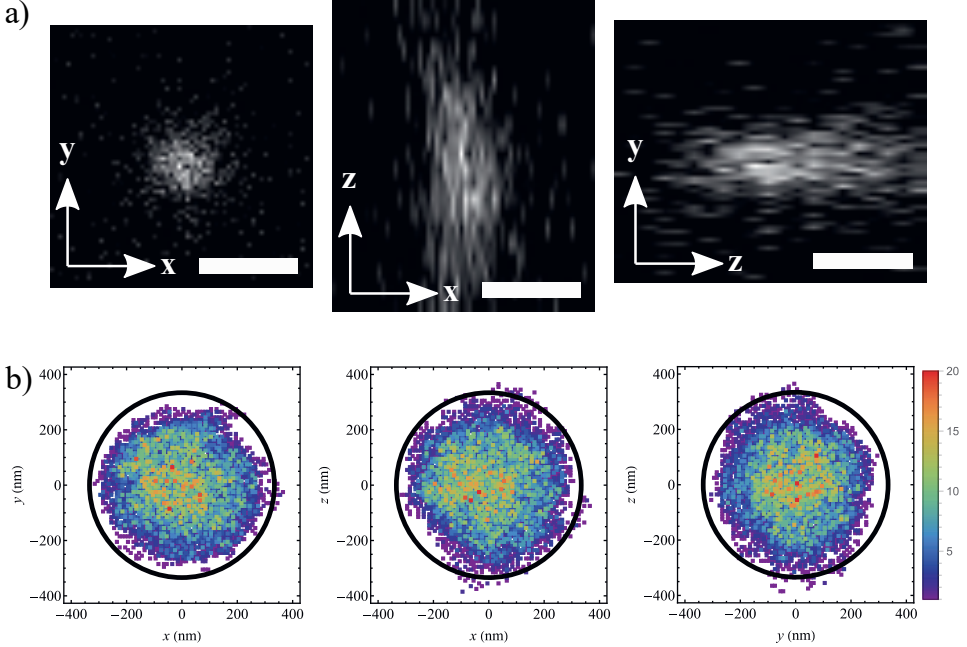


Figure 6: Imaging and tracking of the fluorescent core particle. a) A single z -slice in the xy -plane of a z -stack recorded using 3D fluorescence confocal microscopy and images of the corresponding xz -plane and zy -plane. b) Tracking result for 7 different particles. The black circle indicates the available space to the core particle within the shell. The scale bar represents 1 micron.

Having determined the axial calibration and the tracking error, the diffusion of core particles in the shell could be studied. Seven mobile particles within the shell were imaged and tracked (Figure 6). In Figure 6b, the color of a position indicates how often a particle was found in that particular position. The mobile core particles were most frequently found in the middle of the shell. Due to the larger tracking error in the z dimension, the core particle is sometimes found outside its available space within the shell. However, the tracking error is not so large for that this become a significant problem. Only 1.7% of all particle locations were found outside the space available to the core particle, indicating that our tracking results are sufficiently reliable for studying the diffusion of the particle.

3.3.2. Diffusion of the core particle within the shell

For the experiments of a mobile core within a hollow shell, we once again used the sample shown in Figure 5. Figure 7a shows the mean-centered trajectories of the core of one rattle particle in the x , y and z dimensions. The red, dashed lines correspond to the maximum distance available to the core in the shell. The trajectories show that this particular core

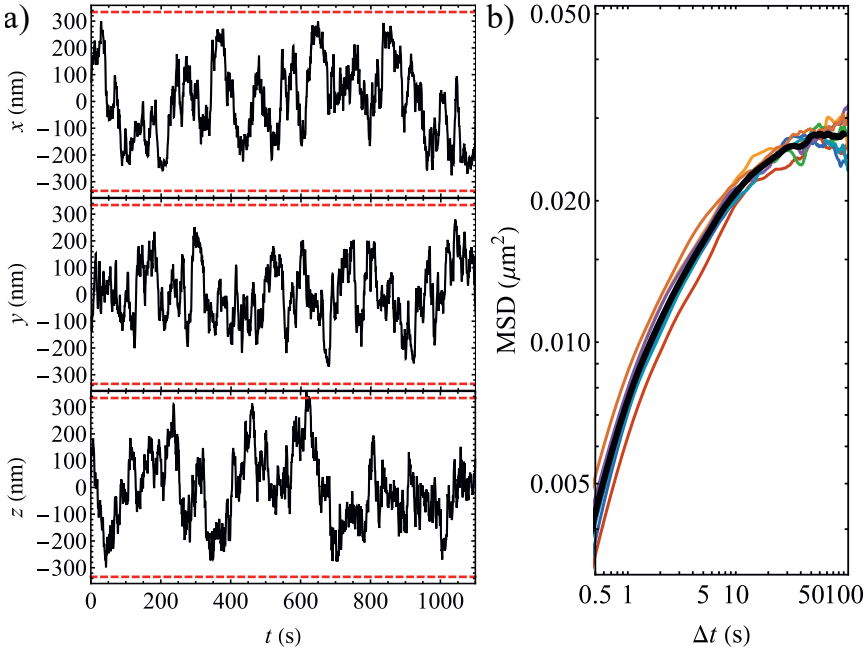


Figure 7: a) One-dimensional trajectories of a core in a rattle particle in the x , y and z dimensions. b) Mean squared displacement of seven different cores in rattle particles versus the lag time (Δt). The black line shows the mean of the MSDs of all seven particles.

moves randomly within these constraints in all dimensions. Figure 7b shows the mean squared displacement (MSD) versus the lag time of seven different cores in rattles along with the mean of the MSD of all these particles. In a log-log plot of the MSD and the lag time, the MSD of a free colloid is a straight line with a slope of 1. In the short lag time regime (up to ~ 0.5 s), the slope of the MSD of the confined core was found to be 0.80, therefore at short time scales a confined colloid diffuses almost the same as a free colloid, except with a significantly reduced diffusion coefficient due to the long range of the hydrodynamic interactions already affecting the core particles when they are diffusing in the center of the shells. However, for lag times of ~ 20 s and higher, the slope approaches 0. The restriction of the increase of the MSD and its deviation from linearity are due to the limited volume available to the core and illustrates the influence of the confinement.

The cores' trajectories found using particle tracking were used to determine the radial and perpendicular diffusion coefficients of the core (D_r and D_p), as described in the Methods, using the script in Appendix B. Radial diffusion is the movement of the core towards and away from the shell, whereas perpendicular diffusion is the movement of the core along the shell wall, as illustrated in Figure 8. The x-axis of both plots shows the radial position of the core within the shell. The experimental data points are the average of 7 different particles, with the

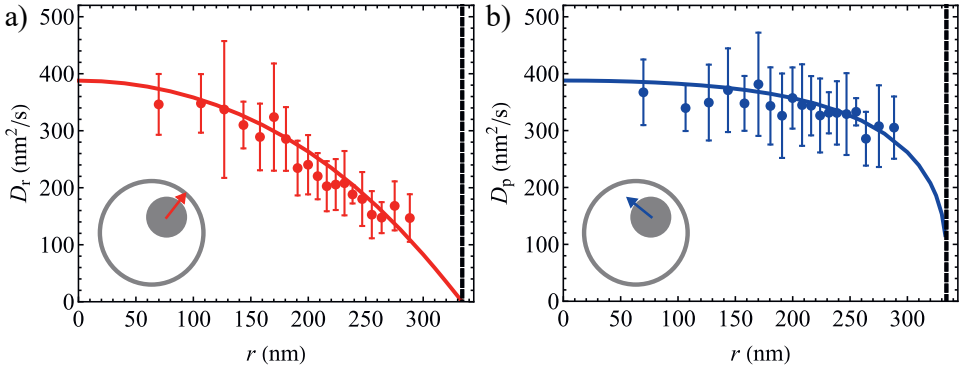


Figure 8: Plots of the dependence of (a) the radial diffusion coefficient and (b) the perpendicular diffusion coefficient on the core's position within the shell. The solid lines show the diffusion coefficient as found in finite-element calculations, corresponding to a viscosity of the liquid of 0.45 Pa s. Each data point represents the mean of seven different cores; the error bars show the spread of the data for the 7 different particles. The vertical dashed black lines indicate the maximum distance that the core particle could have from the middle of the shell due to the inner shell wall.

error bars indicating the spread of the individual particles. The experimental radial diffusion coefficient decreased significantly as the core particle approaches the shell wall, while the perpendicular diffusion coefficient stays mostly constant. This is in excellent agreement with the theoretical curves, the full lines in Figure 8, for which we calculated the diffusion coefficient of a core particle within a shell by solving the Stokes' equations for an incompressible fluid with a moving particle. The calculations describe the experimental data relatively well when a viscosity of the liquid of 0.45 Pa s is assumed. The expected experimental viscosity for our system was 0.35 ± 0.13 Pa s at $T = 18 \pm 2^\circ\text{C}$ and a 1% uncertainty in the volume percent of the glycerol:water mixture,^{176, 177} which, considering the approximations that were made and the uncertainty in the experiments, we consider to be in reasonable agreement. The calculated diffusion coefficient of the core particle in the middle of the shell was furthermore only 20% of the diffusion of a free particle under the same conditions.

In a study by Cervantes-Martinez *et al.* on a single polystyrene colloid confined in a water droplet immersed in oil, similar results were found.¹⁶¹ However, the decrease of the radial diffusion coefficient as the particle approached the liquid-liquid interface was different than for our system. This may be a result of the different boundary conditions for the Stokes flow at the water-oil boundary, compared to our rigid silica shell. However, their experimental data were not compared to calculations.

Aponte-Rivera *et al.* performed a theoretical study on colloidal diffusion in confined geometries.¹⁶² They calculated the radial and perpendicular diffusion coefficients of a particle in a spherical cavity for several different ratios of the core and shell radii. For the largest ratio that was studied ($R_{\text{core}}/R_{\text{shell}} = 0.2$), which is most similar to the ratio of the rattle particles described in this chapter ($R_{\text{core}}/R_{\text{shell}} = 0.42$), the results correspond well to ours. The results

for the 0.2 ratio showed the same difference between the trend of the diffusion coefficient in the radial and perpendicular directions. The study also showed that for smaller ratios, the distance dependence of the radial diffusion coefficient starts to flatten, becoming more similar to the perpendicular diffusion coefficient. Additionally, the study shows the larger the ratio of core to shell radius, the lower the diffusion coefficient in comparison to the free diffusion of the same particle. This shows that for colloidal diffusion in confined geometries, the size ratio between the particle and the confining geometry is an important parameter. As the core was relatively large compared to the shell in our system, this system allowed us to clearly show the difference between the radial and perpendicular diffusion coefficients.

3.3.3. Core-shell interaction

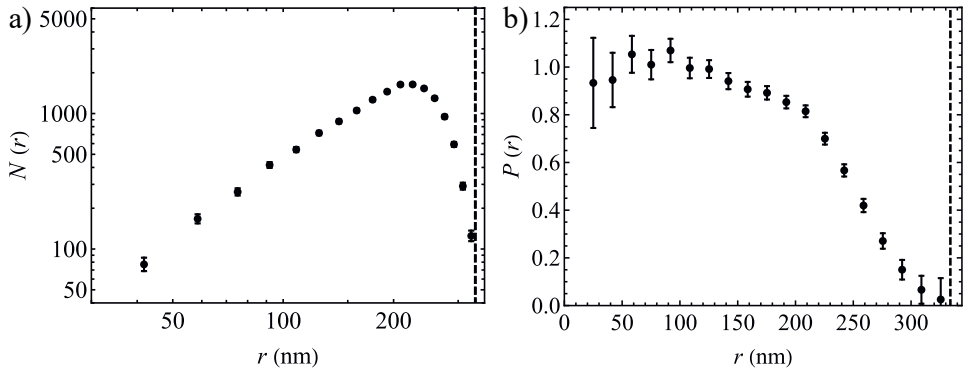


Figure 9: a) Plot of the number of times $N(r)$ the core was found in a certain radial slice within the shell. b) Plot of the normalized probability density $P(r)$ for finding the core at a certain position r within the shell.

Figure 9a shows the number of times a particle was found in a certain radial slice in the shell. To obtain a probability density, the number of times a particle was found in a certain slice of the shell was corrected for the volume of each radial slice within the shell. The result is shown in Figure 9b. The probability density of finding the core at position r decreases as the core approaches the shell more closely, due to a repulsive interaction between the core and the shell as investigated in detail in Chapter 4.

When inspecting Figure 9b more closely, the inflection point and therefore the maximum negative slope of the curve, is found at $r = 256$ nm, which is 78 nm from the shell wall. The Debye length for 5 mM salt is less than 4 nm, so the electrostatic repulsion found here is significantly longer ranged than expected. This seemingly long-ranged repulsion can partly be ascribed to tracking errors, but as the difference between expectation and observation is significant, the long-ranged repulsion is likely also an effect of the geometry of the system, as shown and discussed more fully in Chapter 4. The concave geometry of the shell could lead to a slower decay of the electric potential from the shell surface inside the rattle geometry, leading to longer ranged electrostatic repulsion.

3.4. CONCLUSION

In this chapter we discussed the 3D mobility of a core within a spherical shell in 90:10 glycerol:water solution with 5.00 mM LiCl added salt ($\kappa^{-1} \approx 3.3$ nm). 3D confocal experiments allowed us to track the fluorescent core particle with acceptable tracking errors within an acceptable timeframe. The MSD of core particles showed that in the short-time regime (less than 0.5 s), the colloid diffuses normally, while at longer times the MSD becomes flat due to the spatial confinement of the core within the shell. Our data shows that the radial diffusion became increasingly slow as the core approached the shell wall, while the perpendicular diffusion coefficient remained relatively constant throughout the entire volume of the shell. Finite-element calculations confirmed the slower radial diffusion near the shell wall and also showed that diffusion of the core particle within the shell, both in the radial and perpendicular directions, was found to be around 20% or less of that of a free colloid, depending on its position within the spherical shell. The excellent agreement between experiments and finite-element calculations showed the feasibility of studying dynamics of colloids in the submicron size regime, by recording relatively fast z -stacks using fluorescence confocal microscopy.

Furthermore, we found that an electrostatic repulsion between the core particle and the inner shell wall was longer ranged than expected for an ionic strength of 5 mM. This could be attributed partly to tracking errors, but is likely also due to the concave geometry of the inner shell surface. The interactions within rattle-type particles are investigated in more detail in Chapter 4.

AUTHOR CONTRIBUTIONS

MSc student Daphne M. Dekker (Utrecht University) performed rattle synthesis, the axial calibration of the microscope and early confocal microscopy experiments, particle tracking and wrote part of the chapter under supervision of Tom A.J. Welling. Kanako Watanabe (Tohoku University) and Zahra Peimanifard (Utrecht University) performed the synthesis of the final batch of rattle particles. Tom A.J. Welling performed confocal experiments, particle tracking, data analysis and the finite-element calculations.

ACKNOWLEDGEMENTS

Ernest van der Wee is thanked for useful discussions on the axial calibration of the microscope. We thank Maarten Bransen for supplying the code used for the tracking using a 3D Gaussian fit.

APPENDIX A: 3D GAUSSIAN FIT PARTICLE TRACKING

Script used for the 3D Gaussian particle tracking procedure. The code was written by Maarten Bransen.

```

import matplotlib as mpl
import matplotlib.pyplot as plt
mpl.rc('figure', figsize=(10, 6))
import scipy as sp
from scipy.optimize import least_squares
from stackscroller import stackscroller
import pandas as pd
import numpy as np
import pims
import trackpy as tp

frames = pims.ImageSequenceND('C:/*.tif', axes.identifiers = ['z', 't'])
frames.bundle_axes = ['z', 'y', 'x']
frames.iter_axes = 't'
frames

dz=12 #feature size in pixels
dy=21
dx=21

data=frames[:]

results = pd.DataFrame(columns=['z', 'y', 'x', 'mass', 'particle'])

#define fitfunction generator
def gaussian(z0,y0,x0,mass):
    def g(z,y,x):
        xpart = sp.exp(-(x-x0)**2/(dx/2)**2)
        ypart = sp.exp(-(y-y0)**2/(dy/2)**2)
        zpart = sp.exp(-(z-z0)**2/(dz/2)**2)

        return mass**2*xpart*ypart*zpart
    return g

#loop over stacks in time-series
for i,stack in enumerate(data):
    if i==0:#guessparams for first stack
        guessparams = [i/2 for i in stack.shape]+[1]

    #difference between data array and fitted gaussian
    errorfunc = lambda params: sp.ravel(gaussian(*params)
        (*sp.indices(stack.shape))-stack)

    #least squares minimizing the error function
    fit = least_squares(errorfunc,guessparams)['x']
    print(i)

    #extract results and put in DataFrame
    results.loc[i] = {'z':fit[0], 'y':fit[1], 'x':fit[2], 'mass':fit[3],
        'particle':0}

    #use result as starting guess for next frame
    guessparams = fit

results['frame'] = results.index

results

```

```
results.to_csv('C:/*.csv')
```

APPENDIX B: DIFFUSION IN CONFINED GEOMETRIES

Script used to calculate the direction-dependent and position-dependent diffusion of the core particles.

```
dirplus[x0_] := Module[{x = x0},
  dirpointx = (xdata[[x]] - Mean[xdata]);
  dirpointy = (ydata[[x]] - Mean[ydata]);
  dirpointz = (zdata[[x]] - Mean[zdata]);
  dirpointx2 = (xdata[[x + 1]] - Mean[xdata]);
  dirpointy2 = (ydata[[x + 1]] - Mean[ydata]);
  dirpointz2 = (zdata[[x + 1]] - Mean[zdata]);
  thetapoint = ArcTan[dirpointy/dirpointx];
  lengthpoint = Sqrt[dirpointx^2 + dirpointy^2 + dirpointz^2];
  lengthpoint2 = Sqrt[dirpointx2^2 + dirpointy2^2 + dirpointz2^2];
  dirvelx = (xdata[[x + 1]] - xdata[[x]]);
  dirvely = (ydata[[x + 1]] - ydata[[x]]);
  dirvelz = (zdata[[x + 1]] - zdata[[x]]);
  thetavel = ArcTan[dirvely/dirvelx];
  lengthvel = Sqrt[dirvelx^2 + dirvely^2 + dirvelz^2];
  ratio = lengthpoint/(lengthpoint + lengthvel);
  theta = ArcCos[Dot[{dirpointx, dirpointy, dirpointz},
    {dirvelx, dirvely, dirvelz}]/(lengthpoint*lengthvel)];
  radial = lengthvel*Cos[theta];
  perpendicular = If[lengthpoint > lengthpoint2, lengthvel*Sin[theta],
    -lengthvel*Sin[theta]];
  AppendTo[shorttimedisplacementradperpin, {radial, perpendicular}]]

list = {};
f[rmin0_, rmax0_] := Module[{rmin = rmin0, rmax = rmax0},
  xdata = Mean[{xdata1[[#]], xdata1[[# + 1]]}] & /@
    Table[i, {i, 1, Length[xdata1] - 2}];
  ydata = Mean[{ydata1[[#]], ydata1[[# + 1]]}] & /@
    Table[i, {i, 1, Length[ydata1] - 2}];
  zdata = zfactor*Mean[{zdata1[[#]], zdata1[[# + 1]]}] & /@
    Table[i, {i, 1, Length[zdata1] - 2}];
  shorttimedisplacementradperpin = {};
  If[Sqrt[(xdata[[#]])^2 + (ydata[[#]])^2 + (zdata[[#]])^2] > rmin &&
    Sqrt[(xdata[[#]])^2 + (ydata[[#]])^2 + (zdata[[#]])^2] < rmax &&
    Sqrt[(xdata1[[#]])^2 + (ydata1[[#]])^2 + (zdata1[[#]])^2] < maxdis &&
    Sqrt[(xdata1[[# + 1]])^2 + (ydata1[[# + 1]])^2 + (zdata1[[# + 1]])^2] <
      maxdis (*<= tdata1[[# + 1]] - tdata1[[#]] / (Equal / 1 *)), dirplus[#],
    Nothing] & /@ Table[i, {i, 1, Length[xdata] - 1}];
  tab = Table[i, {i, -maxdisplacement + stepdisplacement/2,
    maxdisplacement - stepdisplacement/2, stepdisplacement}];
  datradin = Transpose[{tab, BinCounts[
    shorttimedisplacementradperpin[[All, 1]],
    {-maxdisplacement, maxdisplacement, stepdisplacement}]}];
  nlmradin = NonlinearModelFit[datradin, {a1*PDF[NormalDistribution[
    shorttimedisplacementradperpin[[All, 1]] // Mean,
    sigma], x], sigma > 2}, {a1, {sigma, 10}}, x];
  datperpin = Transpose[{tab, BinCounts[
    shorttimedisplacementradperpin[[All, 2]], {-maxdisplacement,
    maxdisplacement, stepdisplacement}]}];
  nlmperrin = NonlinearModelFit[datperpin, {a1*PDF[NormalDistribution[
    shorttimedisplacementradperpin[[All, 2]] // Mean, sigma], x],
    sigma > 2}, {a1, {sigma, 10}}, x];
  sradin = sigma /. nlmradin["BestFitParameters"];
```



```

raddiffexp = StandardDeviation[shorttimedisplacementradperpin[[All,
raddiffexpplus = (sradin + nlmradin["ParameterErrors"][[2]])^2/(1*2*time)
// Quiet;
raddiffexpmin = (sradin - nlmradin["ParameterErrors"][[2]])^2/(1*2*time)
// Quiet;
sperpin = sigma /. nlmperpin["BestFitParameters"];
perpdiffexp = StandardDeviation[shorttimedisplacementradperpin[[All,
perpdiffexpplus = (sperpin + nlmperpin["ParameterErrors"][[2]])^2/(1*4*
time) // Quiet;
perpdiffexpmin = (sperpin - nlmperpin["ParameterErrors"][[2]])^2/(1*4*
time) // Quiet;
rmean = Select[If[Sqrt[(xdata[[#]])^2 + (ydata[[#]])^2 + (zdata[[#]])^2]
> rmin && Sqrt[(xdata[[#]])^2 + (ydata[[#]])^2 + (zdata[[#]])^2] < rmax,
Sqrt[(xdata[[#]])^2 + (ydata[[#]])^2 + (zdata[[#]])^2], 0] & /@
Table[i, {i, 2, Length[xdata] - 2}], UnequalTo[0]] // Mean;
AppendTo[list, {rmean, rmin, rmax,
raddiffexp, raddiffexpplus, raddiffexpmin,
perpdiffexp, perpdiffexpplus, perpdiffexpmin,
DeleteCases[shorttimedisplacementradperpin[[All, 1]], 888888] // Length,
shorttimedisplacementradperpin[[All, 2]] // Length, xdata, ydata, zdata,
shorttimedisplacementradperpin[[All, 1]],
shorttimedisplacementradperpin[[All, 2]]}];

maxdis = (1158 - 490)/2;(*maximum distance between core and shell*)
nn = 20;(*amount of points taken for the hydrodynamics plot*)
maxdisplacement = 200;
stepdisplacement = 10;
zfactor = 109.5/115.1;

data = Import["C:\\*.csv"];
xpixel = 41.336;
ypixel = 41.336;
zpixel = 150; (*Fill in appropriate pixel size for data set*)
time = 0.69; (*Fill in appropriate frame time for data set*)
zdata = zfactor*data[[All, 1]];
zdata1 = zdata - Mean[zdata];
ydata = data[[All, 2]];
ydata1 = ydata - Mean[ydata];
xdata = data[[All, 3]];
xdata1 = xdata - Mean[xdata];
rrdata = Sqrt[(xdata1[[#]])^2 + (ydata1[[#]])^2 + (zdata1[[#]])^2] & /@
Table[i, {i, 2, Length[xdata1] - 2}];
rrdata1 = %;
rdata = If[rrdata[[#]] < maxdis, rrdata[[#]], Nothing] & /@
Table[i, {i, 1, Length[rrdata]}];
floorn = Floor[Length[rdata]/nn]
rcutoff = Sort[rdata][[Table[i*floorn, {i, 1, nn}]]]
rbounds = PrependTo[rcutoff, 0]
list = {};
f[rbounds[[#]], rbounds[[# + 1]]] & /@
Table[i, {i, 1, Length[rbounds] - 1}];
list1 = list
(*Repeat for all data sets*)

```


Tunability of interactions between the core and shell in rattle-type particles studied with liquid-cell electron microscopy

ABSTRACT

Yolk-shell or rattle-type particles consist of a core particle that is free to move inside a thin shell. A stable core with a fully accessible surface is of interest in fields such as catalysis and sensing. However, the stability of a charged nanoparticle core within the cavity of a charged thin shell remains largely unexplored. Liquid-cell (scanning) transmission electron microscopy (LC(S)TEM) is an ideal technique to probe the core-shell interactions at nanometer spatial resolution. Here we show by means of calculations and experiments that these interactions are highly tunable. We found that in dilute solutions adding a monovalent salt led to stronger confinement of the core to the middle of the geometry. In deionized water the Debye length κ^{-1} becomes comparable to the inner shell radius R_{shell} , leading to a less steep electric potential gradient and a reduced core-shell interaction, which can be detrimental to the stability of nanorattles. For a salt concentration range of 0.5 – 250 mM the repulsion was relatively long-ranged due to the concave geometry of the shell. At salt concentrations of 100 and 250 mM the core was found to move almost exclusively near the shell wall, which can be due to hydrodynamics, a secondary minimum in the interaction potential or a combination of both. The possibility of imaging nanoparticles inside shells at high spatial resolution with liquid-cell electron microscopy makes rattle particles a powerful experimental model system to learn about nanoparticle interactions. Additionally, our results highlight the possibilities for manipulating the interactions between core and shell that could be used in future applications.

4.1. INTRODUCTION

Rattle-type or yolk-shell particles are particles where a core is enclosed by a hollow and often porous shell, via a core@void@shell structure.^{27–32} When dispersed in a liquid, in our case water, the liquid can enter the porous shell to form a core@water@shell structure with a mobile core particle. The small core particles are often metal or metal oxide nanoparticles with specific catalytic,^{31,35} optical^{34,36} or magnetic³³ properties. Small ions and molecules can travel through the porous shell, which allows them to interact with the core particle inside. Rattle-type particles are promising for application in catalysis,^{31,37–42} biomedicine,^{43,44} drug delivery,^{45,46} sensing,^{47–51} adsorbents,^{52,53} lithium-ion batteries,⁵⁴ optical devices,^{34,36} and many other applications. These may require the particle to move freely, e.g. to maximize accessible surface area, which makes studying the stability of the particle within the shell relevant.

Liquid-cell electron microscopy (EM) is capable of *in situ* imaging of particles at nanometer resolution.^{80,81,91} We recently observed that Brownian motion is unaffected by the electron beam at low enough electron dose rates,¹⁶³ which was reported recently also by Yesibolati and coworkers.¹⁷⁹ As water is an important medium for both biological and synthetic systems and their applications, we decided to use it as a medium in this work. However, nanoscale and sub-micron sized objects in water move too fast to be tracked for most EM imaging systems. Due to the confining nature of the geometry, the particle is unable to leave the shell and can therefore be imaged, even though it diffuses rapidly. In water, the relevant interactions for nanoscale objects are effective at a length scale of nanometers to hundreds of nanometers. Therefore, any technique used to investigate the interaction potential of such objects needs to have nanometer spatial resolution. Other studies have shown that it is possible to infer an interaction potential from observations made with liquid-cell electron microscopy, even if those particles were trapped near the surface of the liquid-cell geometry.^{101,180} Additionally, the flow-through capability of the liquid-cell holder allows control over essential solution parameters such as pH and ionic strength *in situ* and makes it possible to observe direct changes in the interaction potential and the colloidal stability of the core particle within a shell, when the shell is adsorbed to one of the windows of the liquid-cell.

The interactions between spherical charged colloidal particles dispersed in a liquid is an extremely well-studied topic within colloid science^{72–75,156,181–203} and here is certainly not the place to review this topic in any depth.^{74,75,182–187} Understanding the interactions between colloidal particles is not only of importance to almost all applications in which colloids are used, but has over the last century also become an important topic in ‘multiple-particle’ statistical physics where one of the goals is to derive effective potentials from a lower level description.^{74,75,182–187} The description of the interactions between charged spheres that is most often used in theoretical and experimental studies is referred to as the DLVO potential. DLVO refers to Derjaguin, Landau, Verwey and Overbeek, who were the principle investigators that developed the theoretical framework to describe these interactions, mostly in the forties of the previous century.^{72–75,181} It may come as a surprise that the strongly related topics of the dynamics and interactions of a spherical particle that is present inside a liquid-filled spherical

shell are much less well studied^{161,162} despite the already mentioned recent progress in realizing such systems. This lack of knowledge is for instance illustrated by a recent paper which is the first to theoretically describe the dynamics of a single charged colloidal particle in between two flat, confining walls where the range of the double layer repulsion and the distances between the walls are similar.¹⁸⁸ It should additionally be remarked that this flat-plate geometry of the confinement is significantly simpler than that of a spherical particle inside a spherical shell.^{156,188} The reason for the absence of theoretical studies is almost certainly due to a lack of experimental studies in which accurate local dynamics and/or interaction potentials under similar confining geometries have been measured. There is also a strong need for experimental studies on the more-or-less direct measurements of colloid-colloid interaction potentials for nanoparticles (NPs). The reason for the lack of studies is, besides the necessarily higher spatial resolution needed and much smaller volume of the NPs, additional experimental difficulties. For example, optical tweezers cannot be used to measure NP interactions,¹⁹¹ but have been used frequently for larger sized colloids.^{192,193} Additionally, there is also the much higher diffusion coefficient of nanoparticles. These factors combined mean that besides the already mentioned liquid-cell TEM studies, that were performed on nanoparticles close to a surface,^{101,180} we are aware of only a handful of other studies in which NP interactions were more-or-less determined directly,¹⁵⁹ e.g. by cryo TEM studies.^{189,190} However, even in these studies^{189,190} the NPs were either adsorbed onto a liquid interface or close to such an interface which most likely strongly affects the inter particle potentials. Work is under way,¹⁹⁰ also in our group, to try to extend this cryo-TEM methodology to measure the radial distribution functions for 3D NPs systems. However, as mentioned, at present, interaction potentials of 3D systems have only been measured for much larger colloidal particle systems.^{183,192–195} An incomplete set of examples and techniques for such interaction potential measurements is: direct imaging in 3D,¹⁹⁵ optical tweezers^{191–193} and atomic force microscopy.¹⁹⁵

Interesting phenomena arise for conditions where the Debye-Hückel screening length κ^{-1} is larger or similar to the average distance between particles.^{156,193,194,196–203} It was already realized by Overbeek and Albers^{197,198} when they studied the colloidal stability of micron-sized water emulsion droplets in apolar solvents, that for such systems the screening length could achieve much larger values (several μm) as opposed to values that can be obtained in water by deionization (several hundred nm at most) because of the self-dissociation of water. When κ^{-1} becomes larger than the distance between the particles, complete double-layer overlap cannot occur and particles start to experience significant interactions from second shell neighboring particles. Additionally the potentials can become non-additive.²⁰² These combined effects average out repulsions and diminish the stability of these particles when compared to (much) lower volume fraction conditions.^{197,198} It is even possible that the pair potentials under extreme low salt conditions can become more Coulomb-like, rather than follow the Yukawa interaction potential that describes screened charges²⁰⁰ and/or that counter ion condensation takes place (a non-linear screening effect).²⁰¹ The only reason that such drastic effects have not yet been reported for nanoparticles in water is related to the difficulty of measuring potentials between nanoparticles.

However, this phenomenon can be studied for nanoparticles inside spherical shells filled with water mostly because of the particular geometry and (much) smaller distances involved compared to κ^{-1} . Under these conditions, the counterions of the charged particles cannot be neglected w.r.t. the concentration of the background ionic strength and the definition of κ^{-1} becomes more ambiguous.²⁰⁰ Additionally, there are specific issues that are related to the geometry of a shell that is porous to ions. Because of the procedures in which (our) particles with a movable core inside a shell are made, the spherical shells are often (meso)porous. The reason for this is that the liquid-filled shells are often made hollow by either an etching process or a burning away of an interior organic layer. This means that sufficiently small ions can move through the shell from the outside liquid to the inside and vice versa. However, the speed with which ion transport through the shell occurs w.r.t. the dynamics of the moving core particles is usually significantly lower than that of the ions freely diffusing in the liquid, thus possibly undermining certain assumptions made in the theoretical description. The dynamics of the ions going through the shells is not characterized in the present work as well and is left for future work. Additionally, even without the charge-induced interactions, a diffusing particle inside a hollow shell already has a complex position-dependent mobility because of the boundary conditions of the hydrodynamics (Chapter 3).^{156, 161, 162, 188} The coupling between the interactions and the hydrodynamics only complicates this further.¹⁸⁸ However, this involved position dependence also holds promise, as it can be used to locally measure the temperature and/or ionic strength if the dynamics of the ions and interactions with the shells are sufficiently well understood theoretically and controlled experimentally. Moreover, it is clear from the above that this geometry as it already can be studied in a liquid-cell by high resolution imaging is also a powerful experimental model system to learn about interactions of nanoparticles in 3D in different solvents, including water for the first time in experiments.

4.2. METHODS

4.2.1. Liquid-cell STEM

In order to image the rattle-type particles in the electron microscope, we used a liquid-flow TEM holder with corresponding microchips (Hummingbird Scientific, USA). The microchips support 50 nm thick amorphous silicon nitride (SiN) windows with lateral dimensions of 50 by 200 μm^2 . A sample cell consists of two chips separated by a spacer of 250 or 1000 nm in height, depending on the size of the rattles. The two Si chips were glow-discharged for 1 min prior to the experiment in order to make their surfaces more hydrophilic. The microchip with spacer was then placed in a dedicated holder. A 1 μL droplet of the dispersion of rattle-type particles in deionized water was dropcast onto the microchip. The second microchip was placed on the bottom chip with the hydrophilic side facing the opposite chip. The excess liquid was removed with filter paper.

The liquid-cell STEM experiments were carried out using a transmission electron microscope (Tecnai-F20, Thermo-Fischer Scientific), equipped with a field emission gun, and operating at 200 kV. The semi-convergence angle of the electron probe was 10 mrad. The annular dark-field (ADF) detector was used with a camera length of 120 mm. Image series were acquired with TEM imaging & analysis software (TIA). For the experiments with

titania@water@silica rattle-type particles, the beam current measured via the fluorescent screen in vacuum was 37 pA for all videos unless specified differently. A frame recording time of 1 s was used. The number of pixels was 512×512 , which resulted in a pixel size of 4.4–8.8 nm depending on the magnification. These settings resulted in an electron dose rate of $12\text{--}45 \text{ e}^- \text{ nm}^{-2} \text{ s}^{-1}$. For the experiments with gold@water@silica nanorattles, the beam current in vacuum was 85 pA. A frame time of 1 s was used. The number of pixels was 512×512 pixels, which resulted in a pixel size of 3.14 nm. This corresponded to an electron dose rate of $206 \text{ e}^- \text{ nm}^{-2} \text{ s}^{-1}$. The image series acquisitions were at least 180 frames long.

After the holder was inserted into the microscope and before image acquisition started, deionized water was flowed through the cell at a rate of $2 \mu\text{L}/\text{min}$ for 45 min. At least 3 rattle-type particles in different parts of the liquid-cell were then imaged while the flow was turned off. We did not observe any influence of the flow on the particle mobility within the shell, but were concerned about mechanical vibrations and thus left the flow off during measurements. The shell of the rattle-type particle was stuck to the top chip of the liquid-cell and therefore only the core particle inside could move. Each particle was imaged separately and for 180 – 600 s per LiCl concentration. After image series acquisition for one LiCl concentration was completed, the next, more highly concentrated LiCl solution was flowed into the liquid-cell at a rate of $2 \mu\text{L}/\text{min}$ for at least 10 minutes. The flow was then turned off again for image series acquisition. This was repeated for all different salt concentrations for the same 3 particles. At the end of the experiment, a solution of pH 2 (10.0 mM HCl) was flowed into the cell. This made the silica shell charge-neutral^{204–206} and the core particle irreversibly attached to the shell (Figure A10). This allowed us to measure the size of the core particle for that particular rattle-type particle.

4.2.2. Image processing

We used ImageJ (1.51a) and Mathematica (Wolfram, v12.2) to analyze the recordings. We used ImageJ to binarize the individual frames of the videos. These binarized images were then used as a mask to remove the background of the original images. This leaves us with the original intensity of the pixels where the particle was and black everywhere else. We then averaged all those frames into a single image. This average image was then deconvoluted with an image of a titania particle with radius $R_{\text{core}} = 170 \text{ nm}$ as calculated with CASINO (Version 3.3.0.4, see the section on simulating static ADF-STEM images). For this we used a Richardson-Lucy deconvolution algorithm in Mathematica.^{207,208} The remaining image gave a map of the probability of finding the center of the core particle in a certain projected part of the shell, which was corrected for the volume in the plane perpendicular to the image as explained in the Supporting Information (Appendix A).

4.2.3. Reconstructing the 3D interaction potential

Our experimental LC-STEM image series are 2D projections of a 3D system. In order to compare the experimental data to calculations, we need to reconstruct the effect of a 3D interaction potential between the core particle and the shell caused by the 2D projection. As the core particle is moving around randomly *via* Brownian motion, the probability $P(r)$ can

be translated to a interaction potential $U(r)$ via

$$\frac{U(r)}{k_B T} = -\ln(P(r)). \quad (4.1)$$

Here r is the radial spherical coordinate. However, since the probability from our experiments is a 3D probability projected on a 2D plane, a 3D potential needs to be projected on a 2D plane, while correcting for the spherical geometry in the third dimension (Supporting Information). We do this by translating a trial potential

$$U_{\text{trial}} = A \frac{e^{-\kappa r}}{r} \quad (4.2)$$

into a projected probability. Here κ and A are fit parameters. The fit parameters for which the projected probability distribution matches the experimental data most accurately, are assumed to be the parameters in the 3D interaction potential in our experiments.

To translate the trial potential to a projected probability we make a list of available z_i coordinates per cylindrical coordinate ρ , where the maximum z coordinate at projected radial coordinate ρ is given by

$$z_{\text{max}} = \sqrt{(R_{\text{shell}} - R_{\text{core}})^2 - \rho^2}. \quad (4.3)$$

Then we make a list of all the available 3D radial coordinates r_i within the cylindrical coordinate ρ :

$$r_i = \sqrt{\rho^2 + z_i^2}. \quad (4.4)$$

The projected probability $P(\rho)$ is then calculated by averaging all 3D probabilities $P(r)$ that fall into the projected radial coordinates ρ via

$$P(\rho) = \langle P(r_{1,2,\dots,n}) \rangle = \langle e^{-U(r_{1,2,\dots,n})/k_B T} \rangle \quad (4.5)$$

In the final result the interaction potential is expressed as function of the core-shell separation distance $d = (R_{\text{shell}} - R_{\text{core}}) - r$.

4.2.4. Interaction potential calculations

Electrostatic interaction. We performed finite-element calculations using COMSOL Multiphysics (V5.4). The rattle geometry was used in an axisymmetric calculation. We solved the nonlinear Poisson-Boltzmann equation for a symmetric 1:1 electrolyte:

$$-\epsilon_0 \epsilon_r \nabla^2 \psi = 2c_0 \sinh\left(\frac{e\psi}{k_B T}\right). \quad (4.6)$$

Here ψ is the electric potential, ϵ_0 is the permittivity of vacuum, ϵ_r is the dielectric constant of the liquid, c_0 is the monovalent salt concentration, e is the electron charge, k_B is the Boltzmann constant and T is the temperature. On the surface of the core and the shell we put constant surface potential boundary conditions.

We exploited the rotational symmetry of the system to minimize the number of elements required. Due to the large slopes in ion concentration near the charged surfaces, a fine mapped mesh was applied from the boundary of the charged surface to a distance of one or two Debye lengths.^{209,210} The Debye lengths for the salt concentrations under investigation, ranging from 0.5 to 250 mM, were between 15 nm and 0.5 nm. The mapped mesh was designed to be

small near the surface and to expand radially outward. The rest of the geometry was given a free triangular mesh (Supporting Information).

We placed the core at different distances from the shell wall and solved the non-linear Poisson-Boltzmann equation. We solved for the electrostatic force on the core particle by integrating the electric Maxwell stress tensor \mathbf{T} over the surface of the sphere S

$$F = \oint_S \mathbf{T} dS. \quad (4.7)$$

Since we required the force in the z direction, this becomes $\mathbf{T} \cdot \hat{z} = F_r \hat{r} + F_z \hat{z}$, where

$$F_r = \epsilon_0 \epsilon_r \frac{\partial \psi}{\partial r} \frac{\partial \psi}{\partial z} \quad (4.8)$$

$$F_z = \frac{\epsilon_0 \epsilon_r}{2} \left(\left(\frac{\partial \psi}{\partial z} \right)^2 - \left(\frac{\partial \psi}{\partial r} \right)^2 \right). \quad (4.9)$$

The interaction potential was then found by a path integral over the forces at various distances from the shell.

Van der Waals interaction. To calculate the van der Waals (vdW) interaction between a sphere and a shell a relationship is required to determine the interaction between a sphere and an element located at a point a distance d away from the sphere surface.²¹¹ By integrating over the shell volume we obtain the vdW interaction between a sphere and a shell at a distance d from the shell wall.

$$U_{\text{vdW}}(d) = \frac{-16AR_{\text{core}}^3}{3} \int_0^\pi \int_{R_{\text{core}}+d(\theta,a)}^{R_{\text{core}}+d(\theta,a)+T_{\text{shell}}} \frac{r^2 \sin(\theta) dr d\theta}{(r^2 - R_{\text{core}}^2)^3} \quad (4.10)$$

Here A is the Hamaker constant, T_{shell} the thickness of the shell, r and θ the radial distance and polar angle in a spherical coordinate system. Finally, $d(\theta, a)$ is the distance of the core to different parts of the shell depending on the polar angle θ and the displacement from the center of the shell a

$$d(\theta, a) = \sqrt{(R_{\text{shell}} - R_{\text{core}})^2 + a^2 \sin^2(\theta)} - a \cos(\theta). \quad (4.11)$$

R_{core} and R_{shell} are the radius of the core and the inner radius of the shell, respectively. For the titania@water@silica particles the used Hamaker constant was $A_{123} = 6.9 \text{ zJ}$, calculated via the full Lifshitz theory.²¹² The used shell thickness was 25 nm. Equation 4.10 was integrated numerically in Mathematica.

4.2.5. Simulating static ADF-STEM images

To understand the influence of hydrodynamics and the errors in the measurements, we simulated ADF-STEM images of a moving particle within a shell. Therefore, we are first required to simulate ADF-STEM images for a static particle. For this purpose we simulated ADF-STEM images using the CASINO software (Version 3.3.0.4).^{123–125} The physics model used for the total and partial cross sections in the simulation software was that of an empirical analytical fit to the Mott cross sections by Browning *et al.*¹²⁶ The specific parameters of the sample and the electron probe were taken to be as close to the experimental parameters

as possible. However, we chose to use 256 by 256 pixels and twice the pixel size as in the experiments (which had 512 by 512 pixels) in order to reduce the computation time.

We put a 340 nm titania particle at different positions within a shell with a 700 nm inner diameter within a water layer of a micrometer. The electron probe was set to have a semi-convergence angle of 10 mrad and a diameter of 1 nm. The beam distribution was Gaussian. The electron probe had an energy of 200 keV and had its focal point on the middle of the rattle particle geometry. The top of the shell of the rattle geometry was at the same height as the top of the water layer. The pixel size was 8.9 nm and the number of simulated electrons per pixel N was 3528, as calculated from the beam current $I = 0.037$ nA and the pixel dwell time $\tau = 1/256^2$ s via

$$N = \frac{I \cdot \tau}{e} \quad (4.12)$$

where e is the electron charge. The ADF detector with a quantum efficiency of 100% was set to have a minimum and maximum semi-angle of 15 and 300 mrad, respectively. In total 41 static images of a particle in different positions in the shell were simulated.

4.2.6. Simulating ADF-STEM images of a diffusing particle in a shell

We first calculated the diffusion coefficient of the particle in the shell. The diffusion coefficient of the particle depended on the position within the shell, as well as the direction of the displacement. The mobility of the core particle towards the shell (radial diffusion) and along the shell wall (perpendicular diffusion) was investigated using finite-element calculations. More details can be found in the Supporting Information.

When the directional diffusion coefficients at all positions of the core within the shell were known, the particle motion could be simulated. For every pixel that was scanned the particle was moved in a random direction with a velocity in the perpendicular and radial direction that was dependent on its current position within the shell. The random direction of the perpendicular vector v_p was coded by creating 2 normalized vectors v_1 and v_2 that were perpendicular to the radial direction, and choosing a random real number n_r between 0 and 2π . The direction of the perpendicular vector was then chosen using this random real number n_r via

$$v_p = v_1 \cos(n_r) + v_2 \sin(n_r) \quad (4.13)$$

Now that the direction of the radial displacement and the perpendicular displacement is decided, we let the particle move a random step, within the pixel dwell time Δt , in the radial and perpendicular directions based on a normal distribution with standard deviations σ_r and σ_p , respectively. These are related to the radial and perpendicular diffusion coefficients D_r and D_p at the current position via

$$\sigma_r(r) = \sqrt{2D_r(r)\Delta t}, \quad (4.14)$$

$$\sigma_p(r) = \sqrt{4D_p(r)\Delta t}. \quad (4.15)$$

The particle was free to move up until a sharp barrier a certain distance away from the shell wall. When the new simulated position of the particle was not allowed by the imposed

barrier, a new position of the particle was calculated from the old position until that new position was allowed.

When the position of the particle was known for every pixel scanned, the image of the moving particle was formed. This was achieved by taking the position of the particle at the time and finding the 3 static ADF-STEM images that included the core particle closest to that position. The pixel was then given an intensity based on the weighted mean of that same pixel in the 3 chosen ADF-STEM images. The mean was weighted linearly by the absolute distance of the particle position in the static images compared to the real position. This was done for every pixel in an image and for at least 180 images.

4.3. RESULTS & DISCUSSION

In this study, we imaged rattle-type particles in water while changing the salt concentration *in situ*. We investigated two kinds of rattle-type particles (Figure 1). The first kind are composed of a submicrometer-sized titania core and a silica shell (Figure 1a), which were made by removing a polystyrene sacrificial layer by calcination.³⁴ They are promising building blocks for novel optical colloidal crystals, because the locations of cores in the shell compartment can be reversibly controlled using external stimuli.³⁴ The second kind are nanorattles consisting of a gold nanoparticle in a silica shell (Figure 1b), which were synthesized by a surface-protected etching process¹⁷⁴ that removes a sacrificial silica layer and are promising materials for sensing.⁵¹ The diameter of the core, inner diameter of the shell and the thickness of the shell, as well as the zeta potential of the core particle, are reported in Table 1. Details of the synthesis procedure can be found in the Supporting Information and previous work by Watanabe and coworkers.^{34, 51}

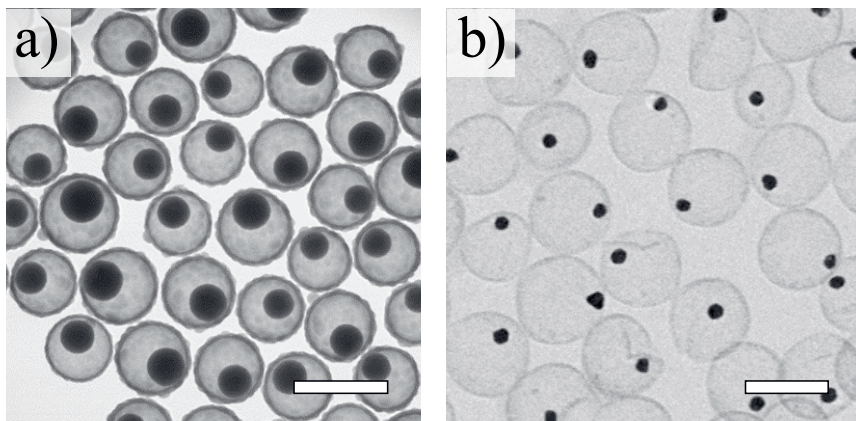


Figure 1: Rattle-type particles used in this study imaged with TEM in vacuum. a) Titania@void@silica rattles. The scalebar represents 1 micron. b) Gold@void@silica rattles. The scalebar represents 250 nm.

Table 1: Measured quantities of the two types of rattles used in this work: core radius R_{core} , inner shell radius $R_{\text{shell,inner}}$, shell thickness T_{shell} and zeta potential of the core ζ_{core} . The zeta potential of the core particle was measured in aqueous solution at a pH of 7 and an ionic strength of 1.00 mM LiCl salt.

Particle	R_{core} (nm)	$R_{\text{shell,inner}}$ (nm)	T_{shell} (nm)	ζ_{core} (mV)
Titania@void@silica	165 ± 18	357 ± 24	27 ± 2	-54 ± 1
Gold@void@silica	17 ± 2	86 ± 5	5 ± 1	-50 ± 4

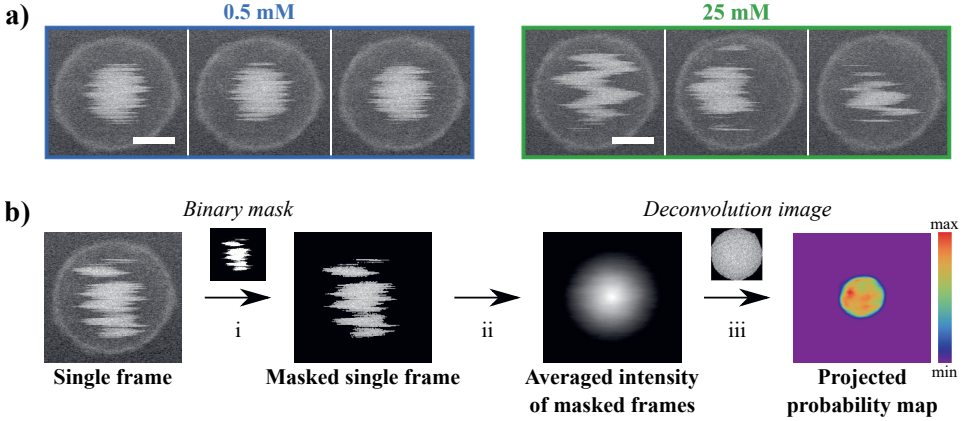


Figure 2: Experimental data and analysis. a) Typical images of a moving titania particle in a shell in 0.500 and 25.0 mM LiCl in water. The frame time was 1 s and the electron dose rate was $45 \text{ e}^- \text{ nm}^{-2} \text{ s}^{-1}$. The scalebars indicate 250 nm. b) Procedure to analyze the data in order to extract the probability of finding the particle at certain positions within the shell. i) For each single frame a binary mask was made that detects the signal of the particle. This mask was used to make a masked single frame that is black everywhere, but had the original intensity of the pixels where the particle was. ii) All masked single frames were averaged to obtain an averaged intensity of the moving core particle. iii) The averaged intensity was corrected for the available volume in the z direction (Supporting Information) and deconvoluted with a modelled image of a titania particle of the same size. This resulted in a projected probability map of where the particle can be found within the projected shell.

In short, the rattle-type particles were investigated using liquid-cell scanning transmission electron microscopy (LC-STEM). The dispersion of rattles in water was dropcast onto a glow-discharged Si microchip in a dedicated holder and a second Si microchip was placed on the bottom chip. The closed holder was introduced into the microscope and deionized water was flowed through the liquid-cell at a rate of $2 \mu\text{L}/\text{min}$ for 45 min. The flow was turned off for imaging of the moving core particle inside a shell that was attached to the electron-transparent window of the liquid-cell. Subsequently, a new LiCl concentration was flowed into the shell at a rate of $2 \mu\text{L}/\text{min}$ for 15 min. The moving core particle was then imaged again with the flow turned off. This procedure was repeated for all salt concentrations. Typical resulting images

for the titania@water@silica rattles in 0.500 and 25.0 mM LiCl (aq) with a frame time of 1 s are shown in Figure 2a. Due to the high mobility of the core particle in water the particle could not be tracked directly. Using the analysis outlined in Figure 2b a measure of the probability of finding the particle at certain positions within the shell was obtained. We filtered the intensity from the core particle of every single frame and averaged those in a single image. We then corrected for the available volume in the z direction (Supporting Information) and deconvoluted with a simulated image of a titania particle to obtain a projected probability map of finding the particle in a certain position within the projected shell. Details of the data acquisition and image simulation and processing are given in the Methods Section.

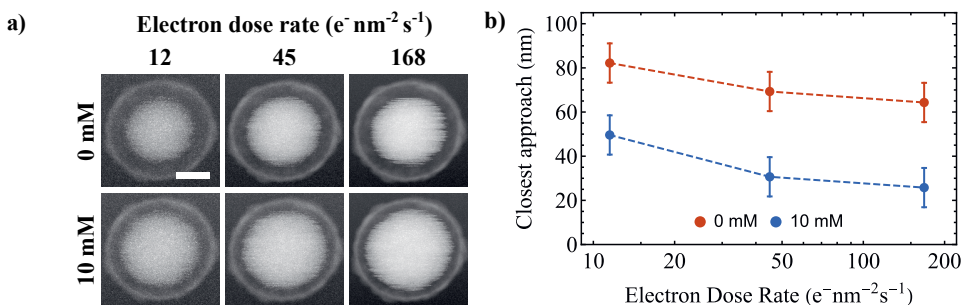


Figure 3: Influence of the electron dose rate on the repulsive interaction within a titania@water@silica rattle-type particle. a) The 6 images show the maximum intensity for each pixel that was reached during the whole image series at a certain electron dose rate. This visualizes what the minimum distance of approach is between the core particle and the shell. The scale bar is 250 nm. All images were taken at the same magnification. b) The minimum distance decreases with the electron dose rate for deionized water and 10.0 mM LiCl in a similar way.

Before results can be interpreted, as in any experiment involving liquid-cell electron microscopy, the influence of the electron beam has to be investigated.²¹³ Figure 3 shows images of the maximum intensity of all pixels throughout the whole image series for a titania core exploring a silica shell. This effectively visualizes how close the core particle was able to approach the shell throughout the complete image series. It is evident that the core particle approached the shell more closely at higher electron dose rates. This means that the electron beam influenced the interactions between the titania particle and the silica shell. Earlier studies have observed changes in the interactions between NPs in LC-STEM and argued they could be caused by either a change in pH¹³⁷ or a change in the ionic strength.¹⁸⁰ A significant change in the local temperature is not expected at these electron dose rates.¹⁰⁸ We used different electron dose rates to investigate titania@water@silica rattle particles in deionized water and in 10.0 mM LiCl in order to distinguish between the pH or the ionic strength being influenced by the electron beam irradiation. We observed that a similar decrease in minimum distance of approach to the shell for increasing electron dose rates occurred in deionized water and 10.0 mM LiCl (Figure 3). From this we infer that the change in ionic strength is not the main contributing factor in our system. We believe the change in the core-shell interaction

can be explained by taking into account a change in pH due to electron-water interactions. As more H_3O^+ than OH^- is produced, the pH drops when water is irradiated with the electron beam.¹³⁷ It is well known that both titania and silica lose charge when the pH drops.^{204–206} Additional experiments on how the influence of the electron beam seems related to pH can be found in the Supporting Information. We performed our experiments for titania@water@silica rattles at a moderate dose rate of $45 \text{ e}^- \text{ nm}^{-2} \text{ s}^{-1}$ to overcome the change of interaction at high dose rate, while obtaining an acceptable signal-to-noise ratio. For this dose rate, the decrease in range of the repulsive interactions due to the electron beam is likely to be only a few nanometers, while the range of interactions for which we extract interaction potentials in this work is $15 - 100 \text{ nm}$.

4.3.1. Interactions within a titania@water@silica rattle-type particle

Having determined the influence of the electron beam, we next aimed to investigate the influence of the ionic strength on the interaction potential between a titania core and a silica shell (Supporting Movie 6). The salt we used was LiCl, as these (solvated) ions most likely diffuse through the porous silica shells.²¹⁴ Figure 4 shows the influence of the salt concentration on the projected probability of finding the titania particle in a certain position within the shell. In Figure 4a the projected probability maps for all salt concentrations are given for a single rattle-type particle. Figure 4b and 4c show the projected probability as a function of the projected core-to-shell distance. The projected probability for a particle in low salt concentrations in Figure 4b was fitted to a 3D interaction potential, resulting in Figure 4d. In short, we assumed a perfectly spherical rattle geometry and used the relation between the interaction potential $U(r)$ and probability $P(r)$ to find a particle at a certain radial position

$$\frac{U(r)}{k_B T} = -\ln(P(r)). \quad (4.16)$$

Projecting a probability derived from a trial potential $U_{\text{trial}} = A \frac{e^{-\kappa r}}{r}$, with κ (the inverse Debye length) and A as fitting parameters, and fitting this to the experimental projected probability of finding the core at a certain radial position allowed us to find a 3D experimental interaction potential, which is eventually expressed as a function of particle-shell distance d . Additional details can be found in the Methods Section. This fitting procedure was not performed for the projected probability for a particle in high salt concentrations in Figure 4c, as the origin of the high projected probability close to the projected shell is uncertain, as will be discussed later. Finally, Figure 4e shows the results of finite-element calculations for a rattle geometry solving the non-linearized Poisson-Boltzmann equation for a symmetric 1:1 electrolyte:

$$-\epsilon_0 \epsilon_r \nabla^2 \psi = 2c_0 \sinh\left(\frac{e\psi}{k_B T}\right). \quad (4.17)$$

Here ψ is the electric potential, ϵ_0 is the permittivity of vacuum, ϵ_r is the dielectric constant of the liquid, c_0 is the salt concentration, e is the electron charge, k_B is the Boltzmann constant and T is the temperature. On the surface of the core and the shell we assumed constant surface potential boundary conditions. Three interesting points arise from Figure 4. First, the electrostatic repulsion had a longer range than expected for sphere-sphere interactions.

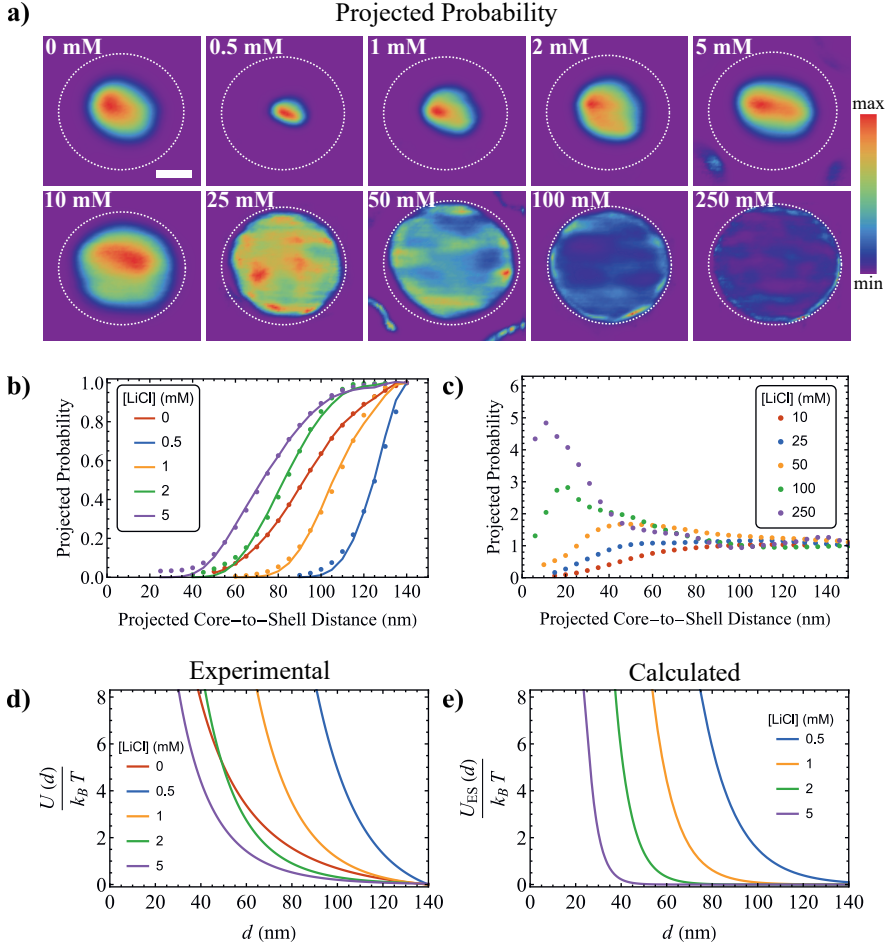


Figure 4: Influence of the salt concentration on the interactions between the titania core and the silica shell in a titania@water@silica rattle-type particle. a) Projected probability maps of finding the core particle in a certain part of the projected shell. The dashed circles show the projected area available to the particle in the shell. The scalebar indicates 100 nm. b-c) Projected probabilities of finding the particle a projected distance away from the shell wall at various salt concentrations. The projected probabilities for each concentration were averaged over 3 different particles. d) 3D interaction potentials obtained from the fits in b. e) Electrostatic interaction potentials calculated by solving the non-linear Poisson-Boltzmann equations with constant surface potential using a finite-element method for a core particle with radius $R_{\text{core}} = 170$ nm and surface potential $\psi_{\text{core}} = -50$ mV inside a shell with inner radius $R_{\text{shell}} = 350$ nm and inner surface potential $\psi_{\text{shell}} = -60$ mV.

Second, when no salt is added the titania particle approached the shell more closely than when 0.500 or 1.00 mM LiCl was added, even though the Debye screening length is significantly

longer in deionized water. Third, the titania particle remained colloidally stable within the shell up to 250 mM LiCl and was found to be more often close to the shell than in the middle of the geometry. We discuss these three phenomena in the following sections.

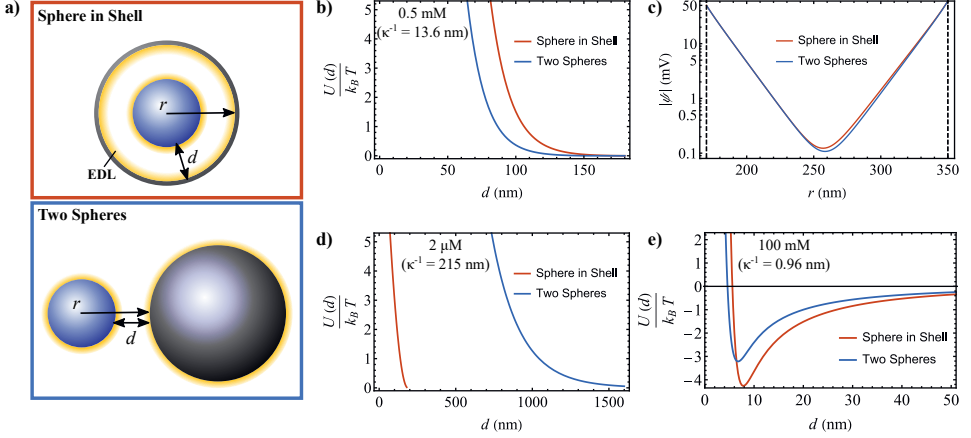


Figure 5: Comparison of the calculated interaction between two spheres and a sphere and a shell. One sphere has the radius (170 nm) and surface potential (-50 mV) of the core particle, while the other sphere has the radius (350 nm) and surface potential (-60 mV) of the inner shell wall. a) The two geometries used for the calculations. b) The interaction potential $U(d)$ for a sphere in a shell compared to two spheres for an ionic strength of 0.5 mM. c) The electric potential ψ as a function of the radial coordinate for the same conditions as in b). The left-hand side of the plot shows the decay of the surface potential from the core particle/small sphere, while the right-hand side of the plot shows the decay of the surface potential from the inner shell wall/large sphere. d-e) The interaction potentials for sphere-sphere and sphere-shell systems for ionic strengths of 2 μ M and 100 mM, respectively. Van der Waals interactions of a sphere within a shell have been included in e).

First, let us turn to the long-ranged electrostatic interaction between a sphere and a shell. The experimental interaction potentials are less steep than the calculated potentials, which is likely due to experimental limitations such as resolution. Using the equations outlined in the work of de Jonge⁹¹ we estimate the resolution in our experimental data to be approximately 11.6 nm in our experiments with titania@water@silica rattle-type particles (Supporting Information). Errors in the determination of the interactions between the core and shell mostly stem from resolution and the 2D projection of a 3D system. The resolution likely leads to errors in determining the projected core-shell distance and less steep interaction potentials. The 2D projected data leads to a lower accuracy of the projected probability when the particle is near the projected shell wall. Despite the errors in the experimental data it shows the same trends as the calculations and the long-ranged character of the interaction potential is present for both the experiments and the calculations. To get more insight in this long-ranged repulsion, we calculated the electrostatic interaction for both a sphere-sphere

system and a sphere-shell system using a finite-element method to solve the non-linear Poisson-Boltzmann equation with constant surface potential boundary conditions. The result for various salt concentrations is shown in Figure 5. For the case of an ionic strength of 0.5 mM in Figure 5b, it is indeed observed that the interaction is longer ranged for a sphere in a shell compared to the interaction between two spheres. The distance d between the two surfaces for which the repulsion is $5 k_B T$ is approximately 65 nm for sphere-sphere interaction, while it is approximately 82 nm for sphere-shell interaction. This difference is more than one Debye length (for 0.5 mM, $\kappa^{-1} = 13.6$ nm), which is quite significant. In Figure 5c it is shown that the potential from the surface of the inner shell wall (right-hand side of the plot) decays more slowly than that of a spherical particle; the difference is more pronounced when the core is off center (Supporting Information). This is due to the concave geometry of the shell as found previously for hollow shells.²¹⁵ This slow decay of the electric potential is the reason for the long-ranged interaction in a sphere-shell system. Furthermore, it is likely a reason why the core particle was stable at 250 mM concentration of LiCl.

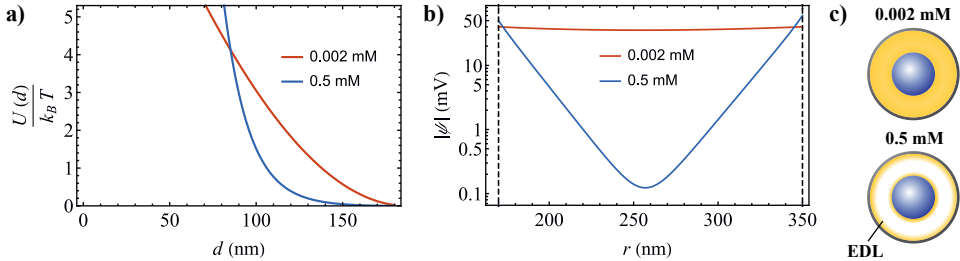


Figure 6: Calculated electrostatic interactions for a particle in a shell for an ionic strength of $2 \mu\text{M}$ ($\psi_{\text{core}} = -40$ mV and $\psi_{\text{shell}} = -40$ mV) and an ionic strength of 0.5 mM ($\psi_{\text{core}} = -50$ mV and $\psi_{\text{shell}} = -60$ mV). a) The interaction potential. b) The electric potential decaying from the core particle surface (left-hand side) and the inner shell surface (right-hand side). c) Schematic representation of the electric double layers within the rattle geometry.

Second, the apparently weak core-shell interaction in deionized water was investigated. In Figure 4b and 4d it is shown that the core particle is less confined to the middle of the shell for deionized water compared to moderate amounts of salt in the solution (0.500 and 1.00 mM LiCl, respectively). Furthermore, the interaction potential in deionized water was less steep than those in moderate amounts of salt. In Figure 5d we observe that the interaction in deionized water (we assume an ionic strength of $2 \mu\text{M}$) for two spheres is in the range of the order of a micron. This range is much larger than the space available in the rattle geometry. As such complete double layer overlap cannot occur and the interaction between core and shell is significantly altered. Figure 6 explores this in more detail by comparing the calculated core-shell interaction in deionized water (ionic strength of $2 \mu\text{M}$, $\kappa^{-1} = 215$ nm) with the interaction for an ionic strength of 0.5 mM ($\kappa^{-1} = 13.6$ nm). The interaction in $2 \mu\text{M}$ salt is significantly less steep than the interaction in 0.5 mM salt. Figure 6b shows that when the core particle is in the middle of the shell, the electric potential ψ originating from the surfaces

of the core and the shell decays to almost 0 in the middle between the two surfaces. However in deionized water, the electric potentials coming from both the surface of the core particle and the inner shell surface hardly decay. This leads to an almost flat electric potential within the entire shell geometry, significantly reducing the electrostatic interaction between core and shell. It is remarkable that this phenomenon was found in water. As previously stated, due to the self-dissociation of water it is difficult to reach ionic strengths lower than $1\text{ }\mu\text{M}$ and Debye lengths larger than 300 nm. The shell geometry helps significantly in this regard. The core particle cannot escape the shell and can only be a maximum distance away from the shell wall at all times. Furthermore, the slower decay of the electric potential from the inner shell surface means the electric potential is even more flat due to the rattle geometry.

Third, we discuss the interesting phenomenon at high ionic strength for which the core particle spends more time near the projected shell than in the middle of the rattle geometry (Figure 4c). One explanation is the presence of an attractive potential that the core experiences when it is close to the shell. The likelihood of van der Waals attractions are a good candidate for such attractions according to the calculations (Methods Section) and as shown in Figure 5e, where the sphere-shell secondary minimum is more severe than the sphere-sphere secondary minimum. However, in our sphere-shell system, there was also an influence of hydrodynamic interactions when the core particle was near the shell wall. This slowed down the particle near the shell wall (Chapter 3), similarly to how it would near a flat surface.^{188,216}

Therefore, we investigated how hydrodynamic slowing down of the core particle shows up in the analysis of our experimental electron microscopy data due to the finite time of our measurements. We note that in equilibrium, the influence of hydrodynamic interactions on the dynamics is not expressed in the shape of the positional probability (density). However, because of the finite time of our measurements and limited samples, the distribution we obtain from our dynamic measurements is not equal to the equilibrium distribution; in our distribution hydrodynamic effects can and do show up. This means we are working with an ‘apparent probability density’. To uncover how much hydrodynamic interactions influenced our experimental data, we simulated ADF-STEM images of a core particle diffusing within a shell. In short, for every timestep (equal to the pixel dwell time) we let the particle (starting from a random position within the shell) move in a random direction according to the position-dependent and direction-dependent diffusion coefficient (Figure A5a). Knowing the position of the particle for the pixel that is currently being scanned, we took the weighted average value of that pixel for the three static simulated images of the rattle particle for which the position of the core particle best resembled the current position. This was done for all pixels in order to form an image of a moving core particle within a shell. We simulated 180 images per series, which is roughly the same amount as the images per salt concentration in the experiments. More details can be found in the Methods Section. Figure 7a shows images resulting from this simulation for which the particle could move freely until it approached 120 or 60 nm from the shell wall, respectively (Figure 7b). The simulated images look similar to the experimental images shown in Figure 2a. In Figure 7c the projected probabilities of finding the particle at a certain distance from the shell from simulated images are shown. We observed that when the

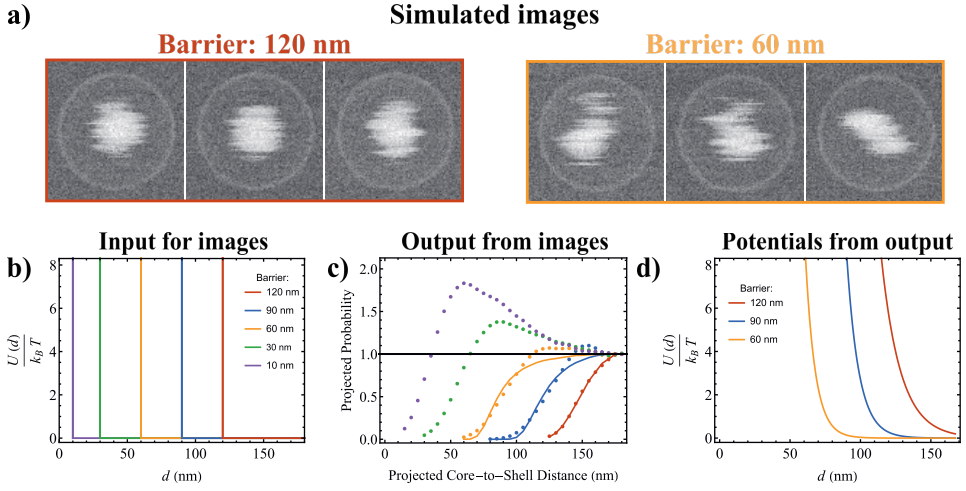


Figure 7: Results obtained by simulating ADF-STEM images of a moving titania core particle ($R_{\text{core}} = 170$ nm) within a silica shell ($R_{\text{shell}} = 350$ nm) in water. a) Example images of a moving core particle that cannot approach the shell wall closer than 120 or 60 nm. b) The input interaction potentials used to simulate the diffusion of a core particle within a shell. c) Projected probability as function of the projected core-to-shell distance for the various simulations performed with potentials shown in b as barriers. d) The resulting apparent interaction potentials found from the projected probability fits in c for the three cases where the particle was confined mostly to the middle.

particle was allowed to approach the shell closely, the projected probability of finding the core particle near the shell wall was higher than in the middle of the shell geometry. Since there was no attractive potential in our simulations, this was a direct consequence of the hydrodynamic slowing down of the core particle. It is thus likely that hydrodynamics effects contribute to the higher projected probability of finding the particle near the projected shell wall found in Figure 4c due to the finite time of our measurements. Both hydrodynamic effects and van der Waals attractions could lead to the increased probability of finding the core particle near the projected shell wall in our measurements. Since it was hard to distinguish between both effects (Supporting Information) we did not attempt to extract the interaction potential at high salt concentrations.

However, when the particle was not allowed to move close to the shell wall the effect of the hydrodynamics proved much more limited. Figure 7d gives a good impression of the systematic error that hydrodynamic interactions, but more importantly limited resolution, would induce on the potentials we extracted in Figure 4d for the cases of moderate salt concentrations (0.5 – 5 mM). Based on these apparent potentials, we are confident in our extracted interaction potentials in Figure 4d.

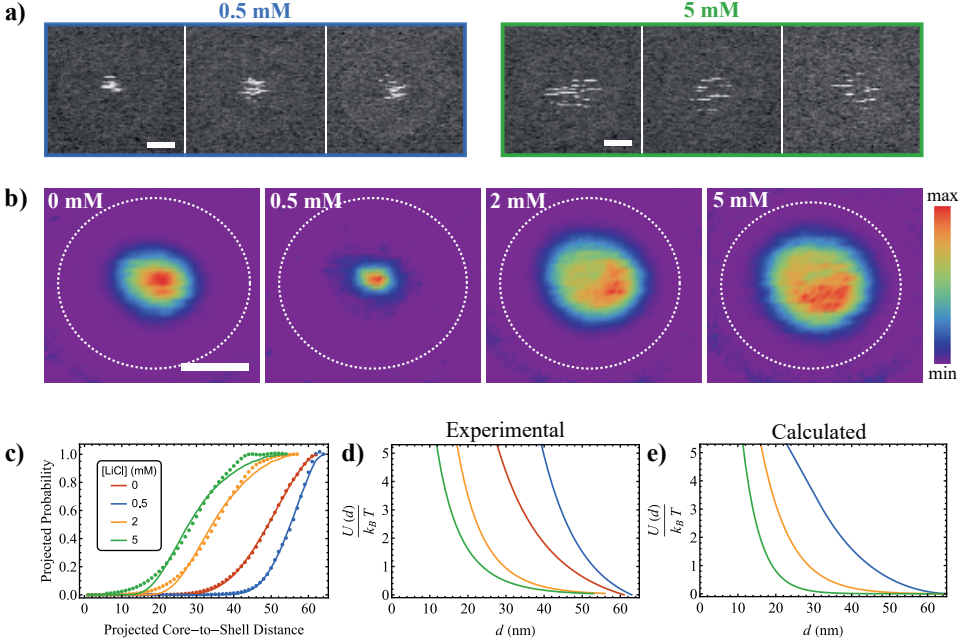


Figure 8: Interactions of a gold nanosphere ($R_{\text{core}} = 17 \text{ nm}$) inside a thin silica shell ($R_{\text{shell}} = 80 \text{ nm}$). a) Example experimental images of a gold particle moving within a silica shell in water with 0.500 or 5.00 mM LiCl. The electron dose rate was $206 \text{ e}^- \text{ nm}^{-2} \text{ s}^{-1}$. b) Projected probability maps of where the gold particle is found in different salt concentrations for a single particle. The dashed circles show the projected area available to the particle in the shell. c) Projected probability as function of the projected core-to-shell distance including fits for a 3D interaction potential. d) 3D experimental interaction potential following from the fits in c. e) Calculated interaction potential by solving the non-linear Poisson-Boltzmann equation for a gold particle ($\psi_{\text{core}} = -50 \text{ mV}$) within a silica shell ($\psi_{\text{core}} = -60 \text{ mV}$) with constant surface potential; we omit the 0 mM result as it is a problematic limit. All scalebars indicate 50 nm.

4.3.2. Interactions within a gold@water@silica nanorattle

Lastly, the interactions between a gold nanosphere ($R_{\text{core}} = 17 \text{ nm}$) and a thin silica shell ($R_{\text{shell}} = 80 \text{ nm}$) were investigated in Figure 8. These particles can really be considered nanorattles and are so small that liquid-cell electron microscopy is the only technique that is able to obtain reliable real-space information on them in water as a solvent. The electron dose rate in these measurements was $206 \text{ e}^- \text{ nm}^{-2} \text{ s}^{-1}$. As found for the titania particle, the experimental interaction potentials are not as steep as the calculated potentials. However, this effect is less pronounced as the resolution is slightly better imaging gold particles (7.8 nm) compared to titania cores (11.6 nm). Especially the calculated and experimental interaction potentials for 2.00 and 5.00 mM LiCl agree excellently. Interestingly, the experimental potential for an ionic strength of 0.500 mM indicates a repulsion of longer range than the calculated

interaction potential. This could be due to an underestimation of the surface potential in the calculations. For gold@water@silica rattles, similarly to the much larger titania@water@silica rattles, the core particle approached the shell more closely without any added salt, compared to the situation for 0.500 mM LiCl. Moreover, we observed many instances of the gold core particle getting stuck to the shell in pure water (Figure A12 and Supporting Movie 8). There are even instances where the particle got stuck to the shell in one frame and the electron beam enables it to move again the next frame. The influence of the electron beam is hard to determine here, but the particle getting stuck to the shell only happens when no salt was added, which hints that the repulsion between the core and shell was lowest for this case. These results indicate that in these nanorattles flat electric potentials can be detrimental to the stability of the core particle within the shell, especially when the surfaces are not highly charged or when they are in a medium with a less polar character than that of water. It is therefore recommended to have some salt present in dispersions of nanorattles at all times if mobility of the core particle is desired.

4.4. CONCLUSION

In conclusion, it was found that it is possible to measure reliable interactions between a core particle and a shell using liquid-cell electron microscopy. We found that the interactions between a titania core and silica shell could be tuned over a large range of ionic strengths. The interactions of a sphere within a shell were found to be significantly more long-ranged compared to the interactions between two spheres under the same conditions. It was also observed that the core particle could approach the shell more closely when no salt was added, compared to the case for moderate salt concentrations (0.5 and 1 mM). Finite-element calculations confirmed this to be due to a flat electric potential within the rattle geometry in deionized water. Furthermore, for salt concentrations above 50 mM, the core particle spent more time close to the shell wall than in the middle of the rattle geometry. Simulations confirmed that hydrodynamic slowing down of the core particle plays a significant role, while calculations also showed a secondary minimum in the potential of a few $k_B T$ was probable at such high salt concentrations as well, contributing to the above mentioned behavior. Due to the limit of our 2D projected experimental data, the extent of both effects could not be determined accurately experimentally.

Lastly, the interactions between a gold nanosphere and a silica nanoshell were measured in aqueous solutions. We found that, due to the flat electric potential within the shell, the nanosphere is less stable within the shell in deionized water, compared to when a moderate amount of salt was added (0.5–5 mM). The results indicate that liquid-cell electron microscopy is a powerful tool to measure interactions of nanoparticles in water, where a high spatial resolution is a requirement.

AUTHOR CONTRIBUTIONS

Tom A.J. Welling performed the liquid-phase electron microscopy experiments, data analysis, the calculations, and the simulations and wrote the manuscript. Kanako Watanabe (Tohoku University) synthesized the rattle particles under supervision of Daisuke Nagao

(Tohoku University). Albert Grau-Carbonell (Utrecht University) helped with useful tips regarding the experimental data analysis. Arnout Imhof (Utrecht University) helped with the concept of flat potentials within the rattles.

ACKNOWLEDGEMENTS

We acknowledge Wessel Vlug for his early work on interactions within rattle-type particles. The authors also acknowledge the EM square center at Utrecht University for access to the microscopes. Especially, Chris Schneijdenberg and Hans Meeldijk are thanked for their assistance.

APPENDIX A: SUPPORTING INFORMATION

Synthesis details

Here we give a detailed description of the synthesis of the two rattle-type particles used in this work. The original works for the titania@void@silica rattle-type particles³⁴ and gold@void@silica rattle-type particles⁵¹ include details and additional schematics for easier understanding.

Titania@void@silica rattle-type particles

Materials. Tetraethyl orthosilicate (TEOS, 95%), titanium tetraisopropoxide (TTIP, 95%), acetonitrile (99.5%), aqueous ammonia solution (NH_3 , 25 wt%), methylamine aqueous solution (40 wt%), ethanol (99.5%), styrene (St, 99%), *p*-styrenesulfonic acid sodium salt (NaSS, 80%), potassium persulfate (KPS, 95.0%) and polyvinylpyrrolidone (PVP, $M_W = 360000$ g/mol) were purchased from FUJIFILM Wako Pure Chemical Corporation (Osaka, Japan). 3-Methacryloxypropyltrimethoxysilane (MPTMS, 95.0%) was obtained from Shinetu Chemical (Tokyo, Japan). The inhibitor for St monomer was removed by using an inhibitor removal column. Poly(allylamine hydrochloride) (PAH, $M_W = 15000$ g/mol) was obtained from Aldrich. The silane coupling agent 3-aminopropyltriethoxysilane (APTES, 95%) was purchased from Chisso Corp (Tokyo, Japan).

Method. Submicrometer-sized titania cores were prepared according to our method previously reported.^{127,217} The titania cores were surface-modified with MPTMS at 35 °C. After an hour reaction under stirring, styrene monomer (50 mM) and an aqueous solution of NaSS were added to the suspension and the mixture was stirred for 1 h. An aqueous solution of KPS was added as an initiator to the suspension at 65 °C. The polymerization was conducted at $[\text{MPTMS}] = 2$ mM, $[\text{KPS}] = 2$ mM, $[\text{NaSS}] = 0.25$ mM, and a titania concentration of 0.065 vol%. To further increase the thickness of the PSt shell, another polymerization of St was conducted at a concentration of 100 mM St with KPS initiator (2.0 mM). The second formation of PSt shell was performed at a core/shell particle concentration of 0.05 vol%.

In the second step, the doubly PSt-coated titania particles were coated with silica.²¹⁸ A suspension of the PSt-coated particles was added to a solution containing PAH and NaCl. The concentrations of the doubly PSt-coated particles, PAH, and NaCl were 0.15 vol%, 0.71 kg/m³, and 36 mol/m³ in the mixture, respectively. After two centrifugation steps to remove nonadsorbed PAH and NaCl, the particles were redispersed into 40 mL of an ethanolic solution containing 0.20 g of polyvinylpyrrolidone (PVP). Two more centrifugation steps were conducted to remove excess PVP, and particles were redispersed into 9.59 mL of ethanol. To the ethanolic solution, 10.6 mL of ammonia solution, silica precursors TEOS (1.0 mL) and APTES (37 μL) were added. The mixed silica precursors were used to form a low-density silica shell suitable for the slight etching of silica.^{219,220} PSt-coated particles coated with silica were dried at 50 °C, followed by heat treatment for 4 h in air in an oven at 500 °C. Particles obtained by the heat treatment were immersed in 30 mL of ammonia solution (15 – 20 mM, approximately pH 11) to slightly etch the silica component of the particles. This detaches the cores from the shells.

Gold@void@silica rattle-type particles

Materials. Hydrogen tetrachloroaurate(III) tetrahydrate ($\text{HAuCl}_4 \cdot 4\text{H}_2\text{O}$, 99.9%), trisodium citrate dihydrate ($\text{Na-cit} \cdot 2\text{H}_2\text{O}$, 99%), tetraethyl orthosilicate (TEOS, 95%), aqueous ammonia solution (NH_3 , 25 wt%), and ethanol (99.5%) were purchased from FUJIFILM Wako Pure Chemical Corporation (Osaka, Japan). Polyethylemine (PEI, $M_W \approx 25000$ g/mol) was purchased from Sigma-Aldrich (Tokyo, Japan). Water was deionized in advance ($> 18.2 \text{ M}\Omega \text{ cm}$).

Method. Citrate-stabilized gold nanoparticles (Au NPs) were synthesized according to previous reports.^{221,222} The Au NPs were employed for the direct silica coating previously reported.²²³ The aqueous suspension of the Au NPs was added to an ethanolic solution of TEOS which was mixed for 15 min under stirring at 35°C . Ten minutes after the addition of the TEOS solution, an aqueous solution of NH_3 was injected into the mixture. The concentrations of TEOS, NH_3 and water were 5 mM, 400 mM and 10.9 M, respectively. The total reaction volume was 30 mL and the concentrations of Au NPs was 0.31 mM. Four hours after the injection of ammonia solution, the mixture was centrifuged twice (8000 g, 10 min) using a dispersion medium of ethanol.

The hollow silica spheres incorporating Au NPs were synthesized by a surface-protected etching process, which is a procedure for the synthesis of hollow silica spheres using polymer with high molecular weight, PEI.⁴⁵ An ethanol solution of PEI was mixed with the ethanol solution of silica-coated gold particles (Au@SiO_2) in a vial by sonication for 15 min. The vial was transferred to a water bath, and then stirred at 35°C for 30 min. The concentrations of PEI and Au@SiO_2 particles were 10 g/L (approximately 0.4 mM) and $5.3 \cdot 10^{-4}$ vol%, respectively. After centrifugation the Au@SiO_2 particles modified with PEI were redispersed in water. The aqueous suspension was stirred at 50°C for 15 h, after which the particles were washed twice more with water.

Zeta potential measurements

The zeta potential of the titania@water@silica and gold@water@silica rattle-type particles was measured with a zeta potential analyzer (Otsuka Electronics, ELSZ-2). Henry's function was used to relate the electrophoretic mobility to the zeta potential. The zeta potential of the titania core was measured with a diluted dispersion of core particles after they were coated with polystyrene and etched again as in the procedure for making the titania@void@silica rattles. The zeta potential of the gold core was measured for as-synthesized gold particles with citrate ligands. The zeta potential of the shell's inside could not be measured and was assumed to be the same as that of the outside (-60 mV).

Volume correction LC-STEM

As the shell has a spherical geometry in 3D, we corrected the probability of finding the particle at a particular position by a geometrical factor which takes into account that the particle has more space in the direction perpendicular to the imaging plane when it is in the middle part of the projected shell than it has when it is near the edge. This correction factor

Table A1: Zeta potential of a titania core measured outside the electron microscope in an aqueous solution with an ionic strength of 1.00 mM. LiCl and HCl were used to get the desired pH at an ionic strength of 1.00 mM.

pH	ζ (mV)
7	-54 ± 1
5	-59 ± 1
3	-9 ± 1

Table A2: Zeta potential of a gold core measured outside the electron microscope in an aqueous solution with an ionic strength of 1.00 mM. LiCl and HCl were used to get the desired pH at an ionic strength of 1.00 mM.

pH	ζ (mV)
7	-50 ± 4
5	-54 ± 1
3	-20 ± 1

is

$$\frac{1}{\sqrt{\rho^2 + (R_{\text{shell}} - R_{\text{core}})^2}}, \quad (4.18)$$

where ρ is the radial distance between the edge of the core particle and the shell and R_{shell} and R_{core} are the radii of the shell and the core, respectively. This projected probability, corrected for the differences in volumes in the direction perpendicular to the imaging plane, is used to analyze the interaction potential for different salt concentrations.

Extra details on finite-element calculations on electrostatic interactions

An example of the mesh used for the finite-element calculations solving the non-linear Poisson-Boltzmann equation in a rattle geometry is shown in Figure A1.

Details of the used parameters in the calculations can be found in Table A3. Additional parameters include the dielectric constant of the liquid ($\epsilon_r = 78.4$), the temperature ($T = 293.15$ K). The surface charge density for the calculation with constant surface charge of a gold sphere in a silica shell in 0.5 mM salt was 3.9 mC/m² for the core and 7.7 mC/m² for the shell.

Table A3: Parameters used for the finite element calculations for titania@void@silica and gold@void@silica rattle-type particles.

Parameter	titania core	silica shell	gold core	silica shell
Radius	170 nm	350 nm	17 nm	80 nm
Surface potential	-50 mV	-60 mV	-50 mV	-60 mV

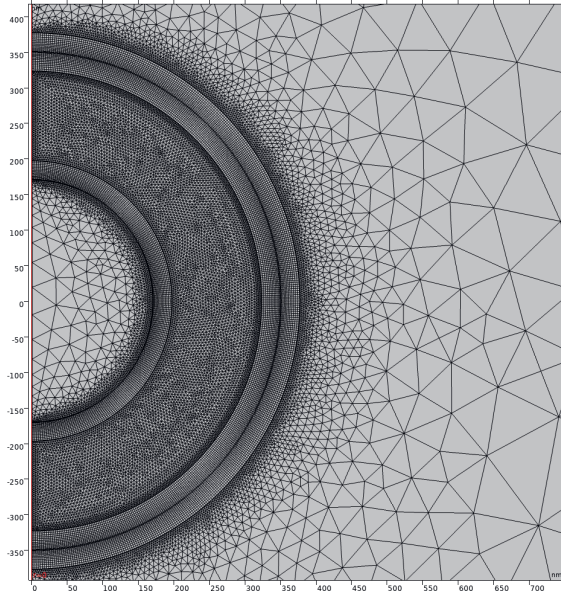


Figure A1: Mesh used for the finite-element calculations on the electrostatic interaction between the core and the shell. In this case, the salt concentration was 0.5 mM and the geometry shown has the size equivalent to the titania@water@silica rattle-type particle.

In order to check our finite-element calculations, the case of two spheres was compared to the analytical solution provided by

$$\frac{U(d)}{k_B T} = Q_1 Q_2 \lambda_B \frac{e^{\kappa(a_1+a_2)}}{(1+\kappa a_1)(1+\kappa a_2)} \frac{e^{-\kappa d}}{d + a_1 + a_2}, \quad (4.19)$$

where $\lambda_B = \frac{e^2}{4\pi\epsilon_0\epsilon_r k_B T}$ is the Bjerrum length, $Q_i = 4\pi\epsilon_0\epsilon_r a_i \psi_i / e(1 + \kappa a_i)$ is the number of charges on particle i and a_i is the particle radius of particle i . One sphere had a radius of 170 nm and a constant surface potential of -50 mV and the other sphere had a radius of 350 nm and a constant surface potential of -60 mV. The result for a salt concentration of 0.5 mM is shown in Figure A2.

Van der Waals interaction calculations: limiting case and shell thickness

As a limiting case, we wanted to see how much our solution of a sphere in a shell as given in the methods section deviated from the solution of a sphere and a flat slab for the case where the vdW interaction is extremely short-ranged, which is achieved by making the shell thickness 0.5 nm. The solution of a sphere and a flat slab is given by²²⁴

$$U_{\text{vdW}} = -\frac{A}{6} \left[\frac{l R_{\text{core}}}{h(h+l)} + \frac{l R_{\text{core}}}{(h+2R_{\text{core}})(h+l+2R_{\text{core}})} - \ln \left(\frac{(h+l)(h+2R_{\text{core}})}{h(h+l+2R_{\text{core}})} \right) \right]. \quad (4.20)$$

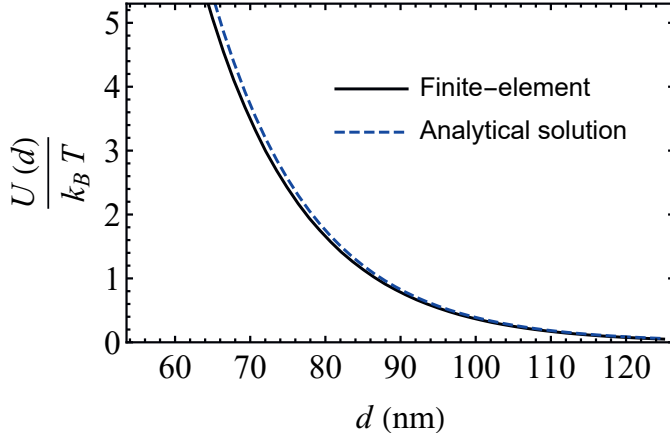


Figure A2: Interaction potential obtained from the finite-element calculations versus the analytical solution for two spheres in 0.5mM salt in water. One sphere has a radius of 170 nm and a constant surface potential of -50 mV and the other sphere has a radius of 350 nm and a constant surface potential of -60 mV.

Here l is the wall thickness and h the distance between the core particle and the wall. The result for $A_{123} = 6.9\text{zJ}$ and a thickness of the flat plate and shell of 0.5 nm is shown in Figure A3.

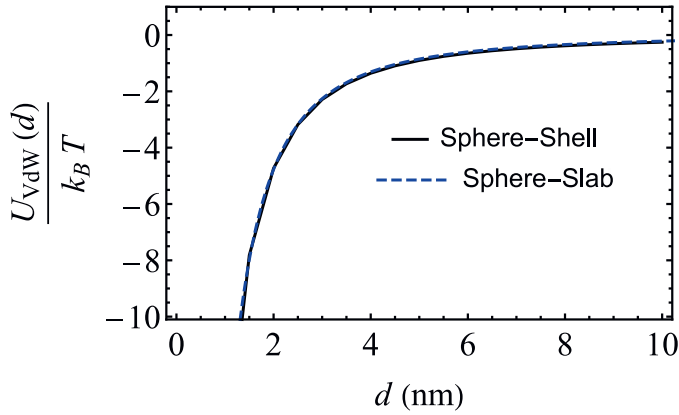


Figure A3: Limiting case for the van der Waals interaction of a sphere in a shell and a sphere and a flat slab. The thickness of the wall/shell is 0.5 nm. The particle radius is 170 nm and the inner shell radius is 350 nm. Due to the short-ranged interaction, the sphere has a similar interaction with the shell as with the flat wall.

Lastly, the shell thickness has an interesting effect on the van der Waals interaction. The interaction is plotted for three shell thicknesses in Figure A4. It shows that by controlling the shell thickness of a rattle particle the van der Waals interactions between the core and shell can be tuned significantly for nano-thicknesses of the shell.

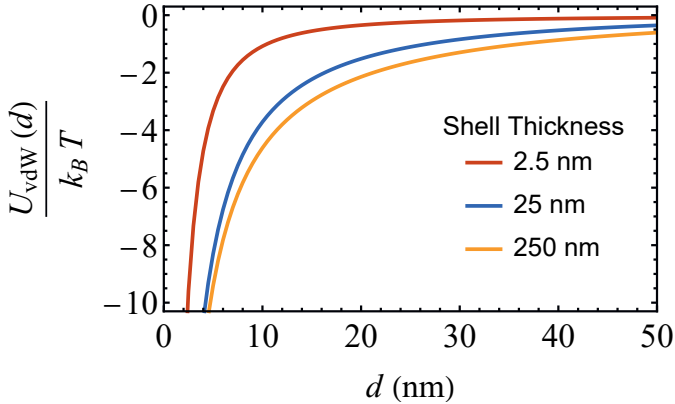


Figure A4: The van der Waals interaction of a sphere in a shell for different shell thicknesses. The particle radius is 170 nm and the inner shell radius is 350 nm. The Hamaker constant is $A_{123} = 6.9 \text{ zJ}$.

Finite-element calculations of the local mobility of the core inside a shell

For the finite-element calculations on how hydrodynamic interactions affected the local core mobility we used COMSOL MultiPhysics (version 5.4). We set up a system with a spherical colloid of radius $R_{\text{core}} = 170 \text{ nm}$ within a shell of radius $R_{\text{shell}} = 350 \text{ nm}$ to represent the rattle particles of the experiments. Both the particle and the shell surface were set to have a no-slip boundary condition. The spherical shell, including the core particle and the liquid, was placed within a cylindrical domain with open boundary conditions (zero normal stress) for the fluid. We solved Stokes's equations for fluid dynamics of an incompressible liquid. The fluid density was taken as $\rho = 1 \cdot 10^3 \text{ kg m}^{-3}$ and the dynamic viscosity used was $\eta = 10^{-3} \text{ kg m}^{-1} \text{ s}^{-1}$ in accordance with the experimental system. A constant velocity boundary condition was applied on the sphere to obtain the translational mobility. To ensure that the laminar flow condition is satisfied, a low velocity of the sphere was used: $v = 10^{-6} \text{ m s}^{-1}$. We solved for the force exerted by the fluid and shell wall on the particle by integrating the hydrodynamic stress tensor over the surface of the sphere. The position of the core particle inside the shell was varied to determine how the force changed with the radial position. Furthermore, we changed the direction of the velocity condition on the core particle to decouple the hydrodynamic force in the radial direction and the force perpendicular to that direction (along the shell wall). The force was then compared to the force on a particle that was free from confinement to determine the diffusion coefficient. When the velocity condition was directed in the radial direction, we exploited the rotational symmetry of the system to minimize the number of mesh elements

required. A full 3D calculation was required when the velocity condition was directed along the shell as the rotational symmetry was broken. Constructing a sufficiently small mesh in this case was only feasible when local refinements of the elements on the surface of the core particle and the shell wall was used. Generally an element size of 2 nm was employed on the surface of the core particle and the element size was allowed to grow radially outward. The mesh on the shell wall was also locally refined. We performed mesh refinement for a few selected calculations and found no significant difference for even smaller element sizes.

The resulting radial and perpendicular diffusion coefficients as function of the radial position of the core particle are shown in Figure A5a. Especially in the radial direction, the mobility of the core depends on the position within the shell.

Increased projected probability to find the core particle near the projected shell at high salt concentrations

We calculated the influence of hydrodynamics and an attractive van der Waals potential on the probability of finding the particle in certain parts of the shell in Figure A5. Figure A5a shows the decrease in the diffusion coefficients towards the shell (radial) and along the shell wall (perpendicular) as the core particle approaches the shell. Figure A5b shows the van der Waals attraction calculated for the system. Figure A5c and A5d show the probability of finding the core particle near the shell in 3D or in a 2D projected image, respectively, under the influence of hydrodynamics or van der Waals attraction present in our system. To determine the influence of the hydrodynamic interactions on the probability, we simulated the mobility of the core particle according to the position-dependent and direction-dependent diffusion coefficient (Figure A5a) with a timestep $\Delta t = 15 \mu\text{s}$ based on the pixel dwell time of our measurements. For the van der Waals interaction, the Boltzmann distribution was used to relate the interaction potential to the probability of finding the particle in a certain position. The increased probability of finding a particle near the shell between a particle under influence of hydrodynamics and a particle under influence of an attractive van der Waals potential is clearly different, due to the long-ranged nature of the indirect hydrodynamic interactions. However, this difference is not clear at all in a 2D projected probability plot, which is used in our analysis of projected microscopy data. Therefore, it is hard to distinguish between the effects of hydrodynamics and van der Waals interactions as being the reason for the increased probability of finding the core particle near the shell. We therefore did not extract the interaction potential from our experimental data at higher salt concentrations.

Influence of the electron beam

As in any experiment involving liquid-cell electron microscopy, the influence of the electron beam has to be investigated. The system of rattle-type particles is ideal for probing the influence of the electron beam on the interactions between surfaces in liquid-cell electron microscopy. We varied the electron dose rate by changing the beam current and imaged the same rattle-type particle. For this experiment we used the titania@water@silica rattle-type particles as well as gold@water@silica nanorattles. The experiment in which we varied the electron dose rate with titania@water@silica rattles is described in the main text.

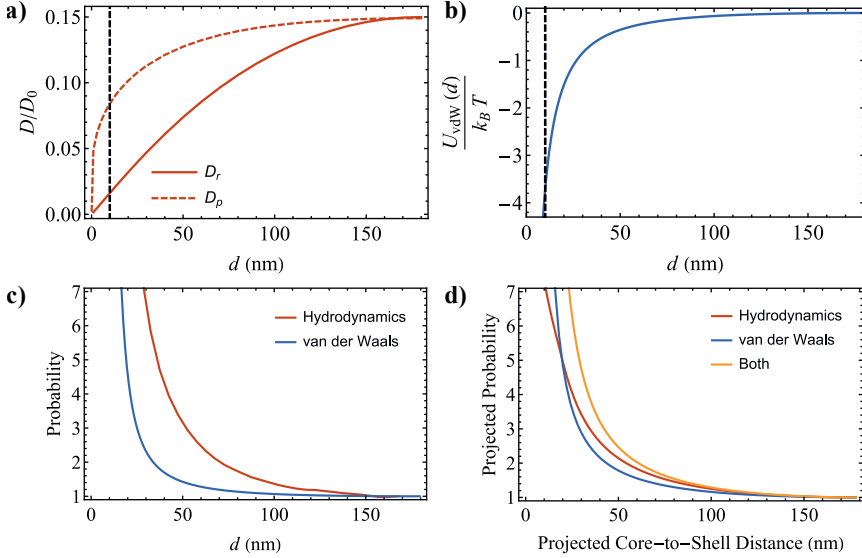


Figure A5: Calculations on the influence of hydrodynamics and an attractive van der Waals potential on the probability of finding a particle a certain distance away from the shell wall in our experiments. a) Calculated diffusion coefficient D of the core particle as function of the distance from the shell wall compared to the diffusion coefficient of a free particle D_0 . The full line represents the diffusion coefficient in the direction towards the shell wall (D_r , radial), while the dashed line represents the diffusion coefficient along the shell wall (D_p , perpendicular). b) Attractive van der Waals interaction potential as function of the distance between the core and shell surfaces. The black dashed lines in a and b represent how close the core particle can approach the shell wall in determining the probabilities in c and d. c) Probability in 3D to find the particle a certain distance away from the shell, while the particle is under the influence of hydrodynamics or an attractive van der Waals potential. d) Projected probability to find the particle a certain distance away from the projected shell in a 2D image, while under the influence of hydrodynamics or an attractive van der Waals potential or both.

In order to give more credibility to the claim in the main text that a drop in pH can explain the reduced interaction between the titania core and the silica shell observed when the electron dose rate is increased, we changed the pH by flowing in different solutions (which all have an ionic strength of 1.00 mM) while imaging at a constant electron dose rate. LiCl and HCl were used to tune the pH and ionic strength. Figure A6 visualizes how closely the core can approach the shell at various pH levels. As the pH decreases, so does the minimum distance between the core and the shell. It is well known that both titania and silica lose charge when the pH drops.^{204–206} Table A1 shows the zeta potential of the titania core measured outside the microscope and shows that the zeta potential drops significantly between pH 5 and 3. It is possible that some silica is left on the surface of the titania particle after the synthesis procedure as the particle is still slightly negatively charged at pH 3. A drop in pH is

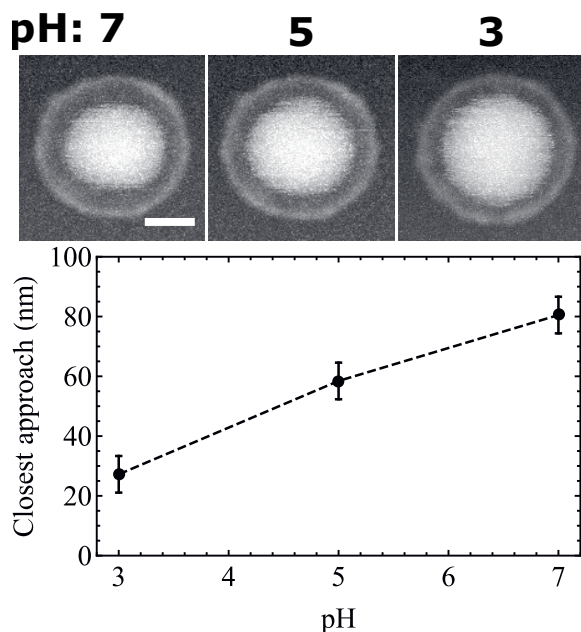


Figure A6: Influence of the pH (tuned with HCl) on the interaction potential within the titania@water@silica rattle-type particle. The three images show for each pixel the maximum intensity that was reached during the whole image series (Supporting Movie 4). It visualizes the minimum distance of approach between the core particle and the shell. The minimum distance decreases with the decrease in pH. The ionic strength is 1.00 mM in all cases. The electron dose rate was $95 \text{ e}^- \text{ nm}^{-2} \text{ s}^{-1}$. The scale bar is 250 nm.

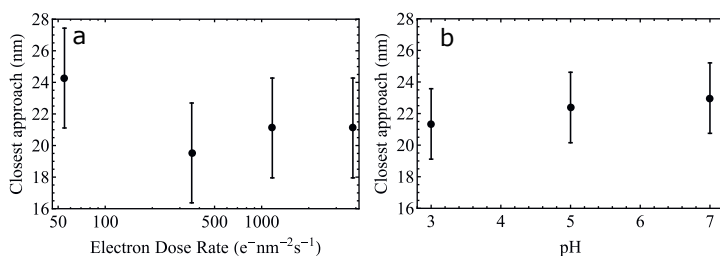


Figure A7: Influence of a) electron dose rate and b) pH on the minimum separation between the gold core and the shell in a gold@water@silica nanorattle, as deduced from Supporting Movies 5 and 6. The ionic strength is 1.00 mM in all cases. The electron dose rate for b) was $179 \text{ e}^- \text{ nm}^{-2} \text{ s}^{-1}$.

a plausible explanation for the reduction in the interaction potential at higher electron dose rates as the charge on the particle decreases significantly.

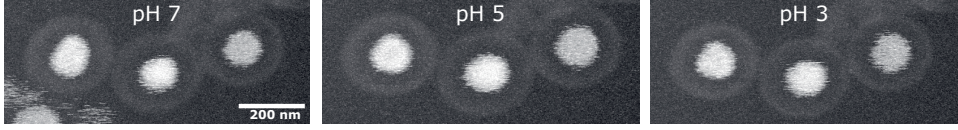


Figure A8: The behavior of gold@water@silica nanorattles at different pH. The three images show for every pixel the maximum intensity that was reached during the whole image series at a certain pH (tuned with HCl). It visualizes the minimum distance to which the core particle can approach the shell. The electron dose rate was $179 \text{ e}^- \text{ nm}^{-2} \text{ s}^{-1}$.

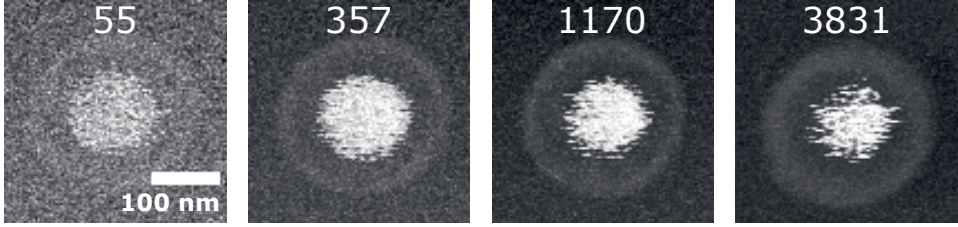


Figure A9: The behavior of gold@water@silica nanorattles at various electron dose rates. The four images show for every pixel the maximum intensity that was reached during the whole image series at a certain electron dose rate. It visualizes the minimum distance to which the core particle can approach the shell. The LiCl concentration was 1.00 mM. The electron dose rate in $\text{e}^- \text{ nm}^{-2} \text{ s}^{-1}$ is shown in each image.

We also investigated the effects of the electron dose rate and pH for gold nanorattles in Figure A7 (and Figures A8 and A9). It was found that both electron dose rate and pH did not have an effect on the interaction between the gold core and the silica shell. This indicates that the pH may indeed be the deciding factor in the effect of the electron beam, at least at moderate electron dose rates.

4.4.1. Resolution

To determine the resolution in our experiments on titania@water@silica rattles we used⁹¹

$$d_{\text{STEM}} = \sqrt{d_{\text{SNR}}^2 + d_{\text{blur}}^2} \quad (4.21)$$

where d_{STEM} is the spatial resolution, d_{SNR} is the resolution due to the signal-to-noise ratio, d_{blur} is the resolution due to the broadening of the STEM probe and where we neglect the initial width of the STEM probe.

The resolution due to the signal-to-noise ratio d_{SNR} was determined via⁹¹

$$d_{\text{SNR}} = \sqrt{\frac{6l_0}{t - l_w}} \left(\frac{tl_w}{D_e} \right)^{1/4} \quad (4.22)$$

where $l_0 = 176 \text{ nm}$ is the mean free path length of the titania particle at 200 keV,²²⁵ $l_w = 300 \text{ nm}$ is the mean free path length of the water,²²⁶ $t = 1 \mu\text{m}$ is the thickness of the water

layer and $D_e = 45 \text{ e}^- \text{ nm}^{-2} \text{ s}^{-1}$ is the electron dose rate. Using these values we arrive at $d_{\text{SNR}} = 11.1 \text{ nm}$.

The resolution due to the broadening of the STEM probe in the water layer at a certain depth z in the sample was calculated via⁹¹

$$d_{\text{blur}}(z) = 1.3 \frac{\lambda^2}{2\pi a_H} z^{3/2} \sqrt{\frac{N_A \rho}{3\pi W}} Z(1 + E/E_0) \quad (4.23)$$

where a_H is the Bohr radius, N_A is Avogadro's constant, ρ is the mass density of water, W the averaged atomic weight (weighted by molar fractions) of water, Z is the atomic number of water, E is the electron energy, and λ is the relativistic wavelength of the electron:

$$\lambda = \frac{hc}{\sqrt{2EE_0 + E^2}} \quad (4.24)$$

with Planck's constant h , the speed of light c , and $E_0 = m_0 c^2$ the rest energy of the electron, with the rest mass of the electron m_0 .

The depth z at which we evaluate d_{blur} is 350 nm, as this is the middle of the rattle geometry from the top of the sample. We then arrive at $d_{\text{blur}} = 3.3 \text{ nm}$. Using d_{SNR} and d_{blur} we obtain for the titania@water@silica rattle-type particles:

$$d_{\text{STEM,titania}} = 11.6 \text{ nm}. \quad (4.25)$$

When we do the same calculations for gold@water@silica rattle-type particles ($l_0 = 74.8 \text{ nm}$,²²⁷ $t = 500 \text{ nm}$, $D = 206 \text{ e}^- \text{ nm}^{-2} \text{ s}^{-1}$ and $z = 80 \text{ nm}$) we obtain:

$$d_{\text{STEM,gold}} = 7.8 \text{ nm}. \quad (4.26)$$

APPENDIX B: SUPPORTING FIGURES

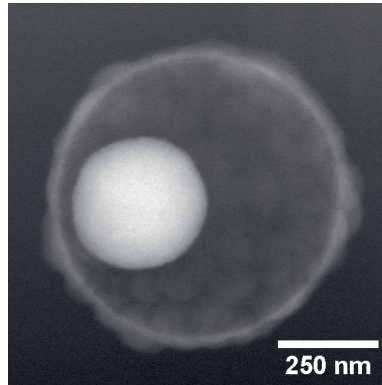


Figure A10: Image of a titania@water@silica rattle-type particle after flowing in a solution of pH 2. The particle irreversibly sticks to the shell wall and this allowed for careful measurement of its size.

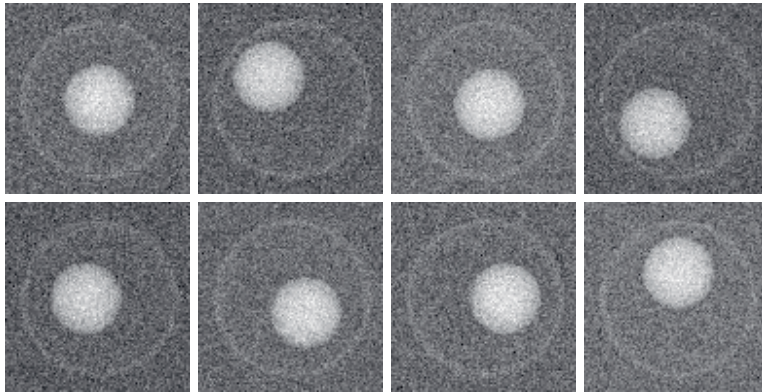


Figure A11: Examples of static simulated ADF-STEM images of a titania core particle ($R_{\text{core}} = 170 \text{ nm}$). within a silica shell (inner shell radius $R_{\text{shell}} = 350 \text{ nm}$). The pixelsize is 8.9 nm and the number of simulated electrons per pixel N was 3528.

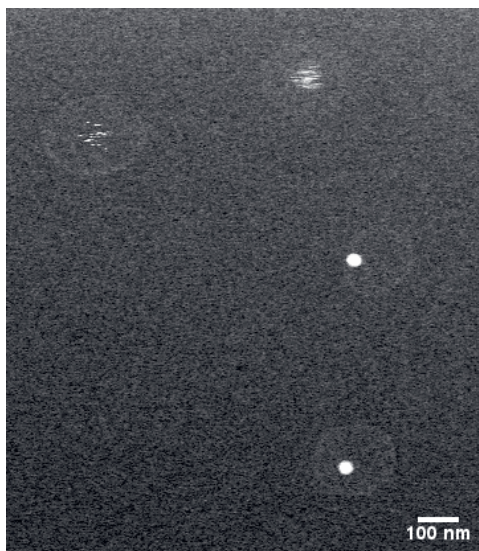


Figure A12: A frame of Supporting Movie 8 of gold@water@silica nanorattles in pure water. This is an example of a case where two gold particles are moving within their respective shells while two other gold particles are stuck.

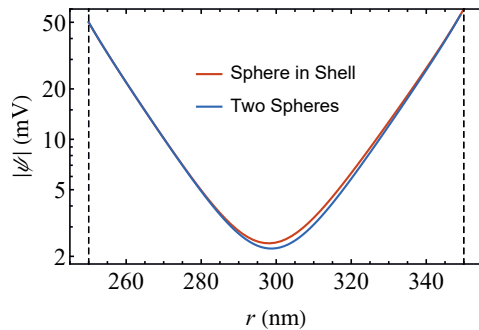


Figure A13: Electric potential for a sphere in a shell and two spheres in 0.5mM salt for the same system as Figure 5 in the main text, except that here the core is placed off center (100 nm from the shell wall). The radial coordinate r is the distance from the center, as in Figure 5.

APPENDIX C: SUPPORTING MOVIES



Supporting Movie 1: Titania@water@silica rattle-type particle in pure water at different electron dose rates. Electron dose rates shown in video in units of $\text{e}^- \text{nm}^{-2} \text{s}^{-1}$.



Supporting Movie 2: Titania@water@silica rattle-type particle in 10.0 mM LiCl at different electron dose rates. Electron dose rates shown in video in units of $\text{e}^- \text{nm}^{-2} \text{s}^{-1}$.



Supporting Movie 3: Titania@water@silica rattle-type particle at different pH. The electron dose rate was $95 \text{ e}^- \text{nm}^{-2} \text{s}^{-1}$.



Supporting Movie 4: Gold@water@silica rattle-type particles at different pH. The electron dose rate was $179 \text{ e}^- \text{ nm}^{-2} \text{ s}^{-1}$.



Supporting Movie 5: Gold@water@silica rattle-type particle in 1.00 mM LiCl at different electron dose rates. Electron dose rates shown in video in units of $\text{e}^- \text{ nm}^{-2} \text{ s}^{-1}$.



Supporting Movie 6: Titania@water@silica rattle-type particle at various salt concentrations. The electron dose rate was $45 \text{ e}^- \text{ nm}^{-2} \text{ s}^{-1}$.



Supporting Movie 7: Gold@water@silica rattle-type particle at various salt concentrations. The electron dose rate was $206 \text{ e}^- \text{ nm}^{-2} \text{ s}^{-1}$.



Supporting Movie 8: Four gold@water@silica nanorattles. The top two gold particles are mobile. However, the particle in the middle is attached to the shell and only gets loose due to interactions with the electron beam. The bottom gold particle is mobile but the electron beam is causing it to sometimes stick to the shell wall for a frame. This shows that gold@void@silica nanorattles may sometimes be unstable in pure water due to a flat electric potential within the shell geometry. The electron dose rate was $206 \text{ e}^- \text{ nm}^{-2} \text{ s}^{-1}$.

Frequency-controlled electrophoretic mobility of a particle within a porous, hollow shell

ABSTRACT

The unique properties of yolk-shell or rattle-type particles make them promising candidates for applications ranging from switchable photonic crystals, to catalysts, to sensors. For the switching modality, the core particle may be manipulated by external fields, however, the various physical effects that control its mobility have received only minor attention. Here, we explore the frequency-dependent dynamic electrophoretic mobility of a charged core particle within a charged, porous shell by application of AC electric fields using liquid-phase electron microscopy (LP-EM) and finite-element calculations. For the latter, we solved the Poisson-Nernst-Planck-Stokes equations for a core particle moving in a solvent with ions due to the electric field, without taking Brownian motion of the core particle into account. Despite this, we were successful in describing the main experimental observations of this system. We found that the core exhibited field-driven motion parallel to the electric field direction or diffusive motion orthogonal to the field, or even random motion, depending on the frequency of the applied field. We infer from our experiments and calculations that the transition frequencies between these regimes are determined by the time it takes for ionic gradients to be established within the yolk-shell geometry both by diffusion and electrophoresis. Furthermore, the fact that ions were able to diffuse through the shell was found to significantly impact the core electrophoretic mobility, as it was established by both experiments and the calculations that changing the porosity of the shells strongly influenced the behavior of the core particle. In contrast, the ionic strength did not have a significant effect on the frequency dependence of the mobility regimes, when the salt concentration was varied from 0.2 to 25 mM in the experiments. Lastly, increasing the shell diameter for a fixed core size was found to shift the transition between the parallel and orthogonal motion regimes to lower frequencies. Our results show how electric fields can enhance the use of yolk-shell particles as building blocks

for switchable photonic crystals and illustrate the many experimental parameters that can be tuned to induce different responses of the core particle to the external electric field.

5.1. INTRODUCTION

Colloidal crystals composed of complex building blocks are promising materials for optical,⁵⁵ electrical⁵⁶ and biomedical applications,⁵⁷ just to mention some fields in which these systems find use. Examples of the former are photonic crystals and structural colors based on colloids, which have received considerable interest over the past decade, as evidenced by a selection of papers.^{53,228–239} Soft, colloid-based materials consisting of building blocks with adjustable separation allow for effective tuning of their optical or other properties via external stimuli, such as temperature or ionic strength, or fields, such as electric or magnetic fields. Such tunability has the potential to diversify the applications of colloidal crystals, and has been used to create chemical or biological sensors,^{58,59} displays^{60,61} and structurally colored paints and inks.^{62,63} Control over the spacing and often also the symmetry of colloidal crystals has been achieved by inclusion of thermosensitive polymers^{64,65} combined with a change in temperature or the application of external electric and magnetic fields.^{66,67} However, previously reported switchable colloidal systems required reconfiguration of the building blocks via external magnetic^{68–70} or electric fields.^{19,23,24,71} It is desirable to create photonic materials where the underlying structure, endowing it with mechanical properties, is not changed but the optical properties can still be varied.

Yolk-shell particles, also referred to as ‘rattle-type’ particles, consist of a mobile core particle within a hollow shell.^{33,34,36,240} As such, yolk-shell colloidal crystals are promising soft matter systems for switchable colloidal systems that do not require a structural reconfiguration of the material to change their properties, as the core particle can be manipulated independently of the shell.^{33,34} It was previously shown that the shells can be assembled into a 2D lattice and that the position of the core particles within the structure can subsequently be controlled using an external magnetic field³³ or alternating current (AC) electric field.³⁴ The assembled structures of the yolk-shell particles in the work of Watanabe and coworkers³⁴ had a lattice constant similar to the wavelength of visible light. If the outer shells of these particles are refractive index-matched with the solvent inside and outside these shells, while the cores are not index-matched, these structures should have uniquely switchable optical properties.²² Without applying an external field, the positions of the core particles are randomized within the shell due to Brownian motion, which significantly broadens the Bragg peaks resulting from coherent scattering of the cores, compared to better defined positions of the cores within their shells. An external electric or magnetic field could position dielectric or magnetic cores at better defined locations within their shells and thus sharpen the Bragg peaks. In this work we clarify how an external AC electric field influences the motion and position of the core particle within the shell, using both experiments and theory.

Colloidal particles dispersed in a liquid acquire a surface charge, which attracts an excess of opposite charges in the liquid to form a diffuse electric double layer (EDL) around the particles. Electrophoresis is the motion of charged colloidal particles in a liquid under an external electric field.^{241–245} In steady state, a charged particle moves with a constant velocity due to the balance between the electric field acting on the particle and the viscous resistance slowing the particle down. The associated electrophoretic mobility μ is defined as the ratio

between the particle's electrophoretic velocity \mathbf{U} and the electric field strength $|\mathbf{E}|$

$$\mu = \frac{|\mathbf{U}|}{|\mathbf{E}|}. \quad (5.1)$$

The electrophoretic mobility depends on the zeta potential ζ of the particle, which is defined as the electric potential at the slipping plane,⁷⁵ where the liquid velocity and the particle velocity are the same. If the slipping plane is located at the particle surface, the zeta potential is the same as the surface potential of the particle. For hard particles with low zeta potentials (in the linear response regime) two limiting cases can be identified for the electrophoretic mobility. When the particle radius a is much greater than the Debye screening length κ^{-1} ($\kappa a \gg 1$) the electrophoretic mobility μ is given by Smoluchowski's equation²⁴⁶

$$\mu = \frac{\epsilon_0 \epsilon_r}{\eta} \zeta, \quad (5.2)$$

where ϵ_0 is the permittivity of vacuum, and ϵ_r and η are the relative permittivity and the viscosity of the electrolyte solution, respectively. In the opposite limiting case, where the Debye screening length κ^{-1} is much larger than the particle size, μ is given by Hückel's equation²⁴⁷

$$\mu = \frac{2\epsilon_0 \epsilon_r}{3\eta} \zeta. \quad (5.3)$$

For the case of arbitrary values of κa , μ can be approximated by Henry's equation,²⁴⁸ which bridges the gap between the two limiting cases

$$\mu = \frac{\epsilon_0 \epsilon_r}{\eta} \zeta f(\kappa a), \quad (5.4)$$

where $f(\kappa a)$ is Henry's function,²⁴⁸ which has limiting values of $2/3$ and 1 for $\kappa a \ll 1$ and $\kappa a \gg 1$, respectively.

When working with alternating current (AC) electric fields, the electrophoretic mobility becomes a function of time and is described using both a magnitude and a phase. The dynamic electrophoretic mobility of the particle is then expressed as

$$\mu = |\mu| e^{i\theta}, \quad (5.5)$$

where $|\mu|$ is the magnitude of the dynamic mobility and θ is the phase angle, which accounts for the response lag between the colloid's mobility and the electric field. In general, the magnitude and phase of the dynamic electrophoretic mobility of a colloidal particle depends on the frequency of the applied electric field, as well as on the particle's surface potential and the thickness of the double layer, represented by κ^{-1} . This is due to the distortion of the electric double layer of the particle caused by the external electric field and the relaxation processes associated with this deformation, as discussed in the original work of Overbeek.²⁴¹

When discussing the time-dependent response of the particle velocity to an external electric field it is important to understand the several relevant time scales. The time scale for which changes in the distribution of charges in the EDL near the particle's surface is described by the Maxwell-Wagner electrolyte relaxation time, which for a non-conducting particle with a low surface conductivity is given by^{249,250}

$$\tau_{\text{MW}} = \frac{1}{\kappa^2 D_{\text{eff}}}, \quad (5.6)$$

where $D_{\text{eff}} = \frac{2D^+D^-}{D^++D^-}$ is the effective diffusivity of the ions in the solution, which follows from electroneutrality. The second time scale relevant to our problem is the time it takes to establish electrolyte concentration variations throughout the solvent in the shell.^{249, 250} This time scale is controlled by diffusion relaxation and for our system is given by

$$\tau_D = \frac{a_{\text{shell}}^2}{D_{\text{eff}}}, \quad (5.7)$$

where a_{shell} is the inner shell radius. Since this time scale governs the relaxation of the electrolyte concentrations throughout the yolk-shell geometry, it stands to reason that it is the most vital to this work. This time scale τ_D is the time required for ionic migrations around the particle to establish a gradient of neutral electrolyte around the particle, which is known as concentration polarization.²⁴⁹ This also leads to a compression of the EDL on one side of the particle, and an expansion of the EDL on the other side. Furthermore, we introduce the time scales for colloidal particles and ions to move over the shell radius. The time scale associated with a colloidal particle to move over the shell radius electrophoretically is given by

$$\tau_{e,p} = \frac{a_{\text{shell}}}{\mu|\mathbf{E}|}. \quad (5.8)$$

The time scale associated with ions moving over the shell radius electrophoretically is given by

$$\tau_{e,i} = \frac{a_{\text{shell}}}{\mu_{i,\text{eff}}|\mathbf{E}|}, \quad (5.9)$$

where $\mu_{i,\text{eff}} = \frac{2\mu_i^+\mu_i^-}{\mu_i^++\mu_i^-}$ is the effective electrical mobility of the ions in the solution and $\mu_{i,\pm} = \lambda_{\pm}/F$, where λ is the molar ionic conductivity and F the Faraday constant.

In previous works, the dynamic electrophoresis of a free colloidal particle was investigated both experimentally^{251, 252} and theoretically.^{241, 250, 253, 254} Much less theoretical studies of the electrophoretic mobility of charged spherical objects within a spherical cavity have been conducted.^{255–263} Specifically, Lee *et al.* calculated the electrophoretic mobility for a charged particle centered in a cavity (having the same charge and twice the size).²⁵⁶ These authors found that the electrophoretic mobility was enhanced compared to the mobility of a free particle when $\kappa a \gg 1$. This was also found in the calculations for dynamic electrophoresis by Tung and coworkers.²⁵⁸ The increased mobility was attributed to the electric-field induced flow near the inner cavity wall, which contributes positively to the velocity of the particle inside the cavity. When $\kappa a \ll 1$ the mobility of the core particle instead reduced due to the overlap of the double layers surrounding the particle and the inner cavity surface. Lee and coworkers have additionally considered the impact of the core-cavity size ratio on the electrophoretic mobility of the core, as well as the influence of the core's position with respect to the shell.²⁶³ They found that the mobility of the particle was sensitive to parameters such as the particle-to-cavity size ratio, the relative position of the particle within its cavity, and the particle-to-cavity charge ratio.

In our theoretical investigation, we drew inspiration from the above studies. However, there are several important differences; (i) our core particle is not stationary, and (ii) ions can migrate through the porous shell, which was found to be important both from experiments and

through calculations. We account for the former in our numerical simulations by updating the position of the core at each time step and imposing its present velocity as the hydrodynamic boundary condition, see the Methods section and Supplementary Information for details. The latter requires a model for ion migration through a porous shell, for which we chose to model a reduced diffusivity of ions through the porous shell compared to their bulk diffusivity, which will be discussed in more detail below. It is good to mention that in experiments, contrary to the aforementioned theoretical studies, the particle also performs Brownian motion, which means it diffuses within the spherical hollow shell.^{34,264} A particle within a shell is able to diffuse around if the electrostatic repulsion is sufficient to keep the particle from sticking to the shell wall by van der Waals interactions.²⁶⁴ Furthermore, the hydrodynamics of a spherical particle within a spherical confining geometry complicates the dynamics further as it makes the diffusion coefficient of the core particle spatially different, reducing its value the closer it gets to the inner wall of the shell.^{161, 162, 264} Combining diffusion of a spherical particle, colloidal interactions and driven particle motion *via* an external electric field inside porous shells has hardly been studied either experimentally and theoretically. However, in an earlier collaboration between our groups, the work of Watanabe and coworkers already showed interesting phenomena for a diffusing colloidal particle in a shell with an external electric field applied.³⁴ In that work it was observed that the core particles (radius 170 nm) moved around within the confines of the spherical hollow shell (inner radius 370 nm, shell thickness 40 nm) in water without added salt due to Brownian motion when no electric field was applied. However, the particles were more strictly confined to the center of the shell when an electric field of $50 - 150 \text{ V mm}^{-1}$ with a frequency in the 1 kHz range was applied.

In this study, we elaborate on the work of Watanabe *et al.*³⁴ and investigate how the diffusive behavior of a diffusive core particle within a porous shell is modified by an external driving AC electric field using both liquid-phase electron microscopy (LP-EM) experiments and finite-element calculations. Recent liquid-phase electron microscopy results have shown that Brownian motion of particles^{163, 179} and interactions resulting from the overlap of EDLs that form next to charged surfaces in contact with a liquid can be observed at low enough electron dose rates where the effects of the electrons could be neglected.²⁶⁴ For this study, we employed yolk-shell particles consisting of a silica core within a silica shell that were synthesized via the methods described in the work of Watanabe and coworkers.³⁴ These particles were specifically chosen as they have dimensions that are of interest for colloidal crystals with optical applications.³⁴ While applying an external AC electric field, we observed the particles using liquid-phase electron microscopy, yielding nanometer resolution⁹¹ and information at the single particle level. The influence of important parameters such as frequency, salt concentration, shell thickness and porosity, and inner shell diameter were systematically explored while keeping the core particles constant. We observed that the core particles moved parallel to and mostly driven by the electric field at low frequencies, while the cores moved diffusively mostly in the direction orthogonal to the electric field at intermediate frequencies. At high frequencies, the motion of the core particles resembled Brownian motion that seemed unaffected by the time-varying electric field. While the frequency-dependent diffusive and driven particle motions of the core particle did not change significantly for LiCl

salt concentrations between 0.2 and 25 mM, the shell porosity was found to have a strong effect. In addition, the experimental results were compared to finite-element calculations. In our model we solve the Poisson-Nernst-Planck-Stokes equations for a charged core particle in a porous, charged shell within a reservoir when an AC electric field is applied. The diffusion, convection and electromigration of ions is calculated and updated in each time step for the electrophoretically moving particle so that the redistribution of the ions throughout the yolk-shell geometry is taken into account. The core particle starts in the middle of the shell and as mentioned does not move *via* Brownian motion but *does* move due to electric and viscous forces, which allows us to make comparisons to our experimental data. It also makes it possible to make optimal use of the symmetry of the problem, while still catching most relevant phenomena as observed in the experiments as is detailed in the following. Our study highlights the important parameters determining the intriguing and complex frequency-dependent way a charged particle behaves when enclosed inside a shell porous for ions when driven by an external AC electric field. Knowledge of these parameters and the different ranges of behavior of the core particle is of importance for optimal design of future switchable particle materials, such as photonic crystals, built up from yolk-shell building blocks.

5.2. METHODS

5.2.1. Liquid-phase electron microscopy experiments

In order to image the rattles in the electron microscope, we used a liquid-flow TEM holder with biasing capabilities (Protochips Poseidon Select, Protochips Inc., USA) and microchips with platinum electrodes. The microchips support 50 nm thick amorphous silicon nitride (SiN_x) windows with lateral dimensions of 50 by 200 μm^2 . The spacer on one of the chips was 1000 nm in height. The two Si chips were glow-discharged (Cressington Power Unit 208) for 1 minute prior to the experiment in order to make their surfaces more hydrophilic. The microchip with spacer was then placed in a dedicated holder. A 1 μL droplet of the dispersion (particle volume fraction approximately 0.1 vol%) was dropcasted onto the microchip. The second microchip with the platinum electrodes was placed on the bottom chip with the hydrophilic side facing the opposite chip. Two of the platinum electrodes were extending on the silicon nitride window of the chip and were spaced 30 μm apart and are 75 nm thick. Some rattle particles stuck to the top window with their shells in between the electrodes, which allowed them to be imaged with the highest resolution and better defined electric field.

The liquid-phase STEM experiments were carried out using a transmission electron microscope (Tecnai 20F, Thermo Fischer Scientific), equipped with a field emission gun, and operating at 200 kV. The semi-convergence angle of the electron probe was 10 mrad. The annular dark-field (ADF) detector was used with a camera length of 120 mm. Image series were acquired with TEM imaging & analysis software (TIA). A frame recording time of 1 s was used. For a typical experiment the number of pixels was 512 \times 512, with a pixel size of 8.8 nm. The screen current was measured to be 3.3 nA. These settings resulted in an electron dose rate of 45 $\text{e}^- \text{nm}^{-2} \text{s}^{-1}$. Some slight deviations in those settings in different experiments did not lead to different behaviour of the core particles. For each frequency of the electric field an image series of 15 to 60 seconds was recorded with a frame time of 1 s. After applying

an electric field of a certain frequency, the field was turned off for at least 20 seconds before an electric field with a different frequency was applied.

The electric field was applied via a Gamry Potentiostat 600+. It was connected in a two electrode configuration to the two electrodes on the electron-transparent window of the chip. A voltage of 3 V was applied which resulted in an electric field of 100 V mm^{-1} (within 5% error, Figure A7) between the two electrodes which were spaced $30 \mu\text{m}$ apart. The imaged particles were attached to the same window as the electrodes and were positioned approximately in the center between the two electrodes to avoid as best as possible electrode polarization effects. The AC electric field was applied for 15–60 seconds to observe the motion of the core particle at a particular frequency. The same aqueous LiCl solution that was already present in the liquid cell was flowed at $2 \mu\text{L/min}$ to avoid bubble formation during electric field application and remove electro-chemical reaction products. Some experiments were performed without flow and the resulting motion of the core particle was observed to be unchanged. The salt concentration within the liquid-cell geometry was changed by flowing in a given aqueous LiCl solution for at least 15 minutes before any electric field experiments were performed. It was confirmed that the new salt concentration was present within the shell by observation of how close the particle could approach the shell.²⁶⁴

5.2.2. Finite-element calculations

We performed finite-element calculations using COMSOL Multiphysics (V5.4). We used an axisymmetric calculation domain to stabilize and speed-up our calculation. Two separate calculations were done. First a calculation was performed in which the colloidal particle was not moving, to acquire the equilibrium EDLs in the yolk-shell geometry, without an electric field, for the case where the core particle was situated in the middle of the yolk-shell geometry. Subsequently, a time-dependent study was performed to calculate the evolution of the ion distribution, fluid flow, and electric potential, as well as the position of the core particle in time. The fluid was assumed to be incompressible and its dynamics captured by the creeping flow form of the Navier-Stokes equations, that is, friction dominates inertia and the Reynolds number is much smaller than unity. Electromigration, convection, and diffusion of ionic species were accounted for using a combination of the Poisson equation and Nernst-Planck equation. The governing equations of the problem are then the following:

$$\nabla^2 \phi = -\frac{\rho_c}{\epsilon_0 \epsilon_r} = -\sum_{j=1}^2 \frac{e z_j n_j}{\epsilon_0 \epsilon_r} = \frac{e(n_- - n_+)}{\epsilon_0 \epsilon_r}, \quad (5.10)$$

$$\frac{\partial n_j}{\partial t} = -\nabla \cdot \left(-D_j \left(\nabla n_j + \frac{e n_j z_j}{k_B T} \nabla \phi \right) + n_j \mathbf{u} \right), \quad (5.11)$$

$$\nabla \cdot \mathbf{u} = 0, \quad (5.12)$$

$$\rho_{\text{fluid}} \frac{\partial \mathbf{u}}{\partial t} = -\nabla p + \eta \nabla^2 \mathbf{u} - \rho_c \nabla \phi. \quad (5.13)$$

In these equations ∇^2 is the Laplace operator, ϕ is the electric potential, ρ_c is the space charge density, ϵ_0 is the permittivity of free space, ϵ_r is the relative permittivity of the liquid, e is the elementary charge, and n_j is the number density of ionic species j . Furthermore, ∇

is the gradient operator, D_j is the diffusion coefficient of ionic species j , \mathbf{u} is the velocity of the fluid and t is time, while ρ_{fluid} and η are the fluid density and viscosity, respectively, and p is the pressure. Note that we chose to limit the number of charged species to two, both of which are monovalent.

We assumed that the surface conductivities of the particle and shell were negligible. Furthermore, the dielectric constant of silica ($\epsilon_r = 3.8$) is much smaller than that of water ($\epsilon_r = 78.4$). Therefore, a constant surface charge density σ boundary condition on the surface of the core particle, as well as on the inner and outer surface of the shell was used.

We assumed a no-slip boundary condition on the surface of the core particle as well as the inner and outer surface of the shell. The fluid velocity on the particle's surface was the same as the velocity of the particle. This leads to the boundary conditions:

$$\mathbf{u} = \mathbf{U}, \quad r = a_{\text{particle}}, \quad (5.14)$$

$$\mathbf{u} = 0, \quad r = a_{\text{shell}}, \quad (5.15)$$

$$\mathbf{u} = 0, \quad r = a_{\text{shell}} + t_{\text{shell}}, \quad (5.16)$$

where \mathbf{U} is the velocity of the particle, a_{particle} the particle radius, a_{shell} the inner shell radius, and t_{shell} the shell thickness. Furthermore, the surface of the particle was impermeable to ions, so that

$$(\mathbf{f}_j - n_j \mathbf{u}) \cdot \hat{\mathbf{n}} = 0, \quad r = a_{\text{particle}}, \quad (5.17)$$

where $\mathbf{f}_j = -D_j(\nabla n_j + (en_j z_j / k_B T) \nabla \phi) + n_j \mathbf{u}$ is the concentration flux of ionic species j and $\hat{\mathbf{n}}$ is the unit normal to the particle surface. The shell was not impermeable to ionic species in the experiments. In our model the shell has a porosity Φ_p and it is therefore possible for ions to diffuse through. The diffusivity of ion species j through the shell $D_{s,j}$ is related to the bulk diffusivity of that ion species D_j via

$$D_{s,j} = \Phi_p D_j. \quad (5.18)$$

Furthermore, the dielectric constant of the shell $\epsilon_{r,s}$ is related to the dielectric constant of water $\epsilon_{r,\text{water}}$ and that of silica $\epsilon_{r,\text{silica}}$ as

$$\epsilon_{r,s} = \Phi_p \epsilon_{r,\text{water}} + (1 - \Phi_p) \epsilon_{r,\text{silica}}. \quad (5.19)$$

The electrophoretic mobility of the particle μ can be expressed as

$$\mu = \mu_R + i\mu_I = \frac{\mathbf{U}}{\mathbf{E}}, \quad (5.20)$$

where $\mathbf{U} = U_R + iU_I$ is the complex particle velocity and $\mathbf{E} = E_z e^{-i\omega t}$ is the external electric field. The velocity of the particle is determined by the electric force and the hydrodynamic drag force acting on it via Newton's second law of motion²⁵⁰

$$\mathbf{F}_e + \mathbf{F}_h = \frac{4}{3} \pi a_{\text{particle}}^3 (\rho_{\text{particle}} - \rho_{\text{fluid}}) \frac{d\mathbf{U}}{dt}, \quad (5.21)$$

where ρ_{particle} is the density of the particle. Immediately after applying an electric field, a colloidal particle starts an accelerated motion.²⁴⁹ The viscous friction leads to a constant

velocity after a time given by the time scale^{249,250}

$$\tau_H = \frac{\rho_{\text{fluid}} a_{\text{particle}}^2}{2\eta}. \quad (5.22)$$

This time scale for our particle of $a_{\text{particle}} = 170$ nm in water is approximately 14 ns (Supporting Figure A13). We stress that the acceleration term is negligible after this initial acceleration period and has a negligible influence on the overall dynamics, as expected for a particle in a fluid at low Reynolds number. Often this is accounted for in modeling by setting the right-hand side of Equation 5.21 to zero, i.e., neglecting the inertia completely, and solving directly for the particle velocity from the hydrodynamic friction. We chose not to make this reduction here, as this would have complicated our numerical solving strategy.

The electric force and hydrodynamic drag force were obtained by integrating the electric and hydrodynamic stress tensor over the surface of the particle, respectively.

$$\mathbf{F}_h = \oint_S \mathbf{T} dS \quad (5.23)$$

$$\mathbf{F}_e = \oint_S \mathbf{M} dS. \quad (5.24)$$

As water was the suspension medium and Stöber-like silica was the material for the shell and core particles in this study, we used the following material parameters: the relative permittivity of the water $\epsilon_r = 78.4$, the relative permittivity of silica $\epsilon_r = 3.8$, the viscosity of the fluid $\eta = 1$ mPa·s, the density of the fluid $\rho_{\text{fluid}} = 1$ g cm⁻³, the density of the core particle $\rho_{\text{particle}} = 2$ g cm⁻³, the temperature $T = 293.15$ K and the ionic diffusivities²⁶⁵ $D_{Li} = 1.022 \cdot 10^{-9}$ m²s⁻¹ and $D_{Cl} = 2.037 \cdot 10^{-9}$ m²s⁻¹.

5.3. RESULTS & DISCUSSION

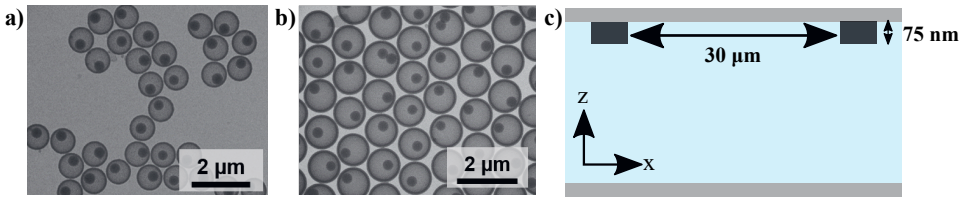


Figure 1: a) Bright-field TEM image of yolk-shell particles consisting of a silica core particle ($a_{\text{particle}} = 170$ nm) within a silica shell (inner radius $a_{\text{shell}} = 370$ nm, thickness $t_{\text{shell}} = 40$ nm). b) Bright-field TEM image of yolk-shell particles consisting of a silica core particle ($a_{\text{particle}} = 170$ nm) within a silica shell (inner diameter $a_{\text{shell}} = 496$ nm, thickness $t_{\text{shell}} = 55$ nm). c) Schematic representation of the liquid-cell geometry in the experiments. The 75 nm thick platinum electrodes were on the top window of the liquid cell and were spaced 30 micron apart. The particles under investigation were located on the top window, approximately in the center between the two electrodes.

5.3.1. Frequency-dependent mobility of the core particle

Liquid-phase electron microscopy experiments were performed to capture the frequency-dependent motion of negatively charged silica core particles within porous, negatively charged silica shells (Figure 1a-b). The particles were synthesized as described in the work of Watanabe and coworkers.³⁴ In short, particles were loaded between two microchips within a commercial liquid-cell holder. The top microchip contained 75 nm thick platinum electrodes spaced 30 μm apart that were used to apply an electric field (Figure 1c). We mostly imaged the yolk-shell particles that were in the middle between the electrodes with the shell attached to the top chip, so that a uniform electric field could be applied with minimal effects of electrode polarization (Figure A7).

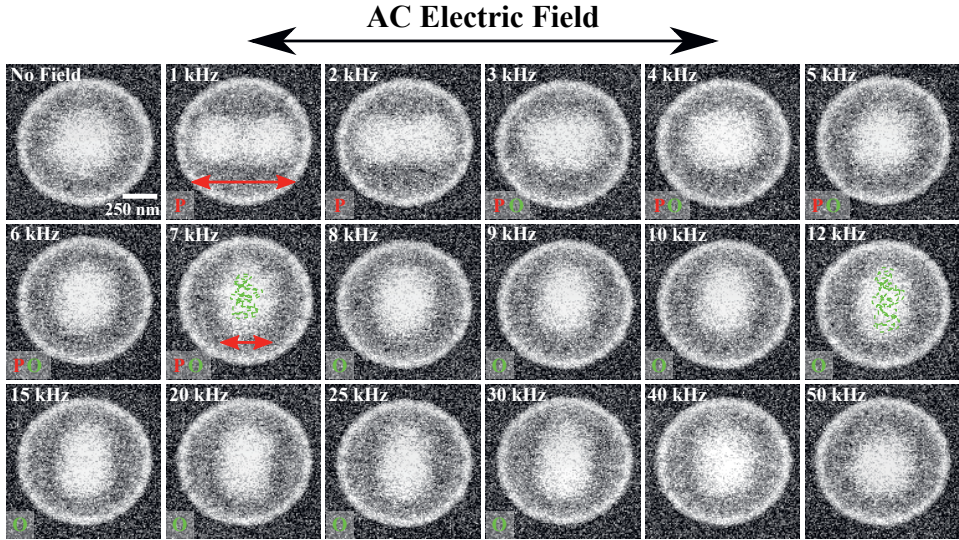


Figure 2: Frequency-dependent mobility of a core particle ($a_{\text{particle}} = 170 \text{ nm}$) within a shell (inner radius $a_{\text{shell}} = 370 \text{ nm}$, thickness $t_{\text{shell}} = 40 \text{ nm}$) under application of a 100 V mm^{-1} AC electric field in aqueous solution of 2.00 mM LiCl. The electron dose rate was $45 \text{ e}^- \text{ nm}^{-2} \text{ s}^{-1}$. The bright area within the shell indicates the part of the cavity that was explored by the core over a 50 s period as observed in Supporting Movie 1. The images here are cropped from the total movie that was 512 by 512 pixels, with a pixel size of 8.75 nm. The frame time was 1 s. At lower frequencies the core was driven by and parallel (P) to the electric field as indicated by the red arrow. At intermediate frequencies (3 – 30 kHz) the core diffused orthogonal (O) to the electric field as indicated by the light green dashed paths. At higher frequencies ($> 40 \text{ kHz}$), there was no significant influence of the electric field.

First, the motion of a core particle (radius $a_{\text{particle}} = 170 \text{ nm}$) within a hollow silica shell (inner radius $a_{\text{shell}} = 370 \text{ nm}$, thickness $t_{\text{shell}} = 40 \text{ nm}$) was observed in an aqueous solution of 2.00 mM LiCl ($\kappa a_{\text{particle}} \approx 26$) using liquid-phase scanning transmission electron microscopy (STEM). The electron dose rate was $45 \text{ e}^- \text{ nm}^{-2} \text{ s}^{-1}$. Figure 2 shows the projected area that the core particle explored within 50 seconds of recording time, when an AC electric field of the

indicated frequency was applied at an electric field strength of 100 V mm^{-1} . Three frequency-dependent regimes were observed, which is best appreciated in Supporting Movie 1. When no field was applied, the cores were seen to explore a certain part of the shell geometry *via* thermal fluctuations constrained by the equilibrium double layers of the core and the shell. When a low frequency electric field of 2 kHz or lower was applied, the motion of the core was driven by the field in a direction parallel to the electric field. The particle was driven from one side of the shell to the other, while the Brownian displacements were suppressed. From 3 to 7 kHz the mostly field-driven core motion gradually changed to diffusive motion orthogonal to the electric field. Supporting Movie 1 shows that in the regime from 3 to 7 kHz there was still a significant displacement of the core in the parallel direction driven by the electric field. However, with increasing frequency the displacement in the parallel direction decreased in magnitude from around 350 nm for 1 – 2 kHz to 120 nm for 7 kHz, and further reducing to 40 nm at 20 kHz. The motion was always centered around the middle of the shell. It was also observed that the diffusive motion in the orthogonal direction gradually increased from 3 to 7 kHz. As mentioned, the motion orthogonal to the electric field was not driven by the electric field, as was the case for the parallel motion. Instead the motion was diffusive-like, which is most readily appreciated from Supporting Movie 1. Apparently, the electric field prevented the core to move away from the center in the direction parallel to the field, which hints at changed ionic double layer interactions due to the electric field. At even higher frequencies, greater than 40 kHz, the core showed diffusive behaviour indistinguishable from when no electric field was applied. The experiments thus revealed several regimes for both directly driven and more diffusive displacements of the core particles in different directions.

Finite-element calculations using COMSOL MultiPhysics were used to provide understanding of the experimental observations. Full details are given in the Methods section and Supporting Information. In short, we solved the coupled equations for fluid dynamics, ionic transport, and electric potential within the yolk-shell geometry. First a calculation for which the colloidal particle did not move was performed to acquire the equilibrium EDLs in the yolk-shell geometry, without an electric field for the case where the core particle was situated in the middle of the yolk-shell geometry. Subsequently, a time-dependent study was performed to calculate the evolution of the ion distribution, fluid flow, and electric potential, and the position of the core particle in time (as calculated from the electric and hydrodynamic forces acting on the particle) during the application of three AC electric field cycles of various frequencies. Because the particle moved during the time-dependent study, the electrophoretic velocity is dependent on both time and position.

In the calculations, for an ionic strength of $I = 2 \text{ mM}$ we used constant surface charge density boundary conditions ($\sigma = -6.3 \text{ mC m}^{-2}$) for the core and the shell, which resulted in a surface potential of -50 mV for the core and -40 mV for the shell. These were roughly in line with measurements of the zeta potential (Supporting Information) and literature values for the zeta potential of Stöber silica particles.²⁶⁶ We should mention that there is an inherent difficulty in measuring the zeta potential of core particles inside shells, as well as the zeta potential of the inner surface of a shells. This is because common techniques such as electrophoretic light scattering cannot easily be used.

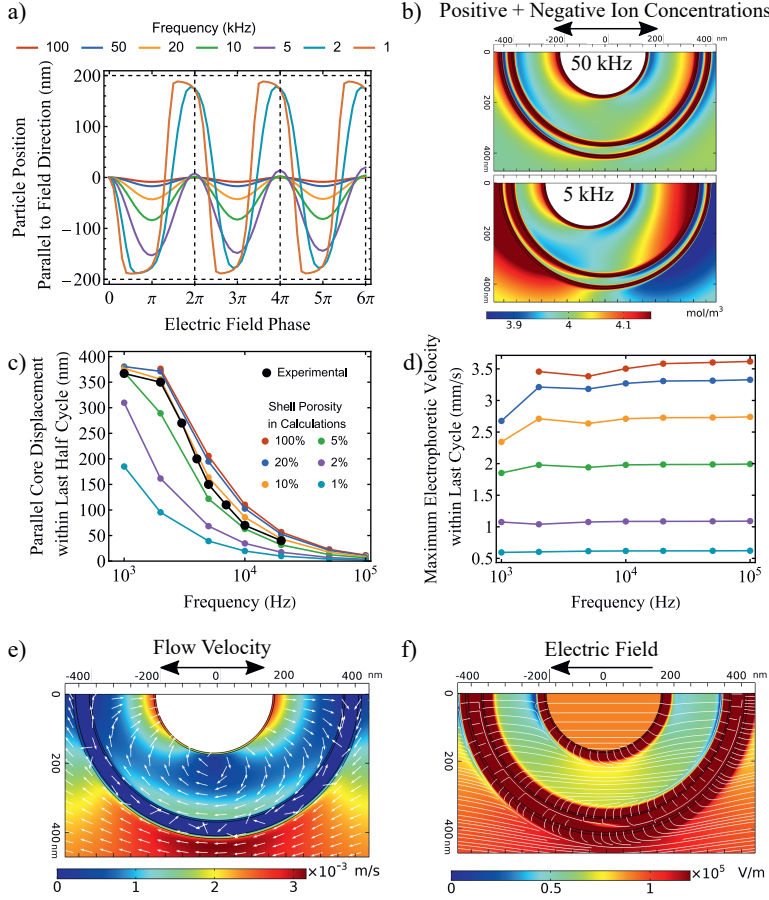


Figure 3: Calculated frequency-dependent mobility of a core particle ($a_{\text{particle}} = 170$ nm, surface potential $\phi = -50$ mV) within a shell ($a_{\text{shell}} = 370$ nm, $t_{\text{shell}} = 40$ nm, surface potential $\phi = -40$ mV) during 100 V mm^{-1} AC electric field application in aqueous solution of 2 mM ionic strength. a) The particle position in time during 3 cycles of the electric field for different frequencies. The porosity of the shell was taken to be 10%. The horizontal dashed lines show the position for which the particle would touch the inner shell wall. b) Concentration of positive plus negative ions after 2.75 cycles of the electric field (5.5π) at 50 and 5 kHz. The double-headed arrow indicates the electric field direction. c) Parallel displacement of the core particle within the last half cycle of the electric field as function of frequency for different shell porosities. A porosity of the shell of 10% results in a core mobility that very closely resembles the experimental mobility of the core particles. d) The maximum electrophoretic velocity of the core particle as function of frequency for different shell porosities. e-f) Flow velocity and electric field after 2.75 cycles of the electric field (5.5π) at 50 kHz. The single-headed arrow in f corresponds to the electric field direction at that point in time.

Figure 3a shows the evolution of the particle position for three cycles of the electric field for different frequencies when a shell porosity of 10% is assumed. In these calculations, the porosity of the shell Φ_p is assumed to determine the diffusivity of ion species j through the shell $D_{s,j}$ compared to the bulk diffusivity of ions D_j as

$$D_{s,j} = \Phi_p D_j. \quad (5.25)$$

While experimentally the actual diffusion coefficient of ions through the shell is unknown, Equation 5.25 allows us to investigate how the porosity of the shell influences our system. For the highest frequency fields, the variation of the field was still sufficiently slow for the particle to track the electric field.²⁵⁰ However, at these frequencies, the electric field switches so fast that the particle moves only a few nanometer, before the electric field changes direction. As such, no interesting behaviour is observed at the highest frequencies (50 – 100 kHz).

At 5 kHz, the particle did not return exactly to the same position after a full electric field cycle was completed. Instead, the particle, while showing sinusoidal behaviour (Figure 3a), also on average moves back to the middle of the yolk-shell geometry. This is likely due to concentration polarization, which disturbs the equilibrium ion concentrations within the yolk-shell geometry (Figure 3b). The time needed for this phenomenon to occur within our system is associated to the time scale associated with diffusive motion of ions over the shell radius $\tau_D \approx 1.0 \cdot 10^{-4}$ s, which corresponds well with a frequency of 5 kHz. The time scale associated with electrophoresis of ions (molar ion conductivities²⁶⁷ 38.6 and $76.4 \Omega^{-1}$ for Li^+ and Cl^- , respectively) over the shell radius for a field strength of 100 V mm^{-1} , $\tau_{e,i} \approx 6.2 \cdot 10^{-5}$ s, also agrees well with the frequencies at which we see significant disturbances in the equilibrium ion concentrations. Figure 3b indeed shows that the changes in the ion concentrations within the shell are more significant for 5 kHz than for 50 kHz, even though changes already occur at 50 kHz. We revisit the trend of the particle migrating back to the middle of the yolk-shell geometry at 5 kHz in more detail later.

For 1 kHz the particle has enough time before the electric field changes direction to closely approach the inner shell wall. At that point the electric double layers of the particle and the inner shell wall overlapped significantly, which did not allow the particle to move further. The particle trajectory at 1 kHz was therefore not symmetric (Figure 3a), as the particle nearly arrested close to the shell, until the field reversed direction. This also explains why the core particle attained a smaller maximum speed for 1 kHz than for higher values of the frequency (Figure 3d) as the particle was arrested near the particle shell before the electric field reached its maximum strength. The particle moving from one side of the shell to the other for a frequency of 2 kHz or lower corresponds relatively well to the time scale for electrophoresis of a 170 nm free particle over the shell radius $\tau_{e,p} \approx 1.1 \cdot 10^{-4}$ s. Furthermore, it agrees well with the experimental results that showed the particle moving from one side of the shell to the other for frequencies of 2 kHz or lower (Figure 2).

Figure 3c-d shows that the porosity of the shell has a large influence on the mobility of the core particle within. The porosity of the shell influences the mobility in the calculations in two ways. First, the porosity determines the dielectric constant of the shell by a weighted average between the dielectric constant of water ($\epsilon_r = 78.4$) and silica ($\epsilon_r = 3.8$). Second, it

determines how fast ions are able to migrate through the shell (Eq. 5.25). The time scale for ion diffusion through the shell is

$$\tau_S = \frac{t_{\text{shell}}^2}{D_{\text{s,eff}}}, \quad (5.26)$$

where t_{shell} is the thickness of the shell and $D_{\text{s,eff}}$ is the effective ion diffusion coefficient through the shell. For a 40 nm thick shell with 100% porosity, and therefore $D_{\text{s,eff}} = D_{\text{eff}}$, $\tau_S \approx 10^{-6}$ s. For a porosity of 1% the time scale for ions to migrate through the shell becomes $\tau_S \approx 10^{-4}$ s, which is similar to the diffusion relaxation time τ_D , which we argued in the introduction to control the dynamics of the core. It was found that porosities of 10% and lower can lead to a significantly reduced electric field within the yolk-shell geometry (Figure A9), which can therefore lead to a reduced electrophoretic velocity of the core.

For now, we focus on the calculations for a shell where a porosity of 10% is assumed, which is in best agreement with the experiments (Figure 3c). From Figure 3 it follows that a change in the porosity of the shell leads to a large difference in the mobility of the particle, which necessitates measurement of the porosity of the shell experimentally in the future work, for instance by looking at the time scale for ions to diffuse through the shell experimentally. For a porosity of 10%, the drop in electric field strength within the yolk-shell geometry is mostly caused by the dielectric constant of the shell (Figures 3f and A8). The electric field strength within the shell is approximately 60 V mm^{-1} . Using Smoluchowski's equation (Eq. 5.2) we calculate that a free particle with a zeta potential of -50 mV in a 60 V mm^{-1} electric field would have an electrophoretic velocity of 2.1 mm s^{-1} , which is significantly lower than that of the same particle in the same electric field in the charged shell (2.7 mm s^{-1}). Such a high mobility of a charged particle in a charged cavity was observed earlier in theoretical studies.^{256,258,263} The particle within the charged shell can move faster than a free particle because the flow coming from the EDL originating from the inner shell wall contributes positively to the particle mobility, as shown in Figure 3e. As such, competing effects of the shell porosity and shell EDL contribute to the mobility of the particle. The shell porosity determines the electric field strength inside the cavity, where the EDL originating from the inner shell wall influences the mobility of the particle by induced flows.

To experimentally test whether the diffusion of ions through the shell indeed influenced the observed driven and diffusive core motion patterns, we changed the porosity of the original sample by both etching the shell further and overgrowing the shell with an extra porous silica layer. This is expected to make the shell easier or harder for the ions to diffuse through, respectively. The etched shell showed larger pores within the shell compared to the original sample, while the thicker shell was increased in thickness compared to the shell of the original sample, from 40 nm to 110 nm thickness, as can be appreciated from Figure 4. The extra layer of the shell that was grown should also be less porous as it was not subjected to any etching steps. Figure 4 shows the projected area that the core explored during the application of the electric field at a certain frequency. The sample with extra etched shells showed similar behaviour as the original sample (Figure 2), except that the orthogonal diffusive motion from the original sample was not observed, and the core was instead mostly confined to the center of the etched shell. The parallel mobility at lower frequencies was the same as for the original

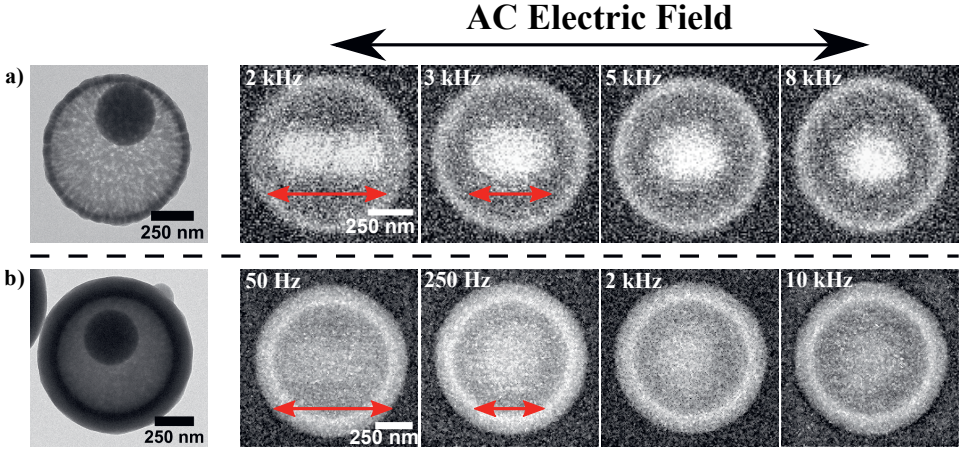


Figure 4: Frequency-dependent mobility of a core particle ($a_{\text{particle}} = 170 \text{ nm}$) within a more porous ($t_{\text{shell}} = 40 \text{ nm}$) (a) or thick ($t_{\text{shell}} = 110 \text{ nm}$) (b) shell under application of a 100 V mm^{-1} AC electric field in aqueous solution of 2.00 mM LiCl . For the etched shell images, the electron dose rate was $148 \text{ e}^- \text{ nm}^{-2} \text{ s}^{-1}$. The pixel size was 8.8 nm , the frame time was 1 s and the total frame was 256 by 256 pixels. For the thick shell images, the electron dose rate was $156 \text{ e}^- \text{ nm}^{-2} \text{ s}^{-1}$. The pixel size was 5.8 nm , the frame time was 1 s and the total frame was 512 by 512 pixels. The images shown are zoom-ins of the original movies. The bright area within the shell indicates the part of the cavity that was explored by the core over a 20 s period as observed in Supporting Movies 2-3. The red arrow indicates that the particle motion is driven by the electric field.

sample. For the thicker shell, the fully parallel motion was only observed when an external electric field of a frequency of 50 Hz was applied. The shift to lower frequencies is in qualitative agreement with the finite-element calculations (Figure 3c). It is likely caused by the lower electric field strength within the shell geometry, possibly also combined with less ions being able to be transported through the shells, which reduced the electrophoretic velocity of the particle within. At higher frequencies no significant orthogonal/suppressed motion was found for the overgrown shell, which is unlike the original sample and the sample with the etched shell. This result can also be explained by the low electric field strength within the shell geometry (Figure A8). When the field inside the yolk-shell geometry is not sufficiently high, the ion concentrations are not significantly disturbed.

5.3.2. Origin of the orthogonal diffusive motion of the core particles

Next we aim to understand the diffusive orthogonal motion of core particles at frequencies around $5\text{-}20 \text{ kHz}$ for the original sample (Figure 2). We performed finite-element calculations for which the core particle was initially placed 100 nm off-center in the direction parallel to the electric field. If the parallel motion is suppressed like in the experiments, we expect the core particle to return to the center of the rattle geometry when the AC electric field is applied.

Figure 5 shows the evolution of the particle position when we placed the particle 100 nm off-center in the direction parallel to the electric field. For all frequencies under consideration the particle moved towards the center. However this effect was largest for the lowest frequency, 5 kHz. The time scale for ion concentrations to be established within the yolk-shell geometry is $\tau_D \approx 1.0 \cdot 10^{-4}$ s. This time scale matches well with those in the frequency range for which the particle motion in the direction parallel to the electric field is suppressed. At these frequencies the ions have enough time to compress/extend the double layers within the yolk-shell geometry.²⁴⁹ From Figure 5 we observe that the particle moves back to the middle of the shell more quickly when it is initially placed at +100 nm from the center, compared to when it is initially placed at -100 nm. This is because the AC electric field first drives the particle in the negative direction, before it directs the particle in the positive direction later in the electric field cycle. As such, when the particle starts at +100 nm the particle is pushed towards the middle initially. A major difference between our numerical calculations and the experiment is that Brownian motion is also present in the latter. To substantiate our claims regarding the mechanisms by which orthogonal motion is achieved, we consider the effects of Brownian motion. The applied field causes the particle to move to the center of the shell in approximately 2 ms, see Figure 5. In contrast, a free particle with a radius of 170 nm moves on average 50 nm in one dimension in 2 ms *via* Brownian motion, which is similar to the distance over which the particle is pushed back by the effects of the electric field. This is an upper bound to the diffusion, as the diffusion of a particle within a shell is reduced compared to that of a free particle (Chapter 3).^{161,162,264} We conclude that the effect of the electric field is strong enough to indeed limit diffusive motion of the core particles in the direction parallel to the electric field.

5.3.3. Influence of ionic strength

Experimentally, three different salt concentrations were used to investigate the influence of the thickness of the equilibrium double layers on the frequency dependence on the core particle motion (Supporting Movies 1, 4, and 5). Figure 6 shows the projected area within the shell that was explored by the core particle at various frequencies of the applied electric field for ionic strengths of 0.200, 2.00, and 25.0 mM ($\kappa a_{\text{particle}} \approx 8, 26, 88$). These concentrations were chosen as the equilibrium EDLs for these concentrations either confine the core particles to the middle of the shell (for 0.200 mM) or allow the core particles to approach the inner shell wall extremely closely (25.0 mM).²⁶⁴ When turning on the AC electric field, we observed similar motion for the core particles for all LiCl concentrations. The core particles exhibited parallel, driven motion at low frequencies (< 3 kHz), orthogonal, diffusive motion at intermediate frequencies (3 – 40 kHz) and random motion at high frequencies (> 40 kHz). An almost identical frequency-dependent motion was observed for all ionic strengths, with only slight differences.

We will now discuss why parallel motion was observed for the core particles at the same range of frequencies for all salt concentrations. Figure 7 shows the calculated and experimental parallel displacement of the core particles as a function of frequency for different salt concentrations. In the calculations we assumed that the core particle had a surface

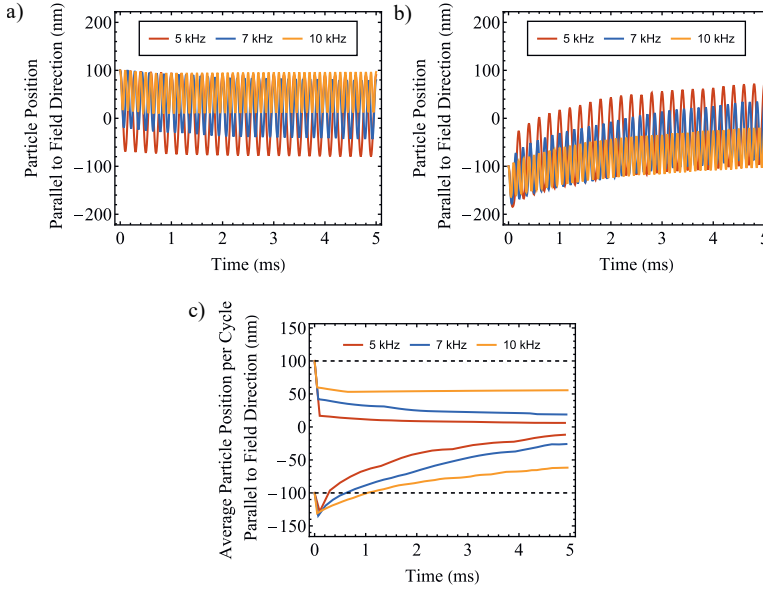


Figure 5: Particle response to the electric field from finite-element calculations at an ionic strength of 2 mM and a shell porosity of 10% when the particle was initially placed off-center in the direction parallel to the electric field. The particle was placed at +100 and −100 nm from the center in a and b, respectively. c) The average position per cycle of the core particle, for the particle starting at +100 and −100 nm from the center. The dashed lines show the particle position when there was no electric field applied (and without Brownian motion). They indicate that equilibrium double layers do not meaningfully push the particle back to the middle in the time scale under investigation. The parameters such as particle size and surface potentials were the same as in Figure 3.

potential of −50 mV for all three salt concentrations. Both the experiments and the finite-element calculations show similar parallel displacement as function of frequency. This is because the Debye lengths are much smaller than the inner shell diameter and the surface potential on the core and the shell are similar for all salt concentrations.

In this study, we did not experimentally investigate the mobility of core particles in pure water without added salt. However, in a previous collaboration between our groups it was observed that in pure water without added salt, core particles were confined to the middle of the yolk-shell geometry for a frequency of 1 kHz while hardly moving in the parallel direction.³⁴ This contrasts sharply with the driven motion from one end of the shell to the other, as observed at 1 kHz for the system with salt. To explain the difference, we calculated the parallel core displacement and maximum electrophoretic velocity for a core particle in 2 μ M salt ($\kappa a_{\text{particle}} \approx 0.8$) and an electric field strength of 100 V mm^{−1}; all other parameters were kept the same as in the other calculations (Figure 7b-c). Our results show that the parallel mobility of the core particle was indeed significantly reduced compared to the experiments in

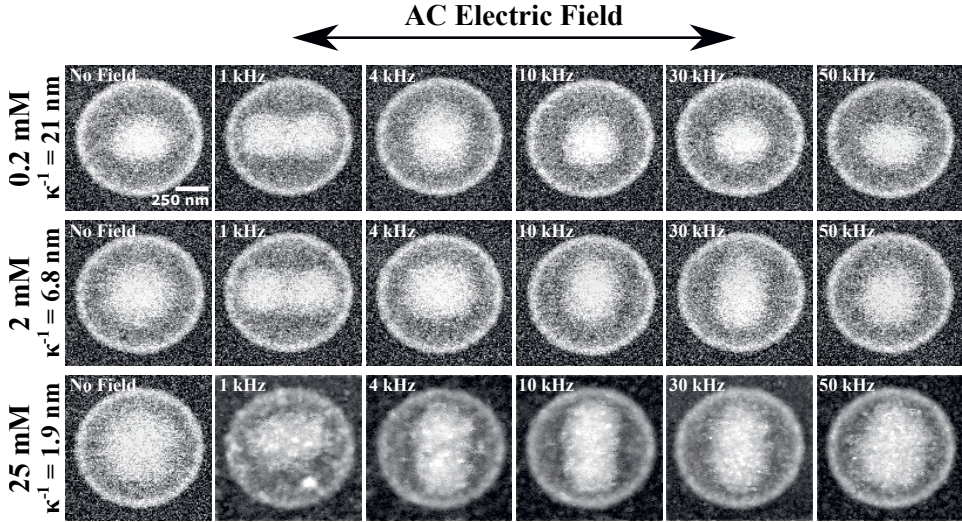


Figure 6: Frequency-dependent displacement and mobility of a core particle within a shell under application of a 100 V mm^{-1} AC electric field for various LiCl concentrations in water. The electron dose rate was $45 \text{ e}^- \text{ nm}^{-2} \text{ s}^{-1}$. The images here are cropped from the total movie that was 512×512 pixels, with a pixel size of 8.75 nm . The frame time was 1 s . The bright area within the shell indicates the part of the shell that was explored by the core over at least a 15 s period as observed in Supporting Movies 1, 4, and 5. The same trend is observed for all salt concentrations. While at lower frequencies the core moves parallel to the electric field, at intermediate frequencies the core moves orthogonal to the electric field. At high frequencies, there is no significant influence of the electric field. The images for 25 mM are cleared up for visibility due to contamination appearing in the sample, especially at low frequency electric fields, as seen in the image for 1 kHz .

this work with higher ionic strength, which may explain why in the low-salt experiments no significant parallel, driven motion was observed at 1 kHz .³⁴

5.3.4. Influence of the inner shell diameter

Lastly, we investigated whether a larger shell would result in different frequency-dependent mobility patterns of the core particle. Figure 8 shows experimental results for the mobility of a core particle ($a_{\text{particle}} = 170 \text{ nm}$) within two different shell sizes (inner radii $a_{\text{shell}} = 370 \text{ nm}$ and $a_{\text{shell}} = 496 \text{ nm}$) and thicknesses ($t_{\text{shell}} = 40 \text{ nm}$ and $t_{\text{shell}} = 55 \text{ nm}$). While the core particle moved parallel at 2 kHz in the smaller shell, it was mostly confined to the middle in the larger shell for this frequency. At a lower frequency of 0.75 kHz , the mobility of the core within the larger shell was completely parallel, similar to the situation for the smaller shell. The transition from orthogonal motion to parallel motion was thus shifted to lower frequencies for a larger shell size. This is due to the longer path that the core particle has to travel in order to reach one side of the shell from the other for a bigger shell.

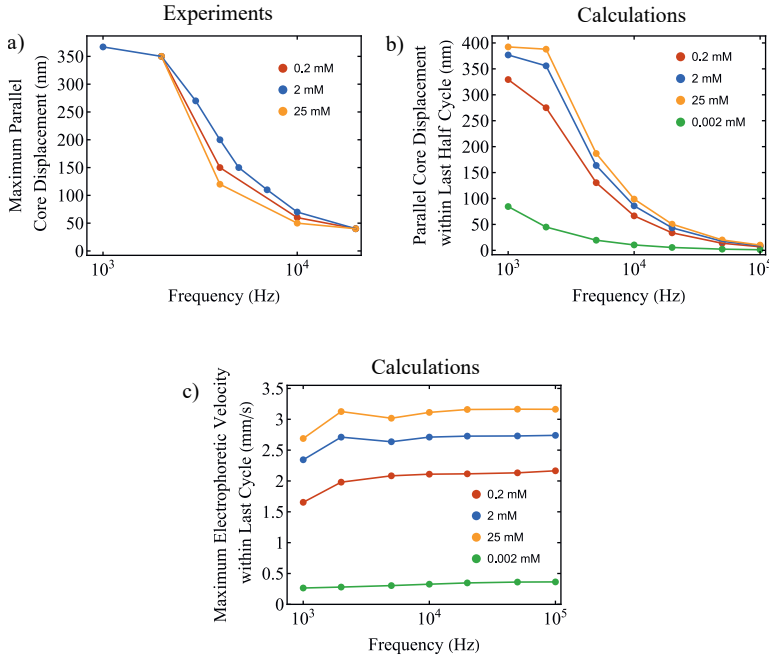


Figure 7: Core particle mobility for different salt concentrations. a) The experimental maximum core displacement parallel to the electric field as obtained from Figure 6 and Supporting Movies 1, 4 and 5. b) The calculated parallel displacement of the core within the last half cycle of the AC electric field for various salt concentrations as function of the frequency of the external AC electric field. c) The maximum electrophoretic velocity within the last cycle of the electric field. For all salt concentrations in the calculations, the core and shell had a surface potential of -50 and -40 mV, respectively. The shell was assumed to have a porosity of 10%.

At a frequency of 10 kHz a particle in the smaller shell only moves diffusively in the direction orthogonal to the electric field, while a particle in the larger shell moves diffusively in all directions (best appreciated in Supporting Movie 6). For a frequency of 4 kHz, however, the particle in the larger shell is confined to only move diffusively in the direction orthogonal to the electric field. The orthogonal motion regime shifting to lower frequencies for the larger shell is likely due to ionic gradients taking longer to be established, due to the larger shell size. This would be in line with our time-scale argument, as τ_D changes from $\tau_D \approx 1.0 \cdot 10^{-4}$ s for the small shell to $\tau_D \approx 1.7 \cdot 10^{-3}$ s for the big shell.

In general, however, the quantitative parallel mobility of the core particles for different frequencies does not match up well with our calculations, even though the increased thickness of the shell was taken into account for the bigger shell (Figure 8c-d). A likely explanation is that the porosity, which is taken the same as that of the small shell at 10%, is overestimated

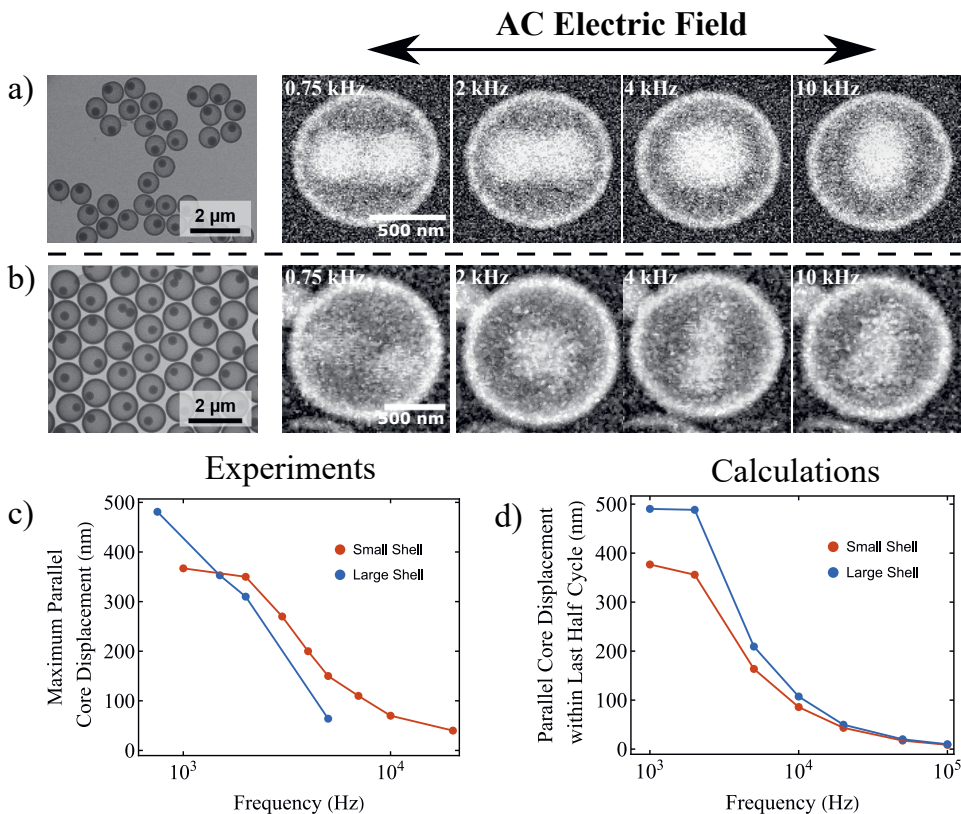


Figure 8: a-b) Frequency-dependent mobility of a core particle ($a_{\text{particle}} = 170$ nm) within a shell under application of a 100 V mm^{-1} AC electric field for a small shell (inner radius $a_{\text{shell}} = 370$ nm, shell thickness $t_{\text{shell}} = 40$ nm) and a bigger shell (inner radius $a_{\text{shell}} = 496$ nm, shell thickness $t_{\text{shell}} = 55$ nm) in 2 mM (aq). For the smaller shell the electron dose rate was $45 \text{ e}^- \text{ nm}^{-2} \text{ s}^{-1}$. The images here are cropped from the total movie that was 512 by 512 pixels, with a pixel size of 8.75 nm. The frame time was 1 s. For the larger shell the electron dose rate was $20 \text{ e}^- \text{ nm}^{-2} \text{ s}^{-1}$. The images are cropped from the total movie that was 512 by 512 pixels, with a pixel size of 12.2 nm. The frame time was 1 s. The bright area within the shell indicates the part of the cavity that was explored by the core over at least a 15 s period as observed in Supporting Movies 1 and 6. c) Experimental parallel displacement of the core particles in small and big shells as function of frequencies. d) Parallel displacement of the core particle in the last half cycle of the electric field in finite-element calculations. The porosity of the shell in the calculations was 10% in both cases and the sizes of the cores and shells were taken the same as the experimental systems. For both the smaller and larger shell, the surface potential of the core was -50 mV and the surface potential of the shell was -40 mV.

in our calculation for the larger shell. Such an overestimate would result in larger parallel motion for the core particle than observed in the experiments.

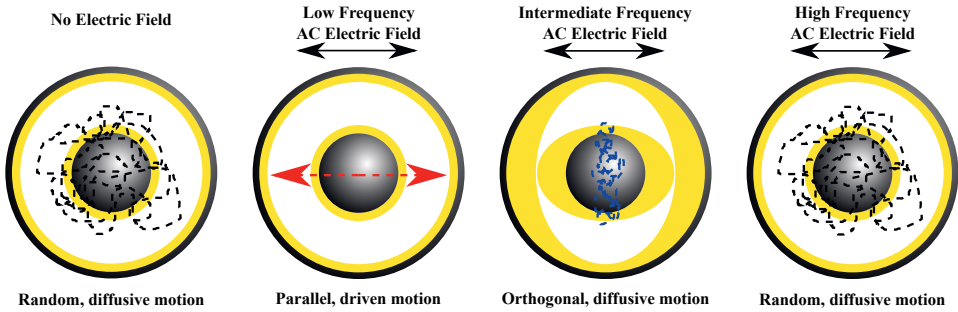


Figure 9: Summary of electrodynamic regimes describing the observed mobility of the core particle within a yolk-shell geometry. When no electric field is applied, the core particle exhibits Brownian motion constricted by the double layers of the core and the shell. At lower frequencies compared to the relaxation time of the ions inside the liquid the core particle has enough time to move from one side of the shell to the other. At intermediate frequencies the ion distributions are significantly affected which results in orthogonal, diffusive motion and extended repulsions between cores and shells. At higher frequencies the electric field can influence the double layers slightly, but not sufficiently to change ionic concentrations within the whole shell geometry, which results in the particle exploring the same part of the shell diffusively as when no field was applied.

5.4. CONCLUSION

In summary, we studied the frequency-dependent mobility of a core particle within a shell subjected to an AC electric field. The observed types of motion exhibited by the cores are recapped in Figure 9. For a core ($a_{\text{particle}} = 170 \text{ nm}$) in a shell ($a_{\text{shell}} = 370 \text{ nm}$, $t_{\text{shell}} = 40 \text{ nm}$) random motion of the cores was observed at high frequencies ($> 40 \text{ kHz}$), predominantly orthogonal diffusive motion was observed at intermediate frequencies ($3 - 40 \text{ kHz}$) and driven, parallel motion was found at low frequencies ($< 3 \text{ kHz}$). The orthogonal diffusive motion of the cores was shown to be due to the establishment of ionic gradients within the yolk-shell geometry limiting parallel excursions, while the parallel motion was directly driven by the electric field and not diffusive. The porosity of the shell was found to significantly influence the core motion within. A more porous shell led to the core particles being more confined to the middle of the shell for the frequencies that showed orthogonal, diffusive motion for the original shell. A thicker, less porous shell significantly decreased the frequency at which parallel, driven motion was observed and orthogonal motion was not observed at any frequency. We suspect that the primary cause of these differences is the reduction in the electric field strength inside the yolk-shell geometry when the shell is made thicker and less porous.

A change of the LiCl concentration from 0.2 to 2 to 25 mM did not change the frequency-dependent motion patterns of the cores significantly in the experiments, as the double layers remained small compared to the particle size for all salt concentrations ($\kappa a_{\text{particle}} \approx 8, 26, 88$, respectively). This was confirmed by our finite-element calculations. Our model could also explain why experiments with the same yolk-shell particle in pure water that were done previously,³⁴ did not show parallel, driven motion at 1 kHz. Lastly, the particles exhibited

orthogonal diffusive motion at a lower frequency for a shell with a larger inner diameter, because it took longer to establish ionic concentration differences within a larger shell.

Despite Brownian motion not being included in the presented calculations, the main physical mechanisms were uncovered. The combined insights obtained by experiment and numerical calculations into the complicated dynamics of this system of yolk-shell particles provides a clear roadmap to their future application as building blocks for e.g. switchable photonic crystals and other advanced applications.

AUTHOR CONTRIBUTIONS

Tom A.J. Welling performed the liquid-phase electron microscopy electric field experiments. The earlier experiments were done together with Albert Grau-Carbonell (Utrecht University). Tom A.J. Welling performed the data analysis and finite-element calculations. Kanako Watanabe (Tohoku University) synthesized the rattle particles as well as the subsequent overgrowth and etching.

ACKNOWLEDGEMENT

We thank prof. Daisuke Nagao (Tohoku University) for continuing to support collaborations with our SCM group. The authors also acknowledge the EM square center at Utrecht University for access to the microscopes. Especially, Chris Schneijdenberg and Hans Meeldijk are thanked for their assistance.

APPENDIX A: SUPPORTING INFORMATION

Details of finite-element calculations

We performed finite-element calculations using the COMSOL 5.4 Multi-Physics Modeling Software. We set up a system with a spherical core particle having a radius of 170 nm. A hollow shell with an inner radius of 370 nm and shell thickness of 40 nm surrounded it with the core particle positioned at the center of the shell. The sizes of the core particle and shell were based on the dimensions of the particles used in experiments, which were synthesized via the method of Watanabe and coworkers.³⁴ The sphere and shell were located on the symmetry axis of a cylindrical fluid domain with a height and width of $5\text{ }\mu\text{m}$. The core particle is allowed to move through the shell due to electric and viscous forces acting upon it. Here we describe the boundary conditions in more detail. We also explain the moving core particle and the mesh during the calculation, and the solver settings.

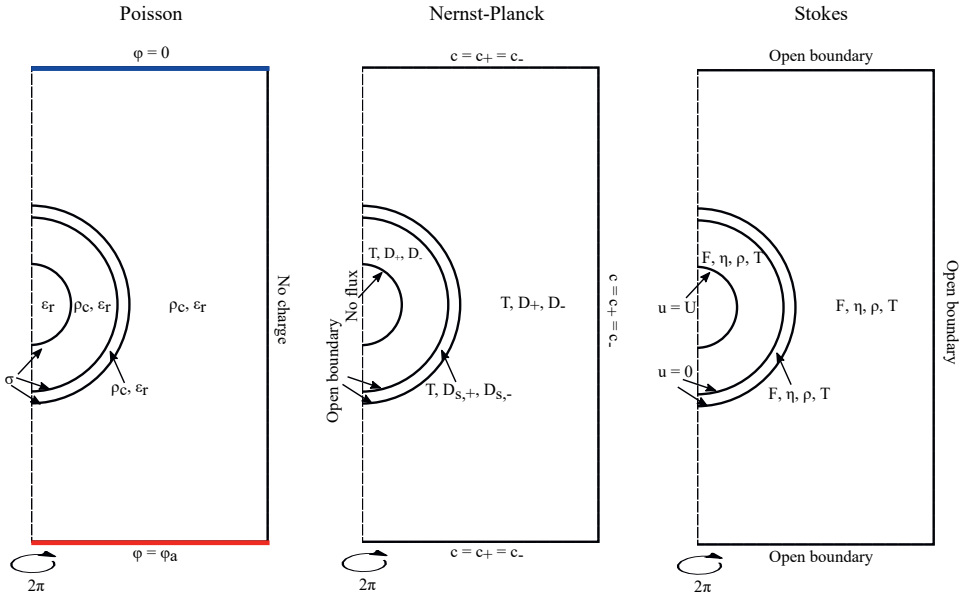


Figure A1: Boundary conditions used for the yolk-shell geometry used in the 2D axisymmetric finite-element calculations.

Boundary Conditions. Figure A1 shows an overview of the boundary conditions used for each equation that was solved, namely the Poisson equation, the Nernst-Planck equation and the Stokes equation for an incompressible fluid. The relevant values for the quantities discussed next are provided in Tables A1 and A2.

The boundary conditions for the Poisson equation. The left panel in Figure A1 shows the relevant boundary conditions. The right boundary of the simulation box carries no charge ($\hat{n} \cdot \nabla \phi = 0$), where \hat{n} is the unit normal to the surface and ϕ is the electric potential). The

lower, red boundary has an applied voltage, whereas the upper, blue boundary is grounded. This setup allowed us to apply an external field with minimal effect of the finite size of the calculation volume. The outer box in the calculation was 5 times larger than shown in Figure A1. All domains have a relative permittivity ϵ_r (see Table A1). Domains with free charges also have a local charge density ρ_c , which is given by the local abundance of ions $\rho_c = N_A e (z_+ c_+ + z_- c_-)$. Here N_A is Avogadro's constant, e the electron charge, z_+ and z_- the charge numbers of the ionic species, and c_+ and c_- the local concentration of the ionic species. The surfaces of the core and the shell carry a charge density σ (see Table A2).

The boundary conditions of the Nernst-Planck equations. The middle panel in Figure A1 shows the relevant boundary conditions. The outer boundaries of the simulation box are held at a constant ion concentration, which means that these regions serve as a reservoir. The fluid has a temperature T and the two types of ions, positive and negative, have diffusion coefficients D_{pos} and D_{neg} , respectively. The ion diffusion coefficients within the silica shell wall $D_{s,j}$ are lower than bulk diffusion coefficients ($D_{s,j} = \Phi_p D_j$), with Φ_p the porosity. The boundary of the core has a no-flux boundary condition ($\hat{n} \cdot (\mathbf{J}_j + \mathbf{u} c_j) = 0$), where \mathbf{u} is the flow velocity and c_j represent the local ion concentrations; \mathbf{J}_{\pm} indicates the associated fluxes. There is an open boundary for ions to go through on the shell walls.

The boundary conditions for the Stokes equations. The right panel in Figure A1 shows the relevant boundary conditions. The outer boundaries of the simulation box are open boundaries ($(-p\mathbf{I} + \eta(\nabla\mathbf{u} + (\nabla\mathbf{u})^T))\hat{n} = 0$). The shell walls have no-slip boundary conditions $\mathbf{u} = \mathbf{0}$. The core particle moves with a velocity calculated from the electric and hydrodynamic forces acting on it as described in the Methods section. The fluid has a density ρ_{fluid} , a viscosity η , a temperature T and a volume force $\mathbf{F} = -eN_A(c_+ + c_-)\nabla\phi$.

Moving core particle and mesh. The rotational symmetry of the system was exploited by performing 2D axisymmetric calculations to minimize the number of elements required. We used local refinement with small elements in the areas of the double layers as shown in Figure A2. The thickness of the refined elements was approximately the same as the Debye length. It is more common to apply a thicker area of refined elements,^{209,210,264} but this was not possible here due to the core being able to approach the shell more closely than two Debye lengths. As we wanted to keep the area of refined elements the same during the whole simulation, these areas had to be less thick. We compensated for the thinner area of refined elements by putting more mesh elements in these areas than is common practice, and also made sure that the elements did not expand too quickly when moving away from these dense mesh areas. However, the size of the elements was allowed to expand radially outward from the double layers (by a factor 1.25, up to a maximum element size of 15 nm).

The core particle could move along the symmetry axis. We determined its velocity \mathbf{U} via the electric force \mathbf{F}_e and the hydrodynamic drag force \mathbf{F}_h acting on it via Newton's second law of motion²⁵⁰

$$\mathbf{F}_e + \mathbf{F}_h = \frac{4}{3}\pi a_{\text{particle}}^3 (\rho_{\text{particle}} - \rho_{\text{fluid}}) \frac{d\mathbf{U}}{dt}, \quad (5.27)$$

where ρ_{particle} and ρ_{fluid} are the density of the particle and fluid, respectively. The electric force and hydrodynamic drag force were obtained by integrating the electric and hydrodynamic

Core particle radius a_{particle}	170 nm
Inner shell radius a_{shell}	370 nm*
Shell thickness t_{shell}	40 nm*
Shell porosity Φ_p	0.01 – 1
Fluid viscosity η	1 mPa s
Fluid density ρ_{fluid}	10^3 kg m^{-3}
Temperature T	293.15 K
Particle density ρ_{particle}	$2 \cdot 10^3 \text{ kg m}^{-3}$
Fluid relative dielectric constant $\epsilon_{r,\text{fluid}}$	78.4
Particle relative dielectric constant $\epsilon_{r,\text{particle}}$	3.8
Shell relative dielectric constant $\epsilon_{r,\text{shell}}$	$(1 - \Phi_p) \epsilon_{r,\text{particle}} + \Phi_p \epsilon_{r,\text{fluid}}$
Positive ion diffusion coefficient D_-	$1.022 \cdot 10^{-9} \text{ m}^2 \text{ s}^{-1}$
Negative ion diffusion coefficient D_+	$2.037 \cdot 10^{-9} \text{ m}^2 \text{ s}^{-1}$
Ion diffusion coefficient in shell $D_{s,j}$	$\Phi_p D_j$
Positive ion charge number z_+	1
Negative ion charge number z_-	-1
Ionic strength I	2 mM**
Core particle surface charge density σ_{particle}	$-6.3 \cdot 10^{-3} \text{ C m}^{-2}$ **
Inner & outer shell surface charge density σ_{shell}	$-6.3 \cdot 10^{-3} \text{ C m}^{-2}$ **
Length of simulation box	5 μm
Voltage V	0.5 V
Frequency f	1 – 100 kHz

Table A1: Typical values for a finite-element calculation. *For the larger shell: $a_{\text{shell}} = 496 \text{ nm}$, $t_{\text{shell}} = 55 \text{ nm}$. ** The values here are for 2 mM salt. In Table A2 we give the values for other salt concentrations.

I	0.002 mM	0.2 mM	2 mM	25 mM
σ_{particle}	$-0.18 \cdot 10^{-3} \text{ C m}^{-2}$	$-2.1 \cdot 10^{-3} \text{ C m}^{-2}$	$-6.3 \cdot 10^{-3} \text{ C m}^{-2}$	$-22.1 \cdot 10^{-3} \text{ C m}^{-2}$
σ_{shell}	$-0.095 \cdot 10^{-3} \text{ C m}^{-2}$	$-2.1 \cdot 10^{-3} \text{ C m}^{-2}$	$-6.3 \cdot 10^{-3} \text{ C m}^{-2}$	$-22.1 \cdot 10^{-3} \text{ C m}^{-2}$

Table A2: Surface charge densities of the core particle and shell for different salt concentrations.

stress tensors over the surface of the particle, respectively.

$$\mathbf{F}_h = \oint_S \mathbf{T} dS \quad (5.28)$$

$$\mathbf{F}_e = \oint_S \mathbf{M} dS \quad (5.29)$$

The particle position was then updated by multiplying the velocity per timestep and the timestep itself. The backward differential formula (BDF) method uses non-uniform steps in

time to solve the physics for each time step. When the mesh in the blue region in Figure A2 became too distorted, it was updated to ensure accurate reproduction of the physics. This was whenever the following criterion was met:

$$\frac{\text{tr}F^T F}{2J^{2/n}} - \frac{n}{2} > 0.5, \quad (5.30)$$

where F is the deformation gradient, J its determinant, and n is the space dimension. The internal COMSOL name for this quantity is "comp1.spatial.lisoMax".

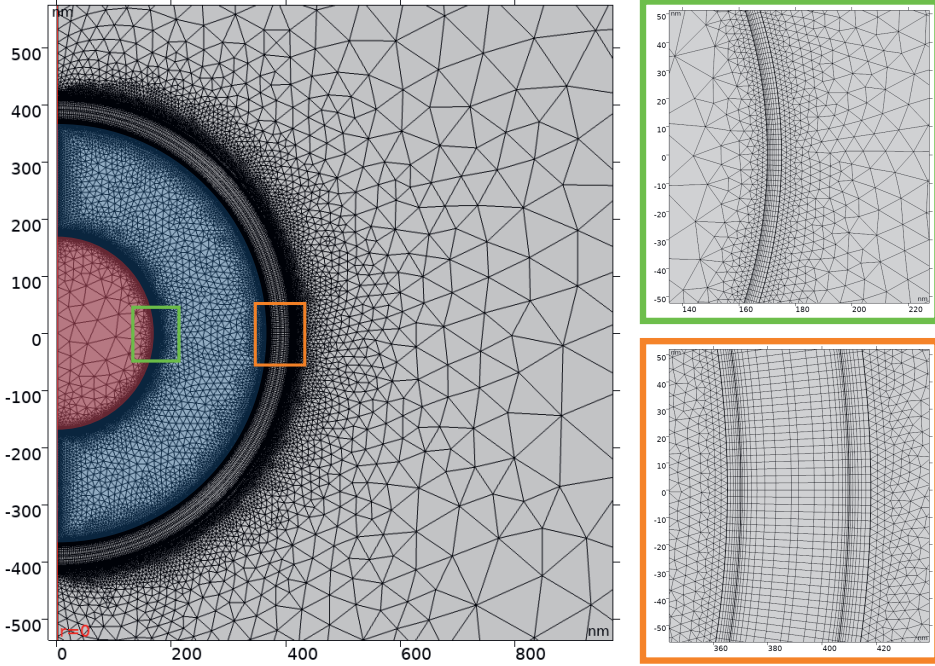


Figure A2: Example of the mesh of the yolk-shell geometry used in the 2D axisymmetric finite-element calculations. The mesh near the surfaces, at the double layers, is extra refined to deal with large changes in concentration and potential over a small length. The mesh of the red domain was moved according to the updated particle position. The mesh of the blue domain was automatically updated when it became too deformed.

We first performed a stationary study with a shell that was open to ions and for which no electric field was applied. During this study the equilibrium double layers could form. This solution was used as an initial configuration to perform the time-dependent calculation with the AC electric field. For this calculation the shell was given a fixed porosity which determined how fast ions diffused through the shell, according to the rules in Table A1. In the time-dependent solver using the BDF method a relative tolerance of 0.01 was used. This controls the relative error in each time step. An absolute tolerance factor of 0.5 is applied to

scaled variables to control the absolute error. The time step taken by the solver was allowed to vary up to a maximum of $1/f/100$, where f is the frequency. Furthermore, backward Euler consistent initialization was used. To solve the system at a certain time step we used a fully coupled solver, with MUMPS as the direct solver for the linear equations.

Model verification. In order to ensure that our finite-element model provided acceptable results for the electrophoresis of a particle, we compared results of our model without the shell with established literature values.^{250,268} First, we compared the stationary electrophoretic velocity from our simulations to the work of O'Brien and White.²⁶⁸ For these calculations we used a constant potential boundary condition to be as close to their conditions as possible. The electric field strength was set to 100 V m^{-1} to be in the regime of low electric field. The results are shown in Figure A3a, which shows good agreement with the work of O'Brien and White.²⁶⁸ Note that in the calculations in this work the scaled zeta potential is 2. Second, we compared the dynamic electrophoretic velocity under an AC electric field to the work of Eric Lee.²⁵⁰ For these calculations we used constant surface charge boundary conditions, as these are also used in the simulations on the yolk-shell system in this work. The electric field strength was set to 100 V m^{-1} to be in the low-field regime. The results of these calculations also agree well with the work of Lee (Figure A3b).²⁵⁰

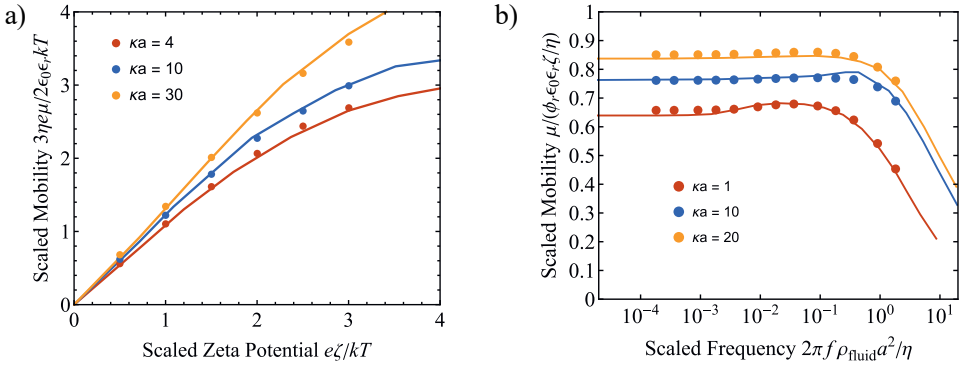


Figure A3: Model verification. a) Results of finite-element calculations of the stationary electrophoretic mobility for various surface potentials and salt concentrations compared to the work of O'Brien and White (solid lines).²⁶⁸ b) Results of finite-element simulations of the dynamic electrophoretic mobility for various salt concentrations and frequencies (scaled surface potential $\phi_r = 2$) compared to the results of Eric Lee (solid lines).²⁵⁰

Mesh refinement. We verified that we had used a sufficiently dense mesh in the areas where this mattered as follows. We made the mesh in the EDL regions 4, 9, and 16 times more dense and ran the simulations for a shell with 100% porosity at 100 V mm^{-1} and 100 kHz . No changes in the electrophoretic velocity of the core particle was observed.

Synthesis, zeta potential, etching and overgrowth of yolk-shell particles

For the synthesis of the original rattle particles the reader is referred to our previous collaborative work.³⁴ The zeta potential of the core particles was measured to be -41 mV in aqueous solution for the same sample used in this study.³⁴ We furthermore measured the zeta potential of the shells and it was found to be -45 ± 7 mV in aqueous solution (2 mM LiCl). However, realistically we do not know the zeta potential of the inner part of the shell (we cannot measure it) and it is likely that the zeta potentials of the core particles may deviate somewhat when they are in the shells. By mechanically cracking the shells it may be possible to measure the zeta potential of the cores in the future. As such, we decided to use the same surface charge density for all silica surfaces in the simulations, leading to -50 mV surface potential for the core and -40 mV surface potential for the shell.

The procedure to grow silica on top of the shell of the original rattle particles is as follows (Figure A4). An aqueous suspension of the rattle particles was mixed with an ethanol solution. The volume fraction of water in ethanol was 0.25, and the total volume of the mixture was 10 mL. After stirring for 5 min at 35°C , 100 μL of 100 mM NaOH ($\geq 98.0\%$, Sigma-Aldrich) aqueous solution was added to the mixture. An ethanol solution of tetraethyl orthosilicate (TEOS, $\geq 98.0\%$, Sigma-Aldrich) (56 μL , 1.8 M) was injected three times with intervals of 45 minutes. The total concentration of TEOS was 30 mM. The reaction was conducted under stirring at 35°C overnight. The obtained particles were centrifuged twice with ethanol and with water.

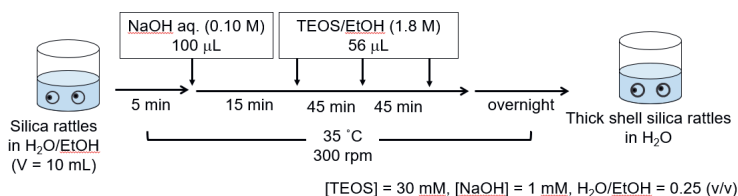


Figure A4: The procedure for overgrowing the shells of the rattle particles.

The procedure to etch the shells of the original rattle sample is as follows (Figure A5). An aqueous solution of NaOH (100 mM, 287 μL) was added to 8.7 mL of the dispersion of rattle particles. The mixture was stirred at 40°C for 7 hours. The solution pH of the mixture was 11.5. The etched particles were centrifuged twice with water, and redispersed in water.

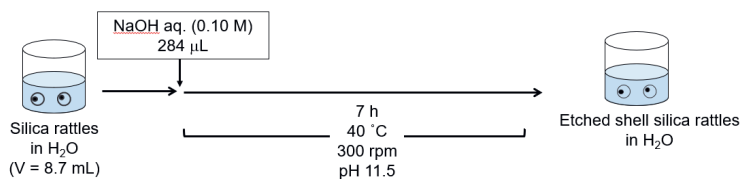


Figure A5: The procedure for etching the shells of the rattle particles.

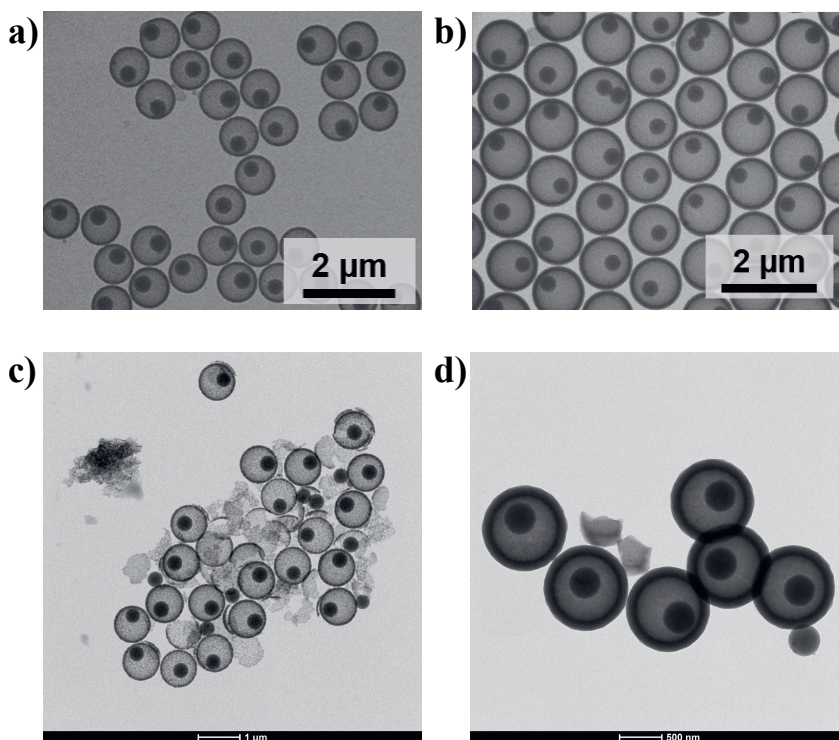


Figure A6: Bright-field TEM images of the four different kinds of rattle-type particles used in this study. a) Silica rattles with a small shell ($a_{\text{shell}} = 370$ nm), b) silica rattles with a large shell ($a_{\text{shell}} = 496$ nm), c) silica rattles with a small shell that is etched more significantly, d) silica rattles with a small shell that is overgrown with silica.

A closer look at the electric field inside the liquid cell and within the rattle geometry

Figure A7 shows the electric field in a 3D environment resembling the liquid-cell geometry in the experiments, where we solved the Poisson equation. The area with water ($\epsilon_r = 78.4$) was 100 by 50 by 2 micron. In this calculation we placed 200 nm thick SiN windows ($\epsilon_r = 9.5$) on the top and the bottom of the water layer. The electrodes were 50 by 5 by 0.075 micron. The middle of the electrodes were spaced 30 μm apart. The height of the liquid cell and thus the water layer within was taken to be 2 μm in this calculation. One electrode was given a constant potential boundary condition of 3 V, while the other was given a ground boundary condition (0 V). The edges of the calculation volume were assumed to have zero charge. It was found that the electric field between the two electrodes was at least 95 V mm^{-1} in the area between the electrodes where the recordings of the yolk-shell particles were done. The electric field did not vary significantly with the z height. We thus expect less than a 5% error in the electric field in our experiments.

We also calculated what the effect of the dielectric constant of the shell was on the electric field within the yolk-shell geometry. Figure A8 shows the field in and around the yolk-shell geometry upon application of a 100 V mm^{-1} electric field. A drop of 21% to an average electric field of 79 V mm^{-1} was observed for a shell thickness of 40 nm and a shell dielectric constant of $\epsilon_r = 11.3$, which corresponds to a shell porosity of 10%.

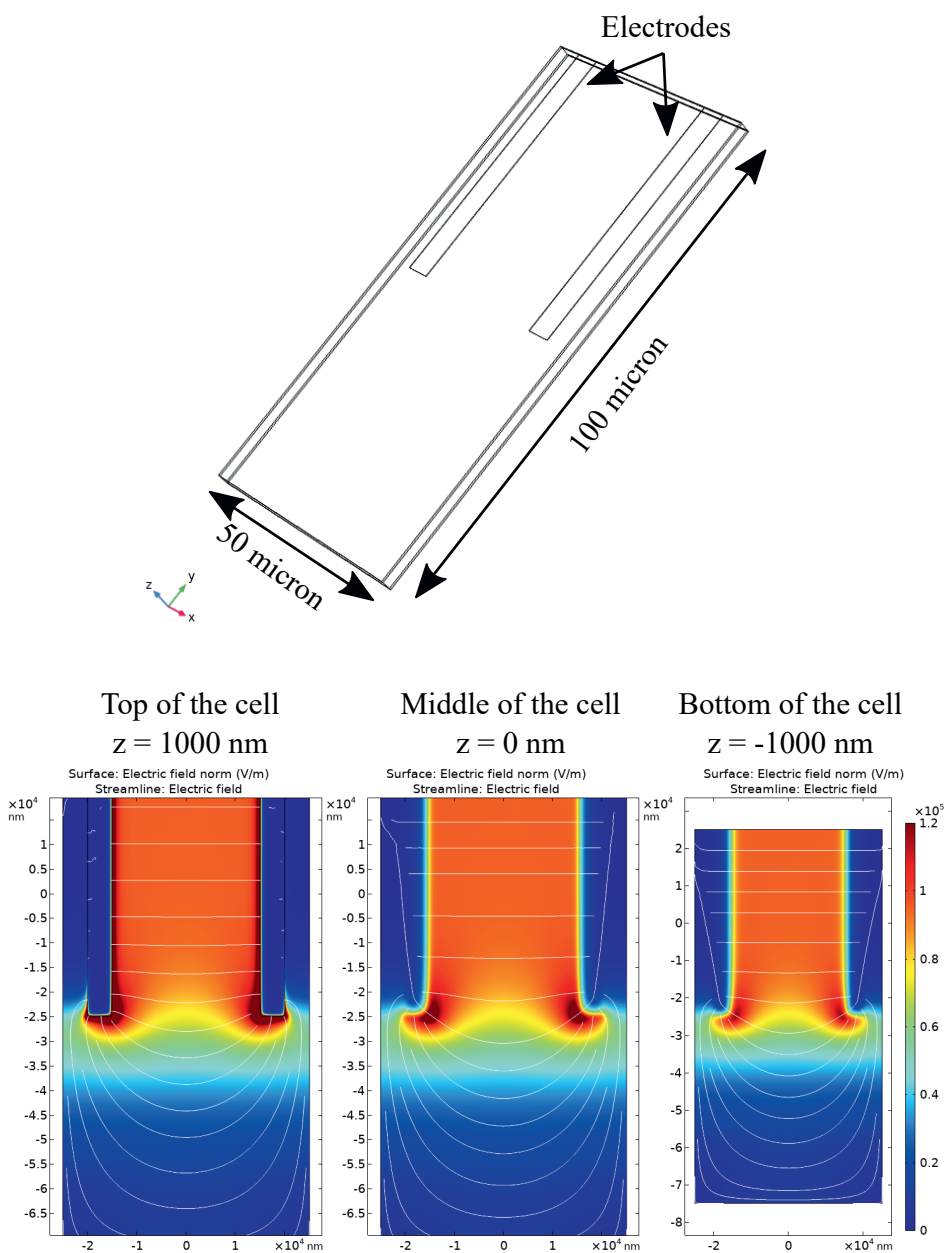


Figure A7: Electric field within a liquid cell geometry calculated by solving the Poisson's equation for a geometry resembling the liquid cell, where the electrodes are spaced $30\text{ }\mu\text{m}$ apart. The color scale indicates the strength of the electric field.

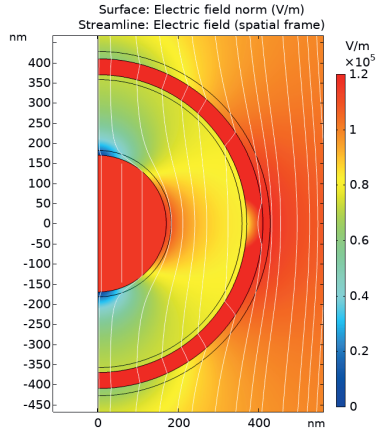


Figure A8: Electric field drop within the rattle geometry by only taking the dielectrics of the shell into account. For this calculation we solved only the Poisson equation to estimate the electric field reduction within the yolk-shell geometry without taking ions and their movement through the shell into account. The dielectric constant of the shell was the same as those in the full calculations with a porosity of the shell of 10%: $\epsilon_r = 11.3$. The surface potential of the core is -50 mV, and that of the shell is -40 mV.

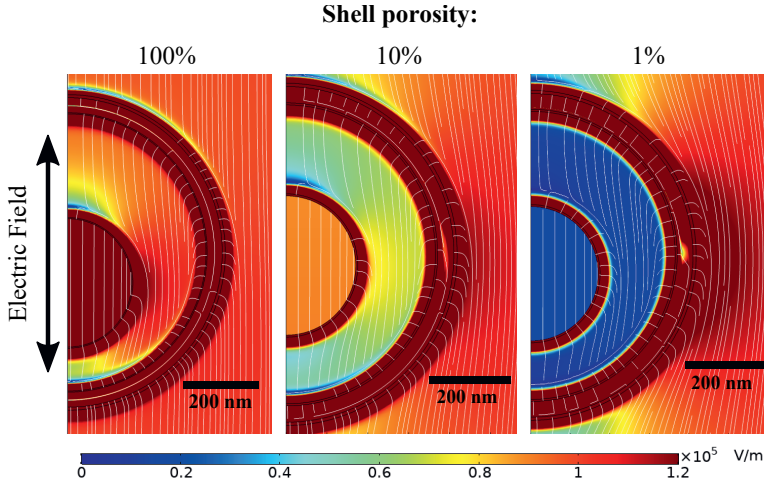


Figure A9: Electric field strength within the rattle geometry at the maximum of the electric field sine wave (at 4.5π , so after 2.25 cycles) for different porosities of the shell (as indicated by the percentages in the subfigure titles). The surface potential of the core is -50 mV, and that of the shell is -40 mV.

APPENDIX B: SUPPORTING FIGURES

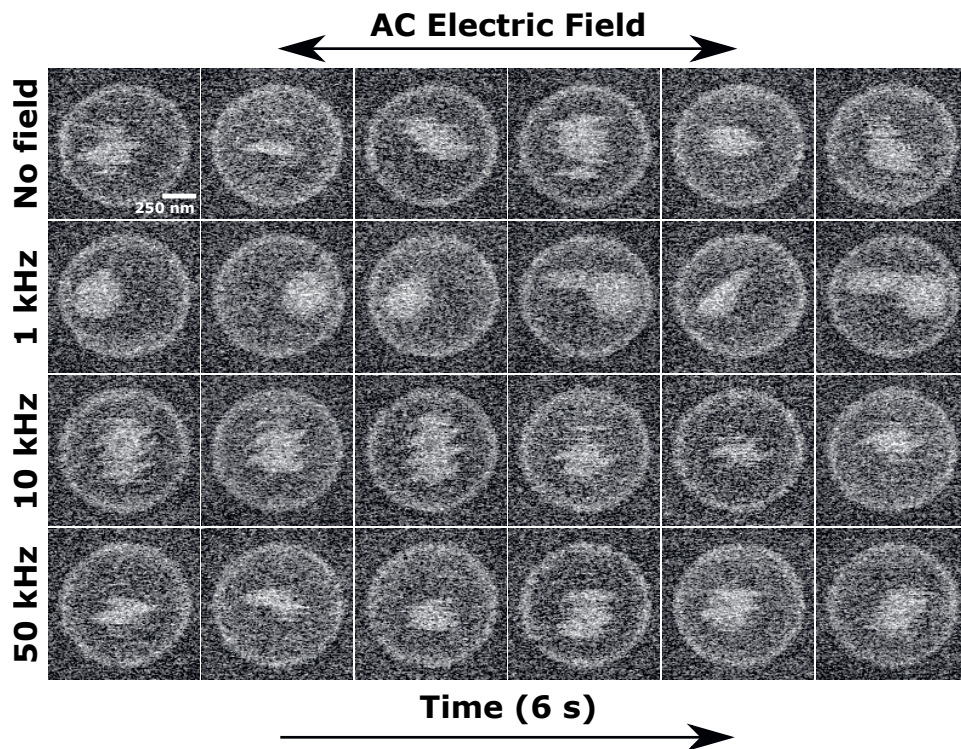


Figure A10: Frequency-dependent mobility of a core particle within a shell under application of a 100 V mm^{-1} AC electric field in aqueous solution of 2.00 mM LiCl . The electron dose rate was $45 \text{ e}^- \text{ nm}^{-2} \text{ s}^{-1}$. For each frequency, six consecutive frames are shown with a frame time of 1 s . While at lower frequencies the core moves parallel to the electric field, at intermediate frequencies the core moves orthogonal to the electric field. At high frequencies, there is no significant influence of the electric field.

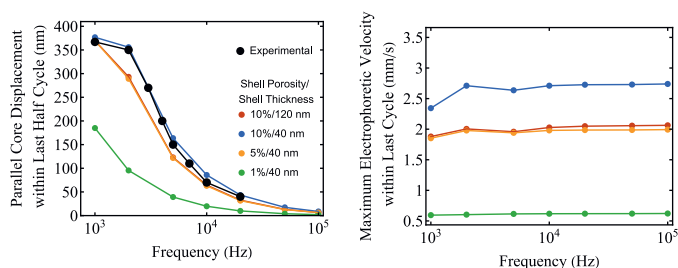


Figure A11: Calculated effect of the thickness of the shell on the displacement and velocity of the core particle. A 120 nm thick shell with 10% porosity has a similar effect on the particle velocity as a 40 nm thick shell with 5% porosity. The other parameters are the same as Figure 3 of the main text.

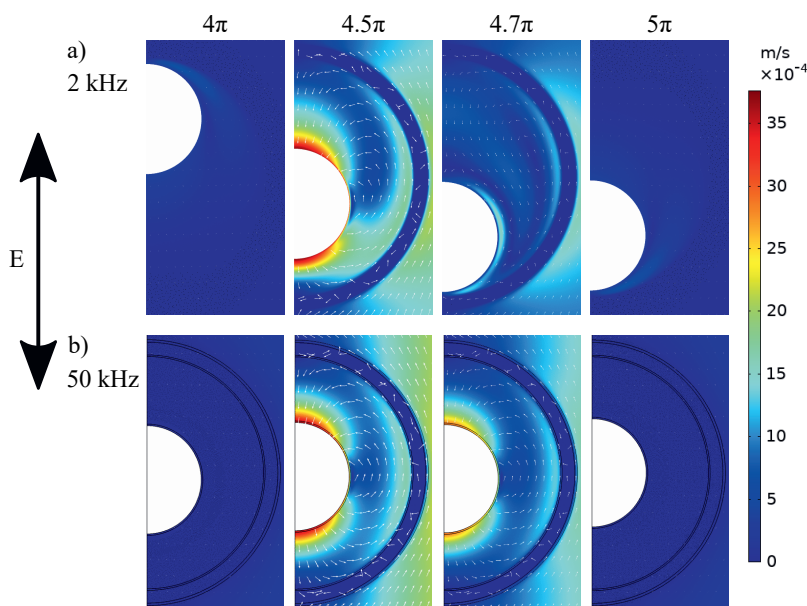


Figure A12: Calculated flow profiles for a yolk-shell geometry for a shell with 100% porosity during the application of a 100 V mm^{-1} AC electric field of 50 and 2 kHz. The first image is after 2 cycles of the electric field and the images that follow are all within half an electric field cycle (phase 4π to 5π). It can be seen that the flow originating from the EDL on the inner shell wall contributes positively to the velocity of the particle. For 2 kHz the flow profile is different, as the particle moves significantly during the electric field cycle. The surface potential of the core is -50 mV , and that of the shell is -40 mV .

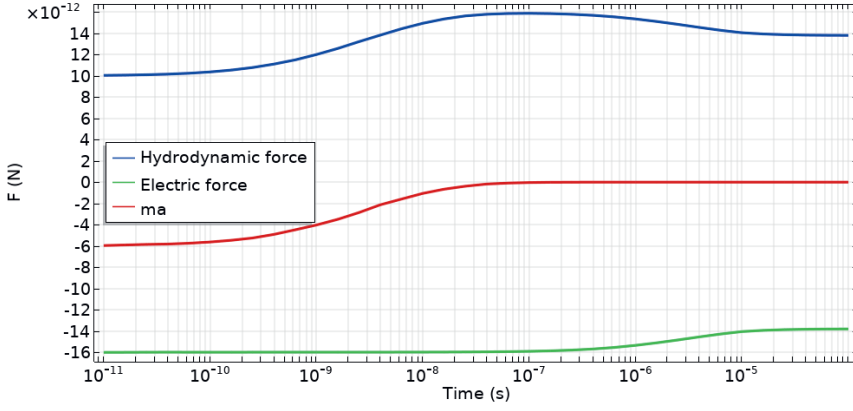


Figure A13: The electric force, hydrodynamic force and the acceleration term as function of time for a free particle ($a_{\text{particle}} = 170 \text{ nm}$, $\kappa a = 1$) when applying a constant electric field of 100 V mm^{-1} . It shows that for the times relevant in our system using an AC electric field with frequencies of 100 kHz or lower, the acceleration term is negligible.

APPENDIX C: SUPPORTING MOVIES



Supporting Movie 1: Experimental liquid-phase electron microscopy movie showing the mobility of a core particle within a yolk-shell geometry in 2 mM LiCl under AC electric field application of varying frequencies at 100 V mm^{-1} . The arrow indicates the direction of the electric field. The electron dose rate was $45 \text{ e}^- \text{ nm}^{-2} \text{ s}^{-1}$.



Supporting Movie 2: Experimental liquid-phase electron microscopy movie showing the mobility of a core particle within a yolk-shell geometry after additional etching in 2 mM LiCl under AC electric field application of varying frequencies at 100 V mm^{-1} . The arrow indicates the direction of the electric field. The electron dose rate was $148 \text{ e}^- \text{ nm}^{-2} \text{ s}^{-1}$.



Supporting Movie 3: Experimental liquid-phase electron microscopy movie showing the mobility of a core particle within a yolk-shell geometry (after shell overgrowth) in 2 mM LiCl under AC electric field application of varying frequencies at 100 V mm^{-1} . The arrow indicates the direction of the electric field. The electron dose rate was $148 \text{ e}^- \text{ nm}^{-2} \text{ s}^{-1}$.



Supporting Movie 4: Experimental liquid-phase electron microscopy movie showing the mobility of a core particle within a yolk-shell geometry in 0.2 mM LiCl under AC electric field application of varying frequencies at 100 V mm^{-1} . The arrow indicates the direction of the electric field. The electron dose rate was $45 \text{ e}^- \text{ nm}^{-2} \text{ s}^{-1}$.



Supporting Movie 5: Experimental liquid-phase electron microscopy movie showing the mobility of a core particle within a yolk-shell geometry in 25 mM LiCl under AC electric field application of varying frequencies at 100 V mm^{-1} . The arrow indicates the direction of the electric field. The electron dose rate was $45 \text{ e}^- \text{ nm}^{-2} \text{ s}^{-1}$.



Supporting Movie 6: Experimental liquid-phase electron microscopy movie showing the mobility of a core particle within a yolk-shell geometry with a large shell in 2 mM LiCl under AC electric field application of varying frequencies at 100 V mm^{-1} . The arrow indicates the direction of the electric field. The electron dose rate was $20 \text{ e}^- \text{ nm}^{-2} \text{ s}^{-1}$.



Supporting Movie 7: Calculated flow profile during the application of three cycles of the electric field as calculated via finite-element calculations for a yolk-shell geometry in 2 mM aqueous LiCl for an electric field with a strength of 100 V mm^{-1} and frequencies of 50 and 2 kHz. The core particle has a surface potential of -50 mV . The shell has a surface potential of -40 mV and a porosity of 10%.



Supporting Movie 8: Calculated total ion concentration profile during the application of three cycles of the electric field as calculated via finite-element calculations for a yolk-shell geometry in 2 mM aqueous LiCl for an electric field with a strength of 100 V mm^{-1} and several frequencies ranging from 100 to 1 kHz. The core particle has a surface potential of -50 mV . The shell has a surface potential of -40 mV and a porosity of 10%.



Supporting Movie 9: Calculated total ion concentration profile and mobility of the core when it is initially placed off-center during the application of three cycles of the electric field as calculated via finite-element calculations for a yolk-shell geometry in 2 mM aqueous LiCl for an electric field with a strength of 100 V mm^{-1} and 5 kHz. The core particle has a surface potential of -50 mV . The shell has a surface potential of -40 mV and a porosity of 10%.

6

Switchable colloidal crystals using assemblies of rattle-type particles with index-matched shells and alternating current electric fields

ABSTRACT

In this chapter, we focus on a promising application of rattle-type particles with movable inner cores and of which the outer shell is refractive index-matched to the solvent inside and inbetween the shells: responsive colloidal crystals switchable with AC electric fields. When the shells of the rattle particles are assembled on a lattice, the core positions can be controlled by an AC external electric field. This can be achieved without changing the lattice spacing and/or the symmetry of the photonic crystal if the shells are index matched and the core particles have a different refractive index from the shell. We showed that applying an AC electric field of low frequencies compared to the time it takes the ions to diffuse over the shell size makes the core particles move coherently in a direction parallel to the electric field thereby creating a relatively well-defined optical lattice of the core particles. When no electric field was applied, however, the particles moved around randomly in the hollow shells via thermal fluctuations. With the low frequency electric field on, the Bragg peak intensity was approximately 2.5 times higher than without an electric field, even for not yet optimized index-matched photonic crystals. This ratio of the intensity of the Bragg peaks when the electric field was off or on could be well quantified through analysis using Debye-Waller factors, which contrary to the temperature-induced effects for atoms and molecules are much larger for these electric-field switched systems. Further improvements of the contrast of the switching are certainly possible and under investigation both experimentally and theoretically.

6.1. INTRODUCTION

6.1.1. Photonic crystals

Color can be chemistry-based and physics-based. Chemically, color originates from absorption of light of certain wavelengths by chemical groups, while the molecules do not absorb light of other wavelengths. Physically, color can come from the way light is coherently and incoherently scattered and diffracted by random or periodically ordered structures. Examples of light interacting with ordered structures in nature are the colors of opals or butterfly wings. Analogous to electrons scattered by atoms on a periodic lattice in a semiconductor as described by the Schrödinger equation, photons are scattered by particles spaced on a regular 3D lattice, now called a photonic crystal, as described by Maxwell's equations. This analogy leads to a so-called photonic band gap for regular 3D crystals with lattice spacings on the order of the wavelength of visible light. In these structures propagation of photonics is prohibited directly by multiple deconstructive interference effects that also give rise to an electronic band gap for semiconductors. The concept of such a photonic band gap was already proposed in 1972 by the Russian scientist Bykov.^{269, 270} Since the concept of a photonic band gap was reintroduced in 1987 by John²⁷¹ and Yablonovitch²⁷² photonic crystals have received an enormous amount of attention as is illustrated by a selection on this topic taken arbitrarily from the last 10 years.^{229, 231, 232, 273} It should be remarked that in the last few decades the realization that also structures with incomplete band gaps, also referred to as stop gaps as they do not prohibit propagation of photons with certain frequencies in only a limited amount of directions within the photonic crystal, are interesting not only for many applications as well, but are also found frequently in nature where they serve to create structural colors. For 3D structures that have a complete or full photonic band gap, not only is the propagation of photons traveling inside the structures not possible, but also the spontaneous emission of photons with a frequency in the band gap can also not occur. This is due to the optical density of states being affected. Thus photonic propagation *and* creation can be manipulated in unprecedented ways for such structures.²⁷⁴

Photonic crystals with enough 3D unit cells and with low enough defects are difficult to realize experimentally. Top-down methods often require complex and expensive equipment and become quite difficult for more than just a few layers/unit cells.^{228–231} Bottom-up building-block assembly is an easier way to realize photonic crystals, but is often associated with more defects than those created by top-down methodology.^{228–231} The most commonly studied 3D photonic crystals are opal-based structures which can be synthesized relatively easily by colloidal self-assembly.²⁷⁵ Especially inverse opals, which are spherical voids arranged in a higher refractive index matrix in the form of a face-centered cubic (fcc) lattice are interesting, as they exhibit a complete photonic band gap if the refractive index of the material of the matrix is larger than 2.8. They can be made by self-assembly of spherical colloidal particles, which can be removed after the interstices are filled up with high index material. This has been shown experimentally in the infrared.^{276, 277}

Another example, a MgCu_2 Laves phase structure, can be achieved with colloidal self-assembly of hard-sphere-like particles as demonstrated in our group.^{171, 278, 279} The MgCu_2

structure is interesting for photonic applications as it consists of a diamond crystal of the large spheres and a pyrochlore lattice of the small spheres. Both of these substructures display a complete photonic band gap for sufficiently high refractive index contrast.^{279, 280} Obtaining the MgCu_2 structure is however non-trivial because the competing MgZn_2 Laves phase was found to be the thermodynamically stable structure in bulk for a binary hard-sphere mixture with a diameter ratio in the range of 0.76-0.84.^{278, 279} However, recently our group experimentally found that the local structure of 70-80% of particles (diameter ratio 0.78) that were self-assembled in slowly drying emulsion droplets was MgCu_2 -like,¹⁷¹ which makes such supraparticles interesting for photonic applications, also in the visible wavelength regime, when made of particles of a high refractive index.

6.1.2. Responsive photonic crystals

Several different applications of photonic crystals can only be realized if the band gap can be manipulated. For instance, the band gap can be manipulated by changing the spacing, which is often accompanied by a change in symmetry of the photonic crystal, in real time. In photonic materials, the wavelength range of a (partial) band gap depends, for a given crystal symmetry and sign of the contrast, on several factors, among which are: (1) the refractive index contrast between the two media, (2) the lattice constant and (3) the volume fraction of particles compared to the surrounding phase. By tuning, or even completely removing, one of these factors, a responsive photonic crystal (RPC) can be realized. Such switchable photonic structures are interesting for applications in color displays,^{281, 282} inks and paints,^{283, 284} optically active components and biological/chemical sensors.²⁸⁵ Good quality RPCs with a good response time could for instance be used as optical switches in optical circuits. RPCs may also be applicable as active color units in color displays and rewritable paper,²⁸² and may provide a solution for the difficulty in making color screens with E-ink technology.^{76, 286}

Self-assembled colloidal crystals can be produced at lower cost and usually with a larger number of unit cells than microfabricated photonic crystals. Therefore, most of the research on RPCs has focussed on using stimuli to manipulate the refractive index of the material or the lattice constant or symmetry of the colloidal crystal. For example, Zhou *et al.*²⁸⁷ tuned the transmission and wavelength of the photonic band gap of an inverse opal structure with BaTiO_3 as the backbone material by changing the temperature. This switching of the photonic properties was attributed to a change in the refractive index caused by a change in temperature close to the Curie point of the ferroelectric material BaTiO_3 .

More commonly, however, the spatial symmetry and/or the lattice constant of the photonic crystal are manipulated by external stimuli. A great example thereof is the work by Honda and coworkers,²⁸⁸ who made a dually tunable photonic crystal composed of thermosensitive gel particles in a pH-sensitive inverse opal gel. By altering the pH, the volume of the inverse opal gel was changed, which allowed for control over the lattice constant and consequently the wavelength of the band gap. Furthermore, by changing the temperature the thermosensitive gel particles within the pores of the inverse opal gel could be initiated to shrink or swell as well. When the gel particles were fully swollen a crystal of those particles was formed

within the inverse opal gel. When the gel particles were shrunken down, the long-ranged order became significantly reduced and the band gap width was significantly decreased, next to being moved to different frequencies. As such, temperature control over the intensity of the colors connected to a band gap was achieved.

Another way to tune the spatial arrangement of particles in a colloidal crystal is by external magnetic fields. For example, Li and coworkers realized a responsive photonic crystal with core-shell structured $\text{Fe}_3\text{O}_4@\text{SiO}_2$ nanorods.²⁸⁹ Combining the features of magnetically RPCs and of magnetically responsive liquid crystals enabled them to change the transmittance and wavelength of a band gap associated with the photonic crystal using a magnetic field with a switching rate of up to 50 Hz. In this work we focus on RPCs with an electric field as external stimulus, which will be discussed in the next section.

6.1.3. Responsive photonic crystals tunable with electric fields

Among the class of responsive photonic crystals, those that can be tuned with an external electric field are promising candidates for several technological applications. An electric field is able to change the optical response of the photonic crystal in several ways: (1) electrochemical processes, (2) reorientation of liquid crystal molecules (which changes the local refractive index and thus the contrast), (3) electrophoretic organization of colloidal particles or (4) changes to the structure indirectly induced by the electric field.²⁹⁰ As an example of an electrochemical process, Lu and coworkers²⁹¹ developed a photonic crystal with quaternized polystyrene-*b*-poly(2-vinyl pyridine) block copolymer which forms a 1D periodic lamellar structure. By applying a positive voltage, negatively charged ions bound to the thin film and the photonic crystal shrank, which resulted in a blue-shift of the reflected peak. When a negative voltage was applied, the reflected peak was red-shifted. These changes could be applied at a sub-second timescale.

It is also possible to create a responsive photonic crystal by using liquid crystals. This can be done because the orientation of the director and thus the refractive index of the material can be switched by external fields, such as electric fields. For example, by infiltrating an inverse opal with a photoresponsive liquid crystal mixture, Kubo and coworkers were able to tune the refractive index of the “voids” in the inverse opal by changing the orientation of the director by an electric field.²⁹²

Electric fields can also induce dipolar interactions between colloids which changes their equilibrium phase to that of a body-centered tetragonal crystal phase.²² Switching such dipolar interactions on and off could also be used to obtain different colloidal crystal symmetries, which changes the photonic properties.

Lastly we discuss the electrophoretic organization of colloidal particles, as this process is closest to the work discussed in this chapter. At high concentrations, monodisperse charged colloidal particles can form ordered structures as they minimize the electrostatic repulsive energy between them. By applying an electric field the lattice constant of the colloidal crystal can be manipulated, as the particles migrate to the oppositely charged electrode. As such, the volume fraction of the particles increases near that electrode, which has consequences for the lattice constant and therefore changes the wavelength of the reflection. For example, Shim *et*

*al.*²⁹³ used a highly sulfonated polystyrene nanoparticle suspension between two ITO glass slides. By applying a DC electric field with a voltage between 0 and -1.8 V they could tune the reflection wavelength from approximately 605 to 505 nm. They also showed that this process was reversible for 12,000 cycles (around 40 min) when an AC electric field (1.2 V at 5 Hz) was applied. This study, and many other studies on RPCs, however concern a partial band gap, where the reflection is angle dependent. One way to create structures with more angle-independent structural colors is by using quasi-amorphous materials, which are structures that have short-range order, but no long-range order.²⁹⁴ Quasi-amorphous structures show angle-independent and non-brilliant photonic colours, due to the isotropy of the structures in combination with the shorter range of the order. Lee and coworkers⁶⁰ demonstrated photonic pixels that were tunable with an electric field over the visible wavelength regime. They used relatively polydisperse Fe_3O_4 nanoparticles and electric fields up to 80 V mm^{-1} . The reflected wavelength peak at 40° shifted only 5 nm maximally for different viewing angles compared to the normal incidence peak, showing relative angle independency of the color. It should be mentioned that for these systems absorption of light also played a role.

6.1.4. Rattle photonic crystals

Our approach to a RPC also uses electric fields. However, instead of tuning the distances and symmetry between the particles, we aim to tune the intensity of the reflected light by turning the order of the scattering units of the crystal on and off with an electric field. This can be done by manipulating the core particle in a rattle with an electric field as described in Chapter 5, as long as the scattering of the shells is reduced to a low value by refractive-index matching and having the core particles with a different refractive index from that of the shells. The concept is shown in Figure 1 and this switching scheme was suggested earlier by Camargo *et al.*²⁹⁵ in 2007 albeit using magnetic fields. However, they do not mention the index matching of the shell, which will likely give the largest possible effects. An external field could be used to manipulate the core particles to be present at a certain position within the shell, while the core particles move around randomly within the hollow shell when the electric field is turned off. Okada and coworkers³³ managed to tune the position of magnetic core particles within a hollow shell with a magnetic field. However, the size of the rattle particle was around 2 micron, which is not suitable for a photonic crystal at visible wavelengths. In the same group, Watanabe *et al.*³⁴ then shrunk down the size of the rattle particles to around 700 nm. In this study they used AC electric fields to tune the position of the titania or silica core particles. By using electric fields instead of magnetic fields they gained several benefits: (1) the switching was significantly faster and (2) the core size and material was no longer limited by the requirement to respond to a magnetic field. The core not being limited to magnetic materials is beneficial as magnetic materials are always absorbing light in the visible wavelength regime. Non-magnetic rattle-type particles are used in this work to study whether they can be used to switch photonic properties of photonic crystals.

While in this work we aim for switchable partial photonic band gaps, we would like to make a comparison between a crystal made of rattle particles and a double inverse opal (DIO) structure,²⁹⁶ which is a structure that has the potential to be used for switchable complete

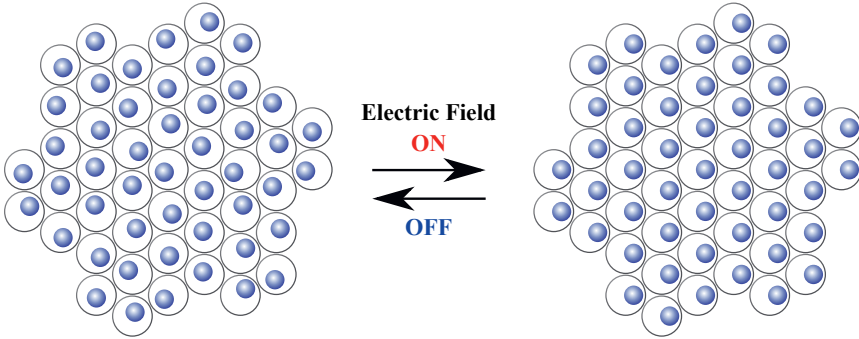


Figure 1: Schematic of the idea where an electric field can be used to create a crystal of the core particles with a rattle crystal. When the electric field is switched off, the particles move around randomly within the shell due to Brownian motion.

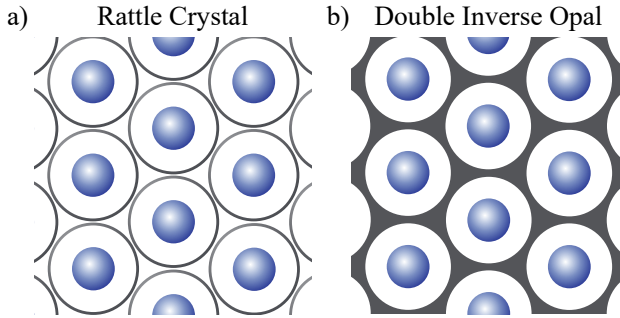


Figure 2: Similar structures of an fcc crystal of rattle particles and a double inverse opal (DIO) structure.

photonic band gaps.^{275,297} A comparison between the two structures is shown in Figure 2. The core particles are in a void space (filled with liquid) in both cases. The difference is that a DIO structure has a backbone that can be of a high refractive index. Ruhl and coworkers²⁷⁵ calculated that such a DIO PC could be used to tune a complete band gap with external fields, when the backbone has a high enough refractive index. They calculated that for a backbone refractive index of 3.2 and a core:void size ratio of 0.525 a switchable complete photonic band gap of 0.9% could be achieved. This complete band gap could be attained by directing the core particles in the (111) direction, while the band gap could be switched off by directing the core particles in the (100) direction. This shows that full photonic band gaps could be accomplished by creating such a structure. However, the current work focusses on the manipulation of the core particles with an electric field to achieve a partial band gap due to a crystal of cores. Our aim is to have a partial band gap when the field is switched on, while the partial band gap is strongly reduced when the electric field is switched off.

6.2. METHODS

6.2.1. Particles

The rattle particles used in this chapter are silica-titania-silica (STS) core particles within a silica shell (Figure 3a). They were synthesized in the same way as the silica rattles in Chapter 5, but using STS cores rather than silica cores. The method to make silica particles coated with titania (ST particles) are described in the work of Mine and coworkers.²⁹⁸ The method of Graf *et al.* was used to coat the ST particles with more silica to make STS core particles. For the synthesis details we refer to the thesis of Hikaru Namigata.²⁹⁹ After the cores were made, the procedure to make rattle-type particles used in the work of Watanabe and coworkers was used.³⁴

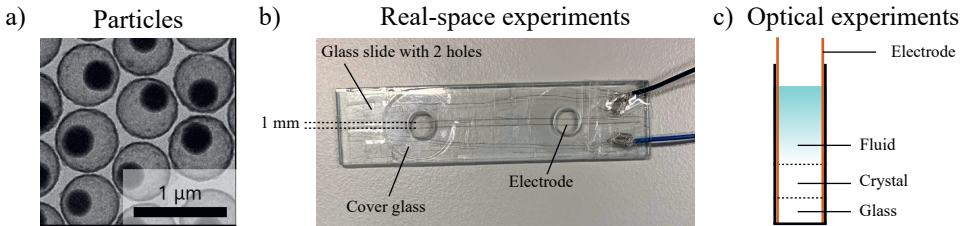


Figure 3: a) Rattle particles with a silica-titania-silica (STS) core particle within a silica shell. b) Photo of the custom electric field cell used for the real-space confocal microscopy experiments. c) Schematic of the sedimentation sample used for the experiments to record the optical reflection spectra.

6.2.2. Confocal microscopy

For confocal microscopy imaging, a custom electric field cell consisting of a cover glass with electrodes on top was used (Figure 3b). A Leica TCS SP8 confocal microscope equipped with a super continuum white light laser (SuperK, NKT Photonics), a PMT detector and a 93x/1.3 NA glycerol confocal objective was used to image the sample. The sample was sequentially scanned with the pinhole set to 1 Airy unit. We measured in reflection mode with the excitation laser set to 495 nm with a detection range of 485-505 nm. The experiments were carried out as follows. The custom electric field cell was glow discharged (Cressington 208) for 10 seconds at 5 mA. The rattle dispersion in water was dropcast on top of the glow-discharged cover glass. In reflection mode we observed the drying of the sample. When the water had almost completely evaporated, which was when a drying front was observed in reflection mode, a solution of 85/15 v% DMSO/water (refractive index $n = 1.46$ at 25 °C and wavelength $\lambda = 546$ nm)³⁰⁰ with 2.0 mM LiCl was added to the sample. The result of this procedure was that the shells had assembled in a 2D hexagonal structure, and the core particles could still move around within the shells.

6.2.3. Analysis

Image analysis. ImageJ 1.52i was used to convert the images to tiff stacks, calculate the maximum projection of a time series of confocal images and to calculate the fast-fourier

transform (FFT) of the real-space images. The particles within the time series were identified and tracked in time, but in 2D only, using Trackpy (v0.4.2), which is a Python implementation of the tracking algorithm by Crocker and Grier.¹²²

Structural analysis. The 2D radial distribution function $g(r)$ was calculated from the 3D coordinates obtained through particle localization in a certain amount of frames. First a histogram of the distances between all pairs of particles was calculated. Next, this histogram was normalized by dividing by the amount of particles analyzed. The radial distribution function was noisy when only one frame was taken. Therefore multiple frames were used to calculate a radial distribution function. For example, each frame with the electric field on could be used to calculate the radial distribution function. Those noisy radial distribution functions were averaged for many frames to get the average radial distribution function when the field was on. To determine the time evolution of the radial distribution function, five frames were grouped together to calculate the $g(r)$ in a small time frame (0.1 s). Subsequent groups of 5 frames were then used to analyze the radial distribution function changing in time to observe the changes in time when the field was turned on and off.

To further analyze the crystal structure of the particles with the electric field on or off, we used the bond orientational order parameters.³⁰¹ A set of numbers was calculated for every particle, based on the spherical harmonics $Y_{l,m}$:

$$q_{l,m} = \frac{1}{n_c(i)} \sum_{j=1}^{n_c(i)} Y_{l,m}(\hat{\mathbf{r}}_{ij}), \quad (6.1)$$

where $n_c(i)$ is the number of nearest neighbors of particle i , l an integer (in our case 6 for hexagonal order), m an integer running from $-l$ to l and $\hat{\mathbf{r}}_{ij}$ the unit vector pointing from particle i to particle j . The nearest neighbors were defined as the particles within cut-off distance r_c from particle i . The cut-off in our case was determined from the first minimum of the radial distribution function, which was around $r_c = 1.38d = 950$ nm, with d the outer shell diameter of the rattles. In order to detect local symmetries in the crystal structure we used local bond order parameters, defined as^{301,302}

$$q_l(i) = \sqrt{\frac{4\pi}{2l+1} \sum_{m=-l}^l |q_{lm}(i)|^2}. \quad (6.2)$$

In our case we are interested in hexagonal order and therefore use the local bond order parameter q_6 :

$$q_6(i) = \sqrt{\frac{4\pi}{13} \sum_{m=-6}^6 |q_{6m}(i)|^2}. \quad (6.3)$$

6.2.4. Optical reflection measurements

For the collection of the reflection spectra, we used a halogen lamp (S-2650, SOMA OPTICS, LTD.) as a light source and a spectrometer (S-2630 model II, SOMA OPTICS, LTD.). The size of the light beam hitting the sample was around 2 mm in diameter, which was smaller than the size of the crystal phase in the 3D rattle crystal. Two quartz cells ($1 \times 10 \times 44$ mm), one with water as a reference and one with the colloidal crystal, were placed

in a cell holder to measure the reflection spectrum (wavelength range: 350 – 1050 nm). First the reflected spectrum of the reference cell was measured 10 times with an exposure time of 15 ms. Next the reflected spectrum of the cell containing the colloidal crystal also dispersed in water was measured 10 times with an exposure time of 15 ms. The reflected spectrum of the signal coming from the rattle crystal sample was normalized by dividing it by the reflected spectrum from the water reference sample. The cell holding the rattle crystal furthermore included 2 copper wires approximately 7 mm apart that were used to apply an electric field.

6.2.5. Debye-Waller factors

The Debye-Waller factor correlates a decrease of Bragg peak intensities with increased average displacement of a particle from its lattice position and increasing Miller indices as caused by thermal fluctuations of the atoms/particles around their equilibrium crystal positions.^{303,304} In this work they are used to explain the differences in the optical response of 3D colloidal crystals of rattle-type particles with and without electric fields. The intensity for scatterers that can move from their lattice position I is related to the scattering intensity of a lattice with fixed scatterers I_0 via^{303,304}

$$\frac{I}{I_0} = \exp\left(-\frac{1}{3}\langle u^2 \rangle G^2\right), \quad (6.4)$$

where $u(t)$ is the distance of the particle from its equilibrium position, \mathbf{G} is the reciprocal lattice vector of the Bragg reflection, and the brackets $\langle \rangle$ indicate a time average. The particle excursions have been assumed isotropic. The exponential term in Equation 6.4 is known as the Debye-Waller factor. The magnitude of the reciprocal lattice vector $|\mathbf{G}|$ is related to the spacing d_{hkl} between planes with Miller indices h, k, l via

$$|\mathbf{G}| = \frac{2\pi}{d_{hkl}}, \quad (6.5)$$

and d_{hkl} for a cubic system is related to the fcc lattice constant a_{fcc} via

$$d_{hkl} = \frac{a_{\text{fcc}}}{\sqrt{h^2 + k^2 + l^2}}. \quad (6.6)$$

The nearest neighbour distance r_{nn} in an fcc lattice with lattice constant a_{fcc} is given by

$$r_{\text{nn}} = \frac{a_{\text{fcc}}}{\sqrt{2}}, \quad (6.7)$$

so that we obtain for the Debye-Waller factor of an fcc crystal:

$$\frac{I}{I_0} = \exp\left(-\frac{2}{3}\pi^2 \frac{\langle u^2 \rangle}{r_{\text{nn}}^2} (h^2 + k^2 + l^2)\right). \quad (6.8)$$

This allows us to calculate the expected change in Bragg peak intensity between the electric field on and off if we know the Miller indices, the nearest neighbour distance r_{nn} and the averaged squared distance of the particle from the lattice position $\langle u^2 \rangle$. This is possible because the scattering of the shell can be neglected compared to the scattering of the core according to Mie theory.³⁰⁵ The scattering of the shell is discussed later in the chapter.

To calculate the Debye-Waller factor for our experimental system, we require knowledge about the time-averaged squared distance $\langle u^2 \rangle$ of the particle from its equilibrium position. For this we require knowledge of the probability to find the particle anywhere in the shell

at a given time. To that end, we performed finite-element calculations using the COMSOL MultiPhysics Modeling Software (v5.4) to calculate the electrostatic repulsion between the core particle and the inner part of the shell. We set up an axisymmetric system with a spherical colloid within a spherical shell, and we solved the non-linearized Poisson-Boltzmann equation with constant surface potential boundary conditions on the surface of the particle and shell. The electric force on the core particle was determined by integrating the Maxwell electric stress tensor over the surface of the core particle. The electric forces on the core particle at radial positions u from the center of the shell were used to construct the electrostatic contribution to the interaction potential $U(u)$. Due to the relatively long-ranged repulsion, van der Waals forces were not taken into account.

The interaction potential $U(u)$ was translated into a probability $P(u)$ of finding the particle a certain radial distance from the center via the Boltzmann relation

$$P(u) = \exp\left(-\frac{U(u)}{k_B T}\right), \quad (6.9)$$

where k_B is the Boltzmann constant and T is the absolute temperature in Kelvin. We determined the time-averaged squared displacement of the core particle from the center of the shell via

$$\langle u^2 \rangle = \frac{\sum_i P(u_i) u_i^2}{\sum_i P(u_i)}. \quad (6.10)$$

Inserting Equation 6.10 in Equation 6.8 allows us to calculate the difference in Bragg peak intensity between the equilibrium state of the rattle crystal and the rattle crystal with a field applied.

6.3. RESULTS & DISCUSSION

6.3.1. Real-space switchable crystal

In Chapter 5, we found that application of an AC electric field could lead to orthogonal or parallel motion of the core particle depending on the frequency of the electric field. To understand which of these motions are useful to realize a switchable colloidal crystal, we assembled a monolayer of rattle particles by solvent evaporation on a glass slide with two copper electrodes (Figure 3b). The rattle particles had a core radius of 165 ± 10 nm, an outer shell radius of 345 ± 10 nm, and a shell thickness of 30 nm. Immediately after the original solvent (water) was evaporated, a solution of 85v% DMSO/15v% (refractive index $n = 1.46$ at 25°C and wavelength $\lambda = 546$ nm)³⁰⁰ water with 2.0 mM LiCl ($\kappa^{-1} = 5.4$ nm) was added. Hexagonal packing of shells was observed in several regions. We applied electric fields of different frequencies and observed the motions of several cores, where the shells were packed in a hexagonal pattern. The results are shown in Figure 4. It was found that the particles were confined in one direction for an electric field of 4 kHz (200 V mm^{-1} , Figure 4b). However, in the direction perpendicular to the electric field the particles moved independent of the other particles close to it. At a certain moment in time, the particles would be at different positions within their shells due to the Brownian motion in the direction orthogonal to the electric field direction. As such, no hexagonal arrangement of the core particles was observed. However, for an electric field of 5 Hz (25 V mm^{-1}) the particles moved collectively in the direction of

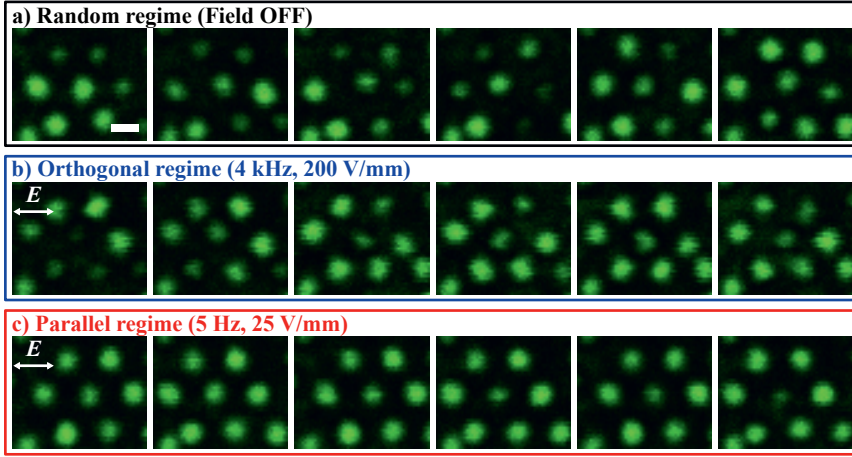


Figure 4: Frames of confocal microscopy image series of electric-field induced changes in hexagonally ordered rattle particles in 85/15 v% DMSO/water with 2.0 mM LiCl. The consecutive frames in each row are separated in time by 0.09 s. a) Particles when the electric field is OFF. b) Particles when an electric field of 4 kHz is applied with a field strength of 200 V mm^{-1} . c) Particles when an electric field of 5 Hz is applied with a field strength of 25 V mm^{-1} . The scalebar in represents 500 nm and all images are at the same magnification. The pixel size is 41.3 nm and the frame time is 0.022 s.

the electric field, while hardly moving in the other directions. As a result, hexagonal order of the core particles was observed in Figure 4c.

Figure 5 schematically shows how the cores moved with respect to the shell and how this can be visualized when the shell is index-matched. Clearly, while the core particles moved significantly compared to the shells in the parallel regime, they did not move with respect to the other cores around them because they all moved coherently, which lead to the hexagonal order of the core particles.

Next, we analyzed the particle positions with the electric field (1 Hz , 25 V mm^{-1}) off and on over a larger area (Figure 6). The lattice structure formed by the core particles was greatly enhanced with the electric field on. In Figure 6e we observed that the radial distribution function $g(r)$ showed sharp peaks when the electric field was turned on, while those peaks were flattened when the electric field was off. However, average long-ranged order was still present even when the electric field was off, due to the arrangement of the shells on a hexagonal lattice. We also found that switching the electric field off and on led to a reversible change in $g(r)$ (Figure 6f). Lastly, in Figure 6g it was shown via the local bond order parameter q_6 that the local hexagonal order is much more pronounced when the electric field is on. We conclude that an AC electric field of low frequency was able to reversibly change the structure of the core particles within shells when those shells are assembled on a lattice.

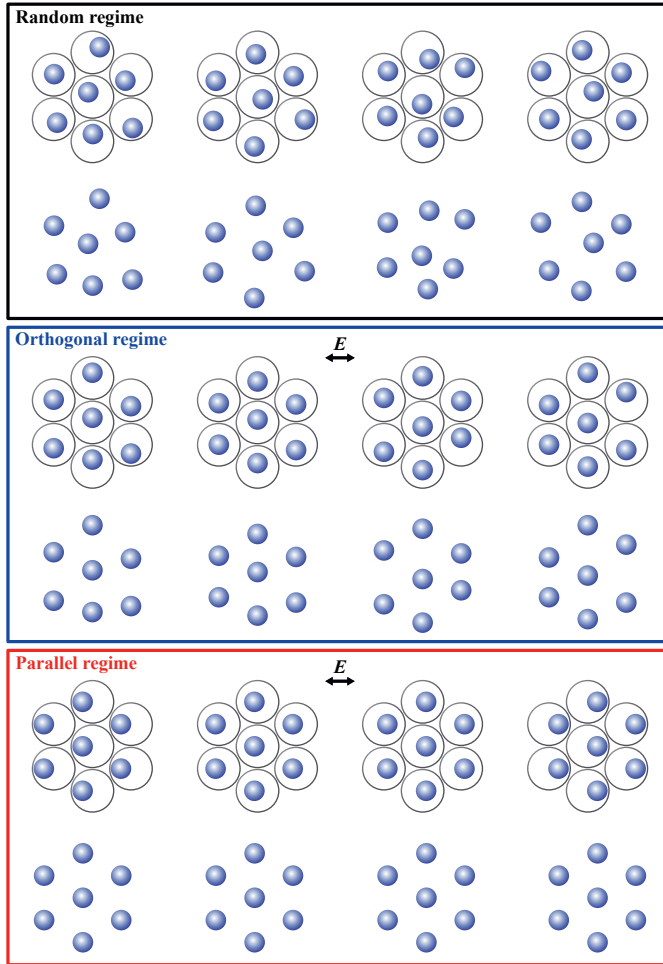


Figure 5: Rattle-type particles consisting of a mobile core particle within a shell, where the shells are assembled on a hexagonal lattice. The random, orthogonal and parallel regimes from Figure 4 are represented. The motion of the core within the shell, as well as what the arrangement of cores looks like when the shell is index-matched is shown.

6.3.2. Strength of Bragg scattering

An important characteristic of a crystal of rattle particles is the optical response, which was measured with and without electric field by our collaborators from Tohoku University. They obtained a 3D crystal of rattle particles via sedimentation in 2.0 mM LiCl in water. As the experiments were done in water, the shell was not index matched. The relative scattering cross section of the shells compared to the cores was calculated via Mie theory³⁰⁵ to elucidate whether the scattering of the shells was negligible. At a wavelength of 700 nm the scattering

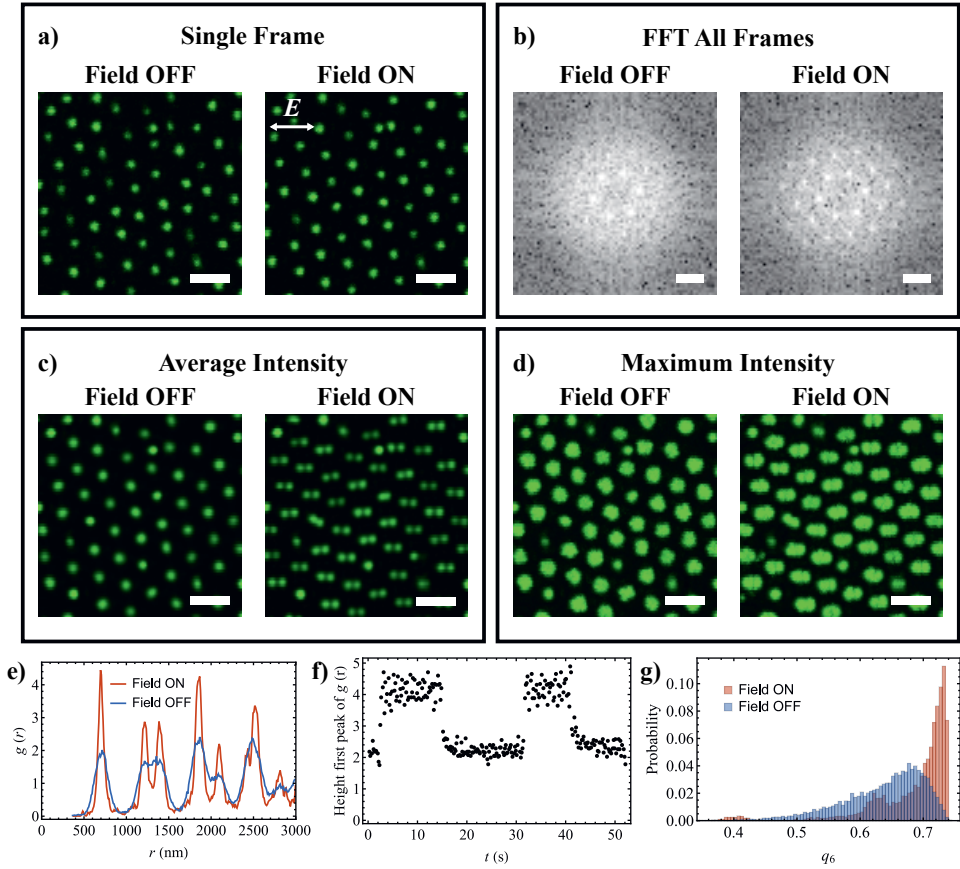


Figure 6: Confocal microscopy results of electric-field (1 Hz, 25 V mm⁻¹) induced changes in assemblies of rattle particles in 85/15 v% DMSO/water with 2.0 mM LiCl. Only the STS core was visible in reflection mode. The electric field had a strength of 25 V mm⁻¹ and a frequency of 1 Hz. a) Single frames taken from the confocal image series with the electric field OFF and ON. b) FFT averaged over many frames with the electric field OFF and ON. c) Average intensity of the frames in the image series with the electric field OFF and ON. d) Maximum intensity of the frames in the image series with the electric field OFF and ON. The scalebar in a) and c-d) represents 1 μm . The scalebar in b) indicates 2 μm^{-1} . The pixel size is 40.4 nm and the frame time is 0.04 s. e) The radial distribution function $g(r)$ averaged over frames with the electric field either ON or OFF. f) Time-dependent height of the first peak in the radial distribution function $g(r)$ to showcase the fast switching by switching the electric field ON and OFF. g) Local bond order parameter q_6 , which can detect hexagonal order, for frames with the electric field either ON or OFF.

cross section of the shell with outer diameter 690 nm and shell thickness 29 nm and a refractive index of $n = 1.45$ in water ($n = 1.33$) was calculated to be $C_{\text{Sca,shell}} = 3.9 \cdot 10^3 \text{ nm}^2$. For the same wavelength a core with diameter 320 nm and a refractive index of $n = 1.95$ had a

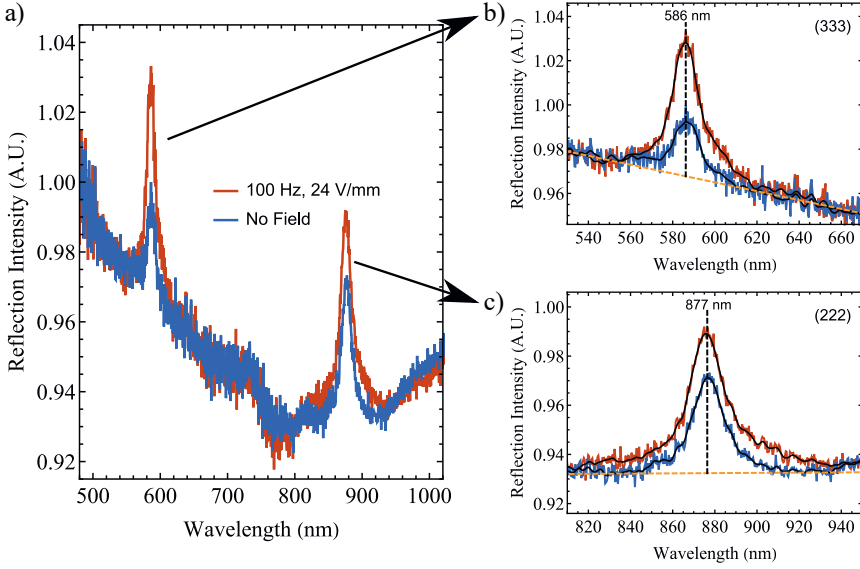


Figure 7: Optical response of an experimental 3D assembly of rattle particles in water (2.0 mM LiCl) with or without an AC electric field (100 Hz at 24 V mm^{-1}). a) Reflection intensity over a large wavelength range. b-c) Close-up of the (222) and (333) reflections of the fcc crystal of rattle particles, respectively. The black line through the optical data is the smoothed data that was used to determine the peak intensities. The orange dashed line indicates the baseline used to determine intensities of the reflection peaks with and without electric field. The optical experiments were performed at Tohoku University, by Hikaru Namigata under the supervision of Kanako Watanabe and Daisuke Nagao.

scattering cross-section of $C_{\text{Sca,core}} = 1.1 \cdot 10^5 \text{ nm}^2$. The refractive index of the core was estimated from the refractive index of silica and titania ($n_S = 1.46$ and $n_T = 2.45$) and the volume of the respective layers (radii $R_S = 90 \text{ nm}$, $R_{ST} = 140 \text{ nm}$, and $R_{STS} = 160 \text{ nm}$) via an effective medium approach. Since the scattering strength of the core is 28 times larger than that of the shell, it is reasonable to assume that the main scattering contribution in the optical experiments is due to the core particles. The optical results of a 3D crystal of rattles particles in 2.0 mM LiCl in water are shown in Figure 7. Two peaks were visible at 586 and 875 nm. These peaks were attributed to the (333) and (222) reflection of an fcc crystal of rattle particles, respectively. From the optical data we calculated the distance between the crystal planes from experimental results via

$$m\lambda = 2d_{\text{hkl}}\sqrt{n^2 - \sin^2\theta}, \quad (6.11)$$

where m is the order of the reflection, λ is the wavelength of the reflection, d_{hkl} is the distance between atomic planes with Miller indices (hkl), n is the refractive index of the medium and θ is the angle between the incident light and the normal direction. For $m = 2$, $\lambda = 877 \text{ nm}$, $n = 1.376$ and $\theta = 0 \text{ rad}$ we obtained $d_{111} = 637.4 \text{ nm}$. For $m = 3$, $\lambda = 586 \text{ nm}$, $n = 1.376$

and $\theta = 0$ rad the result was $d_{111} = 638.8$ nm. We obtained a similar value for d_{111} from both peaks, so we take the mean to obtain $d_{111} = 638.1$ nm.

Next we calculated the nearest neighbour distances for the crystal of rattle particles. Using Equations 6.7 and 6.6 we calculated the nearest neighbour distance r_{nn} as follows

$$r_{nn} = d_{111} \sqrt{\frac{3}{2}} = 781.5 \text{ nm.} \quad (6.12)$$

This is a reasonable value as the outer shell diameter was 690 nm and there was likely electrostatic repulsion between the shells.

Interestingly, the intensity of the two peaks in Figure 7 is increased by the application of an electric field of 100 Hz at 24 V mm^{-1} . This is likely a direct result of the core particles being confined to a more ordered lattice as observed in the real-space experiments in Figure 6. Note that the frequency in the real-space experiments (1 Hz) was much lower than the optical experiments (100 Hz), because the imaging system had to be capable of following the core particle motion in the real-space experiments. The parallel motion, however, was likely to be the same in both experiments (see Chapter 5).

Next, we analyzed the ratio between the peak intensities with the electric field off and on (100 Hz) in more detail. Because the data were relatively noisy the data were smoothed using a Gaussian filter (Mathematica V12.2, with a kernel of radius 2.5 nm), which resulted in the black curves in Figure 7b-c. Furthermore, we used a linear baseline drawn across the bottom of the peak (dashed, orange line in Figure 7b-c). These allowed us to more accurately determine the peak intensity. We found a peak intensity ratio between the field off and on of 0.68 for the (222) reflection and 0.44 for the (333) reflection. We estimate the error on the experimentally found peak intensity ratios at a few percent.

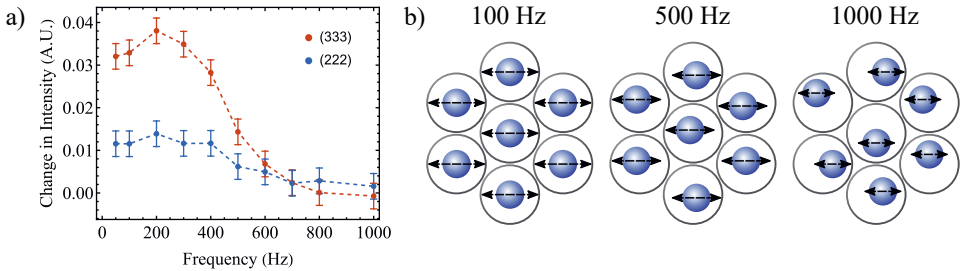


Figure 8: Change in intensity of the Bragg reflections of the (222) and (333) peaks as a function of electric field frequency compared to the reflection intensity without electric field (as in Figure 7). The electric field strength was 24 V mm^{-1} . The optical experiments were performed at Tohoku University, by Hikaru Namigata under the supervision of Kanako Watanabe and Daisuke Nagao.

In a second experiment, the peak intensity as function of electric field frequency was investigated (Figure 8). The electric field strength was 24 V mm^{-1} . For frequencies lower than approximately 300 Hz the peak intensity was relatively constant, which was likely because for such low frequencies the core particle was moved from one end of the shell to the other by the

electric field. Between 300 and 700 Hz the peak intensity decreased gradually with increasing frequency. For these frequencies the particles were unable to move through the whole shell before the field changed direction, which means that the cores are not collectively moving at exactly the same space within the shell. This is visualized in Figure 8b. At higher frequency the core particle is hardly moved by the electric field at all and as such the collective motion behavior of the core particles was lost.

To understand the increase in intensity of the reflection peaks for the field off and on (at 100 Hz) we calculated Debye-Waller factors for our system. If we assume that the crystal of cores is perfect when the field is switched on, the Debye-Waller factor describes the relative peak intensity when the field is off. The Debye-Waller factor describes an exponential decay of Bragg intensities with increasing amplitude of the random thermal motion from the center of the lattice position of a particle and with increasing sum of the squares of the Miller indices of the reflection. For an fcc crystal the Debye-Waller factor is given on the right-hand side of

$$\frac{I}{I_0} = \exp\left(-\frac{2}{3}\pi^2 \frac{\langle u^2 \rangle}{r_{nn}^2} (h^2 + k^2 + l^2)\right). \quad (6.13)$$

Here $\langle u^2 \rangle$ is the mean square distance from its equilibrium position, r_{nn} is the distance between nearest neighbours and h , k and l are the Miller indices. The maximum excursions from its equilibrium position can be tuned in our system by changing the salt concentration. A higher salt concentration allows the particle to approach the shell more closely, which results in a larger average squared distance $\langle u^2 \rangle$ of the particle from its equilibrium position and thus in a smaller Debye-Waller factor.

From experiments, we know that $r_{nn} = 781.5$ nm and the salt concentration is 2 mM. The salt concentration determined the average squared distance $\langle u^2 \rangle$, via the electrostatic repulsion between the core and shell. We calculated the electrostatic repulsion as an interaction potential $U(u)$ between the core particle (core radius $R_{\text{core}} = 165$ nm, core surface potential $\psi_{\text{core}} = -50$ mV) and the inner shell wall (inner shell radius $R_{\text{shell,inner}} = 315$ nm, inner shell surface potential $\psi_{\text{shell,inner}} = -60$ mV) using finite-element calculations. Via the Boltzmann relation the interaction potential can be translated to a probability to find the core particle a certain distance u from the equilibrium position, which can be used to calculate $\langle u^2 \rangle$. The Debye-Waller factors calculated via Equation 6.13 are 0.69 for the (222) reflection and 0.43 for the (333) reflection. The experimental and calculated Debye-Waller factors are given in Table 1 and agree excellently. We furthermore measure $\langle u^2 \rangle$ from the projected data obtained from confocal experiments with the field off as shown in Figure 6. While this data is a 2D projection of a 3D system it still gives a good estimate of what the Debye-Waller factor should be according to the experimental confocal data and Equation 6.13. Table 1 shows that the real-space experiments yield similar Debye-Waller factors as the optical experiments and the calculations, which shows that the Debye-Waller factor can indeed explain the peak height change, despite the shell not being index-matched.

Because the calculated Debye-Waller factors and the peak intensity ratios between the Bragg peaks with the electric field off and on agree well, we used the Debye-Waller factors to investigate theoretically how the peak intensity ratio could be improved. The ideal ratio is as low as possible, to have the biggest difference in peak intensities between the electric field off

	exp. (optical)	exp. (real space)*	calc.
$\langle u^2 \rangle$ (nm)	-	2426 ± 243	2859
I/I_0 (222)	0.68	0.73 ± 0.02	0.69
I/I_0 (333)	0.44	0.49 ± 0.03	0.43

Table 1: The particle mean square distance from the equilibrium position and the corresponding Debye-Waller factors for an fcc crystal of rattle-type particles. The values are given for the optical experiments, the real-space experiments and the calculations. For the optical experiments we only had access to the Debye-Waller factor I/I_0 . For the calculations the Debye-Waller factors were calculated from $\langle u^2 \rangle$ obtained from finite-element calculations. *For the real-space experiments we obtained $\langle u^2 \rangle$ from projected confocal microscopy data and calculated the Debye-Waller factor. Since the confocal experiments show a 2D projection of a 3D system $\langle u^2 \rangle$ is likely underestimated and I/I_0 are likely overestimated.

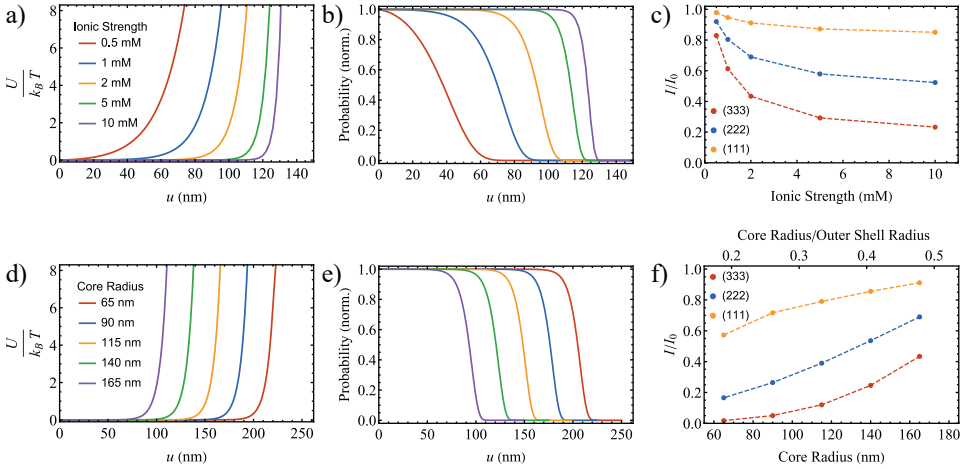


Figure 9: Calculations for the Debye-Waller factor as function of the ionic strength and core size. The nearest neighbour distance r_{nn} is kept constant at 780 nm. a-c) Influence of the ionic strength on the Debye-Waller factor for an fcc crystal of rattle particles with core radius $R_{\text{core}} = 165$ nm, inner shell radius $R_{\text{shell,inner}} = 315$ nm and outer shell radius $R_{\text{shell,outer}} = 345$ nm. a) Interaction potential between core and shell as function of distance from the middle of the shell u . b) Probability to find the core a certain distance from the middle of the shell. c) Debye-Waller factor I/I_0 as function of salt concentration for the reflections of the (111), (222) and (333) planes. d-f) Influence of the core particle radius on the Debye-Waller factor for an fcc crystal of rattle particles with inner shell radius $R_{\text{shell,inner}} = 315$ nm, outer shell radius $R_{\text{shell,outer}} = 345$ nm and an ionic strength of 2 mM. d) Interaction potential between core and shell as function of distance from the middle of the shell u and e) probability to find the core a certain distance from the middle of the shell for different core radii. f) Debye-Waller factor I/I_0 as function of core radius for the reflections of the (111), (222) and (333) planes.

and on. The parameter that we can use to tune the Debye-Waller factor in Equation 6.13 is $\langle u^2 \rangle$. One way to tune this parameter is by adjusting the salt concentration. The higher the salt concentration the shorter the range of the repulsion between the core and the inner shell wall. We calculate how the Debye-Waller factor can be improved, while keeping the nearest neighbour distance r_{nn} and outer/inner shell diameter constant in Figure 9. The electrostatic interaction potential between the core particle and the inner shell wall as function of the particle position from the equilibrium position for various salt concentrations is shown in Figure 9a. This is translated to the probability of finding the particle a certain distance from the equilibrium position in Figure 9b, which was used to calculate the Debye-Waller factors for different salt concentrations and Miller indices in Figure 9c. The Debye-Waller factor decreased for increasing ionic strength, but for an ionic strength higher than 5 mM only a minimal decrease was observed. The Debye-Waller factor can be decreased from 0.43 for 2 mM to 0.23 for 10 mM for the (333) reflection, but great enhancements cannot be achieved this way. This is because the shell size limits how far the core particle is able to move from its equilibrium position, even at high salt concentrations. In Figure 9d-f we investigated how the Debye-Waller factor can be tuned for different core sizes, while keeping the shell size the same, at an ionic strength of 2 mM. We found that by decreasing the core size, and with that the core/shell size ratio, the Debye-Waller factor decreases significantly. For example, by decreasing the core radius from 165 nm to 90 nm (which decreases the size ratio between the core and outer shell radius from 0.48 to 0.26) the Debye-Waller factor for the (333) reflection is decreased from 0.43 to 0.050. As such, decreasing the core/shell size ratio is a viable route to decreasing the Debye-Waller factor and increasing the difference between Bragg peak intensities with the electric field off and on in order to achieve a fully responsive photonic crystal. However, since the scattering intensity also strongly decreases as the core radius decreases, having a small core is undesirable.

A decrease in the core/shell size ratio can be achieved by either making the core particle radius smaller or the shell radius larger. If the outer shell radius is increased, the lattice constant of the crystal is also increased, which shifts the Bragg peaks to higher wavelengths. Increasing the shell radius is easier than decreasing the core particle radius and is a viable way to realize RPCs in the infrared region. To realize RPCs in the visible region, the shell size should remain the same and the core particle size should be decreased to decrease the core/shell size ratio. A problem is that making small particles usually leads to a higher polydispersity. For example, it becomes increasingly more difficult to synthesize monodisperse particles of the high refractive index material TiO_2 at smaller sizes.¹²⁷ Luckily, for a crystal of rattle particles, the polydispersity of the outer shell radius is key and can partially compensate the more polydisperse small core particles.²²⁰

Furthermore, it is clear from Figure 9 that the (333) reflection is a more promising candidate for attaining a significantly switchable Bragg peak in comparison to the (111) reflection as the Debye-Waller factor for the (111) reflection hardly decreases for a smaller core size or higher salt concentration. As such the current size of the shell, which is good for the (333) reflection being in the visible wavelength regime, is optimal for a switchable photonic crystal in the visible wavelength regime.

Lastly, we briefly comment that interesting direction-dependent optical responses should be achievable using electric fields at frequencies for which orthogonal motion was observed in Chapter 5 and Figure 4. In that frequency regime the core particles are hindered to move in the direction parallel to the electric field. Due to the factor $\langle (\mathbf{G} \cdot \mathbf{u})^2 \rangle$ in its derivation,^{303,304} the Debye-Waller factor is sensitive to the particle excursions parallel to the reciprocal lattice vector. By restricting the mobility of the particle in one direction but not in another, some peaks of, for example, the six (222) reflections would increase but not others. This gives rise to direction-dependent optical switching. In the optical experiment described in this Chapter we did not observe such effects. The reasons are twofold. First, we observed the direction perpendicular to the wall of the cuvette in Figure 3c, which is the direction of \mathbf{G} , so that the described effect does not show up. Second, the electric field strength in the optical experiments (24 V mm^{-1}) was likely not enough to significantly disturb double layers, which means the motion of the core particle in the parallel direction is not hindered at the relevant frequencies.

6.4. CONCLUSION

In summary, rattle particles were used as building blocks for a switchable colloidal crystal. With real-space confocal microscopy experiments we found that a low frequency electric field ($< 1 \text{ kHz}$) collectively moved the particles parallel to the electric field direction from one side of the shell to the opposing side, while the particles move randomly within the shell *via* Brownian motion when no field was applied. Higher frequencies (approximately 4 kHz) led to restrictions of excursions parallel to the electric field, but the Brownian motion in the direction orthogonal to the electric field prevented the core particles from being arranged on a lattice. The parallel motion of the core particles at low frequencies was found to significantly increase the peaks in the radial distribution function compared to the case with no electric field applied, which was a reversible process.

Excitingly, the reflections from Bragg peaks in a 3D rattle crystal in water with 2.0 mM LiCl increased in intensity when an electric field of low enough frequency ($< 300 \text{ Hz}$ at 24 V mm^{-1}) was applied. It demonstrated a switchable photonic crystal without changes in interparticle spacings and/or symmetry of the crystal. The peak intensity ratio between electric field off and on was around 0.44 for the (333) reflection of an fcc crystal of rattle particles. The peak intensity ratio between the state where the electric field was off and on could be well explained by calculation of the Debye-Waller factors for the relevant reflections. We used Debye-Waller factors to calculate strategies on how to improve the peak intensity ratio. It was found that, while a higher salt concentration could still improve the ratio slightly, it is most efficient to increase the core/shell size ratio of the rattle particles. However, the scattering strength of the cores has to still be sufficient, which puts a lower limit on the core particle size. Calculations predict that by decreasing the core/shell size ratio to 0.2 a better switchable photonic crystal could be realized where the peak intensity of the (333) reflection with an electric field would be a factor 50 or more higher compared to the equilibrium state. As such, the proof-of-concept as presented in this chapter can still be significantly improved in future work.

AUTHOR CONTRIBUTIONS

Hikaru Namigata (Tohoku University) synthesized the rattle-type particles and performed the optical reflection experiments under supervision of Kanako Watanabe (Tohoku University) and Daisuke Nagao (Tohoku University). Kanako Watanabe helped with the confocal experiments. Tom A.J. Welling did the confocal experiments together with Kanako Watanabe (Tohoku University). Tom A.J. Welling analyzed the confocal data and calculated the Debye-Waller factors.

ACKNOWLEDGEMENTS

We thank Kanako Watanabe for critical reading of the chapter. We thank Arnout Imhof for his suggestion of using Debye-Waller factors to explain the optical results and critical reading of the chapter. Lastly, great appreciation goes out to Daisuke Nagao for establishing the project and for the fruitful collaboration.

Bibliography

- [1] Daniel H. Deutsch. Did Brown observe Brownian motion: probably not. *Bull. Am. Phys. Soc. Abstr.*, 36:1374, 1991.
- [2] Gerhard C. Cadée. Brownian emotion. *Nature*, 354:180, 1991.
- [3] Robert Brown. A brief account of microscopical observations made in the months of June, July and August 1827, on the particles contained in the pollen of plants; and on the general existence of active molecules in organic and inorganic bodies. *The Philosophical Magazine*, 4(21):161–173, 1828.
- [4] Daniel H. Deutsch. Brownian motion. *Nature*, 357:354, 1992.
- [5] Brian J. Ford. Brown’s observations confirmed. *Nature*, 359:265, 1992.
- [6] A. Einstein. Über die von der molekularkinetischen Theorie der Wärme geforderte Bewegung von in ruhenden Flüssigkeiten suspendierten Teilchen. *Annalen der Physik*, 322(8):549–560, 1905.
- [7] Ronald Newburgh, Joseph Peidle, and Wolfgang Rueckner. Einstein, Perrin, and the reality of atoms : 1905 revisited. *American Journal of Physics*, 74(6):478–481, 2006.
- [8] U. Gasser, E. R. Weeks, A. Schofield, P. N. Pusey, and D. A. Weitz. Real-space imaging of nucleation and growth in colloidal crystallization. *Science*, 292(5515):258–262, 2001.
- [9] David G. Grier and Cherry A. Murray. The microscopic dynamics of freezing in supercooled colloidal fluids. *The Journal of Chemical Physics*, 100(12):9088–9095, 1994.
- [10] K. Sandomirski, S. Walta, J. Dubbert, E. Allahyarov, A. B. Schofield, H. Löwen, W. Richtering, and S. U. Egelhaaf. Heterogeneous crystallization of hard and soft spheres near flat and curved walls. *European Physical Journal: Special Topics*, 223(3):439–454, 2014.
- [11] M. Hermes, E. C.M. Vermolen, M. E. Leunissen, D. L.J. Vossen, P. D.J. van Oostrum, M. Dijkstra, and A. van Blaaderen. Nucleation of Colloidal Crystals on Configurable Seed Structures. *Soft Matter*, 7(10):4623–4628, 2011.
- [12] P. N. Pusey. Liquids, freezing and the glass transition. *Les Houches Summer Schools of Theoretical Physics Session LI (1989)*, 1991.
- [13] C. Patrick Royall, Mirjam E. Leunissen, Antti-Pekka Hynninen, Marjolein Dijkstra, and Alfons van Blaaderen. Re-entrant melting and freezing in a model system of charged colloids. *Journal of Chemical Physics*, 124(24), 2006.
- [14] Fiorenza Rancan, Qi Gao, Christina Graf, Stefan Troppens, Sabrina Hadam, Steffen Hackbarth, Cynthia Kembuan, Ulrike Blume-Peytavi, Eckart Rühl, Jürgen Lademann, and Annika Vogt. Skin penetration and cellular uptake of amorphous silica nanoparticles with variable size, surface functionalization, and colloidal stability. *ACS Nano*, 6(8):6829–6842, 2012.
- [15] Andrea R. Tao, Susan Habas, and Peidong Yang. Shape control of colloidal metal nanocrystals. *Small*, 4(3):310–325, 2008.
- [16] Mirjam E. Leunissen, Christina G. Christova, Antti-Pekka Hynninen, C. Patrick Royall, Andrew I. Campbell, Arnout Imhof, Marjolein Dijkstra, René van Roij, and Alfons van Blaaderen. Ionic colloidal crystals of oppositely charged particles. *Nature*, 437(7056):235–240, 2005.
- [17] Ahmet Faik Demirörs, Johan C.P. Stiefelhagen, Teun Visser, Frank Smalenburg, Marjolein Dijkstra, Arnout Imhof, and Alfons van Blaaderen. Long-ranged oppositely charged interactions for designing new types of colloidal clusters. *Physical Review X*, 5(2):1–12, 2015.
- [18] Jianzhong Wu, Bo Zhou, and Zhibing Hu. Phase Behavior of Thermally Responsive Microgel Colloids. *Physical Review Letters*, 90(4):4, 2003.

- [19] Hanumantha Rao Vutukuri, Stéphane Badaire, D. A. Matthijs de Winter, Arnout Imhof, and Alfons van Blaaderen. Directed Self-Assembly of Micron-Sized Gold Nanoplatelets into Oriented Flexible Stacks with Tunable Interplate Distance. *Nano Letters*, 15(8):5617–5623, 2015.
- [20] Zewei Quan, Hongwu Xu, Chenyu Wang, Xiaodong Wen, Yuxuan Wang, Jinlong Zhu, Ruipeng Li, Chris J. Sheehan, Zhongwu Wang, Detlef M. Smilgies, Zhiping Luo, and Jiye Fang. Solvent-mediated self-assembly of nanocube superlattices. *Journal of the American Chemical Society*, 136(4):1352–1359, jan 2014.
- [21] Teun Vissers, Alfons van Blaaderen, and Arnout Imhof. Band formation in mixtures of oppositely charged colloids driven by an ac electric field. *Physical Review Letters*, 106(22):106–109, 2011.
- [22] A. van Blaaderen, M. Dijkstra, R. van Roij, A. Imhof, M. Kamp, B. W. Kwaadgras, T. Vissers, and B. Liu. Manipulating the self assembly of colloids in electric fields. *European Physical Journal: Special Topics*, 222(11):2895–2909, 2013.
- [23] Ahmet Faik Demirörs, Patrick M. Johnson, Carlos M. van Kats, Alfons van Blaaderen, and Arnout Imhof. Directed self-assembly of colloidal dumbbells with an electric field. *Langmuir*, 26(18):14466–14471, 2010.
- [24] Mirjam E. Leunissen, Hanumantha Rao Vutukuri, and Alfons van Blaaderen. Directing colloidal self-assembly with biaxial electric fields. *Advanced Materials*, 21(30):3116–3120, 2009.
- [25] Tao Ding, Kai Song, Koen Clays, and Chen Ho Tung. Fabrication of 3D photonic crystals of ellipsoids: Convective self-assembly in magnetic field. *Advanced Materials*, 21(19):1936–1940, may 2009.
- [26] James W. Swan, Jonathan L. Bauer, Yifei Liu, and Eric M. Furst. Directed colloidal self-assembly in toggled magnetic fields. *Soft Matter*, 10(8):1102–1109, 2014.
- [27] Kaori Kamata, Yu Lu, and Younan Xia. Synthesis and Characterization of Monodispersed Core-Shell Spherical Colloids with Movable Cores. *Journal of the American Chemical Society*, 125(9):2384–2385, 2003.
- [28] Magdalena Priebe and Katharina M. Fromm. Nanorattles or Yolk-Shell Nanoparticles - What Are They, How Are They made, and What Are They Good For? *Chemistry - A European Journal*, 21(10):3854–3874, 2014.
- [29] Zhaogang Teng, Shouju Wang, Xiaodan Su, Guotao Chen, Ying Liu, Zhimin Luo, Wei Luo, Yuxia Tang, Huangxian Ju, Dongyuan Zhao, and Guangming Lu. Facile Synthesis of Yolk-Shell Structured Inorganic-Organic Hybrid Spheres with Ordered Radial Mesochannels. *Advanced Materials*, 26(22):3741–3747, 2014.
- [30] Rahul Purbia and Santanu Paria. Yolk/Shell Nanoparticles: Classifications, Synthesis, Properties, and Applications. *Nanoscale*, 7(47):19789–19873, 2015.
- [31] Jian Liu, Shi Zhang Qiao, Jun Song Chen, Xiong Wen Lou, Xianran Xing, and Gao Qing Lu. Yolk/Shell Nanoparticles: New Platforms for Nanoreactors, Drug Delivery and Lithium-Ion Batteries. *Chemical Communications*, 47(47):12578–12591, 2011.
- [32] Ahmet Faik Demirörs, Alfons van Blaaderen, and Arnout Imhof. Synthesis of Eccentric Titania-Silica Core-Shell and Composite Particles. *Chem. Mater.*, 21(6):979–984, 2009.
- [33] Ayako Okada, Daisuke Nagao, Takuya Ueno, Haruyuki Ishii, and Mikio Konno. Colloidal Polarization of Yolk/Shell Particles by Reconfiguration of Inner Cores Responsive to an External Magnetic Field. *Langmuir*, 29(28):9004–9009, 2013.
- [34] Kanako Watanabe, Haruyuki Ishii, Mikio Konno, Arnout Imhof, Alfons van Blaaderen, and Daisuke Nagao. Yolk/Shell Colloidal Crystals Incorporating Movable Cores with Their Motion Controlled by an External Electric Field. *Langmuir*, 33(1):296–302, 2017.
- [35] Gonzalo Prieto, Harun Tüysüz, Nicolas Duyckaerts, Johannes Knossalla, Guang Hui Wang, and Ferdi Schüth. Hollow Nano- and Microstructures as Catalysts. *Chemical Reviews*, 116(22):14056–14119, 2016.
- [36] Daisuke Nagao, Carlos M. van Kats, Kentaro Hayasaka, Maki Sugimoto, Mikio Konno, Arnout Imhof, and Alfons van Blaaderen. Synthesis of Hollow Asymmetrical Silica Dumbbells with a Movable Inner Core. *Langmuir*, 26(7):5208–5212, 2010.

- [37] Longfei Tan, Dong Chen, Huiyu Liu, and Fangqiong Tang. A Silica Nanorattle with a Mesoporous Shell: An Ideal Nanoreactor for the Preparation of Tunable Gold Cores. *Advanced Materials*, 22(43):4885–4889, 2010.
- [38] Anderson G.M. Da Silva, Thenner S. Rodrigues, Valquírio G. Correia, Tiago V. Alves, Rafael S. Alves, Rômulo A. Ando, Fernando R. Ornellas, Jiale Wang, Leandro H. Andrade, and Pedro H.C. Camargo. Plasmonic Nanorattles as Next-Generation Catalysts for Surface Plasmon Resonance-Mediated Oxidations Promoted by Activated Oxygen. *Angewandte Chemie - International Edition*, 55(25):7111–7115, 2016.
- [39] Joongoo Lee, Ji Chan Park, and Hyunjoon Song. A Nanoreactor Framework of a Au@SiO₂ Yolk/Shell Structure for Catalytic Reduction of *p*-Nitrophenol. *Advanced Materials*, 20(8):1523–1528, 2008.
- [40] Chun Hong Kuo, Yang Tang, Lien Yang Chou, Brian T. Sneed, Casey N. Brodsky, Zipeng Zhao, and Chia Kuang Tsung. Yolk-Shell Nanocrystal@ZIF-8 Nanostructures for Gas-Phase Heterogeneous Catalysis with Selectivity Control. *Journal of the American Chemical Society*, 134(35):14345–14348, 2012.
- [41] Xue Wang, Yapeng He, Yali Ma, Junmin Liu, Yunling Liu, Zhen An Qiao, and Qisheng Huo. Architecture of Yolk-Shell Structured Mesoporous Silica Nanospheres for Catalytic Applications. *Dalton Transactions*, 47(27):9072–9078, 2018.
- [42] Shuang Wu, Joachim Dzubiella, Julian Kaiser, Markus Drechsler, Xuhong Guo, Matthias Ballauff, and Yan Lu. Thermosensitive Au-PNIPAA Yolk-Shell Nanoparticles with Tunable Selectivity for Catalysis. *Angewandte Chemie - International Edition*, 51(9):2229–2233, 2012.
- [43] Lei Fan, Xiangdong Xu, Chunhua Zhu, Jie Han, Lizeng Gao, Juqun Xi, and Rong Guo. Tumor Catalytic-Photothermal Therapy with Yolk-Shell Gold@Carbon Nanozymes. *ACS Applied Materials and Interfaces*, 10(5):4502–4511, 2018.
- [44] Li Sen Lin, Jibin Song, Huang Hao Yang, and Xiaoyuan Chen. Yolk-Shell Nanostructures: Design, Synthesis, and Biomedical Applications. *Advanced Materials*, 30(6):1–30, 2018.
- [45] Lingyu Zhang, Tingting Wang, Lei Yang, Cong Liu, Chungang Wang, Haiyan Liu, Y Andrew Wang, and Zhongmin Su. General Route to Multifunctional Uniform Yolk/Mesoporous Silica Shell Nanocapsules: A Platform for Simultaneous Cancer-Targeted Imaging and Magnetically Guided Drug Delivery. *Chemistry - A European Journal*, 18(39):12512–12521, sep 2012.
- [46] Pengcheng Du and Peng Liu. Novel Smart Yolk/Shell Polymer Microspheres as a Multiply Responsive Cargo Delivery System. *Langmuir*, 30(11):3060–3068, 2014.
- [47] Maryuri Roca and Amanda J. Haes. Silica-Void-Gold Nanoparticles: Temporally Stable Surface-Enhanced Raman Scattering Substrates. *Journal of the American Chemical Society*, 130(43):14273–14279, 2008.
- [48] Binaya K. Shrestha and Amanda J. Haes. Improving Surface Enhanced Raman Signal Reproducibility Using Gold-Coated Silver Nanospheres Encapsulated in Silica Membranes. *Journal of Optics*, 17:114017, 2015.
- [49] Haoqiang Wang, Ruiyu Xu, Han Chen, and Qunhui Yuan. Synthesis of Nitrogen and Sulfur Co-Doped Yolk-Shell Porous Carbon Microspheres and Their Application for Pb(II) Detection in Fish Serum. *Journal of Solid State Chemistry*, 266(March):63–69, 2018.
- [50] Prabhakar Rai, Ji Wook Yoon, Hyun Mook Jeong, Su Jin Hwang, Chang Hoon Kwak, and Jong Heun Lee. Design of Highly Sensitive and Selective Au@NiO Yolk-Shell Nanoreactors for Gas Sensor Applications. *Nanoscale*, 6(14):8292–8299, 2014.
- [51] Kanako Watanabe, Tom A.J. Welling, Sina Sadighikia, Haruyuki Ishii, Arnout Imhof, Marijn A. van Huis, Alfons van Blaaderen, and Daisuke Nagao. Compartmentalization of Gold Nanoparticle Clusters in Hollow Silica Spheres and Their Assembly Induced by an External Electric Field. *Journal of Colloid and Interface Science*, 566:202–210, 2020.

- [52] Shunlong Pan, Jiansheng Li, Gaojie Wan, Chao Liu, Wenhong Fan, and Lianjun Wang. Nanosized Yolk-Shell $\text{Fe}_3\text{O}_4@\text{Zr}(\text{OH})_x$ Spheres for Efficient Removal of Pb(II) from Aqueous Solution. *Journal of Hazardous Materials*, 309:1–9, 2016.
- [53] Linling Zhao, Huarong Liu, Fengwei Wang, and Lai Zeng. Design of Yolk-Shell $\text{Fe}_3\text{O}_4@\text{PMAA}$ Composite Microspheres for Adsorption of Metal Ions and pH-Controlled Drug Delivery. *Journal of Materials Chemistry A*, 2(19):7065–7074, 2014.
- [54] Cuo Wu, Xin Tong, Yuanfei Ai, De Sheng Liu, Peng Yu, Jiang Wu, and Zhiming M. Wang. A Review: Enhanced Anodes of Li/Na-Ion Batteries Based on Yolk-Shell Structured Nanomaterials. *Nano-Micro Letters*, 10(3):1–18, 2018.
- [55] Juan F Galisteo-López, Marta Ibisate, Riccardo Sapienza, and Luis S Froufe-pérez. Self-Assembled Photonic Structures. *Advanced Materials*, 23:30–69, 2011.
- [56] Xin Liu, Yi Zhang, Dengteng Ge, Jiupeng Zhao, and Frank Endres. Three-dimensionally ordered macroporous silicon films made by electrodeposition from an ionic liquid. *Physical Chemistry Chemical Physics*, 14:5100–5105, 2012.
- [57] Vladimir L. Alexeev, Sasmita Das, David N. Finegold, and Sanford A. Asher. Photonic Crystal Glucose-Sensing Material for Noninvasive Monitoring of Glucose in Tear Fluid. *Clinical Chemistry*, 50(12):2353–2360, 2004.
- [58] Jian-tao Zhang, Luling Wang, Daniel N Lamont, Sachin S Velankar, and Sanford A Asher. Fabrication of Large-Area Two-Dimensional Colloidal Crystals. *Angewandte Chemie - International Edition*, 51:6117–6120, 2012.
- [59] Anjal C Sharma, Tushar Jana, Rasu Kesavamoorthy, Lianjun Shi, Mohamed A Virji, David N Finegold, and Sanford A Asher. A General Photonic Crystal Sensing Motif: Creatinine in Bodily Fluids. *Journal of the American Chemical Society*, 126:2971–2977, 2004.
- [60] By Insook Lee, Daihyun Kim, Jinha Kal, Heeyoul Baek, Dongwoo Kwak, and Dahyeon Go. Quasi-Amorphous Colloidal Structures for Electrically Tunable Full-Color Photonic Pixels with Angle-Independency. *Advanced Materials*, 22:4973–4977, 2010.
- [61] Jianping Ge, Howon Lee, Le He, Junhoi Kim, Zhenda Lu, Hyoki Kim, James Goebel, Sunghoon Kwon, and Yadong Yin. Magnetochromatic Microspheres: Rotating Photonic Crystals. *Journal of the American Chemical Society*, 131:15687–15694, 2009.
- [62] Jianping Ge and Yadong Yin. Niche applications of magnetically responsive photonic structures. *Journal of Material Chemistry*, 20:5777–5784, 2010.
- [63] Le He, Mingsheng Wang, Jianping Ge, and Yadong Yin. Magnetic Assembly Route to Colloidal Responsive Photonic Nanostructures. *Accounts of Chemical Research*, 45(9):1431–1440, 2012.
- [64] Jesse M. Weissman, Hari B. Sunkara, Albert S. Tse, and Sanford A. Asher. Thermally switchable periodicities and diffraction from mesoscopically ordered materials. *Science*, 274(5289):959–960, 1996.
- [65] Yukikazu Takeoka and Masayoshi Watanabe. Tuning Structural Color Changes of Porous Thermosensitive Gels through Quantitative Adjustment of the Cross-Linker in Pre-gel Solutions. *Langmuir*, 19(22):9104–9106, 2003.
- [66] Pietro Tierno. Recent advances in anisotropic magnetic colloids: Realization, assembly and applications. *Physical Chemistry Chemical Physics*, 16(43):23515–23528, 2014.
- [67] Daniel Scheid, Gennady Cherkashinin, Emanuel Ionescu, and Markus Gallei. Single-source magnetic nanorattles by using convenient emulsion polymerization protocols. *Langmuir*, 30(5):1204–1209, 2014.
- [68] Stoyan K. Smoukov, Sumit Gangwal, Manuel Marquez, and Orlin D. Velev. Reconfigurable responsive structures assembled from magnetic Janus particles. *Soft Matter*, 5(6):1285–1292, 2009.
- [69] Stephanie H. Lee and Chekesha M. Liddell. Anisotropic magnetic colloids: A strategy to form complex structures using nonspherical building blocks. *Small*, 5(17):1957–1962, 2009.
- [70] Stefano Sacanna, Laura Rossi, and David J. Pine. Magnetic click colloidal assembly. *Journal of the American Chemical Society*, 134(14):6112–6115, 2012.

- [71] Hanumantha Rao Vutukuri, Frank Smalenburg, Stéphane Badaire, Arnout Imhof, Marjolein Dijkstra, and Alfons van Blaaderen. An experimental and simulation study on the self-assembly of colloidal cubes in external electric fields. *Soft Matter*, 10(45):9110–9119, 2014.
- [72] B.V. Derjaguin. On the Repulsive Forces between Charged Colloid Particles and on the Theory of Slow Coagulation and Stability of Lyophobic Sols. *Transactions of the Faraday Society*, 35:203–215, 1940.
- [73] E.J.W. Verwey, J.T.G. Overbeek, and K. Van Nes. *Theory of the Stability of Lyophobic Colloids: The Interaction of Sol Particles Having an Electric Double Layer*. Elsevier Publishing Company, Amsterdam, 1948.
- [74] J Israelachvili. *Intermolecular and Surface Forces*. Academic Press, London, 3 edition, 2011.
- [75] William B. Russel, D. A. Saville, and W.R. Schowalter. *Colloidal Dispersions*. Cambridge University Press, Cambridge, 1989.
- [76] Barrett Comiskey, J.D. Albert, Hidekazu Yoshizawa, and Joseph Jacobson. An electrophoretic ink for all-printed reflective electronic displays. *Nature*, 394(6690):253–255, 1998.
- [77] Duncan Graham-Rowe. Electronic paper rewrites the rulebook for displays. *Nature Photonics*, 1(5):248–251, 2007.
- [78] Alwin R.M. Verschuieren, Leon W.G. Stofneel, Patrick J. Baesjou, Marc H.W.M. Van Delden, Jack J. Van Glabbeek, Kars Michiel H. Lenssen, Manfred Mueller, Johan T.M. Osenga, Gerrit Oversluizen, and Roland M. Schuurbiers. Optical performance of in-plane electrophoretic color e-paper. *J. Soc. Inf. Disp.*, 18:1–7, 2009.
- [79] K. D. Hermanson, S. O. Lumsdon, J. P. Williams, E. W. Kaler, and O. D. Velev. Dielectrophoretic assembly of electrically functional microwires from nanoparticle suspensions. *Science*, 294(5544):1082–1086, 2001.
- [80] Niels de Jonge and Frances M. Ross. Electron Microscopy of Specimens in Liquid. *Nature Nanotechnology*, 103(1):163–164, 2011.
- [81] Frances M. Ross. Opportunities and Challenges in Liquid Cell Electron Microscopy. *Science*, 350(6267):aaa9886, 2015.
- [82] J. Pawley. *Handbook of Biological Confocal Microscopy*. Springer, New York, 2006.
- [83] V. Prasad, D. Semwogerere, and E.R. Weeks. Confocal Microscopy of Colloids. *Journal of Physics: Condensed Matter*, 19(11):113102, 2007.
- [84] Alfons van Blaaderen and Pierre Wiltzius. Real-Space Structure of Colloidal Hard-Sphere Glasses. *Science*, 270(5239):1177–1179, nov 1995.
- [85] David B. Williams and C. Barry Carter. *Transmission Electron Microscopy*. Springer US, Boston, MA, 1996.
- [86] Mark P. Oxley, Andrew R. Lupini, and Stephen J. Pennycook. Ultra-high resolution electron microscopy. *Reports on Progress in Physics*, 80(2):26101, 2016.
- [87] R.F. Egerton, P. Li, and M. Malac. Radiation damage in the TEM and SEM. *Micron*, 35:399–409, 2004.
- [88] R.F. Egerton. *Electron Energy-Loss Spectroscopy in the Electron Microscope*. Springer Science & Business Media, New York, 2011.
- [89] Brent Fultz and James Howe. *Transmission Electron Microscopy and Diffractometry of Materials*. Springer Berlin Heidelberg, 2012.
- [90] Niels de Jonge, Nicolas Poirier-Demers, Hendrix Demers, Diana B. Peckys, and Dominique Drouin. Nanometer-resolution electron microscopy through micrometers-thick water layers. *Ultramicroscopy*, 110(9):1114–1119, 2010.
- [91] Niels de Jonge. Theory of the Spatial Resolution of (Scanning) Transmission Electron Microscopy in Liquid Water or Ice Layers. *Ultramicroscopy*, 187:113–125, 2018.
- [92] Brian D. Leahy, Neil Y.C. Lin, and Itai Cohen. Quantitative light microscopy of dense suspensions: Colloid science at the next decimal place. *Current Opinion in Colloid & Interface Science*, 34:32–46, 2018.

- [93] M.C. Jenkins and S.U. Egelhaaf. Confocal microscopy of colloidal particles: Towards reliable, optimum coordinates. *Advances in Colloid and Interface Science*, 136:65–92, 2008.
- [94] Michael A. Bevan and Shannon L. Eichmann. Optical microscopy measurements of kT-scale colloidal interactions. *Current Opinion in Colloid & Interface Science*, 16(2):149–157, 2011.
- [95] See Wee Chee, Zhaslan Baraissov, N. Duane Loh, Paul T. Matsudaira, and Utkur Mirsaidov. Desorption-mediated motion of nanoparticles at the liquid-solid interface. *Journal of Physical Chemistry C*, 120(36):20462–20470, 2016.
- [96] Paul Alivisatos, Qian Chen, Jessica Smith, Jungwon Park, Kwanpyo Kim, Davy Ho, Haider Rasool, and A Zettl. 3D Motion of DNA-Au Nanoconjugates in Graphene Liquid Cell Electron Microscopy. *Nano Lett.*, 13:4556–4561, 2013.
- [97] Juan Liu, Zhiwei Wang, Anxu Sheng, Feng Liu, Fuyu Qin, and Zhong Lin Wang. In Situ Observation of Hematite Nanoparticle Aggregates Using Liquid Cell Transmission Electron Microscopy. *Environmental Science and Technology*, 50(11):5606–5613, 2016.
- [98] Yuzi Liu, Xiao Min Lin, Yugang Sun, and Tijana Rajh. In situ visualization of self-assembly of charged gold nanoparticles. *Journal of the American Chemical Society*, 135(10):3764–3767, 2013.
- [99] Jingyu Lu, Zainul Aabdin, N. Duane Loh, Dipanjan Bhattacharya, and Utkur Mirsaidov. Nanoparticle dynamics in a nanodroplet. *Nano Letters*, 14(4):2111–2115, 2014.
- [100] Lucas R. Parent, Evangelos Bakalis, Abelardo Ramírez-Hernández, Jacquelin K. Kammeyer, Chiwoo Park, Juan De Pablo, Francesco Zerbetto, Joseph P. Patterson, and Nathan C. Gianneschi. Directly Observing Micelle Fusion and Growth in Solution by Liquid-Cell Transmission Electron Microscopy. *Journal of the American Chemical Society*, 139(47):17140–17151, 2017.
- [101] Alexander S. Powers, Hong-Gang Liao, Shilpa N. Raja, Noah D. Bronstein, A. Paul Alivisatos, and Haimei Zheng. Tracking Nanoparticle Diffusion and Interaction during Self-Assembly in a Liquid Cell. *Nano Letters*, 17:15–20, 2017.
- [102] Maria T. Proetto, Anthony M. Rush, Miao Ping Chien, Patricia Abellan Baeza, Joseph P. Patterson, Matthew P. Thompson, Norman H. Olson, Curtis E. Moore, Arnold L. Rheingold, Christopher Andolina, Jill Millstone, Stephen B. Howell, Nigel D. Browning, James E. Evans, and Nathan C. Gianneschi. Dynamics of soft nanomaterials captured by transmission electron microscopy in liquid water. *Journal of the American Chemical Society*, 136(4):1162–1165, 2014.
- [103] Elisabeth A. Ring and Niels de Jonge. Video-frequency scanning transmission electron microscopy of moving gold nanoparticles in liquid. *Micron*, 43(11):1078–1084, 2012.
- [104] Andreas Verch, Marina Pfaff, and Niels de Jonge. Exceptionally Slow Movement of Gold Nanoparticles at a Solid/Liquid Interface Investigated by Scanning Transmission Electron Microscopy. *Langmuir*, 31(25):6956–6964, 2015.
- [105] E. R. White, Matthew Mecklenburg, Brian Shevitski, S. B. Singer, and B. C. Regan. Charged nanoparticle dynamics in water induced by scanning transmission electron microscopy. *Langmuir*, 28(8):3695–3698, 2012.
- [106] Taylor J. Woehl, Katherine L. Jungjohann, James E. Evans, Ilke Arslan, William D. Ristenpart, and Nigel D. Browning. Experimental procedures to mitigate electron beam induced artifacts during in situ fluid imaging of nanomaterials. *Ultramicroscopy*, 127:53–63, 2013.
- [107] Taylor J. Woehl and Tanya Prozorov. The Mechanisms for Nanoparticle Surface Diffusion and Chain Self-Assembly Determined from Real-Time Nanoscale Kinetics in Liquid. *Journal of Physical Chemistry C*, 119(36):21261–21269, 2015.
- [108] Haimei Zheng, Shelley A. Claridge, Andrew M. Minor, A. Paul Alivisatos, and Ulrich Dahmen. Nanocrystal Diffusion in a Liquid Thin Film Observed by *in Situ* Transmission Electron Microscopy. *Nano Letters*, 9(6):2460–2465, 2009.
- [109] Guanhua Lin, See Wee Chee, Sanoj Raj, Petr Král, and Utkur Mirsaidov. Linker-Mediated Self-Assembly Dynamics of Charged Nanoparticles. *ACS Nano*, 10(8):7443–7450, 2016.

- [110] Guanhua Lin, Xi Zhu, Utkarsh Anand, Qi Liu, Jingyu Lu, Zainul Aabdin, Haibin Su, and Utkur Mirsaidov. Nanodroplet-Mediated Assembly of Platinum Nanoparticle Rings in Solution. *Nano Letters*, 16(2):1092–1096, 2016.
- [111] Eli Sutter, Peter Sutter, Alexei V. Tkachenko, Roman Krahne, Joost de Graaf, Milena Arciniegas, and Liberato Manna. *In situ* microscopy of the self-assembly of branched nanocrystals in solution. *Nature Communications*, 7:11213, 2016.
- [112] Shu Fen Tan, Utkarsh Anand, and Utkur Mirsaidov. Interactions and Attachment Pathways between Functionalized Gold Nanorods. *ACS Nano*, 11(2):1633–1640, 2017.
- [113] Shu Fen Tan, See Wee Chee, Guanhua Lin, and Utkur Mirsaidov. Direct Observation of Interactions between Nanoparticles and Nanoparticle Self-Assembly in Solution. *Accounts of Chemical Research*, 50(6):1303–1312, 2017.
- [114] Xuezheng Tian, Haimei Zheng, and Utkur Mirsaidov. Aggregation dynamics of nanoparticles at solid-liquid interfaces. *Nanoscale*, 9(28):10044–10050, 2017.
- [115] Guomin Zhu, Yingying Jiang, Wei Huang, Hui Zhang, Fang Lin, and Chuanhong Jin. Atomic resolution liquid-cell transmission electron microscopy investigations of the dynamics of nanoparticles in ultrathin liquids. *Chemical Communications*, 49(93):10944, 2013.
- [116] Juyeong Kim, Zihao Ou, Matthew R. Jones, Xiaohui Song, and Qian Chen. Imaging the polymerization of multivalent nanoparticles in solution. *Nature Communications*, 8(1), 2017.
- [117] Max Piffoux, Nabeel Ahmad, Jaysen Nelayah, Claire Wilhelm, Amanda Silva, Florence Gazeau, and Damien Alloyeau. Monitoring the dynamics of cell-derived extracellular vesicles at the nanoscale by liquid-cell transmission electron microscopy. *Nanoscale*, pages 1234–1244, 2018.
- [118] Daniel J. Kelly, Mingwei Zhou, Nick Clark, Matthew J. Hamer, Edward A. Lewis, Alexander M. Rakowski, Sarah J. Haigh, and Roman V. Gorbachev. Nanometer Resolution Elemental Mapping in Graphene-Based TEM Liquid Cells. *Nano Letters*, 18(2):1168–1174, 2018.
- [119] Michael A. Boles, Michael Engel, and Dmitri V. Talapin. Self-Assembly of Colloidal Nanocrystals: From Intricate Structures to Functional Materials. *Chemical Reviews*, 116(18):11220–11289, 2016.
- [120] P. Abellan, T. J. Woehl, L. R. Parent, N. D. Browning, J. E. Evans, and I. Arslan. Factors influencing quantitative liquid (scanning) transmission electron microscopy. *Chemical Communications*, 50(38):4873–4880, 2014.
- [121] Erik Meijering, Oleh Dzyubachyk, and Ihor Smal. Methods for cell and particle tracking. In *Methods in Enzymology*, volume 504, pages 183–200. Elsevier Inc., 1 edition, 2012.
- [122] John C. Crocker and David G. Grier. Methods of Digital Video Microscopy for Colloidal Studies. *Journal of Colloid and Interface Science*, 310(179):298–310, 1996.
- [123] Dominique Drouin, Alexandre Réal Couture, Dany Joly, Xavier Tastet, Vincent Aimez, and Raynald Gauvin. CASINO V2.42 A Fast and Easy-to-Use Modeling Tool for Scanning Electron Microscopy and Microanalysis Users. *Scanning*, 29(3):92–101, 2007.
- [124] Hendrix Demers, Nicolas Poirier-Demers, Alexandre Réal Couture, Dany Joly, Marc Guilmain, Niels de Jonge, and Dominique Drouin. Three-Dimensional Electron Microscopy Simulation with the CASINO Monte Carlo software. *Scanning*, 33(3):135–146, 2011.
- [125] N. Poirier-Demers, H. Demers, D. Drouin, and N. de Jonge. Simulating STEM Imaging of Nanoparticles in Micrometers-Thick Substrates. *Microscopy and Microanalysis*, 17(S2):980–981, 2011.
- [126] R. Browning, T. Z. Li, B. Chui, Jun Ye, R. F.W. Pease, Z. Czyzewski, and D. C. Joy. Empirical Forms for the Electron/Atom Elastic Scattering Cross Sections from 0.1 to 30 keV. *Journal of Applied Physics*, 76(4):2016–2022, 1994.
- [127] Eiichi Mine, Mitsuaki Hirose, Daisuke Nagao, Yoshio Kobayashi, and Mikio Konno. Synthesis of Submicrometer-Sized Titania Spherical Particles with a Sol-Gel Method and Their Application to Colloidal Photonic Crystals. *Journal of Colloid and Interface Science*, 291(1):162–168, 2005.
- [128] Yury Chernyak. Dielectric constant, dipole moment, and solubility parameters of some cyclic acid esters. *Journal of Chemical and Engineering Data*, 51(2):416–418, 2006.

- [129] Nan Jiang. Beam damage by the induced electric field in transmission electron microscopy. *Micron*, 83:79–92, 2016.
- [130] Guangnan Ou, Biyan He, Xuejing Li, and Jianhui Lei. Glycerol Carbonate: A Novel Biosolvent with Strong Ionizing and Dissociating Powers. *The Scientific World Journal*, 2012, 2012.
- [131] Jinglun Wang, Tianqiao Yong, Jianwen Yang, Chuying Ouyang, and Lingzhi Zhang. Organosilicon functionalized glycerol carbonates as electrolytes for lithium-ion batteries. *RSC Advances*, 5:17660–17666, 2015.
- [132] H. Qian, M. P. Sheetz, and E. L. Elson. Single particle tracking. Analysis of diffusion and flow in two-dimensional systems. *Biophysical Journal*, 60(4):910–921, 1991.
- [133] Michael J. Saxton. Single-particle tracking: The distribution of diffusion coefficients. *Biophysical Journal*, 72(4):1744–1753, 1997.
- [134] Xavier Michalet. Mean square displacement analysis of single-particle trajectories with localization error: Brownian motion in an isotropic medium. *Physical Review E - Statistical, Nonlinear, and Soft Matter Physics*, 82(4):1–13, 2010.
- [135] Lucas R. Parent, Evangelos Bakalis, Maria Proetto, Yiwen Li, Chiwoo Park, Francesco Zerbetto, and Nathan C. Gianneschi. Tackling the Challenges of Dynamic Experiments Using Liquid-Cell Transmission Electron Microscopy. *Accounts of Chemical Research*, 51(1):3–11, 2018.
- [136] Joost de Graaf, Toni Peter, Lukas P. Fischer, and Christian Holm. The Raspberry model for hydrodynamic interactions revisited. II. The effect of confinement. *Journal of Chemical Physics*, 143(8), 2015.
- [137] Nicholas M. Schneider, Michael M. Norton, Brian J. Mendel, Joseph M. Grogan, Frances M. Ross, and Haim H. Bau. Electron-Water Interactions and Implications for Liquid Cell Electron Microscopy. *Journal of Physical Chemistry C*, 118(38):22373–22382, 2014.
- [138] Nan Jiang. Note on in situ (scanning) transmission electron microscopy study of liquid samples. *Ultramicroscopy*, 179:81–83, 2017.
- [139] Nan Jiang. Damage mechanisms in electron microscopy of insulating materials. *Journal of Physics D: Applied Physics*, 46(30), 2013.
- [140] Christoph Hanske, Guillermo González-Rubio, Cyrille Hamon, Pilar Formentín, Evgeny Modin, Andrey Chuvilin, Andrés Guerrero-Martínez, Lluís F. Marsal, and Luis M. Liz-Marzán. Large-Scale Plasmonic Pyramidal Supercrystals via Templated Self-Assembly of Monodisperse Gold Nanospheres. *Journal of Physical Chemistry C*, 121(20):10899–10906, 2017.
- [141] Klaus van Benthem, Andrew R. Lupini, Mark P. Oxley, Scott D. Findlay, Leslie J. Allen, and Stephen J. Pennycook. Three-dimensional ADF imaging of individual atoms by through-focal series scanning transmission electron microscopy. *Ultramicroscopy*, 106(11-12 SPEC. ISS.):1062–1068, 2006.
- [142] Niels de Jonge, Rachid Sougrat, Brian M. Northan, and Stephen J. Pennycook. Three-Dimensional Scanning Transmission Electron Microscopy of Biological Specimens. *Microscopy and Microanalysis*, 16:54–63, 2010.
- [143] R. Piazza and A. Parola. Thermophoresis in colloidal suspensions. *Journal of Physics: Condensed Matter*, 20:153102, 2008.
- [144] Stefan Duhr and Dieter Braun. Thermophoretic depletion follows boltzmann distribution. *Physical Review Letters*, 96(16):1–4, 2006.
- [145] Yugang Zhao, Cunlu Zhao, Jinhua He, Yi Zhou, and Chun Yang. Collective effects on thermophoresis of colloids: A microfluidic study within the framework of DLVO theory. *Soft Matter*, 9(32):7726–7734, 2013.
- [146] Emma L. Talbot, Jurij Kotar, Lucia Parolini, Lorenzo Di Michele, and Pietro Cicuta. Thermophoretic migration of vesicles depends on mean temperature and head group chemistry. *Nature Communications*, 8:15351, 2017.

- [147] L. Kovarik, A. Stevens, A. Liyu, and N. D. Browning. Implementing an accurate and rapid sparse sampling approach for low-dose atomic resolution STEM imaging. *Applied Physics Letters*, 109(16), 2016.
- [148] Zihao Ou, Ziwei Wang, Binbin Luo, Erik Luijten, and Qian Chen. Kinetic pathways of crystallization at the nanoscale. *Nature Materials*, 2019.
- [149] Joseph M. Grogan, Nicholas M. Schneider, Frances M. Ross, and Haim H. Bau. Bubble and pattern formation in liquid induced by an electron beam. *Nano Letters*, 14:359–64, 2014.
- [150] John C. Crocker. Measurement of the hydrodynamic corrections to the Brownian motion of two colloidal spheres. *The Journal of Chemical Physics*, 106(7):2837–2840, 1997.
- [151] William Sutherland. A dynamical theory of diffusion for non-electrolytes and the molecular mass of albumin. *The London, Edinburgh, and Dublin Philosophical Magazine and Journal of Science*, 9(54):781–785, 1905.
- [152] Jan K.G. Dhont. *An Introduction to Dynamics of Colloids*. Elsevier, 1996.
- [153] Albert P. Philipse. *Brownian Motion*. Springer, 2018.
- [154] Laurent Lobry and Nicole Ostrowsky. Diffusion of Brownian particles trapped between two walls: Theory and dynamic-light-scattering measurements. *Physical Review B - Condensed Matter and Materials Physics*, 53(18):12050–12056, 1996.
- [155] Dennis C. Prieve. Measurement of colloidal forces with TIRM. *Advances in Colloid and Interface Science*, 82:93–125, 1999.
- [156] E. R. Dufresne, D. Altman, and D. G. Grier. Brownian Dynamics of a Sphere between Parallel Walls. *Europhysics Letters*, 53(2):264–270, 2001.
- [157] Peter Holmqvist, Jan K.G. Dhont, and Peter R. Lang. Anisotropy of Brownian motion caused only by hydrodynamic interaction with a wall. *Physical Review E - Statistical, Nonlinear, and Soft Matter Physics*, 74(2):1–5, 2006.
- [158] Mauricio D. Carbajal-Tinoco, Ricardo Lopez-Fernandez, and José Luis Arauz-Lara. Asymmetry in colloidal diffusion near a rigid wall. *Physical Review Letters*, 99(13):1–4, 2007.
- [159] Shannon L. Eichmann, Samarth G. Anekal, and Michael A. Bevan. Electrostatically Confined Nanoparticle Interactions and Dynamics. *Langmuir*, 24(3):714–721, 2008.
- [160] H.B. Eral, J.M. Oh, D. van den Ende, F. Mugele, and M.H.G. Duits. Anisotropic and Hindered Diffusion of Colloidal Particles in a Closed Cylinder. *Langmuir*, 26(22):16722–16729, 2010.
- [161] A. E. Cervantes-Martínez, A. Ramírez-Saito, R. Armenta-Calderón, M. A. Ojeda-López, and J. L. Arauz-Lara. Colloidal Diffusion inside a Spherical Cell. *Physical Review E - Statistical, Nonlinear, and Soft Matter Physics*, 83(3):1–4, 2011.
- [162] Christian Aponte-Rivera and Roseanna N. Zia. Simulation of Hydrodynamically Interacting Particles Confined by a Spherical Cavity. *Physical Review Fluids*, 1(2):023301, 2016.
- [163] Tom A.J. Welling, Sina Sadighikia, Kanako Watanabe, Albert Grau-Carbonell, Maarten Bransen, Daisuke Nagao, Alfons van Blaaderen, and Marijn A. van Huis. Observation of Undamped 3D Brownian Motion of Nanoparticles Using Liquid-Cell Scanning Transmission Electron Microscopy. *Particle & Particle Systems Characterization*, 37:2000003, 2020.
- [164] Howard Brenner. The slow motion of a sphere through a viscous fluid towards a plane surface. *Chemical Engineering Science*, 16(3-4):242–251, 1961.
- [165] A.J. Goldman, R.G. Cox, and H. Brenner. Slow viscous motion of a sphere parallel to a plane wall - I Motion through a quiescent fluid. *Chemical Engineering Science*, 22(4):637–651, 1967.
- [166] B. Cichocki and R. B. Jones. Image representation of a spherical particle near a hard wall. *Physica A: Statistical Mechanics and its Applications*, 258(3-4):273–302, 1998.
- [167] A. Imperio, J. T. Padding, and W. J. Briels. Diffusion of spherical particles in microcavities. *Journal of Chemical Physics*, 134:154904, 2011.
- [168] Federico Montanarella, Jaco J. Geuchies, Tonnishtha Dasgupta, P. Tim Prins, Carlo van Overbeek, Rajeev Dattani, Patrick Baesjou, Marjolein Dijkstra, Andrei V. Petukhov, Alfons van Blaaderen, and

- Daniel Vanmaekelbergh. Crystallization of Nanocrystals in Spherical Confinement Probed by in Situ X-ray Scattering. *Nano Letters*, 18(6):3675–3681, 2018.
- [169] Bart de Nijs, Simone Dussi, Frank Smalenburg, Johannes D. Meeldijk, Dirk J. Groenendijk, Laura Filion, Arnout Imhof, Alfons van Blaaderen, and Marjolein Dijkstra. Entropy-driven formation of large icosahedral colloidal clusters by spherical confinement. *Nature Materials*, 14(1):56–60, 2015.
- [170] Da Wang, Michiel Hermes, Ramakrishna Kotni, Yaoting Wu, Nikos Tasios, Yang Liu, Bart de Nijs, Ernest B. van Der Wee, Christopher B. Murray, Marjolein Dijkstra, and Alfons van Blaaderen. Interplay between spherical confinement and particle shape on the self-assembly of rounded cubes. *Nature Communications*, 9(1), 2018.
- [171] Da Wang, Tonnishtha Dasgupta, Ernest B. van der Wee, Daniele Zanaga, Thomas Altantzis, Yaoting Wu, Gabriele M. Coli, Christopher B. Murray, Sara Bals, Marjolein Dijkstra, and Alfons van Blaaderen. Binary icosahedral clusters of hard spheres in spherical confinement. *Nature Physics*, 17(1):128–134, 2021.
- [172] Wessel Vlug. *Balls, beams and blocks*. PhD thesis, Utrecht University, 2017.
- [173] Fabian Hagemans, Wessel Vlug, Chiara Raffaelli, Alfons van Blaaderen, and Arnout Imhof. Sculpting Silica Colloids by Etching Particles with Nonuniform Compositions. *Chemistry of Materials*, 29(7):3304–3313, 2017.
- [174] Kanako Watanabe, Kotaro Kuroda, and Daisuke Nagao. Polyethylenimine-Assisted Synthesis of Hollow Silica Spheres without Shape Deformation. *Materials Chemistry and Physics*, 262:124267, 2021.
- [175] T. H. Besseling, J. Jose, and A. van Blaaderen. Methods to calibrate and scale axial distances in confocal microscopy as a function of refractive index. *Journal of Microscopy*, 257(2):142–150, 2015.
- [176] Nian-Sheng Cheng. Formula for the Viscosity of a Glycerol-Water Mixture. *Industrial & Engineering Chemistry Research*, 47(9):3285–3288, 2008.
- [177] Andreas Volk and Christian J Kähler. Density model for aqueous glycerol solutions. *Experiments in Fluids*, 59(5):75, 2018.
- [178] Glycerine Producers’ Association. *Physical Properties of Glycerine and its Solutions*. Glycerine Producers’ Association, 1963.
- [179] Murat Nulati Yesibolati, Kim I. Mortensen, Hongyu Sun, Anders Broström, Sofie Tidemand-Lichtenberg, and Kristian Møhlave. Unhindered Brownian Motion of Individual Nanoparticles in Liquid-Phase Scanning Transmission Electron Microscopy. *Nano Letters*, 20(10):7108–7115, 2020.
- [180] Qian Chen, Hoduk Cho, Karthish Manthiram, Mark Yoshida, Xingchen Ye, and A. Paul Alivisatos. Interaction Potentials of Anisotropic Nanocrystals from the Trajectory Sampling of Particle Motion using in Situ Liquid Phase Transmission Electron Microscopy. *ACS Central Science*, 1(1):150323114811004, 2015.
- [181] E.J.W. Verwey and J.T.G. Overbeek. *Theory of Stability of Lyophobic Colloids*. Elsevier, Amsterdam, 1948.
- [182] Jean-Pierre Hansen and Hartmut Löwen. Effective Interactions between Electric Double Layers. *Annual Review of Physical Chemistry*, 52(1):209–242, 2000.
- [183] Yuncheng Liang, Nidal Hilal, Paul Langston, and Victor Starov. Interaction Forces between Colloidal Particles in Liquid: Theory and Experiment. *Advances in Colloid and Interface Science*, 134-135:151–166, 2007.
- [184] Younjin Min, Mustafa Akbulut, Kai Kristiansen, Yuval Golan, and Jacob Israelachvili. The Role of Interparticle and External Forces in Nanoparticle Assembly. *Nanoscience and Technology: A Collection of Reviews from Nature Journals*, pages 38–49, 2010.
- [185] Carlos A. Silvera Batista, Ronald G. Larson, and Nicholas A. Kotov. Nonadditivity of Nanoparticle Interactions. *Science*, 350:1242477, 2015.
- [186] David A. Walker, Bartłomiej Kowalczyk, Monica Olvera de la Cruz, and Bartosz A. Grzybowski. Electrostatics at the Nanoscale. *Nanoscale*, 3(4):1316–1344, 2011.
- [187] Vincent Dahirel and Marie Jardat. Effective Interactions between Charged Nanoparticles in Water: What Is Left from the DLVO Theory? *Current Opinion in Colloid and Interface Science*, 15(1-2):2–7, 2010.

- [188] Yael Avni, Shigeyuki Komura, and David Andelman. Brownian Motion of a Charged Colloid in Restricted Confinement. *Physical Review E*, 103(4):42607, 2021.
- [189] Mark Klokkenburg, Roel P.A. Dullens, Willem K. Kegel, Ben H. Ern , and Albert P. Philipse. Quantitative Real-Space Analysis of Self-Assembled Structures of Magnetic Dipolar Colloids. *Physical Review Letters*, 96(3):037203, 2006.
- [190] Jos van Rijssel, Marte van Der Linden, Johannes D. Meeldijk, Relinde J A van Dijk-Moes, Albert P. Philipse, and Ben H. Ern . Spatial Distribution of Nanocrystals Imaged at the Liquid-Air Interface. *Physical Review Letters*, 111(10):1–5, 2013.
- [191] Carlo Bradac. Nanoscale Optical Trapping: A Review. *Advanced Optical Materials*, 6(12):1800005, 2018.
- [192] David G. Grier. A Revolution in Optical Manipulation. *Nature*, 424(6950):810–816, 2003.
- [193] Djamel El Masri, Peter van Oostrum, Frank Smalenburg, Teun Vissers, Arnout Imhof, Marjolein Dijkstra, and Alfons van Blaaderen. Measuring Colloidal Forces from Particle Position Deviations inside an Optical Trap. *Soft Matter*, 7(7):3462–3466, 2011.
- [194] C. P. Royall, M. E. Leunissen, and A. van Blaaderen. A New Colloidal Model System to Study Long-Range Interactions Quantitatively in Real Space. *Journal of Physics: Condensed Matter*, 15(48):S3581–S3596, 2003.
- [195] Hans-J rgen Butt, Brunero Cappella, and Michael Kappl. Force Measurements with the Atomic Force Microscope: Technique, Interpretation and Applications. *Surface Science Reports*, 59(1-6):1–152, oct 2005.
- [196] Anand Yethiraj and Alfons van Blaaderen. A Colloidal Model System with an Interaction Tunable from Hard Sphere to Soft and Dipolar. *Nature*, 421(6922):513–517, 2003.
- [197] W. Albers and J. Th G. Overbeek. Stability of Emulsions of Water in Oil. I. The Correlation between Electrokinetic Potential and Stability. *Journal of Colloid Science*, 14(5):501–509, 1959.
- [198] W. Albers and J. Th G. Overbeek. Stability of Emulsions of Water in Oil. II. Charge as a Factor of Stabilization against Flocculation. *Journal of Colloid Science*, 14(5):510–518, 1959.
- [199] N.A. Mishchuk, A. Sanfeld, and A. Steinchen. Interparticle Interactions in Concentrate Water–Oil Emulsions. *Advances in Colloid and Interface Science*, 112(1):129–157, 2004.
- [200] Sunil K. Sainis, Jason W. Merrill, and Eric R. Dufresne. Electrostatic Interactions of Colloidal Particles at Vanishing Ionic Strength. *Langmuir*, 24(23):13334–13337, 2008.
- [201] David A.J. Gillespie, James E. Hallett, Oluwapemi Elujoba, Anis Fazila Che Hamzah, Robert M. Richardson, and Paul Bartlett. Counterion Condensation on Spheres in the Salt-Free Limit. *Soft Matter*, 10(4):566–577, 2014.
- [202] Jason W. Merrill, Sunil K. Sainis, and Eric R. Dufresne. Many-Body Electrostatic Forces between Colloidal Particles at Vanishing Ionic Strength. *Physical Review Letters*, 103(13):138301, 2009.
- [203] Samuel D. Finlayson and Paul Bartlett. Non-Additivity of Pair Interactions in Charged Colloids. *Journal of Chemical Physics*, 145(3):034905, jul 2016.
- [204] T. F. Tadros and J. Lyklema. Adsorption of Potential-Determining Ions at the Silica-Aqueous Electrolyte Interface and the Role of Some Cations. *Journal of Electroanalytical Chemistry and Interfacial Electrochemistry*, 17(3-4):267–275, 1968.
- [205] Dimitri A. Sverjensky. Prediction of Surface Charge on Oxides in Salt Solutions: Revisions for 1:1 (M^+L^-) Electrolytes. *Geochimica et Cosmochimica Acta*, 69(2):225–257, 2005.
- [206] Motoyoshi Kobayashi, Fr d ric Juillerat, Paolo Galletto, Paul Bowen, and Michal Borkovec. Aggregation and Charging of Colloidal Silica Particles: Effect of Particle Size. *Langmuir*, 21(13):5761–5769, 2005.
- [207] William Hadley Richardson. Bayesian-Based Iterative Method of Image Restoration. *Journal of the Optical Society of America*, 62(1):55, 1972.
- [208] L. B. Lucy. An Iterative Technique for the Rectification of Observed Distributions. *The Astronomical Journal*, 79(6):745, 1974.
- [209] Georg Rempfer, Gary B. Davies, Christian Holm, and Joost De Graaf. Reducing Spurious Flow in Simulations of Electrokinetic Phenomena. *Journal of Chemical Physics*, 145(4), 2016.

- [210] Georg Rempfer, Sascha Ehrhardt, Christian Holm, and Joost de Graaf. Nanoparticle Translocation through Conical Nanopores: A Finite Element Study of Electrokinetic Transport. *Macromolecular Theory and Simulations*, 26(1):1–14, 2017.
- [211] Americo Boza Troncoso and Edgar Acosta. The van der Waals Interactions in Sphere-Shell and Cone-Shell Configurations. *Journal of Physical Chemistry B*, 116(48):14051–14061, 2012.
- [212] Lennart Bergström. Hamaker Constants of Inorganic Materials. *Advances in Colloid and Interface Science*, 70:125–169, 1997.
- [213] Albert Grau-Carbonell, Sina Sadighikia, Tom A.J. Welling, Relinde J.A. van Dijk-Moes, Ramakrishna Kotni, Maarten Bransen, Alfons van Blaaderen, and Marijn A. van Huis. *In Situ* Study of the Wet Chemical Etching of SiO₂ and Nanoparticle@SiO₂ Core-Shell Nanospheres. *ACS Applied Nano Materials*, 4(2):1136–1148, 2021.
- [214] Ivan U. Vakarelski, Naofumi Teramoto, Cathy E. McNamee, Jeremy O. Marston, and Ko Higashitani. Ionic Enhancement of Silica Surface Nanowear in Electrolyte Solutions. *Langmuir*, 28(46):16072–16079, 2012.
- [215] Yannick Hallez and Martine Meireles. Modeling the Electrostatics of Hollow Shell Suspensions: Ion Distribution, Pair Interactions, and Many-Body Effects. *Langmuir*, 32(40):10430–10444, 2016.
- [216] Sven H. Behrens and David G. Grier. Pair Interaction of Charged Colloidal Spheres near a Charged Wall. *Physical Review E*, 64(5):050401, 2001.
- [217] Tadao Sugimoto and Takashi Kojima. Formation Mechanism of Amorphous TiO₂ Spheres in Organic Solvents. 1. Roles of Ammonia. *The Journal of Physical Chemistry C*, 112(48):18760–18771, 2008.
- [218] Christina Graf, Dirk L.J. Vossen, Arnout Imhof, and Alfons van Blaaderen. A General Method to Coat Colloidal Particles with Silica. *Langmuir*, 19(17):6693–6700, 2003.
- [219] Dong Chen, Nlin Li, Fangqiong Tang, and Shuo Qi. Facile and Scalable Synthesis of Tailored Silica "Nanorattle" Structures. *Advanced Materials*, 21(37):3804–3807, 2009.
- [220] A. van Blaaderen and A. Vrij. Synthesis and Characterization of Monodisperse Colloidal Organo-Silica Spheres. *Journal of Colloid and Interface Science*, 156(1):1–18, 1993.
- [221] B.V. Enustun and John Turkevich. Coagulation of Colloidal Gold. *Journal of the American Chemical Society*, 85(21):3317–3328, 1963.
- [222] Neus G. Bastús, Joan Comenge, and Víctor Puentes. Kinetically Controlled Seeded Growth Synthesis of Citrate-Stabilized Gold Nanoparticles of up to 200 nm: Size Focusing *versus* Ostwald Ripening. *Langmuir*, 27(17):11098–11105, 2011.
- [223] Eiichi Mine, Akira Yamada, Yoshio Kobayashi, Mikio Konno, and Luis M Liz-Marzán. Direct Coating of Gold Nanoparticles with Silica by a Seeded Polymerization Technique. *Journal of Colloid and Interface Science*, 264(2):385–390, 2003.
- [224] Vladimir P. Zhdanov. Nanoparticles in a Nanochannel: van der Waals Interaction and Diffusion. *Physics Letters A*, 381(34):2832–2836, 2017.
- [225] G. G. Fuentes, E. Elizalde, F. Yubero, and J. M. Sanz. Electron Inelastic Mean Free Path for Ti, TiC, TiN and TiO₂ as Determined by Quantitative Reflection Electron Energy-Loss Spectroscopy. 33(3):230–237, 2002.
- [226] Murat Nulati Yesibolati, Simone Laganá, Shima Kadkhodazadeh, Esben Kirk Mikkelsen, Hongyu Sun, Takeshi Kasama, Ole Hansen, Nestor J. Zaluzec, and Kristian Mølhave. Electron Inelastic Mean Free Path in Water. *Nanoscale*, 12:20649, 2020.
- [227] H. Shinotsuka, S. Tanuma, C. J. Powell, and D. R. Penn. Calculations of Electron Inelastic Mean Free Paths . X . Data for 41 Elemental Solids over the 50 eV to 200 keV Range with the Relativistic Full Penn Algorithm. *Surface and Interface Analysis*, 47(9):871–888, 2015.
- [228] Geoffrey A Ozin, Kun Hou, Bettina V Lotsch, Ludovico Cademartiri, Daniel P Puzzo, Francesco Scotognella, Arya Ghadimi, and Jordan Thomson. Nanofabrication by self-assembly. *Materials Today*, 12(5):12–23, 2009.

- [229] Georg von Freymann, Vladimir Kitaev, Bettina V. Lotsch, and Geoffrey A. Ozin. Bottom-up assembly of photonic crystals. *Chemical Society Reviews*, 42(7):2528–2554, 2013.
- [230] Nicolas Vogel, Markus Retsch, Charles André Fustin, Aranzazu Del Campo, and Ulrich Jonas. Advances in Colloidal Assembly: The Design of Structure and Hierarchy in Two and Three Dimensions. *Chemical Reviews*, 115(13):6265–6311, 2015.
- [231] Zhongyu Cai, Zhiwei Li, Serge Ravaine, Mingxin He, Yanlin Song, Yadong Yin, Hanbin Zheng, Jinghua Teng, and Ao Zhang. From colloidal particles to photonic crystals: Advances in self-assembly and their emerging applications, 2021.
- [232] Zhiwei Li and Yadong Yin. Stimuli-Responsive Optical Nanomaterials. *Advanced Materials*, 31(15):1807061, 2019.
- [233] Ralf B Wehrspohn and Johannes Üpping. 3D photonic crystals for photon management in solar cells. *Journal of Optics*, 14(2):24003, 2012.
- [234] Youfeng Yue and Jian Ping Gong. Tunable one-dimensional photonic crystals from soft materials. *Journal of Photochemistry and Photobiology C: Photochemistry Reviews*, 23:45–67, 2015.
- [235] Yukikazu Takeoka. Fusion materials for biomimetic structurally colored materials. *Polymer Journal*, 47(2):106–113, 2015.
- [236] Sergey Gaponenko, Hilmi Volkan Demir, Christian Seassal, and Ulrike Woggon. Colloidal nanophotonics: the emerging technology platform. *Optics Express*, 24(2):A430–A433, 2016.
- [237] Hakan Inan, Muhammet Poyraz, Fatih Inci, Mark A. Lifson, Murat Baday, Brian T. Cunningham, and Utkan Demirci. Photonic crystals: emerging biosensors and their promise for point-of-care applications. *Chemical Society Reviews*, 46(2):366–388, 2017.
- [238] Jue Hou, Mingzhu Li, and Yanlin Song. Recent advances in colloidal photonic crystal sensors: Materials, structures and analysis methods. *Nano Today*, 22:132–144, 2018.
- [239] Eric S.A. Goerlitzer, Robin N. Klupp Taylor, and Nicolas Vogel. Bioinspired Photonic Pigments from Colloidal Self-Assembly, jul 2018.
- [240] Kanako Watanabe, Daisuke Nagao, Haruyuki Ishii, and Mikio Konno. Rattle-type colloidal crystals composed of spherical hollow particles containing an anisotropic, movable core. *Langmuir*, 31(19):5306–5310, 2015.
- [241] J.T.G. Overbeek. Theory of Electrophoresis. *Kolloid-Beihfte*, 54, 1943.
- [242] H. Ohshima. Electrophoresis. In *Reference Module in Chemistry, Molecular Sciences and Chemical Engineering*. Elsevier, 2016.
- [243] A. V. Delgado (ed). *Interfacial Electrokinetics and Electrophoresis (1st ed.)*. CRC Press, 2002.
- [244] Robert J. Hunter. *Zeta Potential in Colloid Science*. Academic Press, New York, 1981.
- [245] Robert J. Hunter. *Foundations of Colloid Science, Volumes I and II*. Clarendon Press, Oxford, 1991.
- [246] M. von Smoluchowski. Elektrische Endosmose und Strömungsströme. In E. Greated, editor, *Handbuch der Elektrizität und des Magnetismus*, pages 366–428. Leipzig, 1921.
- [247] E. Hückel. Die Kataphorese der Kugel. *Phys. Z.*, 25:204–210, 1924.
- [248] D. C. Henry. The Cataphoresis of Suspended Particles. Part I. The Equation of Cataphoresis. *Proc. R. Soc. Lond. A*, 133:106–129, 1931.
- [249] V. N. Shilov, A. V. Delgado, F. González-Caballero, J. Horno, J. J. López-García, and C. Grosse. Polarization of the electrical double layer. Time evolution after application of an electric field. *Journal of Colloid and Interface Science*, 232(1):141–148, 2000.
- [250] Eric Lee. Dynamic Electrophoresis of Rigid Spherical Particles. *Interface Science and Technology*, 26:123–142, 2019.
- [251] Sophie E. Gibb and Robert J. Hunter. Dynamic mobility of colloidal particles with thick double layers. *Journal of Colloid and Interface Science*, 224(1):99–111, 2000.
- [252] D. Mizuno, Y. Kimura, and R. Hayakawa. Dynamic electrophoretic mobility of colloidal particles measured by the newly developed method of quasi-elastic light scattering in a sinusoidal electric field. *Langmuir*, 16(24):9547–9554, 2000.

- [253] Christine S. Mangelsdorf and Lee R. White. Electrophoretic Mobility of a Spherical Colloidal Particle in an Oscillating Electric Field. *J. Chem. Soc. Faraday Trans.*, 88(24):3567–3581, 1992.
- [254] Hiroyuki Ohshima. Dynamic Electrophoretic Mobility of a Spherical Colloidal Particle. *Journal of Colloid and Interface Science*, 232:431–438, 1996.
- [255] Andrew L. Zydney. Boundary Effects on the Electrophoretic Motion of a Charged Particle in a Spherical Cavity, 1995.
- [256] Eric Lee, Jhih-Wei Chu, and Jyh Ping Hsu. Dynamic electrophoretic mobility of a sphere in a spherical cavity. *Journal of Colloid and Interface Science*, 205:65–76, 1998.
- [257] Jhih Wei Chu, Wen Hsun Lin, Eric Lee, and Jyh Ping Hsu. Electrophoresis of a sphere in a spherical cavity at arbitrary electrical potentials. *Langmuir*, 17(20):6289–6297, 2001.
- [258] Cheng Pang Tung, Eric Lee, and Jyh Ping Hsu. Dynamic electrophoretic mobility of a sphere in a spherical cavity. *Journal of Colloid and Interface Science*, 260(1):118–125, 2003.
- [259] Shih Han Lou, Eric Lee, and Jyh Ping Hsu. Dynamic electrophoresis of a sphere in a spherical cavity: Arbitrary surface potential. *Journal of Colloid and Interface Science*, 285(2):865–871, 2005.
- [260] Eric Lee, Wei Lun Min, and Jyh Ping Hsu. Dynamic electrophoresis of a droplet in a spherical cavity. *Langmuir*, 22(8):3920–3928, 2006.
- [261] Jyh Ping Hsu, Zheng Syun Chen, Ming Hong Ku, and Li Hsien Yeh. Effect of charged boundary on electrophoresis: Sphere in spherical cavity at arbitrary potential and double-layer thickness. *Journal of Colloid and Interface Science*, 314(1):256–263, 2007.
- [262] Wei J. Chen and Huan J. Keh. Electrophoresis of a charged soft particle in a charged cavity with arbitrary double-layer thickness. *Journal of Physical Chemistry B*, 117(33):9757–9767, 2013.
- [263] Tai C. Lee and Huan J. Keh. Electrophoretic motion of a charged particle in a charged cavity. *European Journal of Mechanics, B/Fluids*, 48:183–192, 2014.
- [264] Tom A.J. Welling, Kanako Watanabe, Albert Grau-Carbonell, Joost de Graaf, Daisuke Nagao, Arnout Imhof, Marijn A. van Huis, and Alfons van Blaaderen. Tunability of Interactions between the Core and Shell in Rattle-Type Particles studied with Liquid-Cell Electron Microscopy. *ACS Nano*, 15(7):11137–11149, 2021.
- [265] Kazuko Tanaka and Masao Nomura. Measurements of tracer diffusion coefficients of lithium ions, chloride ions and water in aqueous lithium chloride solutions. *Journal of the Chemical Society, Faraday Transactions 1: Physical Chemistry in Condensed Phases*, 83(6):1779–1782, 1987.
- [266] A. van Blaaderen, J. Peetermans, G. Maret, and J.K.G. Dhont. Long-time self-diffusion of spherical colloidal particles measured with fluorescence recovery after photobleaching. *The Journal of Chemical Physics*, 96(6):4591–4603, 1992.
- [267] R.A. Robinson and R.H. Stokes. *Electrolyte Solutions*. Butterworths, London, 1959.
- [268] Richard W. O'Brien and Lee R. White. Electrophoretic mobility of a spherical colloidal particle. *Journal of the Chemical Society, Faraday Transactions 2: Molecular and Chemical Physics*, 74:1607–1626, 1978.
- [269] Vladimir P Bykov. Spontaneous Emission in a Periodic Structure. *Soviet Journal of Experimental and Theoretical Physics*, 35:269, 1972.
- [270] Vladimir P Bykov. Spontaneous Emission from a Medium with a Band Spectrum. *Kvant. Elektron*, 1:1557–1577, 1974.
- [271] Sajeev John. Strong localization of photons in certain disordered dielectric superlattices. *Physical Review Letters*, 58(23):2486–2489, 1987.
- [272] Eli Yablonovitch. Inhibited Spontaneous Emission in Solid-State Physics and Electronics. *Physical Review Letters*, 58(20):2059–2062, 1987.
- [273] M. Li, X. Lai, C. Li, and Y. Song. Recent advantages of colloidal photonic crystals and their applications for luminescence enhancement. *Materials Today Nano*, 6:100039, 2019.
- [274] John D. Joannopoulos, Steven G. Johnson, Joshua N. Winn, and Robert D. Meade. *Photonic Crystals: Molding the Flow of Light*. Princeton University Press, Princeton, 2008.

- [275] Tilmann Ruhl, Peter Spahn, Christian Hermann, Cecile Jamais, and Ortwin Hess. Double-inverse-opal photonic crystals: The route to photonic bandgap switching. *Advanced Functional Materials*, 16(7):885–890, 2006.
- [276] Alvaro Blanco, Emmanuel Chomski, Serguel Grabtchak, Marta Ibisate, Sajeew John, Stephen W. Leonard, Cefe Lopez, Francisco Meseguer, Hernan Miguez, Jessica P. Mondla, Geoffrey A. Ozin, Ovidiu Toader, and Henry M. Van Driel. Large-scale synthesis of a silicon photonic crystal with a complete three-dimensional bandgap near 1.5 micrometres. *Nature*, 405(6785):437–440, 2000.
- [277] Yurii A. Vlasov, Xiang-Zheng Bo, James C. Sturm, and David J. Norris. On-chip natural assembly of silicon photonic bandgap crystals. *Nature*, 414(6861):289–293, 2001.
- [278] Antti-Pekka Hynninen, Job H.J. Thijssen, Esther C.M. Vermolen, Marjolein Dijkstra, and Alfons van Blaaderen. Self-assembly route for photonic crystals with a bandgap in the visible region. *Nature Materials*, 6(3):202–205, 2007.
- [279] A.-P. Hynninen, L. Filon, and M. Dijkstra. Stability of LS and LS_2 crystal structures in binary mixtures of hard and charged spheres. *The Journal of Chemical Physics*, 131(6):64902, 2009.
- [280] E.C.M. Vermolen, J.H.J. Thijssen, A. Moroz, M. Megens, and A. van Blaaderen. Comparing photonic band structure calculation methods for diamond and pyrochlore crystals. *Optics Express*, 17(9):6952–6961, 2009.
- [281] Daniel P. Puzzo, Andre C. Arsenault, Ian Manners, and Geoffrey A. Ozin. Electroactive Inverse Opal: A Single Material for All Colors. *Angewandte Chemie*, 121(5):961–965, 2009.
- [282] Ke Chen, Qianqian Fu, Siyun Ye, and Jianping Ge. Multicolor Printing Using Electric-Field-Responsive and Photocurable Photonic Crystals. *Advanced Functional Materials*, 27(43):1702825, 2017.
- [283] Hyoki Kim, Jianping Ge, Junhoi Kim, Sung-eun Choi, Hosuk Lee, Howon Lee, Wook Park, Yadong Yin, and Sunghoon Kwon. Structural colour printing using a magnetically tunable and lithographically fixable photonic crystal. *Nature Photonics*, 3(9):534–540, 2009.
- [284] Yejing Liu, Hao Wang, Jinfa Ho, Ryan C Ng, Ray J H Ng, Valerian H Hall-Chen, Eleen H H Koay, Zhaogang Dong, Hailong Liu, Cheng-Wei Qiu, Julia R Greer, and Joel K W Yang. Structural color three-dimensional printing by shrinking photonic crystals. *Nature Communications*, 10(1):4340, 2019.
- [285] Entao Tian, Jingxia Wang, Yongmei Zheng, Yanlin Song, Lei Jiang, and Daoben Zhu. Colorful humidity sensitive photonic crystal hydrogel. *Journal of Materials Chemistry*, 18(10):1116–1122, 2008.
- [286] Y Chen, J Au, P Kazlas, A Ritenour, H Gates, and M McCreary. Flexible active-matrix electronic ink display. *Nature*, 423(6936):136, 2003.
- [287] Ji Zhou, C Q Sun, K Pita, Y L Lam, Y Zhou, S L Ng, C H Kam, L T Li, and Z L Gui. Thermally tuning of the photonic band gap of SiO_2 colloid-crystal infilled with ferroelectric BaTiO_3 . *Applied Physics Letters*, 78(5):661–663, 2001.
- [288] M. Honda, T. Seki, and Y. Takeoka. Dual tuning of the photonic band-gap structure in soft photonic crystals. *Advanced Materials*, 21(18):1801–1804, 2009.
- [289] Hai Li, Chaoran Li, Wei Sun, Yuzhu Wang, Wenqiang Hua, Jingjing Liu, Shumin Zhang, Zhijie Chen, Shenghua Wang, Zhiyi Wu, Qishan Zhu, Rujun Tang, Jia Yu, Le He, Geoffrey A. Ozin, and Xiaohong Zhang. Single-Stimulus-Induced Modulation of Multiple Optical Properties. *Advanced Materials*, 31(23):1–6, 2019.
- [290] Luca Nucara, Francesco Greco, and Virgilio Mattoli. Electrically responsive photonic crystals: a review. *Journal of Materials Chemistry C*, 3(33):8449–8467, 2015.
- [291] Yijie Lu, Cong Meng, Hongwei Xia, Guangzhao Zhang, and Chi Wu. Fast electrically driven photonic crystal based on charged block copolymer. *Journal of Materials Chemistry C*, 1(38):6107–6111, 2013.
- [292] Shoichi Kubo, Zhong-Ze Gu, Kazuyuki Takahashi, Akira Fujishima, Hiroshi Segawa, and Osamu Sato. Control of the Optical Properties of Liquid Crystal-Infiltrated Inverse Opal Structures Using Photo Irradiation and/or an Electric Field. *Chemistry of Materials*, 17(9):2298–2309, 2005.

- [293] Tae Soup Shim, Shin Hyun Kim, Jae Young Sim, Jong Min Lim, and Seung Man Yang. Dynamic modulation of photonic bandgaps in crystalline colloidal arrays under electric field. *Advanced Materials*, 22(40):4494–4498, 2010.
- [294] Kazuhide Ueno, Aya Inaba, Yuta Sano, Masashi Kondoh, and Masayoshi Watanabe. A soft glassy colloidal array in ionic liquid, which exhibits homogeneous, non-brilliant and angle-independent structural colours. *Chemical Communications*, 24:3603–3605, 2009.
- [295] Pedro H.C. Camargo, Zhi Yuan Li, and Younan Xia. Colloidal building blocks with potential for magnetically configurable photonic crystals. *Soft Matter*, 3(10):1215–1222, 2007.
- [296] Hikaru Namigata, Kanako Watanabe, Saya Okubo, Masashi Hasegawa, Keishi Suga, and Daisuke Nagao. Double-Inverse-Opal-Structured Particle Assembly as a Novel Immobilized Photocatalytic Material. *Materials*, 14(1), 2021.
- [297] Durga P. Aryal, Kosmas L. Tsakmakidis, Cécile Jamois, and Ortwin Hess. Complete and robust bandgap switching in double-inverse-opal photonic crystals. *Applied Physics Letters*, 92(1):11109, 2008.
- [298] Eiichi Mine, Mitsuaki Hirose, Masaki Kubo, Yoshio Kobayashi, Daisuke Nagao, and Mikio Konno. Synthesis of Submicron-Sized Titania-Coated Silica Particles with a Sol-Gel Method and Their Application to Colloidal Photonic Crystals. *Journal of Sol-Gel Science and Technology*, 38(1):91–95, 2006.
- [299] Hikaru Namigata. Master Thesis (Tohoku University): 3D photonic crystals composed of rattle-type particles with electrically switchable inner structure, 2021.
- [300] R.G. LeBel and D.A.I. Goring. Density, Viscosity, Refractive Index, and Hygroscopicity of Mixtures of Water and Dimethyl Sulfoxide. *Journal of Chemical and Engineering Data*, 7(1):100–101, 1962.
- [301] Paul J. Steinhardt, David R. Nelson, and Marco Ronchetti. Bond-orientational order in liquids and glasses. *Physical Review B*, 28(2):784–805, 1983.
- [302] Wolfgang Lechner and Christoph Dellago. Accurate determination of crystal structures based on averaged local bond order parameters. *The Journal of Chemical Physics*, 129(11):114707, 2008.
- [303] Charles Kittel. *Introduction to Solid State Physics*. Wiley, New York, 1996.
- [304] A. Bierbaum, C. Dux, and H. Versmold. Observation of the Debye-Waller factor in a colloidal single crystal. *Molecular Physics*, 93(4):615–618, 1998.
- [305] S.J. Oldenburg. *Light Scattering from Gold Nanoshells*. PhD thesis, Rice University, 2000.

Summary

This thesis describes the study of nanoscale rattle-type particles, also called yolk-shell particles, using liquid-cell electron microscopy, confocal microscopy and finite-element calculations. Rattle-type particles consist of a core particle within a hollow, porous shell. When these particles are dispersed in a liquid the core particle can be made mobile, which makes them reminiscent of rattles. Rattle-type particles are particularly interesting for optical applications. As such, the size of most of the particles used in this thesis are similar to the wavelength of visible light. By assembling the shells on a periodic lattice and manipulating the core particles independently of the shells, switchable colloidal crystals can be realized. In this work we studied the mobility of the core particles within the shell, as well as the colloidal interactions between the core particle and the shell in which the core moves around. We furthermore investigated how the core particles could be controlled using electric fields, so that rattle-type particles could be used as building blocks for switchable colloidal crystals. Another aim of this work was to develop the new field of liquid-cell electron microscopy. Specifically, we were interested in investigating whether the technique could be used to study the self-assembly of nanoparticles. Rattle-type particles were used as a model system to investigate whether Brownian motion, colloidal interactions and the effect of external fields could be studied in liquids in an electron microscope without significant electron beam effects, as these are crucial elements in the self-assembly of nanoparticles.

Colloidal particles in a liquid move around due to thermal fluctuations *via* Brownian motion. However, in a liquid-cell the sample is irradiated with high-energy electrons, which generally results in particles becoming attached to one of the walls of the liquid-cell. The particles typically move slightly near the wall under the influence of the electron beam, but this in no way resembles Brownian motion of particles in three dimensions. In **Chapter 2** we tackled the challenge of observing Brownian motion of particle in three dimensions within an electron microscope. Using low electron dose rates (less than $10 \text{ e}^- \text{ nm}^{-2} \text{ s}^{-1}$) and viscous liquids we could observe that 350 nm titania particles exhibited diffusion that was consistent with Brownian motion. However, it was difficult to discern if they were moving in 3D. Smaller 77 nm gold particles were observed to get blurry during some stretches of the recorded videos, due to their movement along the direction of the electron beam. The blurriness originated from the broadening of the electron beam when the beam had to travel further through the liquid before it encountered a particle. This was confirmed when we simulated the image formation with electrons by Monte Carlo methods. These results show that liquid-cell scanning transmission electron microscopy is able to record 3D Brownian motion of nanoparticles, which is the first step to being able to do self-assembly experiments in liquid in the electron microscope.

The Brownian motion of a particle within a shell is complicated by the hydrodynamic interactions between the core particle and the surrounding shell. In **Chapter 3** we imaged

the diffusion of core particles within their shells in 3D with fluorescence confocal microscopy. It was found that the diffusion of the particle towards the shell wall and along the shell wall could be decoupled. The diffusion coefficient of the particle moving towards the shell wall decreased relatively quickly when approaching the shell, while the diffusion coefficient of the particle moving along the shell wall remained relatively stable, regardless of the particle position within the shell. These findings were corroborated by finite-element calculations that solved Stokes' equations for fluid dynamics of an incompressible fluid resulting in the calculation of the hydrodynamic force acting on the particle when moving within the shell. Hydrodynamic slowing down of particles within a confining geometry is of interest in areas of research such as the dynamical behavior of biological and other soft matter systems and helps us to understand the complex dynamics within a rattle-type particle.

An important aspect of using rattle-type particles in switchable colloidal crystals is the extent to which the core explores the entirety of the shell without external fields. In **Chapter 4** the part of the shell that the core particles explored was imaged using liquid-cell electron microscopy. First, we showed that the influence of the electron beam on the interactions within the rattle-type particles was similar to that of a change in pH in the aqueous solvent. Understanding how the electron beam influenced the interactions allowed us to study those interactions while minimizing the beam effects. It was found that in aqueous solutions without added salt, the electric double layers originating from the core and shell surfaces were long enough to overlap significantly even if the core particles were located in the middle of their respective shells. This led to a decrease in the electrostatic repulsion between the core and shell, which allowed the core particle to explore a significant portion of the shell. When the solution was changed to aqueous 0.5 mM LiCl, the core particle was much more confined to the middle of the shell, despite the shorter electric double layers. In general, it was confirmed by finite-element calculations solving the nonlinear Poisson-Boltzmann equation that the electrostatic repulsion between core and shell was longer ranged than that between two spheres of the same dimensions and charge. This was attributed to the concave geometry of the inner side of the shell. Furthermore, an apparent attraction between the core and shell at high salt concentrations (100 – 250 mM) was found in the 2D projected microscopy images. Using the knowledge of the hydrodynamics gained previously and by simulating how the images were formed with electrons, it was found that the hydrodynamic slowing down of the core particle and the finite time of our measurements were able to (partly) explain the apparent attraction. As such, both hydrodynamics and van der Waals attractions could explain the observed apparent attraction. Lastly, we showed that the interactions of a nanoparticle (radius 17 nm) within a shell could be measured using liquid-cell electron microscopy. These results allow us to tune the part of the shell the core particles explore without an external field, which is required to design switchable colloidal crystals with rattle-type particles as building blocks.

After understanding and tuning the interactions between the core particles and their shells with the salt concentration, we shifted our attention to the manipulation of the core particles with an external electric field. In **Chapter 5** we systematically investigated the response of the core particles to an external AC electric field as function of frequency, shell thickness and porosity, salt concentration, and inner shell radius, while keeping the core particle size

constant. In 2 mM aqueous solution we observed several core particle (radius 170 nm) mobility patterns within the shell (inner radius 370 nm) for frequencies between 1 to 50 kHz. At low frequencies (below 3 kHz) the core particles moved parallel to the electric field from one side of the shell to the other. This movement was driven by the electric field. At intermediate frequencies (5 – 20 kHz) diffusive motion of the core particles orthogonally to the electric field was observed. At high frequencies (above 40 kHz) the particle mobility resembled that of Brownian motion as if no electric field was applied. Finite-element calculations solving the Poisson-Nernst-Planck-Stokes equations for electric potential, ion migration, and fluid flow in a rattle geometry in an AC electric field were employed to understand these mobility patterns. In these simulations the core particle was allowed to move during the simulations according to the electric and viscous forces acting upon it. It was found that for frequencies around 5 kHz the ionic distributions within the shell were significantly disturbed compared to steady state such that the core particle was pushed towards the middle of the shell. This effect was strong enough to overcome Brownian motion, leading to the diffusive motion only in the direction orthogonal to the electric field in the experiments. For frequencies below 3 kHz the calculations also resulted in the core particle moving from one side of the shell to the other, like in the experiments. The finite-element calculations also predicted that the porosity of the shell would influence the electric field within the shells, and thus the mobility of the core particles within. This was experimentally observed as a more porous shell led to more restricted mobility of the core particles at intermediate frequencies. Furthermore, thicker, less porous shells led to the parallel, driven core movement shifting to lower frequencies. In this chapter, we experimentally used salt concentrations of 0.2, 2 and 25 mM. For these salt concentrations the frequency-dependent mobility patterns were similar, which was corroborated by the calculations. Our finite-element model was furthermore used to explain why in previous work restricted motion of the core particles was found at 1 kHz in aqueous solution without added salt. Finally, a larger inner shell radius was found to shift the earlier observed mobility patterns to lower frequencies. This work shows the interesting and complex electrokinetics of mobile particles within porous shells under AC electric field application and allows us to manipulate the core particle position within the shell.

In the chapters mentioned above, we investigated the interactions between the core particles and shells, as well as the possibility of manipulating the core particle with an external AC electric field. In **Chapter 6** we combined these studies to create a switchable colloidal crystal. First, rattle-type particles were assembled on a 2D lattice and the core particles were imaged using confocal microscopy. The frequency regime for which the core particles collectively moved from one side of their shell to the other was found to be the most suitable frequency regime to use for switchable colloidal crystals of rattle-type particles. For the 2D lattices, the core particles moved around within their shells randomly with no electric field. As such the distances between the core particles were relatively random and the radial distribution function did not have sharp peaks. When the electric field was switched on, the core particles moved throughout their shells while having regular distances between core particles and therefore the radial distribution function had sharper peaks. We furthermore found that the switching between the state of the particles with the electric field on or off was

reversible. Our collaborators at Tohoku University assembled a 3D face-centered cubic crystal of rattle-type particles in 2 mM aqueous solution. When applying an electric field (100 Hz, 24 V mm^{-1}), the reflection intensities of the Bragg peaks were increased. The increase could be explained by Debye-Waller factors. Finally, we used Debye-Waller factors to calculate how to improve the change in Bragg peak intensity between the states when the field is off or on. An increase in the salt concentration from 2 mM to 10 mM was found to only enhance the change in Bragg peak intensity by less than a factor 2. However, changing the core-to-shell ratio from 0.5 to 0.25 was predicted to enhance the Bragg peak intensity change by a factor 10 approximately. These results help to design a switchable photonic crystal with greatly enhanced Bragg peak intensities when an electric field is switched on, compared to when it is off.

In general, in this thesis, we explore the dynamics and interactions of rattle-type particles and how these particles can be used to obtain switchable photonic crystals by using electric fields. Furthermore, we show that liquid-phase electron microscopy can be used to study colloidal interactions at high spatial resolution.

Samenvatting

Dit proefschrift beschrijft een onderzoek naar ‘rammelaardeeltjes’, ook wel yolk-shelldeeltjes genoemd, met behulp van vloeistofcel-elektronenmicroscopie, confocale microscopie en finite-element berekeningen. Deze rammelaardeeltjes zijn deeltjes die bestaan uit een kerndeeltje binnen een hol, poreus schilletje. Als deze samengestelde deeltjes zich in een vloeistof bevinden kunnen de kerndeeltjes bewegen, waardoor je het effect van een rammelaar krijgt. De deeltjes zijn vooral interessant voor optische toepassingen. De afmetingen van de meeste deeltjes die in dit proefschrift worden bestudeerd, komen daarom ongeveer overeen met de golflengte van zichtbaar licht. Door de rammelaardeeltjes op een periodiek rooster samen te voegen en de kerndeeltjes onafhankelijk van de schilletjes waar ze in zitten te manipuleren, kunnen schakelbare kolloïdale kristallen gerealiseerd worden. In dit werk hebben we de beweging van de kerndeeltjes binnen hun schilletje bestudeerd, alsmede de kolloïdale interacties tussen het kerndeeltje en het schilletje waarin het kerndeeltje beweegt. Verder onderzochten we hoe de kerndeeltjes beïnvloed kunnen worden door elektrische velden, opdat ‘rammelaar deeltjes’ gebruikt kunnen worden als bouwstenen voor een schakelbaar kolloïdaal kristal. Een ander doel van dit werk was om het nieuwe veld van vloeistofcel-elektronenmicroscopie naar een hoger niveau te tillen. We waren vooral geïnteresseerd in de vraag hoe de techniek gebruikt zou kunnen worden om de zelf-organisatie van nanodeeltjes te bestuderen. Rammelaardeeltjes werden gebruikt als modelsysteem om te onderzoeken of Brownse beweging, kolloïdale interacties en het effect van externe velden met deze techniek bekeken kon worden in vloeistoffen in de elektronenmicroscopie zonder significante invloed van de elektronenbundel, omdat dit cruciale elementen zijn in het zelf-organiseren van nanodeeltjes.

Kolloïdale deeltjes in een vloeistof ondervinden Brownse beweging door toedoen van thermische fluctuaties, maar in een vloeistofcel wordt het monster bestraald met elektronen van hoge energie, waardoor de deeltjes doorgaans vast blijven zitten aan de wanden van de vloeistofcel. De deeltjes bewegen dan doorgaans een klein beetje terwijl ze in de buurt van de wanden blijven door de invloed van de elektronenbundel. Dit heeft echter niks weg van Brownse beweging in drie dimensies. In **Hoofdstuk 2** gingen we de uitdaging aan om Brownse beweging van deeltjes in drie dimensies te observeren in de elektronenmicroscopie. Door een lage dosis elektronen (minder dan $10\text{ e}^- \text{ nm}^{-2} \text{ s}^{-1}$) en stroperige vloeistoffen te gebruiken konden we diffusie van 350 nm titania deeltjes observeren met de elektronenmicroscopie die consistent was met Brownse beweging. Het was echter moeilijk om te achterhalen of ze echt in drie dimensies bewogen. Kleinere goud deeltjes van 77 nm werden wazig op bepaalde tijdstippen tijdens het opnemen van de video, omdat ze in de richting parallel aan de elektronenbundel bewogen. Het wazig worden van de deeltjes kwam door het breder worden van de elektronenbundel wanneer de bundel verder door de vloeistof heen moest voordat deze een deeltje bereikte. Dit werd bevestigd toen we de beeldvorming met elektronen simuleerden met

Monte Carlo-methoden. Deze resultaten laten zien dat het mogelijk is om met vloeistofcel-elektronenmicroscopie de 3D Brownse beweging van nanodeeltjes te observeren. Dit is de eerste stap om zelf-organisatie experimenten in vloeistof in de elektronenmicroscopie mogelijk te maken.

De Brownse beweging van een deeltje binnen een schilletje is lastiger te begrijpen door de hydrodynamische interacties tussen het kerndeeltje en het schilletje wat eromheen zit. In **Hoofdstuk 3** brachten we de diffusie van kerndeeltjes binnen hun schilletje in beeld in 3D met confocale fluorescentie-microscopie. Het werd duidelijk dat de diffusie van een deeltje richting het schilletje en de diffusie van een deeltje langs het schilletje ontkoppeld konden worden. De diffusiecoëfficiënt van een deeltje dat richting het schilletje bewoog werd relatief snel minder wanneer het deeltje dichter bij het schilletje kwam. Daarentegen bleef de diffusiecoëfficiënt van een deeltje dat in de richting langs het schilletje bewoog relatief stabiel, onafhankelijk van de positie van het deeltje binnen het schilletje. Deze bevindingen werden bevestigd door finite-element-berekeningen die Stokes' vergelijkingen voor vloeistofdynamica van een onsamendrukbare vloeistof oploste en resulteerde in de berekening van de hydrodynamische kracht die op het deeltje werkte wanneer dit deeltje bewoog in een schilletje. Het hydrodynamisch afremmen van deeltjes binnen een begrensde geometrie is interessant voor vakgebieden zoals het dynamische gedrag van biologische en andere zachte materie-systemen. Bovendien helpen deze metingen ons om de complexe dynamica binnen een rammelaardeeltje te begrijpen.

Een belangrijk aspect van het gebruik van rammelaardeeltjes binnen schakelbare kolloïdale kristallen is de mate waarin het kerndeeltje het volledige volume binnen het schilletje kan bezoeken zonder externe velden. In **Hoofdstuk 4** werd het deel van het schilletje dat door de kerndeeltjes bezocht kon worden in beeld gebracht met vloeistofcel-elektronenmicroscopie. Ten eerste lieten we zien dat de invloed van de elektronenbundel op de interacties binnen het rammelaardeeltje vergelijkbaar was met een verandering in pH van de waterige oplossing. De kennis van de invloed van de elektronenbundel op de interacties maakte het mogelijk dat we deze interactie konden bestudeerden terwijl we de invloed van de bundeleffecten minimaliseerden. We kwamen te weten dat in waterige oplossingen zonder toegevoegd zout de elektrische dubbellagen, die van de oppervlakten van het kerndeeltje en het schilletje afkwamen, lang genoeg waren om significant te overlappen, zelfs wanneer een kerndeeltje zich in het midden van het schilletje bevond. Dit zorgde ervoor dat de elektrostatistische afstoting tussen het kerndeeltje en het schilletje niet hoog was, waardoor het kerndeeltje een redelijk groot deel van het volume binnen de schil kon bezoeken. Wanneer we de deeltjes in een waterige oplossing met 0.5 mM LiCl bekeken was het deeltje veel meer opgesloten in het midden van het schilletje, ondanks de kortere elektrische dubbellagen. In het algemeen werd bevestigd door finite-element-berekeningen die de niet-lineaire Poisson-Boltzmann vergelijking oplosten, dat de elektrostatistische afstoting van een kerndeeltje in een schilletje hoger was dan dat tussen twee sferische deeltjes met dezelfde grootte en elektrische lading. Dit kwam door de concave geometrie van de binnenkant van het schilletje. Verder werd er een ogenschijnlijke aantrekkingskracht tussen het kerndeeltje en het schilletje in hoge zoutconcentraties (100 – 250 mM) gevonden in de 2D geprojecteerde microscopieplaatjes. Met de kennis over de hydrodynamica binnen

een rammelaardeeltje die we eerder vergaard hebben en door het simuleren van beeldvorming door elektronen, konden we bepalen dat het hydrodynamisch afremmen van het kerndeeltje en de eindige tijd van onze metingen de schijnbare attractie (deels) konden verklaren. Vandaar dat zowel hydrodynamica als Van der Waals-attracties de geobserveerde schijnbare attractie tussen het kerndeeltje en de schil zouden kunnen verklaren. Tenslotte lieten we zien dat interactie van een nanodeeltje (straal 17 nm) binnen een schilletje gemeten kon worden met vloeistofcel-elektronenmicroscopie. Deze resultaten helpen ons om het deel van het schilletje dat de kerndeeltjes bezoeken, af te stemmen zonder een extern veld, hetgeen nodig is om schakelbare kolloïdale kristallen te maken met rammelaardeeltjes als bouwstenen.

Nadat we de interacties tussen de kerndeeltjes en hun schilletjes begrepen en konden afstemmen met de zoutconcentratie, verlegden we onze aandacht naar het manipuleren van de kerndeeltjes met een extern elektrisch veld. In **Hoofdstuk 5** onderzochten we systematisch hoe kerndeeltjes reageerden op een extern AC elektrisch veld als functie van de frequentie van het veld, de dikte en porositeit van het schilletje, de zoutconcentratie en de binnenstraal van het schilletje, terwijl we de grootte van de kerndeeltjes gelijk hielden. In waterige oplossing met 2 mM zout observeerden we verschillende mobiliteitspatronen van een kerndeeltje (straal 170 nm) binnen een schilletje (binnenstraal 370 nm) voor frequenties tussen de 1 en 50 kHz. Bij lage frequenties (lager dan 3 kHz) bewogen de kerndeeltjes van de ene kant van het schilletje naar de andere, parallel aan het elektrisch veld. Deze beweging werd aangedreven door het elektrisch veld. Bij tussenliggende frequenties (5 – 20 kHz) werd diffuse beweging van kerndeeltjes orthogonaal aan het elektrisch veld geobserveerd. Bij hoge frequenties (boven 40 kHz) deed de beweging van kerndeeltjes denken aan Brownse beweging alsof er geen elektrisch veld van toepassing was. Finite-element-berekeningen die de Poisson-Nernst-Planck-Stokes vergelijkingen voor het elektrisch potentiaal, ionmigratie en vloeistofstromen oplosten voor een rammelaargeometrie in een AC elektrisch veld werden gebruikt om deze mobiliteitspatronen te begrijpen. In deze simulaties kon het kerndeeltje bewegen naar aanleiding van de elektrische en viskeuze krachten die erop werkten. We vonden dat voor frequenties rond 5 kHz de verdeling van ionen binnen het schilletje significant veranderd was ten opzichte van de situatie zonder elektrisch veld. Dit leidde er toe dat het kerndeeltje teruggeduwd werd naar het midden van het schilletje. Dit effect was sterk genoeg om Brownse beweging te overwinnen, waardoor het tot de diffuse beweging van kerndeeltjes in de richting orthogonaal aan het elektrisch veld leidde in de experimenten. Voor frequenties onder de 3 kHz resulteerden de berekeningen ook in een kerndeeltje dat van een kant van het schilletje naar de andere kant bewoog, zoals in de experimenten. De finite-element-berekeningen voorspelden ook dat de porositeit van het schilletje het elektrisch veld binnen de schil zou beïnvloeden en daardoor ook de beweging van de kerndeeltjes. Dit werd ook experimenteel geobserveerd. Een schilletje dat meer poreus was leidde tot een beperktere mobiliteit van de kerndeeltjes bij de tussenliggende frequenties. Bovendien bewogen kerndeeltjes die zich in een dikkere, minder poreuze schil bevonden pas parallel aan het elektrisch veld op veel lagere frequenties dan voorheen. In dit hoofdstuk hebben we in experimenten zoutconcentraties van 0,2, 2 en 25 mM gebruikt. Voor deze zoutconcentraties waren de frequentie-afhankelijke mobiliteitspatronen vergelijkbaar, hetgeen bevestigd werd door de berekeningen. Ons finite-element-model werd bovendien gebruikt om

uit te leggen waarom er in een eerder werk beperkte mobiliteit van de kerndeeltjes geobserveerd werd voor 1 kHz in waterige oplossing zonder toegevoegd zout. Tenslotte vonden we dat een grotere binnenstraal van de schil leidde tot een verlaging van de frequenties die nodig waren om de voorheen geobserveerde mobiliteitspatronen te observeren. Dit werk laat de interessante en complexe electrokinetiek van mobiele deeltjes binnen poreuze schilletjes zien tijdens het gebruik van AC elektrische velden. Bovendien stelt het ons in staat om de positie van een kerndeeltje binnen een schil te manipuleren.

In de bovengenoemde hoofdstukken onderzochten we de interacties tussen kerndeeltjes en het schilletje waarin ze zich bevonden en ook hoe we kerndeeltjes konden manipuleren met behulp van een extern AC elektrisch veld. In **Hoofdstuk 6** hebben we deze studies gecombineerd om een schakelbaar kolloïdaal kristal te maken. Ten eerste werden rammelaar-deeltjes samengepakt op een 2D rooster en werden de kerndeeltjes in beeld gebracht met confocale microscopie. De frequenties waarvoor de kerndeeltjes collectief van de ene naar de andere kant van hun schilletje bewogen werden de meest geschikte frequenties bevonden om te gebruiken voor een schakelbaar kolloïdaal kristal van rammelaar-deeltjes. Zonder elektrisch veld bewogen de kerndeeltjes willekeurig door hun schilletje heen. Daardoor waren de afstanden tussen kerndeeltjes redelijk willekeurig en had de radiale distributiefunctie geen scherpe pieken. Wanneer het elektrisch veld aangezet werd bewogen de kerndeeltjes collectief van de ene naar de andere kant in hun schilletjes terwijl de afstand tussen de kerndeeltjes dus hetzelfde bleef en de radiale distributiefunctie scherpe pieken kreeg. Verder vonden we ook dat het aan- en uitzetten van het elektrisch veld tot een reversibel effect op de beweging van de kerndeeltjes leidde. Onze medewerkers in Tohoku University voegden de rammelaar-deeltjes samen in een 3D face-centered cubic kristal in 2 mM waterige oplossing. Wanneer een elektrisch veld (100 Hz, 24 V mm⁻¹) aangezet werd nam de intensiteit van de Bragg-pieken toe. Deze toename kon verklaard worden door middel van Debye-Waller-factoren. Tenslotte gebruikten we Debye-Waller-factoren om te berekenen hoe de verandering in intensiteit van de Bragg-pieken tussen de situaties met en zonder elektrisch veld het best verbeterd kon worden. Een verhoging van de zoutconcentratie van 2 tot 10 mM zou de verandering in Bragg-piekintensiteit slechts met minder dan een factor 2 verbeteren. Daarentegen zou een verandering van de ratio tussen de grootte van een kerndeeltje en een schilletje van 0.5 tot 0.25 de Bragg-piekintensiteitsverandering met ongeveer een factor 10 kunnen verbeteren. Deze resultaten helpen om een schakelbaar fotonisch kristal te maken met een groot verschil tussen de Bragg-piekintensiteiten wanneer het elektrisch veld aan of uit staat.

In het algemeen onderzoeken we in dit proefschrift de dynamica en interacties van rammelaar-deeltjes en hoe deze deeltjes gebruikt kunnen worden om schakelbare fotonische kristallen te maken door middel van elektrische velden. Bovendien laten we zien dat vloeistofcel-elektronenmicroscopie gebruikt kan worden om kolloïdale interacties te bestuderen met een hoge resolutie.

Acknowledgements

First of all, I would like to express my gratitude towards my supervisors Marijn, Joost and Alfons. Thank you for allowing me to do my Ph.D. research under your guidance. To my daily supervisor Marijn, thank you for always being supportive in every regard. You are a great scientist and manager at the same time. Besides, you allowed me to go to Japan when I asked for that, I will never forget it. You take care of your students, and that is a great asset. Joost, thank you for your patience in supervising an experimentalist dabbling in finite-element calculations. While you were in no way obligated to do so, you were happy to teach me, which resulted in our request for you to be added as my co-promotor. You also always made time for me extremely quickly whenever I needed help or when my less-than-stellar writing needed some touching up. Alfons, your knowledge of the field is always stated here. And it is incredible, mind-boggling. However, I would like to say that you are not just a great scientist, but you were also a great coach for me. You pushed the exact right buttons to allow me to improve myself with your great, great feedback. You supplied me with the tools, and I am forever grateful. I thank all of you for giving me so much freedom in my scientific research. It was an honor.

Next up we have the liquid cell team, Sina and Albert. I cannot imagine how different this journey would have been without you. A pleasant working environment with great friends was most definitely key to any sliver of success. Sina, from the moment I stepped into your office to ask you to do my first liquid-cell experiment with me it felt comfortable. It had to be as the first year of experiments were rough in a scientific sense, but somehow never in any other sense. We had great times, especially during the Antwerp EMAT school (San Remo and Don Giovanni man...) and other trips to conferences. Even now you live in Den Haag, we are constantly coming up with excuses for one of us to travel the (admittedly tiny) distance. Albert, we already knew one another from the Nanomaterials Master here in Utrecht and I remember being hyped when I heard you were in talks with Marijn to come back to Utrecht to do your Ph.D. Realistically, you were a key component to get our spirits up with your relentless positivity. You were also always in for a drink and if a new Star Wars or Marvel or any other geeky movie came out, you bet we were already on our way to see it. Besides that you are just a really good scientist and somehow great at designing beautiful covers. Thank you both for contributing so positively to my Ph.D. Thanks also to Shahrzad and Paula to being the better halves of already great people.

I would also like to thank the rest of the scientific staff of the SCMB group: Arnout, Marjolein, René, Patrick, Freddy, Laura, Krassimir, Hans, Gerhard, and Lisa. Thank you for the valuable comments and suggestions during group meetings. They certainly enhanced my research. Arnout, thank you for your input on double layers within the rattle-type particles and their response to electric fields, as well as your suggestion of looking at Debye-Waller

factors. I am honored to have worked in a group with such a nice atmosphere and great knowledge.

My research would not have been possible without the help of the technical and supporting staff. Chris and Hans, thanks for always taking the time to have a chat and for creating a nice atmosphere at the Electron Microscopy Center in general. I spent a lot of time at the microscopes, first mostly in the Kruijt building and later in the Androclus building. Your awesome support during these years was critical. I would name your qualities separately, but regardless of professional position or any other differences, to me it seems you guys are inseparable. Thanks for all the great moments we shared. Peter and Dave, thanks for your willingness to help me with all sorts of problems that arose when I used computers or other equipment, no matter how trivial. I would like to thank Judith, Fabian, Elleke, and Relinde for giving me a safe and well-organized lab environment to work in. Hester, Dianne, and Marion, I would like to thank you for helping me with official procedures during these years. Hester, I appreciated your help with receiving and sending packages to Japan!

Thanks to the in-situ electron microscopy community in Utrecht besides SCMB. Nynke, Mark, Lars, Savannah, Nienke, Min and Kris, thanks for sharing your knowledge and obstacles. I would also like to express my gratitude to Krijn and Petra for allowing me to continue to do research with electron microscopes in Utrecht while Kanako was still here.

Next I would like to thank all the people in the SCMB group during my time here. Specifically, I thank those whom I had the pleasure of sharing an office with: Dnyaneshwar & Xiaodan (albeit shortlived), Berend, Roy, Robin & Sina. Thanks also to Rama and Naveed for being ever present in the SCMB group and facilitating the great atmosphere. Thanks to the noisy Italian office neighbours Gabriele, Emanuele & Massi. Maarten, thank you for being a bit of a constant for me throughout my time in SCMB, starting from the shared time during our Master projects. Thank you Harith & Zahra for making me feel connected to the group beyond my contract after the pandemic. Thank you Daphne for being a great master student during challenging times! Next I would like to specifically express my gratitude to the people guiding me in SCMB before my Ph.D. research. Wiebke, thank you for being exactly the supervisor I needed during my Master thesis and to this day. Thanks to Patrick & Fabian for teaching me the ropes in my Bachelor. Great appreciation goes out to Jessi as well for always having time when needed, even though you were not required to. I am grateful to all former and current members of the SCMB group I somewhat overlapped with. Simone, Ernest, Wessel, Guido, Nick, Giulia, Tonnishita, Vassilis, Doug, Carmine, Chris, Somil, Murphy, Xiaobin, Vats, Pepijn, Henriëtte, Sid, Da, Harini, Rik, Anna, Frankje, Ravi, Ajoy, Federico, Alberto, Arya, Kelly, Marjolein, Willem, Diogo, Gerardo, Stijn, Mark, Erik, and Sander thank you for contributing to such a nice working environment.

長尾先生、私を何度も受け入れてくれてありがとうございます。長尾ラボの学生、ありがとうございます。光と明、残りのPhD生活もがんばれ！浩さん、智子さん、泊まらせてくれてありがとうございます。まりちゃん、兄貴、色々なところに連れて行ってくれてありがとうございます。

I cannot overstate how different my last four years would have been had I not met you, Kanako. Thank you for allowing us to blossom. We managed to make it work while living

far apart for over 2 years. When you moved to Utrecht in the midst of a pandemic, it was exactly what I needed. Words cannot describe. ありがとうね。

Tenslotte, mam, pap en Emma. Em, je hebt me altijd op jouw manier gesupport, en ik zou het op geen andere manier willen hebben. Pap, mam, zonder jullie was ik nergens geweest. Jullie staan altijd voor me klaar, hoe bizar de situatie ook is. Jullie zullen zeggen dat dat is omdat jullie ouders zijn, maar goed. Bedankt.

List of Publications

THIS THESIS IS BASED ON THE FOLLOWING PUBLICATIONS:

- **T.A.J. Welling**, S. Sadighikia, K. Watanabe, A. Grau-Carbonell, M. Bransen, D. Nagao, A. van Blaaderen, M.A. van Huis, Observation of undamped 3D Brownian motion of nanoparticles using liquid-cell scanning transmission electron microscopy, *Particle and Particle Systems Characterization*, 2020, 37, 6, 2000003 (**Chapter 2**)
- **T.A.J. Welling**, D.M. Dekker, Z. Peimanifard, S. Sadighikia, K. Watanabe, A. van Blaaderen, and M.A. van Huis, Colloid diffusion and hydrodynamic interactions in a rigid spherical shell, *in preparation* (**Chapter 3**)
- **T.A.J. Welling**, K. Watanabe, A. Grau-Carbonell, J. de Graaf, D. Nagao, A. Imhof, M.A. van Huis, A. van Blaaderen, Tunability of interactions between the core and shell in rattle-type particles studied with liquid-cell electron microscopy, *ACS Nano*, 2021, 15, 7, 11137 – 11149 (**Chapter 4**)
- **T.A.J. Welling**, A. Grau-Carbonell, K. Watanabe, D. Nagao, J. de Graaf, M.A. van Huis, and A. van Blaaderen, Frequency-controlled mobility of a particle within a porous yolk-shell geometry in electric fields, *submitted* (**Chapter 5**)
- H. Namigata, **T.A.J. Welling**, K. Suga, A. Imhof, M.A. van Huis, A. van Blaaderen, D. Nagao, K. Watanabe, Colloidal crystals from rattle-type particles with control over the Bragg scattering strength using an external AC electric field, *in preparation* (**Chapter 6**)

OTHER PUBLICATIONS BY THE AUTHOR:

- M.J.J. Mangnus, J. Zom, **T.A.J. Welling**, A. Meijerink, F.T. Rabouw, Finite-Size Effects on Energy Transfer between Dopants in Nanocrystals, *ACS Nanoscience Au*, 2021, Accepted
- A. Grau-Carbonell/S. Sadighikia, **T.A.J. Welling**, R.J.A. Moes, R. Kotni, M. Bransen, A. van Blaaderen, and M.A. van Huis, *In situ* study of the wet chemical etching of SiO₂ and Nanoparticle@SiO₂ core-shell nanospheres, *ACS Applied Nano Materials*, 2021, 4, 2, 1136-1148

- S. Sadighikia/A. Grau-Carbonell, **T.A.J. Welling**, R. Kotni, F. Hagemans, A. Imhof, M.A. van Huis, and A. van Blaaderen, Low-dose liquid cell electron microscopy investigation of the complex etching mechanism of rod-shaped silica colloids, *Nano Select*, 2020, 2, 2, 313-327
- K.Watanabe, **T.A.J.Welling**, S. Sadighikia, H. Ishii, A. Imhof, M.A. van Huis, A. van Blaaderen, D. Nagao, Compartmentalization of gold nanoparticle clusters in hollow silica spheres and their highly dense assembly induced by an external electric field, *Journal of Colloid and Interface Science*, 2020, 566, 202-210
- J.E.S. van der Hoeven, **T.A.J. Welling**, T.A.G. Silva, J.E. van den Reijen, C. La Fontaine, X. Carrier, C. Louis, A. van Blaaderen, and P.E. de Jongh, *In situ* observation of atomic redistribution in alloying gold-silver nanorods, *ACS Nano*, 2018, 12, 8, 8467-8476
- J.E. van den Reijen, S. Kanungo, **T.A.J. Welling**, M. Versluijs-Helder, T.A. Nijhuis, K.P. de Jong, P.E. de Jongh, Preparation and particle size effects of Ag/ α -Al₂O₃ catalysts for ethylene epoxidation, *Journal of Catalysis*, 2017, 356, 65-74

Oral and Poster Presentations

PART OF THIS THESIS WAS PRESENTED AT:

- EMAT Workshop on Transmission Electron Microscopy, 2017, Antwerp (Belgium) (poster)
- European Colloid and Interface Society (ECIS), 2018, Ljubljana (Slovenia) (oral)
- Nanoseminar, 2018, Utrecht (the Netherlands) (oral)
- European Colloid and Interface Society (ECIS), 2019, Leuven (Belgium) (poster)
- Okinawa Colloids, 2019, Nago (Japan) (oral)
- First Materials Science EM meeting, 2020, Utrecht (the Netherlands) (oral)
- Physics@Veldhoven, 2020, Veldhoven (the Netherlands) (poster)
- Gordon Research Conference on Liquid Phase Electron Microscopy, 2020, Barga (Italy) (oral & poster)

About the author

Tom Welling was born on the 22nd of February in 1993, Oosterhout, the Netherlands. He attended the ‘Sint-Oelbertgymnasium’ in Oosterhout and graduated in 2011. After high school he started the Physics & Astronomy bachelor at Utrecht University, which he graduated in 2014. He performed the research for his Bachelor’s project (“Manipulating the Refractive Index with Responsive Colloids”) under supervision of dr. Patrick Baesjou in the group of prof. Alfons van Blaaderen. Fascinated by his Bachelor’s project he started the Master Nanomaterials Science at Utrecht University. In 2017 he graduated after performing his Master’s research (“Optical Properties and Alloying of Metal Nanorods”) under supervision of dr. Wiebke Albrecht and prof. Alfons van Blaaderen. In February 2017 he started his PhD research supervised by dr. Marijn van Huis and prof. Alfons van Blaaderen. During his PhD research he spent several months in the group of prof. Daisuke Nagao at Tohoku University. He presented the work described in this thesis at many international conferences, until the covid-19 pandemic brought that to a screeching halt. Currently he is working on in-situ gas-cell electron microscopy to study the decomposition of methane into carbon nanofibers and hydrogen gas using nickel-based catalysts in the Materials Chemistry & Catalysis group at Utrecht University under the supervision of prof. Krijn de Jong and prof. Petra de Jongh.

